

N72-20342
9G90-8

NIMBUS EARTH RESOURCES OBSERVATIONS

TECHNICAL REPORT NO. 2

NOVEMBER 1971

CONTRACT NO. NAS 5-21617

**CASE FILE
COPY**

ROMEO R. SABATINI

GEORGE A. RABCHEVSKY

JOHN E. SISSALA

prepared for
NATIONAL AERONAUTICS AND SPACE ADMINISTRATION
GODDARD SPACE FLIGHT CENTER
GREENBELT, MARYLAND



ALLIED RESEARCH ASSOCIATES, INC.
VIRGINIA ROAD • CONCORD, MASSACHUSETTS

NIMBUS EARTH RESOURCES OBSERVATIONS
TECHNICAL REPORT # 2
CONTRACT No. NAS 5-21617
ERRATA SHEET

Page No. xii Figure 3-4 - Change reference to 0.7 to $1.3\mu\text{m}$ to read 3.4 to $4.2\mu\text{m}$.

Page No. 2 Table 1-1 - Change last foot note reference to ERLS to IRLS.

Page No. 31 Figure 2-11 d. - Top center of Map references Rio Uruguay change to Rio Paraguay.

Page No. 40 Figure 2-17 - Nimbus 4 IDCS image change year date to read 1970.

Page No. 72 Table 2-4 - Under column for Orbit No. change 1774 to 1714.

Page No. 134 Figure 3-10 - First picture Orbit 245 change date to read 26 April 1970.

Page No. 140 Line 9 - Change date 15 March 1969 to read 15 April 1969.

Page No. 145 Figure 3-20 - Top left picture Orbit 44 change date from 17 May to 18 May.

Page No. 175 6.2 Section 2 - Reference to Ackerman should be Ackermann.

Page No. 177 6.2 Section 2 - Reference to Hovis M should read Hovis W.

Page No. 198 Line 10 - Change $20\mu\text{m}$ to $30\mu\text{m}$.

Page No. 223 Line 5 - Change Nimbus II to read Nimbus III.

NIMBUS EARTH RESOURCES OBSERVATIONS

TECHNICAL REPORT NO. 2

NOVEMBER 1971

CONTRACT NO. NAS 5-21617

ROMEO R. SABATINI

GEORGE A. RABCHEVSKY

JOHN E. SISSALA

prepared for
NATIONAL AERONAUTICS AND SPACE ADMINISTRATION
GODDARD SPACE FLIGHT CENTER
GREENBELT, MARYLAND



ALLIED RESEARCH ASSOCIATES, INC.
VIRGINIA ROAD • CONCORD, MASSACHUSETTS

FOREWORD

This report illustrates the potential for utilizing data gathered by the Nimbus Meteorological Satellites to study the earth surface and its physical properties. The contents of the report were developed from an extensive survey of the literature, from responses to personal inquiries to Government and private research agencies, both domestic and foreign, and from the results of inhouse projects not previously published. We apologize to those investigators whose studies are not included in this survey, and hope they will bring them to our attention for inclusion in possible later volumes of this report. Meteorological applications of the Nimbus Satellite are widely discussed in other publications.

Section 1 of this report introduces the reader to the Nimbus data applicable to the study of the earth and its resources, and to the problems of resolution and cloud cover. Geological and hydrological applications of the Nimbus data are discussed in Section 2, and oceanographic applications in Section 3. Section 4 presents applications of the data to other fields, such as cartography, agriculture, forestry, urban analysis, etc. References and bibliography for each section are provided in Section 6. The Appendixes contain relevant information on: (1) The Nimbus orbit and experiments (Appendix A), (2) surface and atmospheric effects on HRIR and THIR radiation measurements (Appendix B), and (3) noise problems in the AVCS, IDCS, HRIR, and THIR data (Appendix C).

ACKNOWLEDGEMENTS

Several other ARA staff members participated in the preparation of this report. Mr. J. Greaves (now with NASA/GSFC) wrote parts of Section 3. Mr. E. Merritt contributed Section 4.3, Urban Analysis. Messrs. J. Barnes, D. Chang, P. Sherr, and Miss M. Fowler contributed to the editing effort.

The authors acknowledge the assistance of Mr. John Lindstrom, NASA Nimbus Data Utilization Manager, in obtaining the Nimbus data necessary for this report; Dr. V. Salomonson of NASA/LMES in providing the data on the THIR accuracy and information about runoff in the Indus River Valley; Dr. J. Pouquet of NASA/LMES (presently at San Diego State College, California) in the Parana and Niger River studies; and Dr. K. Szekiolda of NASA/LMES in providing figures of the Somali coast upwelling.

The authors also wish to express special thanks to Drs. P. Lowman, N. MacLeod, N. Short, and Mr. H. Blodget, all of NASA/GSFC, for their valuable criticism and helpful comments on Section 2 of this report.

TABLE OF CONTENTS

	<u>Page</u>
FOREWORD	iii
ACKNOWLEDGEMENTS	iv
LIST OF FIGURES	viii
LIST OF TABLES	xvii
SECTION 1	
INTRODUCTION	1
1.1 Nimbus Experiments and Data Collection	1
1.2 Resolution	3
1.3 Cloud Cover	10
SECTION 2	
GEOLOGIC AND HYDROLOGIC APPLICATIONS OF NIMBUS DATA	13
2.1 Introduction	13
2.2 Regional Geomorphology	14
2.2.1 Landscape Evolution	16
2.2.2 Relief	16
2.2.3 Drainage Patterns and Geomorphic Provinces	19
2.2.4 Paleogeomorphology	25
2.2.5 Geomorphic Processes	30
2.3 Regional Geology	33
2.3.1 Regional Outcrop Patterns and Provinces	38
2.3.2 Tectonic and Structural Features	47
2.3.3 Discrimination of Lithologies	55
2.4 Volcanic and Hydrothermal Activity	68
2.5 Regional Hydrology	73
2.5.1 Surface Moisture and Surface Water Identification	73
2.5.2 Snow Surveillance	87
2.5.3 Lake Surveillance Studies	100
SECTION 3	
OCEANOGRAPHIC APPLICATIONS OF NIMBUS DATA	119
3.1 Introduction	119
3.2 Sea Surface Temperature	120
3.3 Sea Surface Current Boundaries	124
3.4 Upwelling and Sea State	129
3.5 Sea Ice	130

TABLE OF CONTENTS, contd.

	<u>Page</u>
3.5.1 Ice Concentrations	130
3.5.2 Pack Ice Boundaries	133
3.5.3 Open Water Areas Within the Polar Pack Ice	137
3.5.4 Iceberg Identification and Movement	140
SECTION 4 MISCELLANEOUS APPLICATIONS OF NIMBUS DATA	147
4.1 Cartographic and Topographic Revisions in Remote Areas	147
4.2 Tonal Boundaries in Nimbus Imagery	147
4.3 Urban Analysis	153
4.3.1 Satellite Estimates of Population	153
4.3.2 Richmond/Petersburg Evaluation	154
4.4 Data Collection from Remote Platforms	155
4.5 Brush and Forest Fire Detection	164
4.6 Ship Plumes	164
SECTION 5 CONCLUSIONS AND RECOMMENDATIONS	169
SECTION 6 REFERENCES AND BIBLIOGRAPHIES (BY SECTION)	173
6.1 Section 1	173
6.2 Section 2	175
6.3 Section 3	184
6.4 Section 4	190
APPENDIX A THE NIMBUS ORBIT AND EXPERIMENTS	193
A.1 The Nimbus Orbit	193
A.2 Description of Nimbus Experiments	193
A.2.1 Nimbus 1 Experiments	193
A.2.2 Nimbus 2 Experiments	196
A.2.3 Nimbus 3 Experiments	197
A.2.4 Nimbus 4 Experiments	199
A.2.5 Nimbus E Experiments	201
A.2.6 Nimbus F Experiments	204
A.3 Archival and Dissemination of Nimbus Data	204
APPENDIX B SURFACE EMISSIVITY AND ATMOSPHERIC EFFECTS ON NIMBUS HRIR AND THIR DATA	207
B.1 Introduction	207
B.2 Surface Emissivity and Atmospheric Effects on Nimbus HRIR and THIR Temperatures	207

TABLE OF CONTENTS, contd.

	<u>Page</u>
B.2.1 Effects of Surface Emissivity	207
B.2.2 Effects of Atmospheric Absorption	211
B.3 Daytime 3.8 μ m HRIR Measurements	212
B.4 Daytime Nimbus 3 HRIR Measurements	218
B.5 Conclusion	228
References	229
APPENDIX C	
SYSTEM NOISE IN THE NIMBUS AVCS, IDCS, HRIR, AND THIR DATA	231
C.1 Introduction	231
C.2 Nimbus 1	231
C.2.1 HRIR	231
C.2.2 AVCS	231
C.3 Nimbus 2	231
C.3.1 HRIR	231
C.3.2 AVCS	234
C.4 Nimbus 3	234
C.4.1 HRIR	234
C.4.2 IDCS	237
C.5 Nimbus 4	241
C.5.1 THIR	241
C.5.2 IDCS	241
C.6 Electronic Filtering	241
References	247
APPENDIX D	
GLOSSARY OF TERMS	249
D.1 Definitions and Acronyms	249
APPENDIX E	
ABBREVIATIONS	255

LIST OF FIGURES

<u>Figure</u>		<u>Page</u>
1-1	The Gulf of California area as imaged by various Nimbus sensors of different ground resolution and spectral range.	6
1-2	Apollo photographs of the Gulf of California area (originals were in color).	7
1-3	Aerial photomosaic of Los Angeles and Mojave Desert areas.	8
1-4	This is an enlarged portion of the Nimbus 1 AVCS image shown in Figure 2-26.	9
2-1	Nimbus 1 AVCS photograph of the Columbia River Basin and northwestern United States taken on orbit 124, 5 September 1964.	17
2-2	Nimbus 2 nighttime HRIR equivalent blackbody temperature map of Senegal, Mauritania, and Mali, western Africa taken on orbit 2206, 28 October 1966, near the beginning of the regional dry season.	18
2-3	Nimbus 1 HRIR photofacsimile taken over the southwestern United States on orbit 36, near midnight on 30 August 1964.	18
2-4	Nimbus AVCS photograph of the Canadian Rockies, British Columbia, and Alberta taken on orbit 197, 10 September 1964.	20
2-5	Nimbus 1 AVCS photograph of the Paris Basin taken on orbit 236, 13 September 1964, with a classification of geomorphic provinces.	22
2-6	Vegetation map of the Paris Basin derived from published vegetation maps.	23
2-7	Nimbus 1 AVCS photograph of southwestern France and northeastern Spain taken on orbit 46, 31 August 1964.	24
2-8	Nimbus 1 HRIR equivalent blackbody temperature map of the Nile Delta and surrounding area taken on orbit 345, 20 September 1964, with an associated terrestrial features map.	26
2-9	Nimbus 3 daytime HRIR reflectance maps (0.7 to 1.3 μm) of Central Mali, Africa.	28
2-10	Nimbus 3 daytime HRIR reflectance map of the Upper Niger River Valley, Africa taken on orbit 2965, 21 November 1969.	29
2-11	Nimbus 3 daytime HRIR reflectance maps illustrating the areal and temporal distribution of reflectance values in portions of Argentina, Brazil, Paraguay, and Uruguay.	31
2-12	Nimbus 2 nighttime HRIR equivalent blackbody temperature map of the Mexican Tuxpan-Culican coast.	32
2-13	Nimbus 1 AVCS photograph of northwestern Egypt taken on orbit 323, 19 September 1964, showing the distribution of sand dune fields and the positions of former shorelines in the vicinity of the El Fayum Depression.	34

LIST OF FIGURES, contd.

<u>Figure</u>		<u>Page</u>
2-14	Nimbus 4 IDCS photographs showing the migration of a Sahara dust storm across western Africa and the Atlantic during April 1970.	35
2-15	Nimbus 1 AVCS photograph of the Persian Gulf and the Tigris-Euphrates River delta taken on orbit 249, 14 September 1964.	36
2-16	A selection of Nimbus photographs illustrating the effects of land-forms on cloud patterns and distributions.	37
2-17	Analyses of Nimbus images showing mesoscale geologic features.	40
2-18	Map of major drainage and fault lines in the Canadian Rockies.	42
2-19	Nimbus 1 APT view of the complexly folded Appalachian Mountains in the Pennsylvania region taken on orbit 254, 14 September 1964.	43
2-20	Nimbus 1 AVCS photograph of the Chesapeake Bay region and vicinity taken on orbit 137, 6 September 1964.	44
2-21	USGS aerial photograph of a portion of the Piedmont approximately 30 miles west of Fredericksburg, Virginia taken on 20 February 1960 from 30,000 ft.	45
2-22	Panoramic view of the Shenandoah Mountains, Pendleton County, West Virginia.	45
2-23	Nimbus 1 AVCS photograph of southwestern Wyoming-northwestern Colorado, and northeast Utah taken on orbit 109, 4 September 1964 as compared to topographic and geologic maps of the region.	46
2-24	General geologic map of central France and corresponding Nimbus 1 AVCS photograph taken on orbit 236, 13 September 1964	48
2-25	Geologic interpretation of Nimbus 1 AVCS photograph of southern California taken on orbit 285, 16 September 1964.	49
2-26	Nimbus 1 AVCS photograph of southern California taken on orbit 168, 8 September 1964 showing the distribution of major fault lines.	50
2-27	Comparison between Nimbus 3 daytime HRIR image, orbit 711, 6 June 1969 and structural provinces map of Saudi Arabia.	52
2-28	Nimbus 1 AVCS photograph of the Sayan Mountains and vicinity, USSR taken on orbit 320, 19 September 1964.	53
2-29	Hydrologic and geologic interpretations of Nimbus 1 AVCS photograph of a portion of Ellesmere Island taken on orbit 207, 11 September, 1964.	56
2-30	Diurnal variation in temperature at the equinox and at 30° (north or south) derived using Eq. 2-4 for surfaces of quartz sand, sandstone, and granite.	62
2-31	Nimbus 2 nighttime HRIR temperature map of the Nafud Desert area of Saudi Arabia taken on orbit 846, 17 July 1966.	62

LIST OF FIGURES, contd.

<u>Figure</u>		<u>Page</u>
2-32	Nimbus 1 HRIR photofacsimile taken over South America near midnight on orbit 246, 14 September 1964.	65
2-33	Lithological interpretation of the Paris Basin as compared to a Nimbus 1 AVCS photograph taken on orbit 236, 13 September 1964.	67
2-34	Nimbus 4 IDCS photograph of an ash plume from Beerenberg volcano, taken on orbit 2231, 21 September 1970.	69
2-35	Nimbus 1 HRIR image of Hawaiian Islands and vicinity taken on orbit 250, 14 September 1964.	71
2-36	Nimbus 2 nighttime HRIR photofacsimile observation of Surtsey taken on orbit 1541, 8 September 1966.	74
2-37	Analog traces of Nimbus 2 HRIR data.	75
2-38	Changing near-infrared (0.7 to 1.3 μm) reflectance patterns in the lower Mississippi Valley recorded by the Nimbus 3 daytime HRIR during 1969.	78
2-39	Analyses of computer-produced Nimbus 3 daytime HRIR (0.7 to 1.3 μm) reflectance maps of the Mississippi River Valley area.	79
2-40	Rapid reflectance changes of the lower Mississippi Valley as recorded by Nimbus 3 daytime HRIR during May 1969.	80
2-41	Temporal sequence of Nimbus 3 daytime HRIR reflectance patterns along the White River in Arkansas during 1969.	81
2-42	Analyses of computer-produced Nimbus 3 daytime HRIR (0.7 to 1.3 μm) reflectance maps of the Ouachita River during 1969.	82
2-43	An Apollo 9 near-infrared (0.68 to 0.89 μm) picture taken on 9 March 1969 showing the Ouachita River flood that was later recorded by Nimbus 3 daytime HRIR.	84
2-44	Temporal surface moisture and flood conditions of the Paraguay-Parana Rivers flood plain as imaged by Nimbus 3 daytime HRIR during 1969.	85
2-45	Seasonal changes in the Lake Chad region recorded by the Nimbus 3 daytime HRIR.	86
2-46	Seasonal soil moisture and vegetation changes in the Niger Inland Delta area recorded by the Nimbus 3 daytime HRIR.	88
2-47	Temporal sequence of Nimbus 3 daytime HRIR showing western Africa-Niger River area.	89
2-48	Changing winter snow cover pattern along the east coast of the United States as recorded by the Nimbus 3 DRID.	90

LIST OF FIGURES, contd.

<u>Figure</u>		<u>Page</u>
2-49	Relationship between snow brightness on satellite imaging and snow depth for non-forested area.	92
2-50	Nimbus 2 APT picture of the eastern United States taken on orbit 3333, 20 January 1967.	92
2-51	Nimbus 3 IDCS observation of the Hudson Bay area showing a vegetation boundary accentuated by snow cover, taken on orbit 219, 30 April 1969.	94
2-52	Nimbus 4 IDCS observation of snow and ice over Siberia and the Arctic Ocean, taken on orbit 4900, 8 April 1971.	95
2-53	Nimbus 4 IDCS observation of snow and ice over Alaska and the Bering Straits area, taken on orbit 4774, 29 March 1971.	96
2-54	Seasonal area extent of snow cover in the Himalayas as recorded by Nimbus 3 IDCS.	97
2-55	Snow cover extent over the Indus River watershed from April 1969 to March 1970 compared with the mean monthly discharge of the Indus River near Attock, northern West Pakistan.	98
2-56	Nimbus 2 HRIR temperature maps of Lake Michigan derived from digitized data.	102
2-57	Comparison of average temperatures of Lake Michigan obtained from Nimbus 2 HRIR.	103
2-58	Surface temperatures of Lake Michigan from an infrared airborne radiometer thermometer flight, 18 October 1966.	103
2-59	Portion of an analysis of Lake Erie surface temperatures based on digitized Nimbus 2 nighttime HRIR data taken on orbit 1290, 20 August 1966.	104
2-60	Ice melt conditions of four lakes in northern Canada as observed by Nimbus 2 APT system during the 1966 breakup period.	105
2-61	Fort Peck Reservoir, Montana as viewed by Nimbus 1 AVCS photograph taken on orbit 299, 17 September 1964.	107
2-62	Growth of Lake Nasser formed by the Aswan High Dam on the Nile River as recorded by Nimbus imagery.	108
2-63	Monitoring of Lake Volta, Africa by Nimbus 3 daytime HRIR.	109
2-64	Monitoring of the Okavango Basin, Africa by Nimbus 3 daytime HRIR	110
2-65	Nimbus 1 AVCS image of northwestern Nevada showing good contrast separation between lake beds (white and light gray), alluvium (intermediate gray), forested mountains (dark gray), and lakes (black) taken on orbit 285, 16 September 1964.	112

LIST OF FIGURES, contd.

<u>Figure</u>	<u>Page</u>
2-66 Nimbus 1 AVCS image of the Mojave Desert, California taken on orbit 285, 16 September 1964.	113
2-67 Nimbus 1 AVCS image of southern Iran, orbit 323, 19 September 1964, showing terrain features.	114
2-68 Gemini 5 photograph of southern Iran, 22 August 1965.	115
2-69 Gemini 5 photograph of Lavar Maidan in southern Iran, 22 August 1965.	115
2-70 Enlargement of a portion of a Nimbus 1 AVCS image of the Great Salt Lake area, Utah, taken on orbit 197, 10 September 1964.	116
3-1 Average surface temperature of the south Indian Ocean obtained from the Nimbus 2 MRIR 10 to 11 μm channel for the 14 June - 7 July 1966 period.	123
3-2 Nimbus 4 THIR photofacsimile (11.5 μm channel, daytime) taken on orbit 5, 8 April 1970, showing the Gulf Stream thermal boundary.	125
3-3 Nimbus 2 HRIR photofacsimile (3.8 μm channel, nighttime) taken on orbit 1235, 16 August 1966, showing the Falkland-Brazil currents boundary near the Atlantic coast of South America.	126
3-4 Photofacsimile and schematic analysis of Nimbus 2 HRIR daytime measurements (0.7 to 1.3 μm) taken on 25 May 1966, orbit 137 over the south Atlantic Ocean showing the Falkland-Brazil current boundaries.	127
3-5 Photofacsimile and schematic analysis of Nimbus 2 HRIR nighttime measurements on 19 September 1966, 2130 GMT (orbit 1698), near South Africa.	127
3-6 Position of the north wall of the Gulf Stream during October 1966, derived from Nimbus 2 HRIR nighttime measurements.	128
3-7 Changing thermal pattern at the beginning of an upwelling near the Somali Coast as recorded by Nimbus 2 HRIR on 3 and 6 July 1966.	131
3-8 Anomalous sunglint pattern in the Gulf of California as recorded by Nimbus 2 AVCS, orbit 126, 24 May 1966.	131
3-9 Nimbus 4 Direct Readout IDCS mosaic of Antarctica, January 1971.	132
3-10 Baffin Bay ice survey from Nimbus 4 IDCS pictures.	134
3-11 Pack-ice boundaries between 28 August and 22 September 1964.	135
3-12 Average Antarctic pack-ice boundaries for July 1966, 1969, and 1970 derived from Nimbus data.	135
3-13 Average Antarctic pack-ice boundaries for August 1966, 1969, and 1970 derived from Nimbus data.	135

LIST OF FIGURES, contd.

<u>Figure</u>		<u>Page</u>
3-14	Annual development of a lead (long, linear ice-free area) near the Antarctic coast during late August - early September.	138
3-15	Nimbus 3 IDCS pictures recorded during August and September 1969 monitored the development of an offshore lead along the east coast of the Antarctic peninsula.	139
3-16	Nimbus 2 observations of short-term changes in the sea-ice regime along the coast of MacRobertson Land, Antarctica.	141
3-17	Snow and ice conditions from Iceland to Canada on 15 April 1969 as shown by a Nimbus 3 IDCS mosaic.	142
3-18	Nimbus 1 observations of a tabular iceberg on the eastern coast of the Antarctic peninsula.	143
3-19	Nimbus 3 IDCS picture taken on orbit 2459, 14 October 1969, shows the 1969 location of a tabular iceberg detected in 1964.	144
3-20	Nimbus 2 AVCS observations of a 20-mile long tabular iceberg in the Antarctic Ocean, May-August 1966.	145
3-21	Nimbus 2 AVCS observations of an ice floe along the east coast of Greenland in 1966.	146
4-1	Changing Antarctic coastline observed by Nimbus satellites.	148
4-2	Antarctic map revisions derived from a Nimbus 1 AVCS picture recorded on orbit 184, 9 September 1964.	149
4-3	Nimbus 3 HRIR daytime image (orbit 1172, 10 July 1969) of northern United States and Canada showing tonal boundary extending across central Canada.	151
4-4	Nimbus 1 AVCS photograph of the Gulf of Danzig area, Poland taken on orbit 89, 3 September 1964.	152
4-5	Nimbus 1 AVCS photograph of the Chesapeake Bay area taken on orbit 137, 6 September 1964, compared with population map of same area.	156
4-6	Actual (U. S. Census Bureau, 1960) vs Nimbus estimated population measurements.	157
4-7	Richmond/Petersburg area map (from U. S. Geological Survey 1:250,000 map, Richmond, Virginia Quadrangle, 1964).	158
4-8	Richmond area map (from U. S. Geological Survey 7.5 Minute Quadrangle Map, 1964).	159
4-9	Comparison of "Density Slicing" display of the Richmond area in Figure 4-5a and the urban area of Richmond as shown in Figure 4-7.	160
4-10	Computer-produced map of the U. S. east coast derived from ITOS Scanning Radiometer data (19 October 1970), showing thermal anomalies correlation with major urban centers.	161

LIST OF FIGURES, contd.

<u>Figure</u>	<u>Page</u>
4-11 Nimbus IRLS oceanographic buoy system.	162
4-12 Movement of drifting buoy as tracked by Nimbus 3 IRLS during August 1969.	162
4-13 Elk tracked by the Nimbus 3 IRLS on the National Elk Refuge, Jackson Hole, Wyoming.	163
4-14 Aerial view of 14,410 ft Mt. Rainier, Washington.	165
4-15 Southern California brush fire smoke plumes.	166
4-16 Nimbus 3 IDCS observations of ship plumes in the Northeast Pacific.	167
A-1 The Nimbus orbit.	194
A-2 Nimbus subsatellite track.	194
B-1 Relationship between effective radiance, I_m , measured by the 3.4 to 4.2 μm channels of the Nimbus 1, 2, and 3 HRIR and equivalent blackbody temperature for an emissivity of 1 and 0.9.	210
B-2 Relationship between effective radiance measured by the 11.5 μm channel of the Nimbus 4 THIR and equivalent blackbody temperature for an emissivity of 1 and 0.9.	210
B-3 Comparison of a Nimbus 4 THIR photofacsimile and a concurrent IDCS picture taken on orbit 177, 21 April 1970, showing the effect of a dust storm over the Sahara Desert.	213
B-4 Theoretical surface temperature minus HRIR equivalent blackbody temperature as a function of zenith angle for the model atmospheres of Table B-2.	215
B-5 Surface emissivity effect on the theoretical temperature differences as a function of zenith angle.	215
B-6 Calculated departure of Nimbus 2 HRIR equivalent blackbody temperatures from ground surface temperature as a function of local zenith angle for three different air masses.	216
B-7 Calculated departure of Nimbus 4 THIR 11.5 μm channel temperatures from ground surface temperature as a function of local zenith angle for 10 different atmospheres specified in Table B-3.	216
B-8 Average correction due to atmospheric absorption as a function of the observed Nimbus 4 THIR equivalent blackbody temperatures for nadir angles of observation $\leq 30^\circ$.	219
B-9 Daytime effective radiance I_m , measured by the Nimbus 2 HRIR and equivalent surface temperature for various surface emissivities.	219
B-10 Effective spectral response of the Nimbus 3 HRIR instrument.	221
B-11 Spectral solar irradiance received on a normal surface at the top of the atmosphere.	221

LIST OF FIGURES, contd.

<u>Figure</u>		<u>Page</u>
B-12	Path of solar radiation through the atmosphere to the Nimbus HRIR sensor.	224
B-13	Effective radiance vs equivalent blackbody temperature for the Nimbus 3 HRIR.	224
B-14	Transmissivity of turbid atmosphere in the 0.7 to 1.3 and 3.4 to 4.2 μm bands of the HRIR, for dry atmosphere and for atmosphere formed from Elterman's (1968) data on turbid atmosphere and Fowle's water vapor transmission.	226
B-15	Total path transmissivity $\bar{T}_{\alpha_1} \bar{T}_{\theta_1}$, of the atmosphere in the 0.7 to 1.3 μm band with 2 cm of precipitable water, for observations at the nadir and at $\pm 20^\circ$ from nadir.	226
B-16	Contribution of the 0.7 to 1.3 μm band to the effective reflectance, ρ measured by the Nimbus 3 daytime HRIR, as a function of surface reflectance r_1 , and total atmospheric path transmissivity.	227
C-1	Two sequential Nimbus 1 AVCS pictures taken on orbit 196 of the Andes in South America, showing the "ghosting" effect.	232
C-2	Noise equivalent temperature difference for Nimbus 2 HRIR as a function of target temperature.	233
C-3	Spectrum analysis performed on a Nimbus 2 HRIR analog visicorder scan.	233
C-4	A comparison of filtered and unfiltered computer produced Nimbus 2 HRIR temperature maps of Lake Michigan taken on orbit 1916, 6 October 1966.	235
C-5	Photofacsimile print of Nimbus 2 HRIR data taken on 13 August 1966 on orbit 1197 showing, as indicated, the area of reflected sunlight interference during satellite day-night transition, recognizable by a broad band of darker stripes across the film strip.	236
C-6	Sample Nimbus 3 HRIR and IDCS pictorial data from orbit 1837, 29 August 1969, containing noise attributed to flutter in the HDRSS-A tape recorder.	236
C-7	Spectral analyses of unfiltered Nimbus 3 HRIR data from HDRSS-A and HDRSS-B tape recorders, orbit 3046, 27 November 1969.	238
C-8	Root mean square (rms) variation of the equivalent blackbody temperatures in the range 270 to 290 $^\circ\text{K}$ from the Nimbus 3 HRIR night-time data.	239
C-9	Spectral analyses of filtered Nimbus 3 HRIR data from HDRSS-A and HDRSS-B tape recorders, orbit 3046, 27 November 1969.	240
C-10	Sample Nimbus 4 IDCS and THIR pictorial data containing noise attributed to flutter in the HDRSS-A tape recorder.	242

LIST OF FIGURES, contd.

<u>Figure</u>		<u>Page</u>
C-11	Spectral analyses of unfiltered Nimbus 4 THIR data from HDRSS-A and HDRSS-B tape recorders.	243
C-12	Root mean square (rms) variation of the equivalent blackbody temperatures in the range 270 to 290°K from the Nimbus 4 THIR 11.5 μm channel.	244
C-13	Nimbus HRIR and THIR data flow showing the points at which the various filters available can be applied.	245
C-14	A comparison of filtered and unfiltered Nimbus 3 daytime HRIR image taken on orbit 3045, 27 November 1969.	245

LIST OF TABLES

<u>Table</u>	<u>Page</u>
1-1 Non-Meteorological Applicability of Nimbus Experiments	2
1-2 Nimbus Data Collection Figures	2
1-3 Resolution and Area Coverage of the Nimbus Sensors	4
2-1 Applicability of Nimbus Data to Geological and Hydrological Studies	15
2-2 Thermal Inertia $(\rho c \lambda)^{1/2}$ for Various Surfaces	59
2-3 Theoretical and HRIR Average Surface Temperature Differences for the Nafud Desert Area in Saudi Arabia	63
2-2 Nimbus 2 Orbits on which the Surtsey Volcanic Eruption Appears as a Dark Spot Anomaly on the HRIR Imagery	72
3-1 Nimbus Observables and Applications	121
3-2 Nimbus Sensors Capable of Oceanographic Measurements	121
3-3 Antarctic Circumpolar Pack Ice Areas for July and August 1966, 1969, and 1970 Derived from Nimbus 2 AVCS and Nimbus 3 and 4 IDCS	136
A-1 Orbital Characteristics	195
B-1 Reflectance (\bar{r}) and Emissivity (\bar{E}) of Common Terrain Features	209
B-2 Surface Temperatures and Total Gas Content for Model Atmospheres of Figure B-4 at Zenith Angle of 0°	214
B-3 Computations of Atmospheric Effects on THIR-Derived Temperatures	214

1. INTRODUCTION

1.1 Nimbus Experiments and Data Collection

Nimbus satellites and their sensors, designed primarily for meteorological observation, have provided voluminous amounts of data useful to an improved understanding of atmospheric processes. However, some of these data have also been successfully applied in other branches of the earth sciences. The results of some of these applications have afforded useful insights to the Earth Resources Satellite Program. Oceanography, geology, geography, hydrology and cartography are among the disciplines that have benefitted from the Nimbus data. Non-meteorological applications of the Nimbus data (see also Sabatini and Sissala, 1968) are the subjects of this report.

The four Nimbus satellites launched to date have carried a variety of imaging and non-imaging sensor systems which have collected useful data for earth resources studies. The sensory experiments on board the Nimbus satellites have increased from three on Nimbus 1 to ten on Nimbus 4. Table 1-1 lists the Nimbus experiments and their applicability to non-meteorological studies. Table 1-2 shows the amounts of data which have been obtained from each of the Nimbus sensor systems. The Nimbus User's Guides and Catalogs (see Section 6 for specific references and bibliographies) published by NASA and available through the National Space Science Data Center provide complete descriptions of the Nimbus experiments and data coverage and availability.

Most of the studies of the earth conducted with Nimbus sensory data have used data from the AVCS,* IDCS, HRIR, THIR and Direct Readout Systems (APT, DRID, DRIR) in the pictorial format, or computer digital printouts from the HRIR and THIR systems. Some MRIR data from Nimbus 2 and 3 have been used for the mapping of sea surface temperatures. Less has been reported on the use of the IRLS system because of its more recent implementation. However, its capability to collect data from remote platforms makes this system potentially invaluable for many earth resources applications. Some of these applications are discussed in subsequent sections of this report.

Data from the other Nimbus radiation sensors, the IRIS, SIRS, FWS, SCR, and MUSE (see Appendix A for a brief explanation) are generally not useful for earth resources studies. The first four sensors have low spatial resolution, making them inappropriate even though each can provide surface temperature measurements. The IRIS and FWS, for example, record the infrared energy spectrum of the surface and except for the low resolution (60 to 150 km diameter spots), would have a potential for the identification of natural surface characteri-

*See Table 1-1 or Appendix E for a list of abbreviations.

TABLE 1-1
NON-METEOROLOGICAL APPLICABILITY OF NIMBUS EXPERIMENTS*

Satellite	Launch Date	End of Regular Operations	MRIR	HRIR	AVCS	IDCS	SIRS	IRIS	APT	RTTS	THIR	MUSE	SCR	FWS	BUV	IRLS
Nimbus 1	28 Aug 1964	22 Sept 1964		▲	▲				▲							
Nimbus 2	15 May 1966	15 Nov 1966	●	▲	▲				▲							
Nimbus 3	14 Apr 1969	4 Feb 1970 [†]	●	▲		▲	●	●		▲		●				▲
Nimbus 4	8 Apr 1970	Operational**				▲	●	●		▲	▲	●	●	●	●	▲

▲ Non-meteorological applications possible

● Meteorological applications mainly

APT - Automatic Picture Transmission	IRLS - Interrogation Recording and Location System
AVCS - Advanced Vidicon Camera System	MRIR - Medium Resolution Infrared Radiometer
BUV - Backscatter Ultraviolet Radiometer	MUSE - Monitor of Ultraviolet Solar Energy
FWS - Filter Wedge Spectrometer	RTTS - Real Time Transmission System
HRIR - High Resolution Infrared Radiometer	SCR - Selective Chopper Radiometer
IDCS - Image Dissector Camera System	SIRS - Satellite Infrared Spectrometer
IRIS - Infrared Interferometer Spectrometer	THIR - Temperature Humidity Infrared Radiometer

*A brief description of the Nimbus experiments is given in Appendix A.

**Operational as of 8 April 1971.

[†]Limited operation of MUSE, ERLS and MRIR continues as of the date of this report.

TABLE 1-2
NIMBUS DATA COLLECTION FIGURES

Nimbus 1 (Launch - 28 August 1964)		Last Effective Orbit
AVCS	11,600 pictures	369
APT	2,000 pictures	354
HRIR	100 hours	368
<u>Nimbus 2 (Launch - 15 May 1966)</u>		
AVCS	114,003 pictures	1,444
APT	148,810 pictures	13,029
HRIR	2,190 hours	2,455
MRIR	1,313 hours	985
DRIR	1,370 hours	2,455
<u>Nimbus 3 (Launch - 14 April 1969)</u> (Data through 25 September 1970)		
IDCS	41,494 pictures	3,840
HRIR	5,684 hours	3,922
MRIR	3,268 hours	3,975
DRID	72,075 pictures	7,095
DRIR	12,745 hours	7,095
IRIS	1,738 hours	1,332
SIRS	8,389 hours	7,143
MUSE	8,521 hours	7,143
IRLS	21,190 data frames	5,934
<u>Nimbus 4 (Launch - 8 April 1970)</u> (Data through 28 February 1971)		
IDCS	30,656 pictures	To date
THIR (11.5 μm)	4,819 hours	"
THIR (6.7 μm)	2,801 hours	"
DRID	Selected Coverage	"
DRIR	Selected Coverage	"
IRIS	6,372 hours	"
SIRS	6,684 hours	"
MUSE	6,784 hours	"
BUV	6,627 hours	"
FWS	1,316 hours	815
SCR	6,784 hours	To date
IRLS	22,027 data frames	"

stics through their spectral characteristics. The IRIS data have, in fact, been used in limited instances to provide coarse identification of desert sand areas through the detection of the reststrahlen effect* in the recorded infrared spectrum (Hanel and Conrath, 1970). The MUSE, on the other hand, measures the solar spectrum and is not earth-oriented. No further discussion of these experiments will therefore be presented except for the brief description in Appendix A.

1.2 Resolution

The type of earth surface features which can be identified in Nimbus data is dependent on the geometric and spectral resolutions of the sensors, and the geometric size, contrast and spectral reflectance and/or emittance characteristics of the phenomena being observed. Table 1-3 gives the maximum theoretical sub-satellite point resolutions of the Nimbus sensors determined by the instantaneous geometric fields of view for the scanning sensors (HRIR, THIR, and MRIR), the image spot size on the vidicon for the AVCS and APT, and the aperture of the image dissector tube for the IDCS. Ground resolutions range from approximately 330 meters for the Nimbus 1 AVCS images taken at a 423 km altitude, to about 3 km for the Nimbus 3 and 4 IDCS. The resolutions for the HRIR and THIR scanning radiometers are approximately 8 km.

Electronic noise degrades considerably the theoretical resolution of some of the Nimbus data. Appendix C reviews the effects of noise on the Nimbus data and some of the efforts to attenuate it. All of the Nimbus 2 AVCS was affected by a 10 kc interference pattern which greatly deteriorated the data (see, for example, Figures 3-20 and 3-21). Nimbus 3 and 4 IDCS, HRIR, and THIR data stored on the HDRSS-A tape recorder contain strong noise components which show up as a herringbone pattern on the pictorial data (see Appendix C, Figures C-6, C-10, for examples). Nimbus 3 and 4 IDCS, HRIR, and THIR data stored on the alternate HDRSS-B tape recorder are relatively free of noise. Nimbus 1 AVCS data have the highest resolution of all the Nimbus data (330 meters for pictures taken near satellite perigee), and are relatively free of noise. Unfortunately, the short lifetime of the Nimbus 1 spacecraft (1 month) limited to a few hundreds the number of AVCS pictures useful to earth resources studies. Even the best Nimbus 1 AVCS resolution is, of course, poorer than the 100 meters or better planned for the Earth Resources Technology Satellite (ERTS), and is two orders of magnitude less than the conventional aerial photographs that photogeologists usually work with.

*See Appendix D for definition.

TABLE 1-3
RESOLUTION AND AREA COVERAGE OF THE NIMBUS SENSORS

NIMBUS	AVCS		APT		HRIR	
	Picture Coverage*	Swath Width (horizon to horizon)	Picture Coverage	Swath Width (horizon to horizon)	Picture Coverage	Swath Width (horizon to horizon)
NIMBUS 1	300 x 1200 km (at perigee) 650 x 3000 km (at apogee) Resolution at SSP**	1800 km (at perigee) 6500 km (at apogee) Resolution at SSP	850 x 850 km (at perigee) 1950 x 1950 (at apogee) Resolution at SSP	1800 km (at perigee) 6500 km (at apogee) Resolution at SSP	3.3 km (at perigee) 7.5 km (at apogee)	3.3 km (at perigee) 7.5 km (at apogee)
	AVCS		APT		HRIR	
NIMBUS 2	750 x 3700 km Resolution at SSP	7100 km Resolution at SSP	2200 x 2200 km Resolution at SSP	7100 km Resolution at SSP	9.3 km	7100 km Resolution at SSP
	0.92 km	60 km	2.2 km	9.3 km		60 km
NIMBUS 3	IDCS		APT		HRIR	
	2700 x 2700 km Resolution at SSP	7100 km Resolution at SSP	DRID - Same as IDCS DRIR - Same as IIRIR	7100 km Resolution at SSP	150 km	7100 km Resolution at SSP
NIMBUS 4	IDCS		APT		THIR	
	2700 x 2700 km Resolution at SSP	7100 km Resolution at SSP	DRID - Same as IDCS DRIR - Same as THIR	7100 km Resolution at SSP	94 km	7100 km Resolution at SSP
					45 km	Resolution at SSP
					60 km	Resolution at SSP
					110 km	Resolution at SSP
					60 km	Resolution at SSP
					45 km	Resolution at SSP
					60 km	Resolution at SSP
					110 km	Resolution at SSP

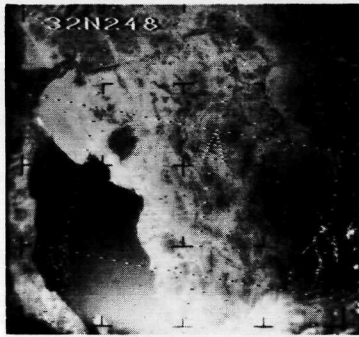
*The AVCS picture coverage is given as the approximate coverage of three simultaneous pictures slightly side-lapping.

**The resolution at the subsatellite point (SSP) is the best resolution available. The resolution lessens away from the SSP.

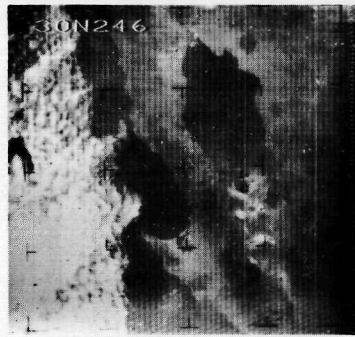
***Horizon not visible.

Figure 1-1 showing the Gulf of California area illustrates the relative resolutions of the various Nimbus sensors. A comparison of Figure 1-1 to the Apollo photograph of the same area (Figure 1-2) gives a good idea of the lower Nimbus resolutions. Figure 1-3 is an aerial photomosaic of an area around Los Angeles. Part of the same area as seen by Nimbus 1 is presented in Figure 1-4. Figure 1-4 is a portion of the entire Nimbus 1 AVCS frame shown in Figure 2-26. When we try to compare the aerial photomosaic to even the best of Nimbus images, only gross features can be correlated. The myriad of shade and pattern variations found on the aerial photomosaic are lost in a few pallid shades of gray on the Nimbus 1 photograph. Thus Nimbus images are no substitute for the large-scale (small area) studies that have traditionally been performed with aerial photographs. Nevertheless, the large area covered by an individual Nimbus image is well suited for showing the interrelationship of large geologic features and their regional setting. For example, Figures 1-4 and 2-26 show at a glance the location of the major faults of the area, while it would take a mosaic consisting of hundreds of aerial photographs specially processed to attenuate differences of gray scale and solar illumination to show the same areas.

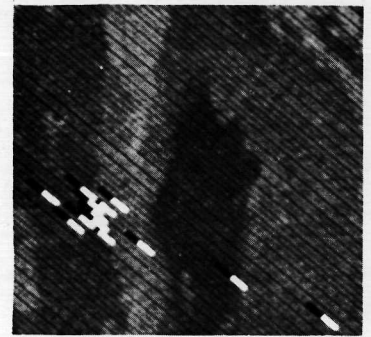
Surface features and events approaching the theoretical resolution of the Nimbus sensors may at times be detected in the processed data. Beaches, for example, often stand out distinctly on Nimbus 1 AVCS pictures because their high reflectances are in sharp contrast to the dark ocean, although the widths of the beach areas may be smaller than the resolving power of the AVCS. Similarly, a small water body of the size of a resolution element or smaller may be picked out in the AVCS, IDCS or HRIR daytime data, if it is located in a bright vegetation-free area. A subresolution volcanic eruption such as the Surtsey (Figure 2-36) or Beerenberg (Figure 2-34) eruption may be monitored by the HRIR or THIR because of extreme temperature contrasts and/or an accompanying smoke plume detectable in the visible IDCS and near-infrared daytime HRIR sensors. Target enhancement factors other than those due to high contrast have been noted. Some major highways have been detected in Nimbus 1 AVCS photographs (Kilston et al, 1966), certainly not because of their width, but because the cleared deforested areas surrounding them have increased the "effective" target size. Many rivers of widths less than one kilometer stand out prominently in the radiation pictures, although the resolution of the HRIR is generally not better than 3.3 km. The prominence of the rivers, as Nordberg and Samuelson (1965) explain, is apparently due to increased moisture and consequently increased heat capacity of the grounds along these rivers, thus making them warmer at night than the adjacent drier regions. In general, however, the Nimbus sensors provide imagery for observing phenomena larger than the resolution sizes shown in Table 1-3.



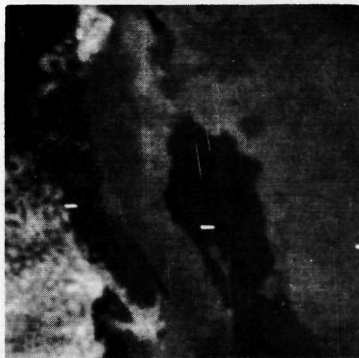
NIMBUS 1 AVCS
D/O 80
2 SEP 1964
VISIBLE
RES. .6 km



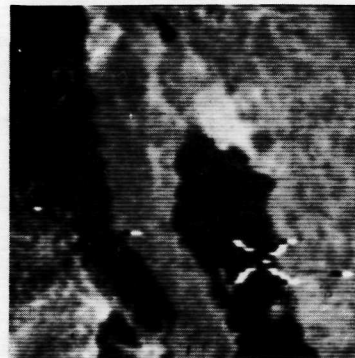
NIMBUS 2 AVCS
D/O 206
30 MAY 1966
VISIBLE
RES. .9 km



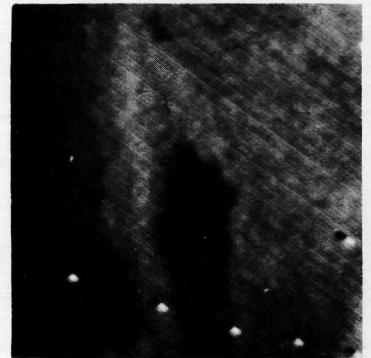
NIMBUS 2 HRIR(N)
D/O 1837
30 SEP 1966
3.5 - 4.1 μ m
RES. 9.3 km



NIMBUS 3 IDCS
D/O 127
23 APR 1969
VISIBLE
RES. 3.3 km



NIMBUS 3 HRIR(D)
D/O 127
23 APR 1969
.7 - 1.3 μ m
RES. 8.5 km



NIMBUS 3 HRIR(N)
D/O 2936
19 NOV 1969
3.4 - 4.2 μ m
RES. 8.5 km



NIMBUS 4 IDCS
D/O 87
14 APR 1970
VISIBLE
RES. 3.3 km



NIMBUS 4 THIR(D)
D/O 87
14 APR 1970
10.5 - 12.5 μ m
RES. 7.7 km



NIMBUS 4 THIR(N)
D/O 3679
7 JAN 1971
10.5 - 12.5 μ m
RES. 7.7 km

AVCS - ADVANCED VIDICON
CAMERA SYSTEM

IDCS - IMAGE DISSECTOR
CAMERA SYSTEM

HRIR - HIGH RESOLUTION
INFRARED RADIOMETER

THIR - TEMPERATURE HUMIDITY
INFRARED RADIOMETER

(D) - DAYTIME

(N) - NIGHTTIME

RES. - RESOLUTION
AT SUBSATELLITE POINT

Figure 1-1 The Gulf of California area as imaged by various Nimbus sensors of different ground resolution and spectral range.

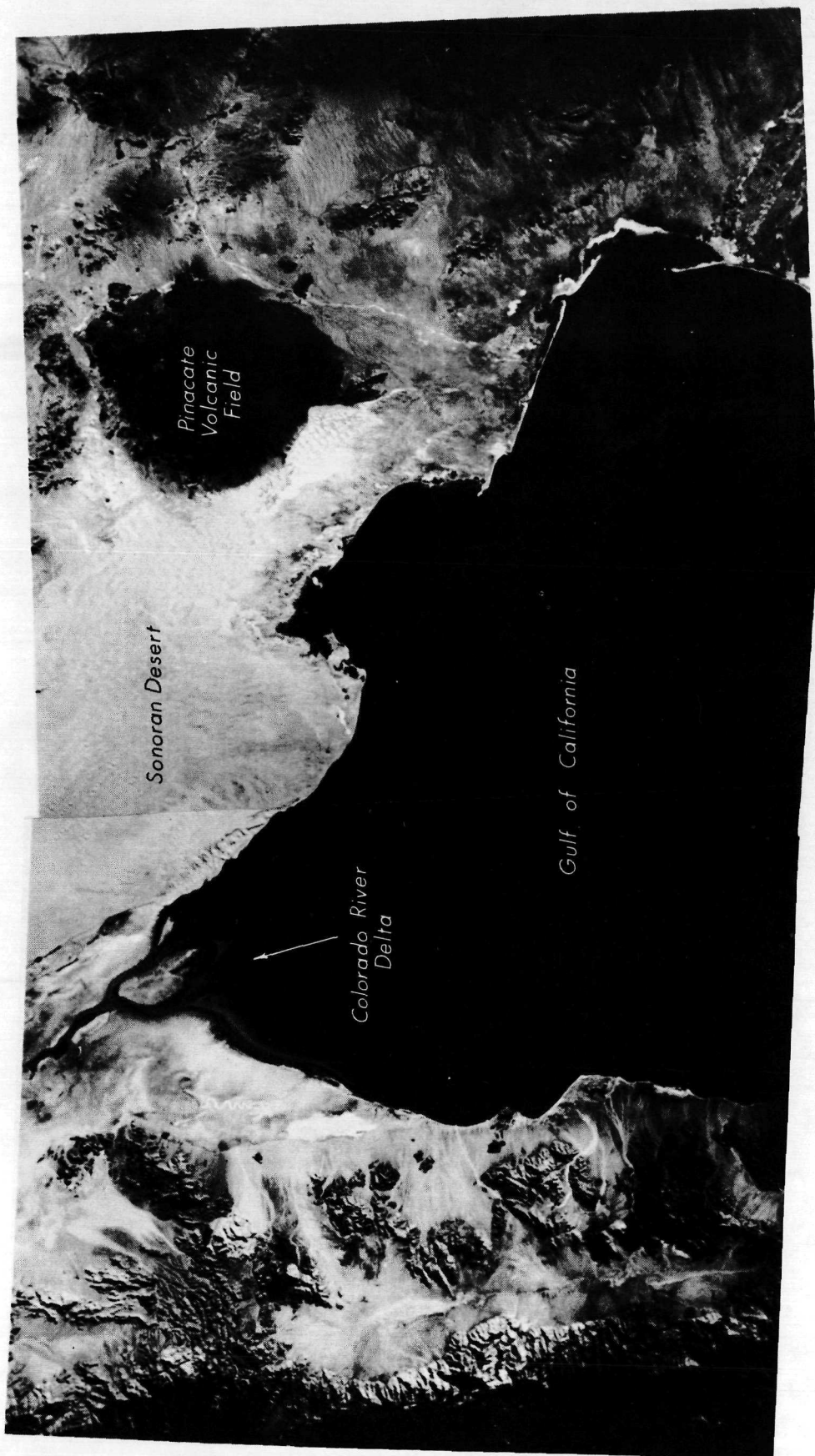


Figure 1-2 Apollo photographs of the Gulf of California area (originals were in color).



Figure 1-3 Aerial photomosaic of Los Angeles and Mojave Desert areas (Courtesy of Aero Service, Philadelphia, Pa.) (The original photomosaic constructed with hundreds of aerial photographs taken in 1953-1954 is at a scale of 1:400,000, with an estimated resolution of a few meters and covers an area of 100 x 135 miles. Santa Catalina Island is visible near the bottom. Part of the Mojave Desert is located in the upper half of the mosaic. The scar-like feature that runs diagonally from the top left corner to the right side of the image is the San Andreas fault line dividing the southern end of the Mojave Desert from the San Gabriel Mountains.)

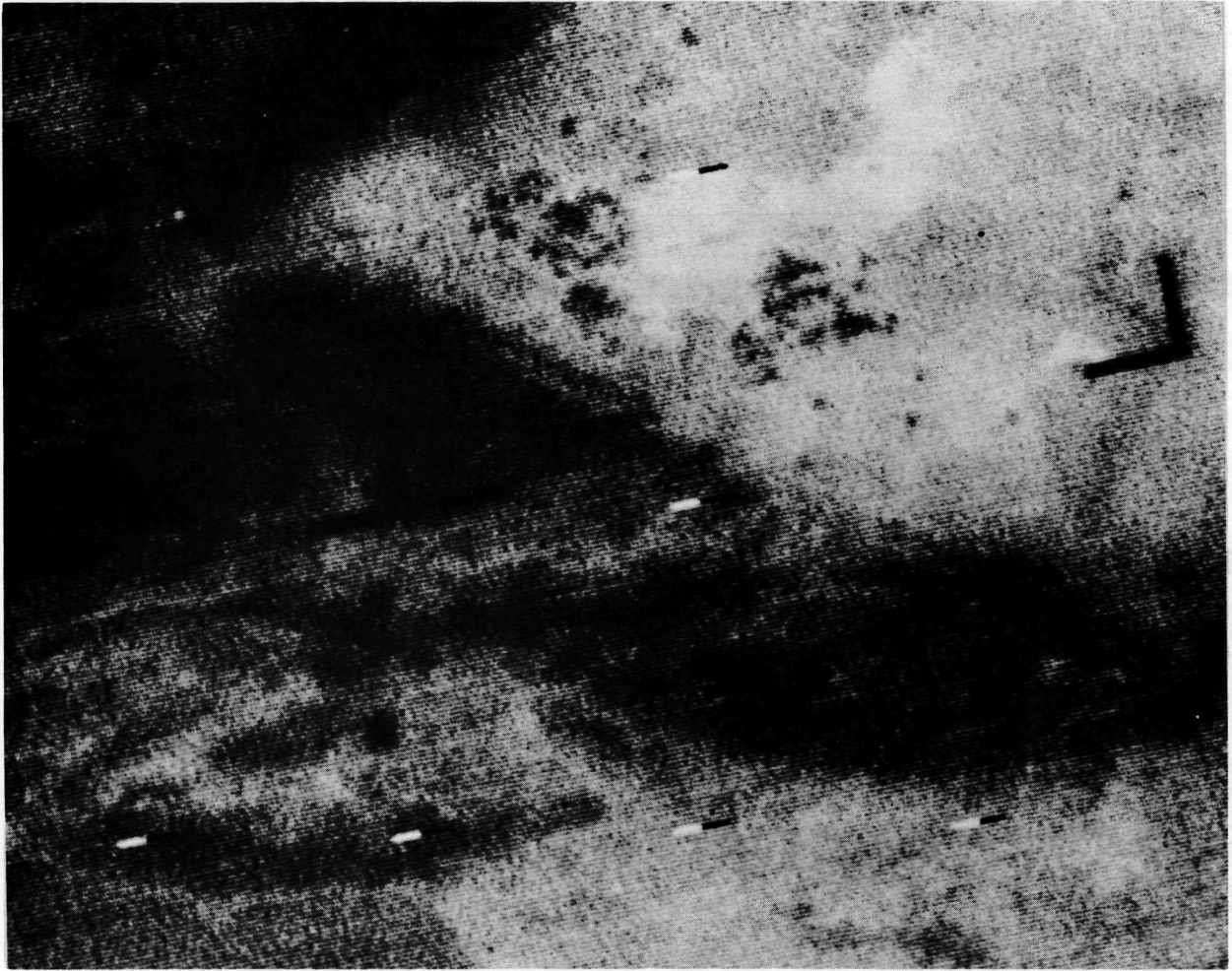


Figure 1-4 This is an enlarged portion of the Nimbus 1 AVCS image shown in Figure 2-26. The area is located north of Los Angeles and corresponds to the upper half of the photomosaic in Figure 1-3. Notice the sharp tonal contrast between the Mojave Desert and the mountain areas south and west of it. Well defined tonal boundaries, not apparent in the aerial photomosaic of Figure 1-3, locate the major faults in this area (see Figure 2-26 for map of faults). Cultivated fields in the Mojave, individually distinguishable in the photomosaic of Figure 1-3, appear here as a conglomerate of dark spots when observed at an estimated resolution of 530 meters by Nimbus 1 AVCS. The wealth of detail present in the aerial photomosaic is lost in a few shades of gray in this Nimbus 1 AVCS photograph.

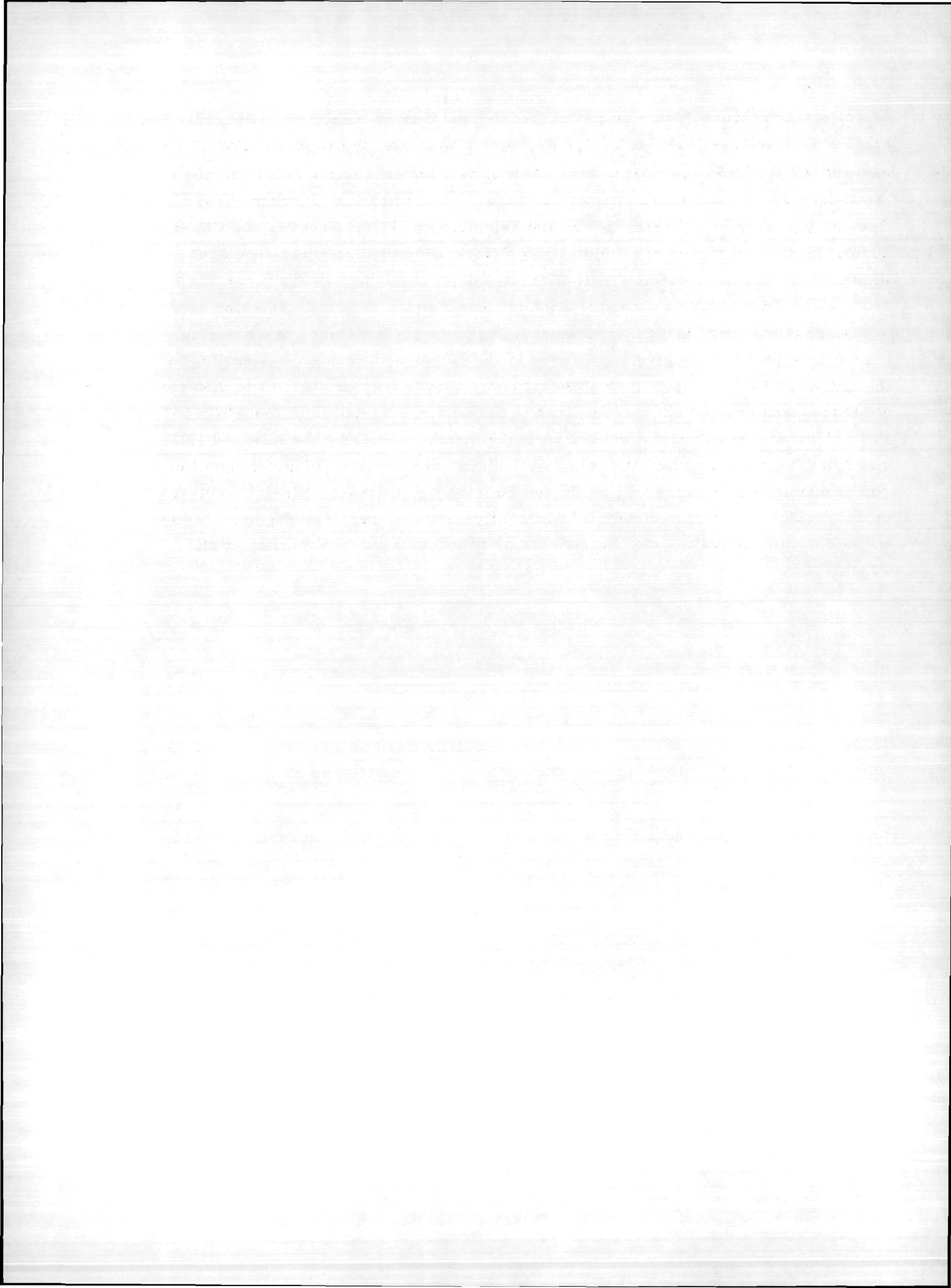
1.3 Cloud Cover

Of the half a million or so television pictures and 15,000 hours of HRIR, THIR and DRIR imagery, approximately half of the imaged areas contain information applicable to non-meteorological studies of the earth, assuming that on the average the earth is 50% cloud-free. Although cloud-free pictures are preferred, pictures showing partial cloud cover may also be useful for studies of the processes at the earth's surface. Even the images showing total cloud cover can be considered useful in the sense that they can be utilized in the compilation of cloud cover statistics necessary for the planning of earth resources missions. Glaser et al (1968), Barnes and Chang (1968), Sherr et al (1968), Salomonson (1969), Greaves et al (1969), and Williamson and Warnecke (1969) have used Nimbus data in cloud cover studies and statistics applicable to earth resources satellite missions.

For proper evaluation and design of ERTS or other satellite sensors for observation of surface features, cloud statistics defining the frequency and size of cloud-free areas at specific locations and times over the earth are needed. In applications which involve the monitoring of static or slow changing phenomena (i. e., the geology or geomorphology of an area) complete coverage of the region can be obtained by combining partial cloud-covered pictures from different satellite passes. However, if a time-varying phenomenon is to be monitored as, for example, sea surface temperature, complete or nearly complete coverage of an area has to be achieved in the shortest time possible. In many of these applications 80% coverage would be considered adequate with the data in the remaining areas "filled in" by extrapolation. The cloud data base developed by Sherr et al (1968) and discussed by Greaves et al (1969) shows, for example, that over the eastern United States, with a Nimbus-type orbit, 80% cloud-free coverage of a 100-mile diameter area can be obtained at 40% probability from three consecutive February passes, while the probability is greater than 50% in the more favorable August situation. However, if a 100% cloud-free coverage is desired, February would be more favorable because of the high incidence of totally clear skies in February relative to August in this area. This brief example illustrates one aspect of the cloud problem in the design of earth resources missions.

Cloud differentiation from the background is another problem facing the analyst of satellite data. Cloud elements less than the resolution spot size of a sensor, and not easily differentiated from the background, may still affect the reflectance or temperature value measured by the sensor for that resolution element. Identifying cloud contaminated data points is especially problematical in the HRIR and THIR measurements. Usually a cloud contaminated resolution element is colder or more reflective than the background. The magnitude of the contamination is proportional to the spot area occupied by the colder cloud surface. Temperature

or reflectance thresholds or statistical techniques may be employed to separate the contaminated values from the analysis (see, for example, Smith et al, 1970). Concurrent MRIR albedo and water vapor channel data may aid in the selection of cloud-free areas for surface temperature analysis in the MRIR Temperature Channel (Greaves et al, 1968; Shenk and Salomonson, 1970; Greaves and Chang, 1970). Use of the higher resolution IDCS picture to determine cloud-free areas in the infrared data is possible with Nimbus 4 data where both the infrared THIR and visible IDCS data are recorded simultaneously in the daytime. In some areas of high persistence of clouds or clear sky, AVCS or IDCS pictures taken during the daytime passes may give a good clue to the cloud conditions corresponding to the nighttime HRIR temperature observations. Clouds may be difficult to differentiate from a snow or ice background, and at times cirrus invisible in the AVCS or IDCS pictures appreciably affect temperature measurements by the infrared HRIR and THIR instruments. In all cases, a knowledge of the meteorological conditions and climatology of an area will aid in determining the presence of invisible cirrus or subresolution cumulus clouds. Additionally, texture, persistence, and shadows will aid in discriminating clouds from ice or snow surfaces (see Barnes et al, 1970).



2. GEOLOGIC AND HYDROLOGIC APPLICATIONS OF NIMBUS DATA

2.1 Introduction

The Nimbus satellites flown to date were designed by NASA primarily for meteorological purposes, a task in which great success has been achieved. Nevertheless, substantial information on terrestrial features and events is contained in Nimbus data and much has already been described in published reports.

Large-scale detailed geologic and hydrologic analyses are not feasible with Nimbus data, but small-scale (large area) studies are possible. Gross geologic structural trends such as major faults and outcrop patterns may, at times, be recognized, and studies have shown that the spatial distribution of gray tones often reflect real distributions of surface relief, vegetation cover, ground moisture, soil characteristics, or surface lithology. Additionally, the general outline of large topographic features, snow cover and drainage systems can be easily distinguished and a few occurrences of volcanic activity have been described. The usefulness of Nimbus data to hydrology is suggested in various publications which have analyzed inland hydrologic conditions and ice fields. The following is a partial list of features that have so far been identified on the Nimbus imagery. The most useful Nimbus sensor is mentioned first.

- 1) Continents and islands in contrast to seas and oceans. AVCS*, APT, HRIR (0.7 to 1.3 μm), IDCS**, THIR (10 to 12 μm), HRIR (3.4 to 4.2 μm)
- 2) Mountain ranges in contrast to lowlands. AVCS, APT, HRIR (3.4 to 4.2 μm), THIR (10 to 12 μm), HRIR (0.7 to 1.3 μm), IDCS
- 3) Regional geologic outcrop patterns and major lava flows. AVCS, HRIR (0.7 to 1.3 μm), APT, IDCS
- 4) Regional geomorphic provinces and tectonic lineaments. AVCS, APT, HRIR (0.7 to 1.3 μm), IDCS
- 5) Seasonal soil moisture/vegetation patterns. HRIR (0.7 to 1.3 μm)
- 6) Drainage networks and snow cover. AVCS, APT, IDCS
- 7) Ice caps, ice shelves and sea ice. AVCS, IDCS, APT, HRIR (3.4 to 4.2 μm), THIR (10 to 12 μm), HRIR (0.7 to 1.3 μm)

*In this list AVCS refers to the Nimbus 1 AVCS.

**IDCS images generally show little contrast over land and between land and water, although they provide detailed information of cloud and snow since the system's transfer function tends to favor gray-scale tonal rendition near the white end of the gray scale.

On a more local scale, a number of additional features have been distinguished:

- 1) Volcanic craters and possible thermal zones. HRIR (3.4 to 4.2 μm), THIR (10 to 12 μm)
- 2) Terrain thermal reversals; i. e., warmer slopes surrounding a cooler desert basin or flanking mountains. HRIR (3.4 to 4.2 μm), THIR (10 to 12 μm)
- 3) Large lakes and reservoirs, usually warmer than the surroundings at night and less reflective during the day. AVCS, APT, HRIR (0.7 to 1.3 μm), HRIR (3.4 to 4.2 μm), THIR (10 to 12 μm), IDCS
- 4) Narrow stream courses and flanking moist zones in desert environments. HRIR (3.4 to 4.2 μm), THIR (10 to 12 μm), HRIR (0.7 to 1.3 μm)
- 5) Thermal patterns in desert soil. HRIR (3.4 to 4.2 μm), THIR (10 to 12 μm)
- 6) Possible buried or abandoned river sources, especially in arid lands. HRIR (0.7 to 1.3 μm), HRIR (3.4 to 4.2 μm), THIR (10 to 12 μm)
- 7) Distribution of sands and possibly the condition of playa surfaces. AVCS, APT, IDCS, HRIR (3.4 to 4.2 μm), THIR (10 to 12 μm)

Table 2-1 shows an assessment of the applicability of Nimbus data to geological and hydrological studies. The assessment is based mainly on a review of the literature and personal experience with the data. The following sections of the report will provide detailed discussions of many of the applications listed in Table 2-1. These discussions have been confined to broad topical headings. Tectonic lineaments and outcrop patterns are treated under Regional Geology; fossil river channels and distribution of ranges and plains under Regional Geomorphology; snow distribution and soil moisture conditions under Regional Hydrology; and Mauna Loa and Kilauea craters and Surtsey eruption under Volcanic and Hydrothermal Activity.

2.2 Regional Geomorphology

Geomorphology is that branch of geology which deals with the study of land forms and their evolution. Since the general configuration of the earth's surface is often clearly recorded on Nimbus imagery, the synoptic small-scale observations made daily will contribute to an understanding of the evolution of the earth's surface and associated land forms. These observations provide a permanent record of the present form of the earth's surface.

TABLE 2-1
 APPLICABILITY OF NIMBUS DATA TO
 GEOLOGICAL AND HYDROLOGICAL STUDIES

Sensors Applications	Nimbus 1 AVCS	Nimbus 1 and 2 APT	Nimbus 2 AVCS	Nimbus 3 and 4 IDCS	Nimbus 1, 2, 3 Nighttime HRIR (3.4 to 4.2 μm)	Nimbus 3 Daytime HRIR (0.7 to 1.3 μm)	Nimbus 4 THIR (11.5 μm)
Regional Geomorphology	▲	▲	●	●	●	▲	●
Relief	●	●			▲	●	▲
Drainage Patterns	▲	▲	●	●	●	▲	●
Synoptic Geology	▲	▲	●	●	▲	▲	▲
Lithological Discrimination	●				●	●	●
Volcanic Eruptions	●	●	●	●	●	●	●
Coastal Sedimentation	▲	●		●		●	
Playa Conditions	▲	●		●	●	●	●
Large Dust Storms	▲	▲	▲	▲	●		●
Surface Moisture					▲	▲	▲
Surface Water Temperature					▲		▲
Snow Cover	▲	▲	▲	▲	●	●	●
Ice	▲	▲	▲	▲	●	●	●

Suitability of Sensor: ▲ Good
 ● Fair

NOTE: HRIR and THIR Grid Print Maps are best suited for quantitative studies; photofacsimiles are used for qualitative analyses and selection of the Grid Print Maps.

2.2.1 Landscape Evolution

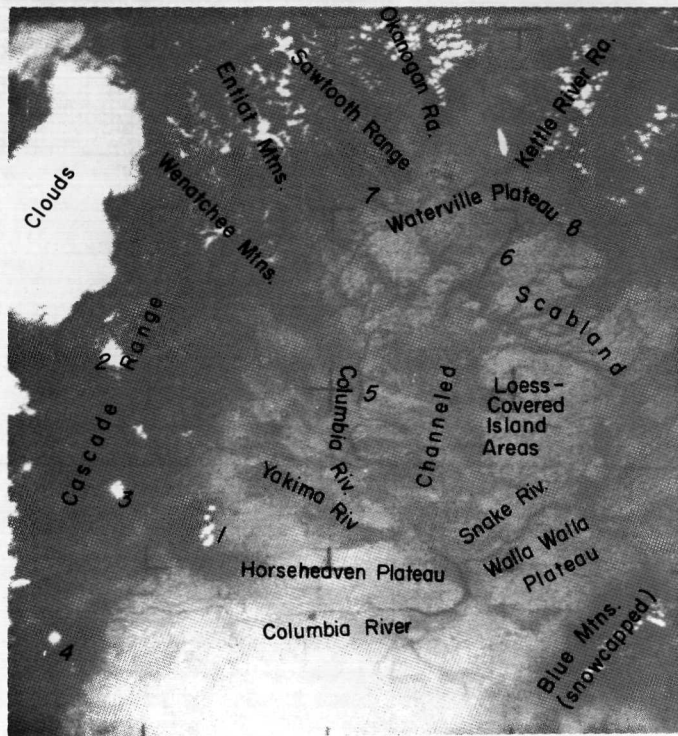
Figure 2-1 is a Nimbus 1 AVCS photograph of the Columbia River Basin of the United States. According to the interpretation by Griggs (1967), this photograph clearly shows the channeled scablands caused by a major flood in Late Pleistocene time, a flood due to the sudden failure of an ice dam at Pand Oreille Lake and the resulting release of the waters of Lake Missoula. In the upper-right portion of the figure, the dark irregular lines are drainage channels resulting from the blockage of the Columbia River by the continental ice sheet during the last ice age. The lighter gray shading outlines soil-covered areas and the dark gray shading shows areas of volcanic bedrock where soil has been removed by stream erosion. This photograph provides a striking illustration to the theory that the Columbia River had been blocked and overflowed the higher elevations.

According to Pouquet (1968a) it may be possible at times to associate lower nighttime surface temperatures in the HRIR (or THIR) data with soil erosion. Erosion washes away the $A_0 - A_1$ horizons revealing the A_2 horizon which is usually poorer in moisture-retaining humus, lower in heat capacity and, consequently, cooler at night. As an example, Pouquet in a later publication (1969a) presents an HRIR grid-print map of the wide and flat area south of the Senegal River (Figure 2-2) characterized by numerous patches of higher temperature unexplained either by elevation or by river courses. According to Pouquet the patches that are "warm" depict what is left of acceptable soils, while most of the rest of the area is "cooler" than it should be as a consequence of soil erosion.

2.2.2 Relief

Relief cannot be directly measured from Nimbus imagery. Approximations and inferences, however, are possible. With HRIR or THIR temperature data these approximations are possible since the surface temperature decreases with height following the altimetric rule of 5 to 10^oK per kilometer (5^oK/km for wet adiabatic, 10^oK/km for dry adiabatic lapse rate). On HRIR or THIR nighttime photofacsimiles, the lowlands generally appear darker (warmer) than the colder highlands.* An example presented by Nordberg and Samuelson (1965) is shown here to illustrate the correspondence of HRIR temperature to relief. Figure 2-3 is a Nimbus 1 HRIR image of the southwestern United States. The dark (warm) streaks in the upper portion of Figure 2-3, correspond to blackbody temperatures of about 290^oK, while

*On the HRIR and THIR positive images dark shades of gray represent high temperatures (e.g., water, lowlands), light shades of gray represent low temperatures (e.g., clouds, snow, highlands).



- | | |
|---|-------------------------------|
| 1) Mt. Adams, 12,307 ft (snow capped) | 5) Priest Rapids Reservoir |
| 2) Mt. Rainier, 14,408 ft (snow capped) | 6) Grand Coulee Reservoir |
| 3) Mt. St. Helens, 9,671 ft (snow capped) | 7) Lake Chelan |
| 4) Mt. Angel (snow capped) | 8) Franklin D. Roosevelt Lake |

Figure 2-1 Nimbus 1 AVCS photograph of the Columbia River Basin and northwestern United States taken on orbit 124, 5 September 1964.

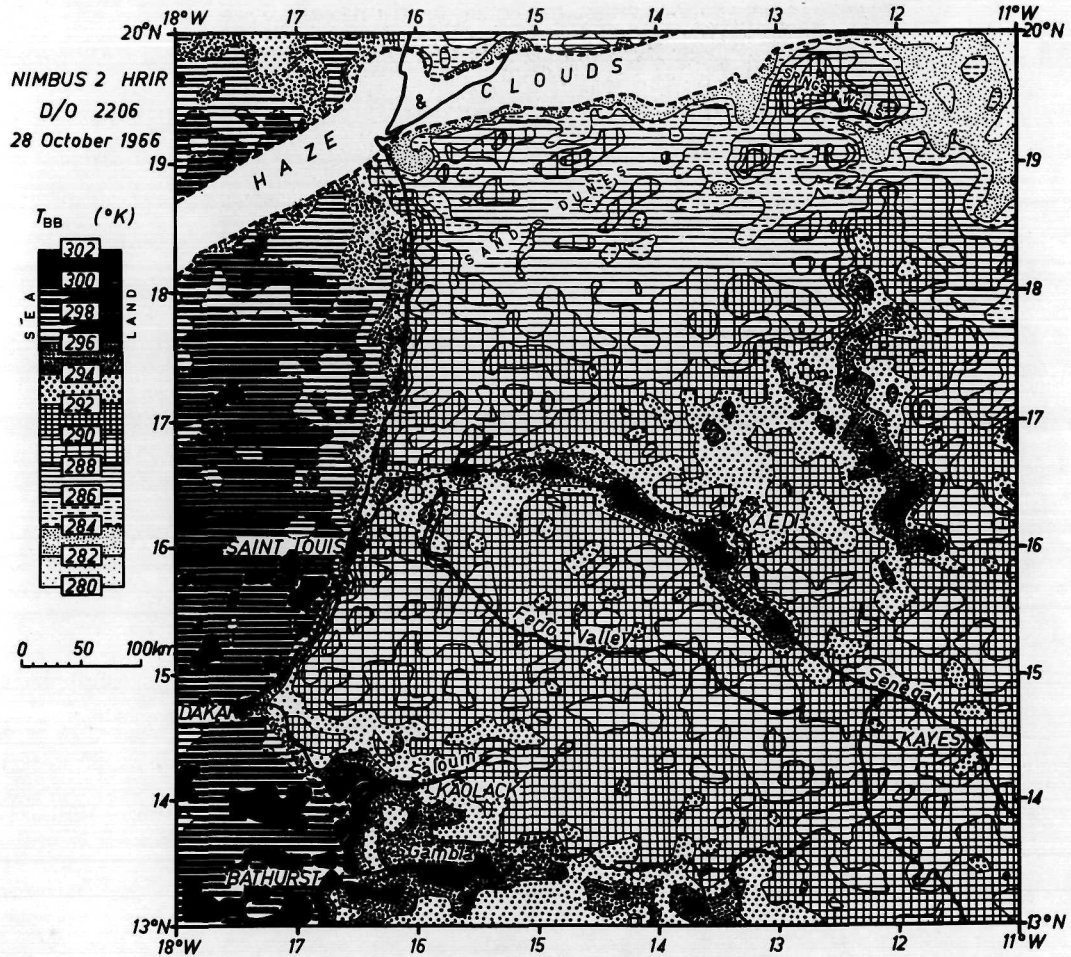


Figure 2-2 Nimbus 2 nighttime HRIR equivalent blackbody temperature map of Senegal, Mauritania, and Mali, western Africa taken on orbit 2206, 28 October 1966, near the beginning of the regional dry season. (Pouquet, 1969a)



Figure 2-3 Nimbus 1 HRIR photofacsimile taken over the southwestern United States on orbit 36, near midnight on 30 August 1964. Dark shades represent warm surfaces, light shades represent cold surfaces. (Nordberg and Samuelson, 1965)

the lighter (colder) gray tones in the surrounding regions correspond to about 275°K. The warmer streaks were identified as Death Valley and the Grand Canyon which occupy lower elevations. A temperature difference of about 15°K between the Death Valley floor and the surrounding highlands 1800 meters above the valley floor gives a decrease with altitude of about 8.3°K/km.

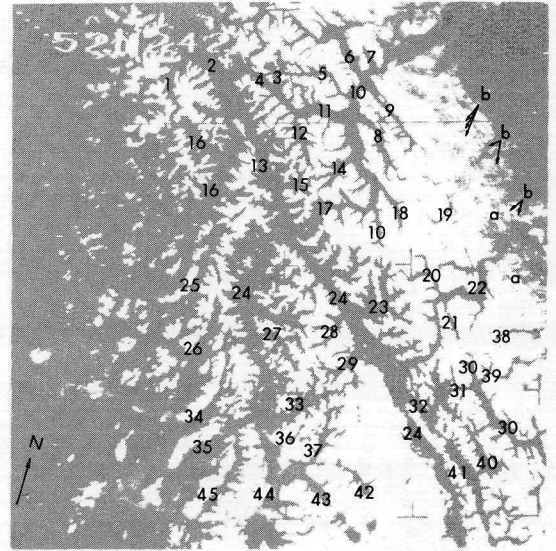
In the photographic data, shadow effects have been used for estimates of relief. Using a Nimbus 1 AVCS photograph, Popham and Samuelson (1965) estimated the heights of two peaks in a mountain range of northwestern Greenland. By measuring the shadows cast by these peaks on the top of the Petermann glacier, they determined the height of the mountains to be 3100 feet (945 meters) and 2600 feet (792 meters) above the glacier. The measured height differences, however, may also be due to a difference in the glacier height due to surface slope. Working from the assumption that the peaks were of the same height, Popham and Samuelson deduced that there would be a difference of 900 feet (274 meters) in the height of the glacier and that the higher elevation values would be found in the vicinity of the "3100 feet" peak. They concluded that, for Nimbus 1 resolution, the error in the measured heights of the two peaks lies between 100 and 200 feet (30 and 61 meters).

On AVCS and IDCS photographs the gray tones corresponding to varying surface reflectances are not reliable indicators of relative relief. For example, the crest of the Blue Ridge in Virginia (Figure 2-20) stands 608 meters above the Great Valley to the west and 760 meters above the Piedmont to the east. But the Great Valley appears much lighter than the Piedmont, which in turn is still lighter than the Ridge. The darker tones are due to the forest cover on the Ridge, and the lighter tones of the Valley correspond to farmland; in this picture reflectances may be correlated with topography only indirectly. However, the shape and the pattern of the low reflectance areas usually prove to be good guides in determining whether the feature is a valley, a lake, or a densely vegetated mountain range.

2.2.3 Drainage Patterns and Geomorphic Provinces

The surficial drainage patterns of large catchment basins or mountain ranges stand out vividly on most AVCS and IDCS photographs, especially when highlighted by thin, fresh snow. The arrangement of streams in a drainage system may reflect structural or lithologic control of underlying rocks or may be related to other factors, such as steepness of slope, climate, and type of weathering. Lacking any other criteria, drainage patterns are also of great help for delineation of various regional geomorphic provinces.

Figure 2-4 illustrates the drainage pattern of the Canadian Rockies accentuated by a snow cover. The glaciers on the major mountain peaks are not distinguishable, but the major river systems and some tributaries are evident; in fact, the



Letters a and b on the photograph refer to snow bands of various widths, the wider bands representing the higher elevations of the Big Horn and Brazeau Ranges. The prominent snowless lineament running from the top left to the bottom right of the picture is the Rocky Mountain Trench, in which flow the Fraser and Columbia Rivers

- | | |
|--------------------------|-------------------------|
| 1. Azure River | 25. Adams River |
| 2. Fraser River | 26. Seymour River |
| 3. Moose River | 27. Downie Creek |
| 4. Moose Lake | 28. Gold River |
| 5. Snaring River | 29. Beaver River |
| 6. Snake Indian River | 30. Bow River |
| 8. Maligne River | 31. Amiskwi River |
| 9. Rocky River | 32. Kicking Horse River |
| 10. Athabasca River | 33. Illecillewaet River |
| 11. Miette River | 34. Perry River |
| 13. Canoe River | 35. Mabel Lake |
| 14. Whirlpool River | 36. Akolkolex River |
| 15. Hugh Allan Creek | 37. Incomappleux River |
| 16. North Thompson River | 38. Clearwater River |
| 17. Wood River and Lakes | 39. Pipestone River |
| 18. Sunwapta River | 40. Cross River |
| 19. Brazeau River | 41. White River |
| 22. Saskatchewan River | 42. Duncan River |
| 23. Bush River | 43. Trout Lake |
| 24. Columbia River | 44. Upper Arrow Lake |
| | 45. Shuswap River |

Figure 2-4 Nimbus AVCS photograph of the Canadian Rockies, British Columbia, and Alberta taken on orbit 197, 10 September 1964.

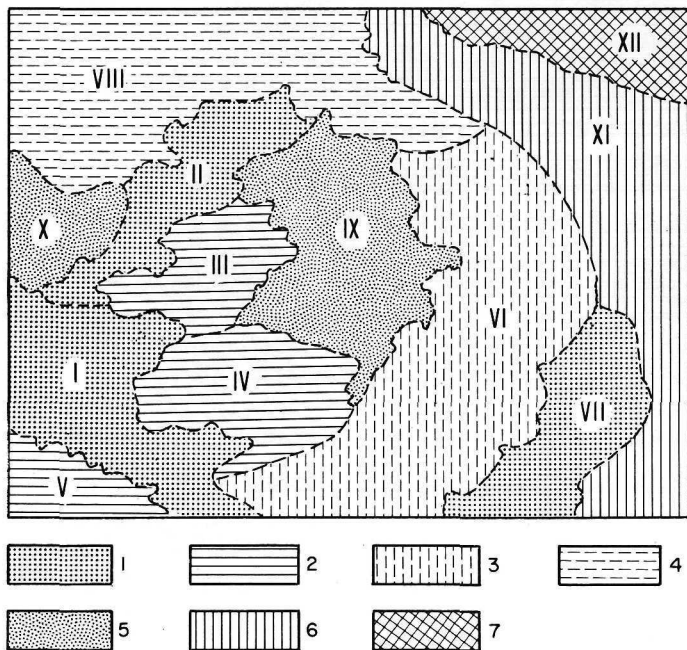
regional hydrologic net stands out so boldly that the area may be subdivided into geomorphic provinces on the basis of drainage patterns alone. The dendritic or reticulate patterns west of the Fraser, Canoe and Columbia Rivers are developed on the Upper Mesozoic igneous and Precambrian metamorphic lithologies, especially in the southwest (Purcell, Selkirk and Monashee Mountains), whereas the rectangular or trellis drainage patterns in the eastern part coincide with the Upper Paleozoic to Middle Mesozoic sedimentary belts (Rabchevsky, 1970b). The hydrologic net in the upper-right corner of the photograph does not stand out as distinctly as it does in the center of the picture. This is due to the thinner snow cover and to the coniferous forest of the Interior Plains and the Rocky Mountain foothills.

Another example of the correlation of a Nimbus 1 AVCS photograph to geomorphic provinces is illustrated in Figure 2-5. Kondrat'yev et al (1968) distinguished seven landscape types and twelve geologic formations within the confines of the Paris Basin. It is doubtful, however, that Vinogradov's (1967, 1969) interpretation of the type of vegetal cover inherent in Figure 2-6 was possible without previous familiarity with the region or existing published information. In most cases, it is difficult, if not impossible, to distinguish vegetation from rock outcrops at ground resolutions poorer than 100 meters. The discrimination becomes even more difficult when the rock covers a large area and is dense and dark in color, like basaltic lava, coal, or bituminous limestone.

The southeastern France and northeastern Spain regions were described by Hasser (1966) from a Nimbus 1 AVCS photograph (Figure 2-7). His conclusion was that although major mountain ranges and drainage systems are recognizable, detailed geologic mapping is impractical. The most conspicuous feature seen on this print is the Pyrenees mountain chain, appearing dark gray due to the vegetation cover. The Ebro River Valley and irrigation system appears light gray and is conspicuous because of its drainage pattern, sparse vegetation, and bare soil. Clouds in the southeastern corner of the photograph obscure the Catalonia province of Spain.

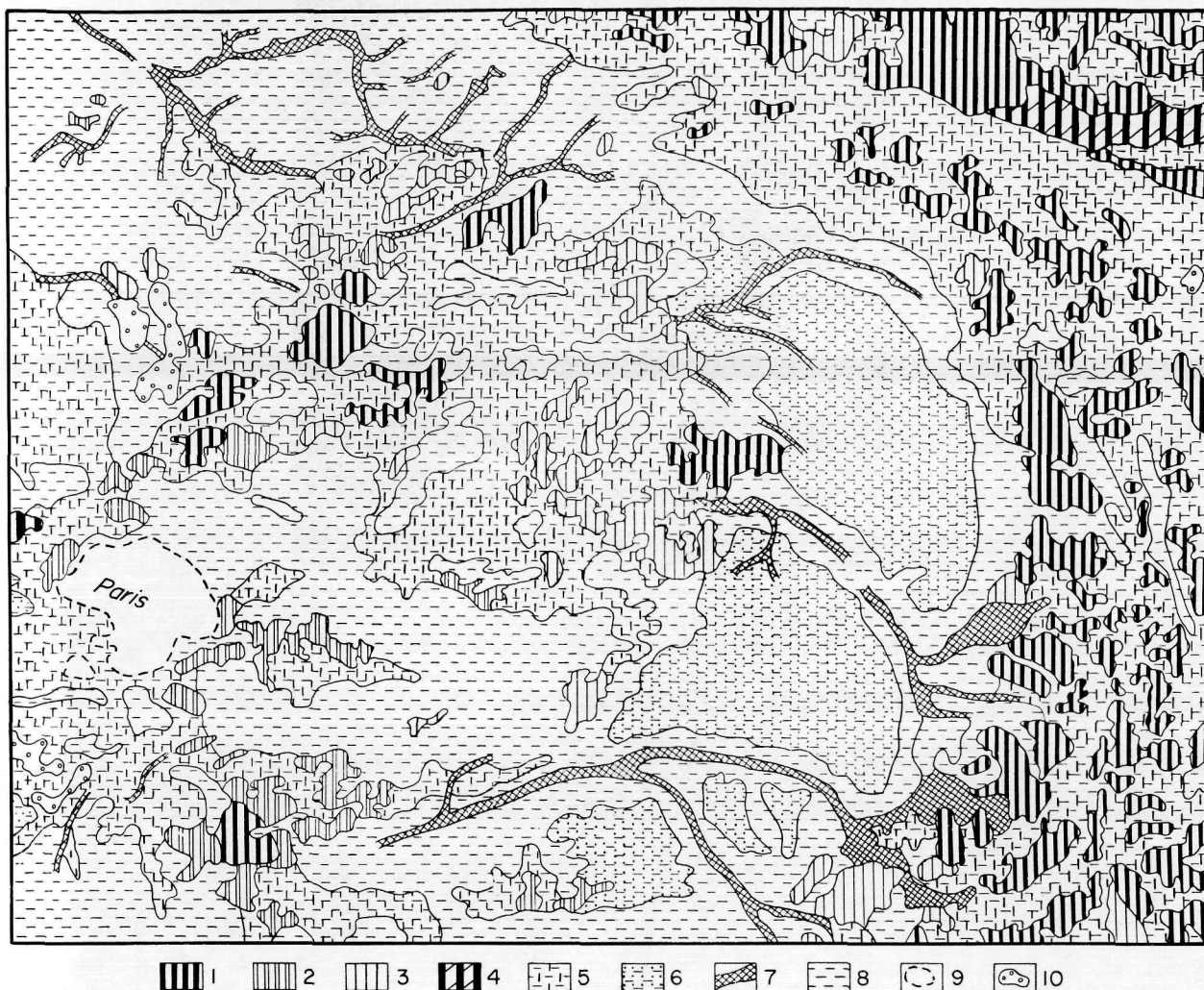
On the basis of this Nimbus 1 AVCS photograph alone, the gray levels were found by Hasser (1966) to correspond generally to the following terrestrial features:

Gray Levels on Nimbus 1 AVCS Image of SW France and NE Spain (Figure 2-7)	Terrestrial Features
1) Light-gray	Soil, thin vegetation
2) Light-gray to medium dark gray lineaments	Drainage systems
3) Dark-gray	Forested mountain ranges
4) Generally sharp boundaries	Boundary between water bodies, and terrain features (snow vs bare ground)
5) Generally gradational	Boundary between forests and plains



(1) The landscape of the lowlands of the Seine and Oise Rivers is represented by the winding lines of the big rivers, the dark compact spots of oak-hornbeam forests on the hillsides, and the uneven grey to light-grey tone of the arable land. (2) The landscape of the flat limestone plateau of Brie, Valois, Beauce (mostly treeless) is characterized by fields of even light-grey tone divided by dark-grey elongated stripes of oak forests situated along the cuestas, tectonic lines, and river valleys. (3) The landscape of the low chalky cuesta ridges of Champagne (mostly wasteland) is distinguished by the lightest light-grey tone, together with the low-contrast large marbly pattern of summer oak-pine forests which is extremely noticeable against the background of narrow strips of transit rivers. (4) The landscape of the seaside plains of Picardie is notable by the homogeneous light-grey to grey tone with the low-contrast fine texture and dark winding lines of the river valleys. (5) The landscape of the hilly elevations of Marne, Bray, with its oak forests, is represented by a vaguely spotty, relatively contrasting pattern consisting of compact, dark-grey to darkish-grey spots of forests, occupying the largest part of the entire area and separated by narrow light-grey spaces of wasteland. (6) The landscape of the cuesta elevations of Argonne is identified by lengthwise oriented, dark to dark-grey spots and the stripes of oak-beech forests on the ridges, separated by the strips of consequent valleys with arable lands. (7) The landscape of the mid-high mountains of Ardennes, covered by oak-beech forests with an admixture of birch and spruce, can be distinguished partly by the massive, elongated dark spots of the forests and partly by the low-contrast texture of the open woodlands.

Figure 2-5 Nimbus 1 AVCS photograph of the Paris Basin taken on orbit 236, 13 September 1964, with a classification of geomorphic provinces (Twelve geologic formations [Roman numerals] are discussed in the original paper - Kondrat'yev et al, 1968)



(1) Hornbeam, beach, and winter oak forests. (2) Chestnut-mixed oak forests. (3) Mixed oak forests. (4) Beach and winter oak forests. (5) Mixed oak forests, fields, vineyards, orchards, and other agricultural lands. (6) Summer oak forests, second-generation pines, fields (barren ground and vineyards). (7) Flood plain, lowland forests, and shrubs with fields, swamps, orchards, and gardens. (8) Cultivated fields, vineyards and orchards. (9) Areas devoid of natural vegetation. (10) Vegetated regions overcast by a thick cumulus cloud cover.

Figure 2-6 Vegetation map of the Paris Basin derived from published vegetation maps (Vinogradov, 1969). (Compare this map with the Nimbus 1 AVCS photograph in Figure 2-5.)

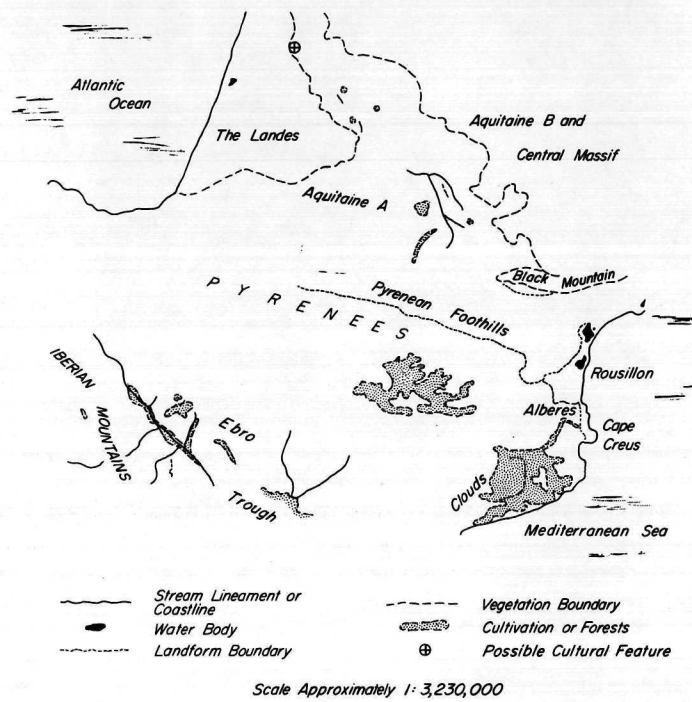
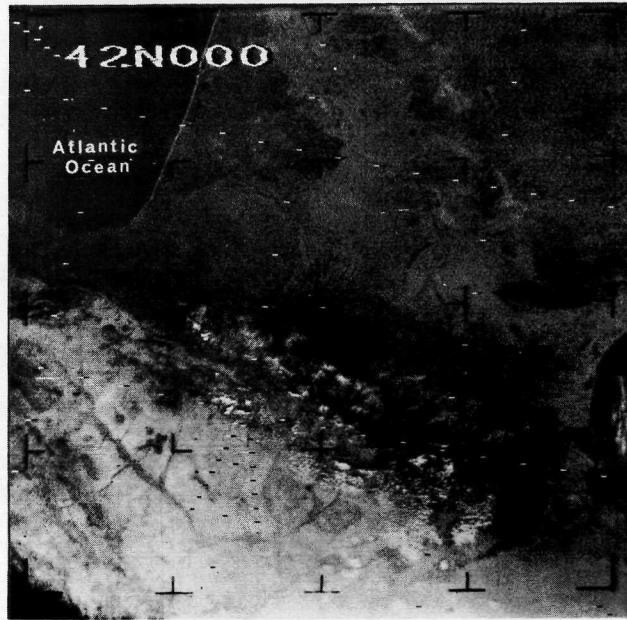


Figure 2-7 Nimbus 1 AVCS photograph of southwestern France and northeastern Spain taken on orbit 46, 31 August 1964. (Hasser, 1966)

Drainage patterns per se are not well distinguished on Nimbus HRIR and THIR imagery; regional geomorphic provinces and geomorphic elements, however, when accentuated by soil moisture or vegetation, stand out prominently. At times, geomorphic and geologic features which might be obscure on the photofacsimile become evident on the digitized grid-print maps.

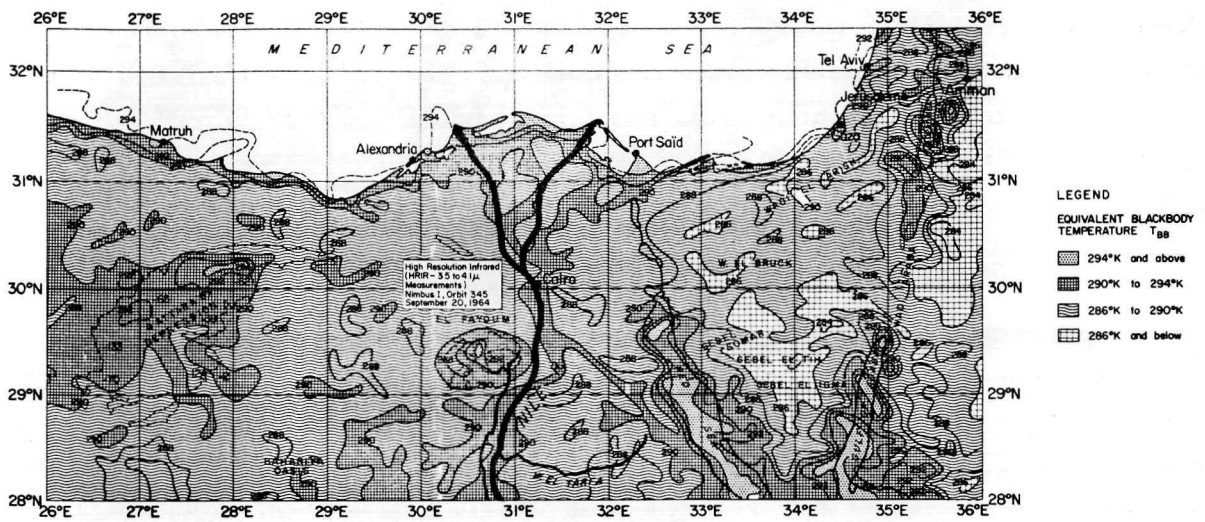
2.2.4 Paleogeomorphology

Paleogeomorphology is the study of land forms and processes operating on the earth's surface prior to recent times. Analysis of HRIR and THIR data may provide us not only with information on the present-day ground conditions, but also may give us some insight into the paleogeomorphology of an area. One fascinating application of HRIR and THIR data is their possible capability of delineating buried, abandoned, or fossil drainage channels. The detection of ancient drainage channels, especially in arid regions, is of extreme importance for irrigation and land reclamation purposes, as these areas are the most apt to retain moisture and, therefore, most adaptable to irrigation projects. The propensity of these ancient channels to store moisture is what makes them detectable in the HRIR and THIR data. Moisture raises the heat capacity of surficial materials, enabling them to conserve more efficiently the heat of the day. Thus, these ancient channels should appear anomalously warmer in the nighttime HRIR or THIR temperature maps. Moisture also lowers the albedo of a surface and, therefore, especially in the rainy season, ancient drainage channels should appear darker and less reflective in the Nimbus 3 daytime HRIR data.

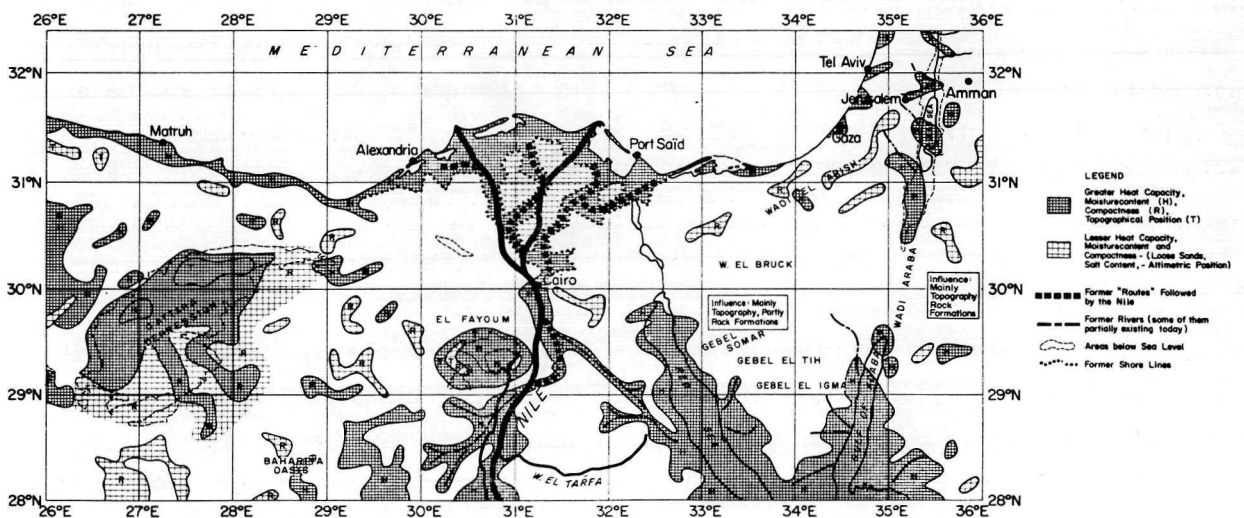
A few studies now exist where abandoned courses of rivers, former shorelines and flood plains have been tentatively identified on the Nimbus imagery and discussed. However, discovery of these ancient features may be impossible with Nimbus data alone. The investigator has to have a thorough knowledge of the geology and hydrology of the area, possibly substantiated by field work.

Examples of abandoned or fossil drainage channels, landscapes, shorelines, etc., are numerous and spread over the entire globe. None of the examples presented below, illustrating such features as detected by the Nimbus HRIR data, are actually newly found. The Nimbus data provide an added, repetitive, large area look at these obscure terrestrial features which is not practically possible with conventional surveying methods and suggests a new way for geological detection and analysis.

The former courses of the Nile River, as detected by Nimbus 1 HRIR nighttime measurements and interpreted by Pouquet (1968b), are illustrated in Figure 2-8b. These areas tend to coincide with the elongated warmer strips visible on the map (Figure 2-8a). The word "course" in this and subsequent examples is used broadly, involving areas affected by the former channels, and by the spreading of moisture through and along the alluvium.



a. Map of equivalent blackbody temperature, T_{bb}



b. Map of geomorphological features

Figure 2-8 Nimbus 1 HRIR equivalent blackbody temperature map of the Nile Delta and surrounding area taken on orbit 345, 20 September 1964 with an associated terrestrial features map. (Pouquet, 1968)

Other abandoned or intermittent river channels may be found on either side of the Dead Sea, the Red Sea and the Gulf of Aqaba. The Wadi or intermittent rivers retain moisture long after a rain and are thus detectable by their warmer temperatures. The southern prolongation of the Dead Sea, following the elongated depression (average 80 meters below sea level) is warmer, not because of its lower elevation but because of its greater moisture content.

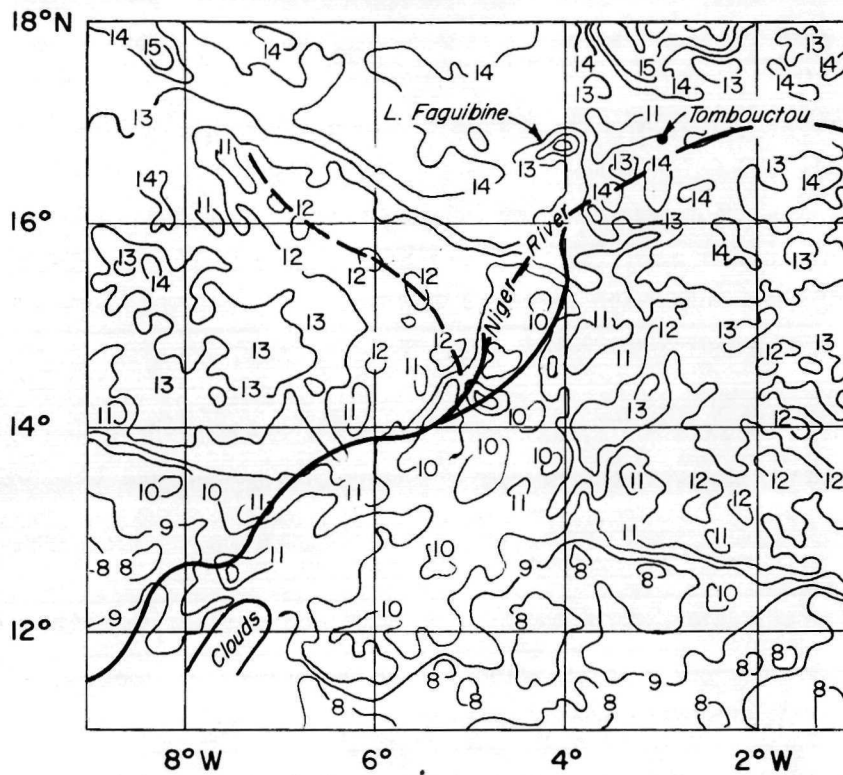
Pouquet (1968b) used Nimbus 3 nighttime HRIR temperature maps in a similar manner to evaluate the past history of the Amargosa and Colorado Rivers. Strips of warm areas in the vicinity of the rivers are again suggested to be the result of ground moisture stored in the "fossil" alluvium. Other areas where Nimbus HRIR data illustrate similar paleogeomorphological features are:

- 1) The former route of the Senegal River, western Africa (Pouquet, 1969a).
- 2) The possible former link between the Karakoro and Senegal Rivers, western Africa (Pouquet, 1969b).
- 3) The suggested former course of the Niger River, western Africa (Pouquet and Rabchevsky, 1970a; MacLeod, 1970b; Rabchevsky, 1971).
- 4) Stream piracy and former route of the Parana River, eastern South America (Pouquet and Rabchevsky, 1970).

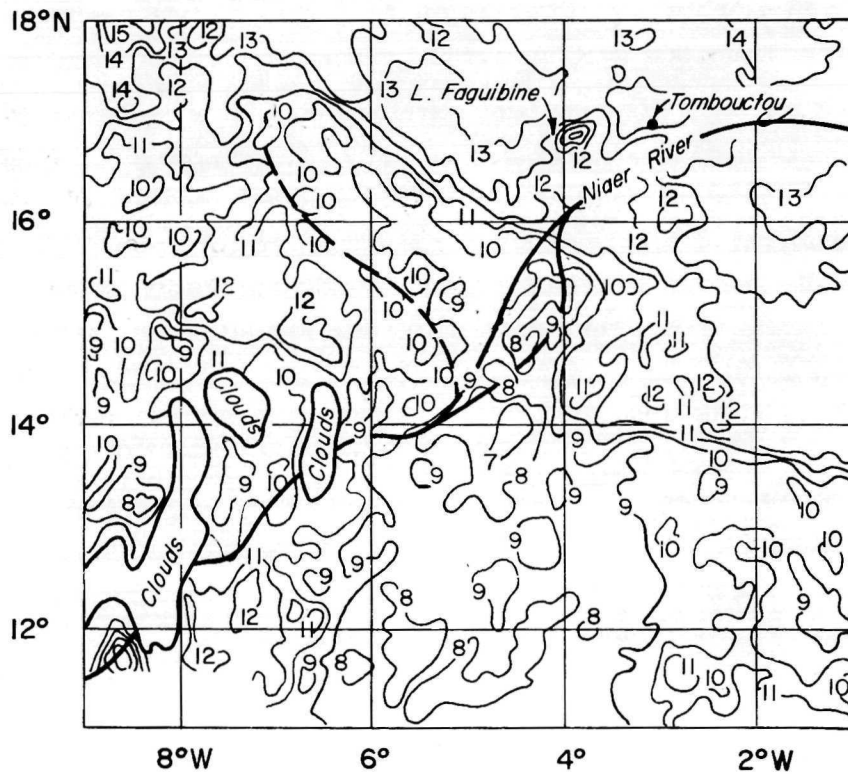
Figures 2-9 and 2-10 illustrate the distribution of Nimbus 3 HRIR daytime reflectance patterns in the Niger River Valley and vicinity expressed in quantitative values. * A pronounced, elongated low reflectance pattern trending NW-SE appears in the northwest quadrant of Figure 2-9b. This pattern is not present on all maps, but appears only after periods of regional rainfall and is probably caused by moisture stored in the porous ferruginous (lateritic) soils and alluvium, and by the resultant vegetation growth. It is hypothesized that this low reflectance feature may represent the ancient course of the Niger River. Speculation of the existence of a former route of the Niger River is not new (McGinnies et al, 1970). The significance of this interpretation, however, is in the probable ability of the Nimbus satellite remote sensors to detect such obscure terrestrial features.

MacLeod (1970b) has also discussed the detection of the former course of the Niger River on Nimbus 3 HRIR images. He presents a series of photofacsimiles, several of which (during June and July) show increased contrast between the Upper Niger and its surroundings. The course of the ancient river also appears north of Segou. He concludes that, "It is reasonable to assume that the increasing contrast results from an increase in the area of surface water; the only other surface that shows as dark in the HRIR images is basalt, such as the outcropping of the Ahaggar

*The grid print maps used in these examples were not filtered for noise present in the data (see Appendix C for a discussion of the noise). Filtering the data would appreciably improve the analysis (MacLeod, 1971; personal communication).



a. Orbit 1074, 3 July 1969



b. Orbit 1772, 24 August 1969

Figure 2-9 Nimbus 3 daytime HRIR reflectance maps (0.7 to $1.3 \mu\text{m}$) of Central Mali, Africa. (The projected former course of the Niger River is accentuated by the dashed lines.)

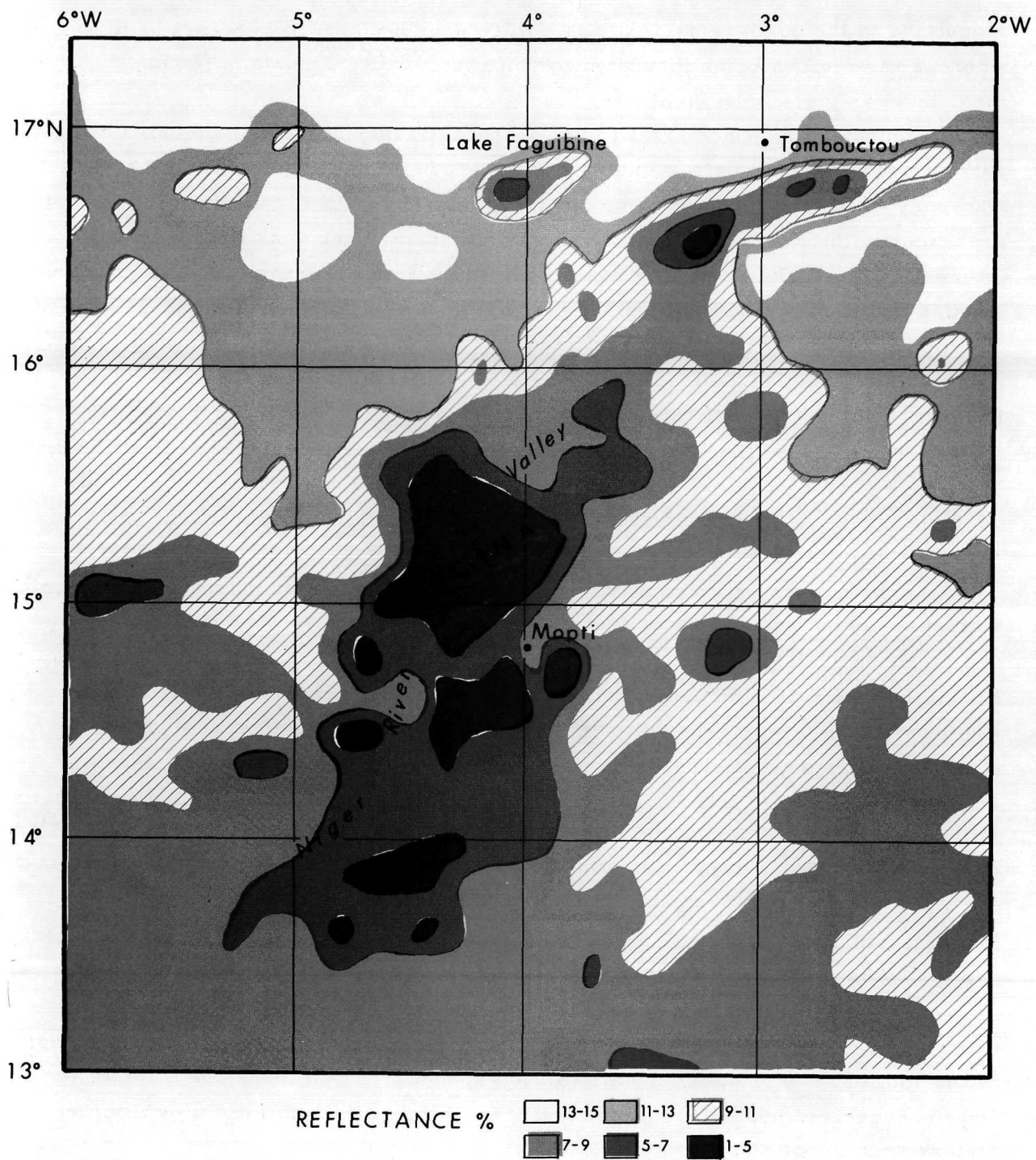


Figure 2-10 Nimbus 3 daytime HRIR reflectance map of the Upper Niger River Valley, Africa taken on orbit 2965, 21 November 1969.

Mountains in the north central Sahara, which does not change in form month to month; whereas the regions being inundated by floodwaters do change both in shape and in tone, and can thereby be identified."

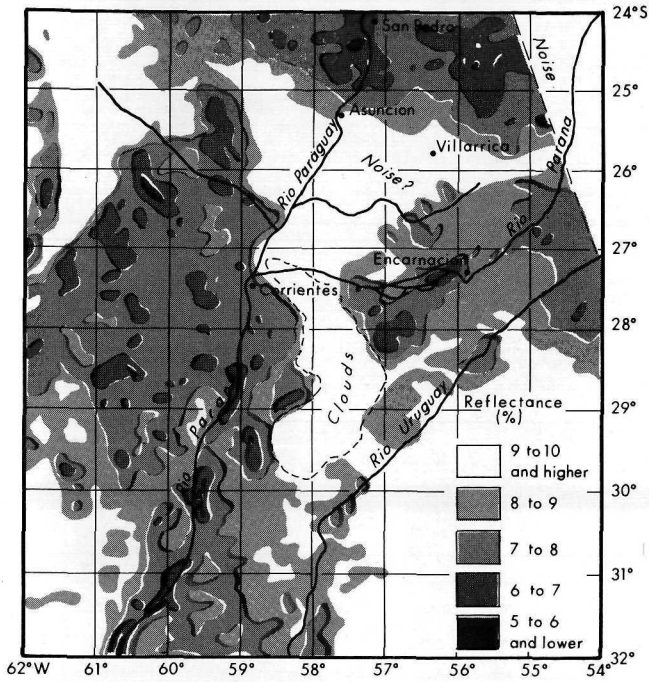
Floodplains, which are an integral part of river systems, may also be studied with Nimbus radiation data. The spring season reflectance patterns in the Parana-Paraguay River basins, South America, are illustrated in Figure 2-11d. The swampy area west of the Paraguay River has a low reflectance, as does the conspicuous and interesting triangular area east of it, with its apex at Encarnacion. This same triangular pattern occurs also on other maps (Figures 2-11a, 2-11b and 2-11c). Pouquet and Rabchevsky (1970) hypothesized that this triangular area represents an ancient floodplain constructed by the former routes of the Parana and Paraguay Rivers. Precluding the final analysis supported by ground investigations, they further hypothesized that the Parana River in the geologic past flowed from Encarnacion to Goya and acquired its present sharp Encarnacion-Corrientes bend only recently. Such an interpretation would imply stream piracy by a tributary of the Paraguay River, originating at Corrientes.

Besides former stream courses and floodplains, other paleogeomorphological features may be studied or verified through the use of the Nimbus data. Included are fossil or shrinking lakes, swamps, exposed soil "horizons", and ancient shorelines. For example, former positions of the sea (shorelines) are suggested in Figures 2-12 and 2-2. The dotted pattern along the Mexican Tuxpan-Culican coast (Figure 2-12) corresponds to part of an offlap marine series (Pouquet, 1969b). Pouquet (1969a) notes that the 290°K isotherm in Figure 2-2 outlines the earlier shoreline along the Gambia and Senegal coasts, West Africa. A Nimbus 1 AVCS photograph in Figure 2-13 shows the former shorelines of the El Fayum Depression and Lake Birket Qarum, Egypt, viewed from a height of 560 km by a sensor designed for meteorological observations. Consequently, the superior ERTS sensors will easily be able to image even smaller geomorphological features.

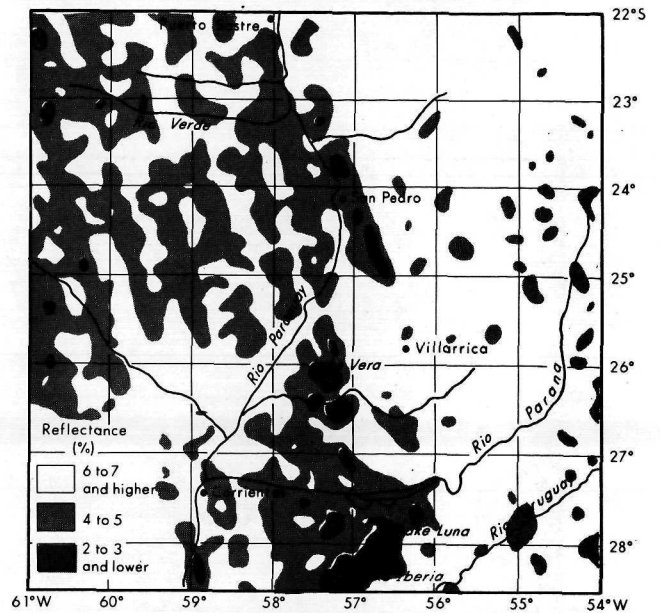
We want to emphasize that the "paleogeomorphological" features briefly described on the preceding pages are not new to geologists. What is novel, though, is the applicability of satellite data to such specialized studies. The availability and the suggested possible applications of the Nimbus data definitely justify their further analysis and exploitation.

2.2.5 Geomorphic Processes

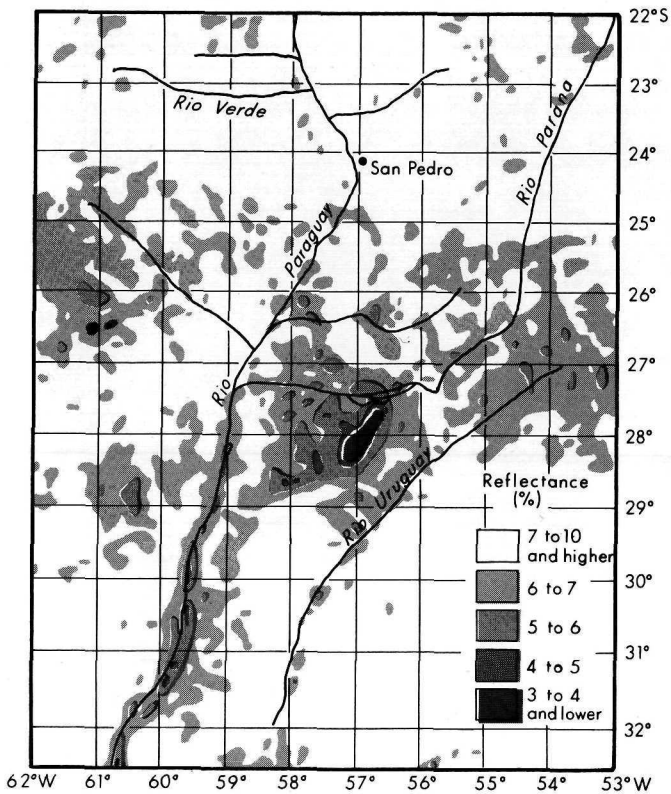
Geomorphic processes are all those physical and chemical changes which effect a modification of the earth's surface and are due to running water, glaciers, ground water, waves and currents, wind, weathering, volcanism and diastrophism. The effects of running water on regional geomorphology and their analyses from



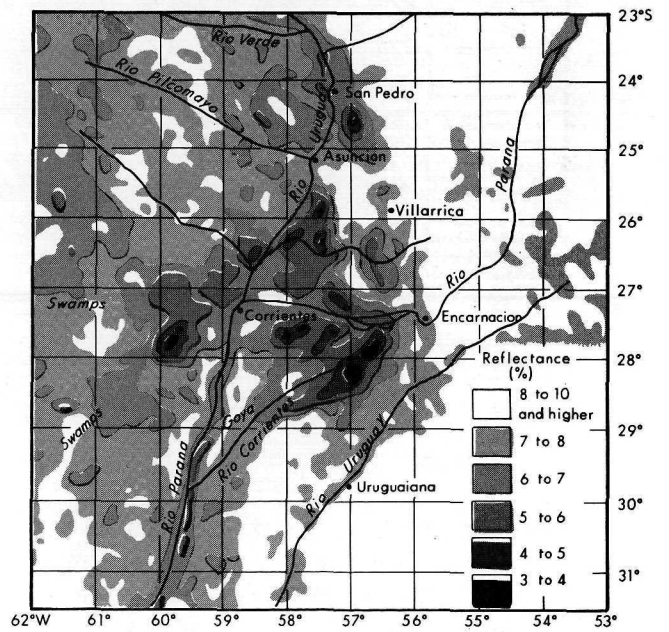
a. Orbit 394, 13 May 1969



b. Orbit 769, 10 June 1969



c. Orbit 1426, 29 July 1969



d. Orbit 2619, 26 October 1969

Figure 2-11 Nimbus 3 daytime HRIR reflectance maps illustrating the areal and temporal distribution of reflectance values in portions of Argentina, Brazil, Paraguay, and Uruguay. (Note the low reflectance of the swampy area west of the Paraguay River and the Parana River floodplain.)

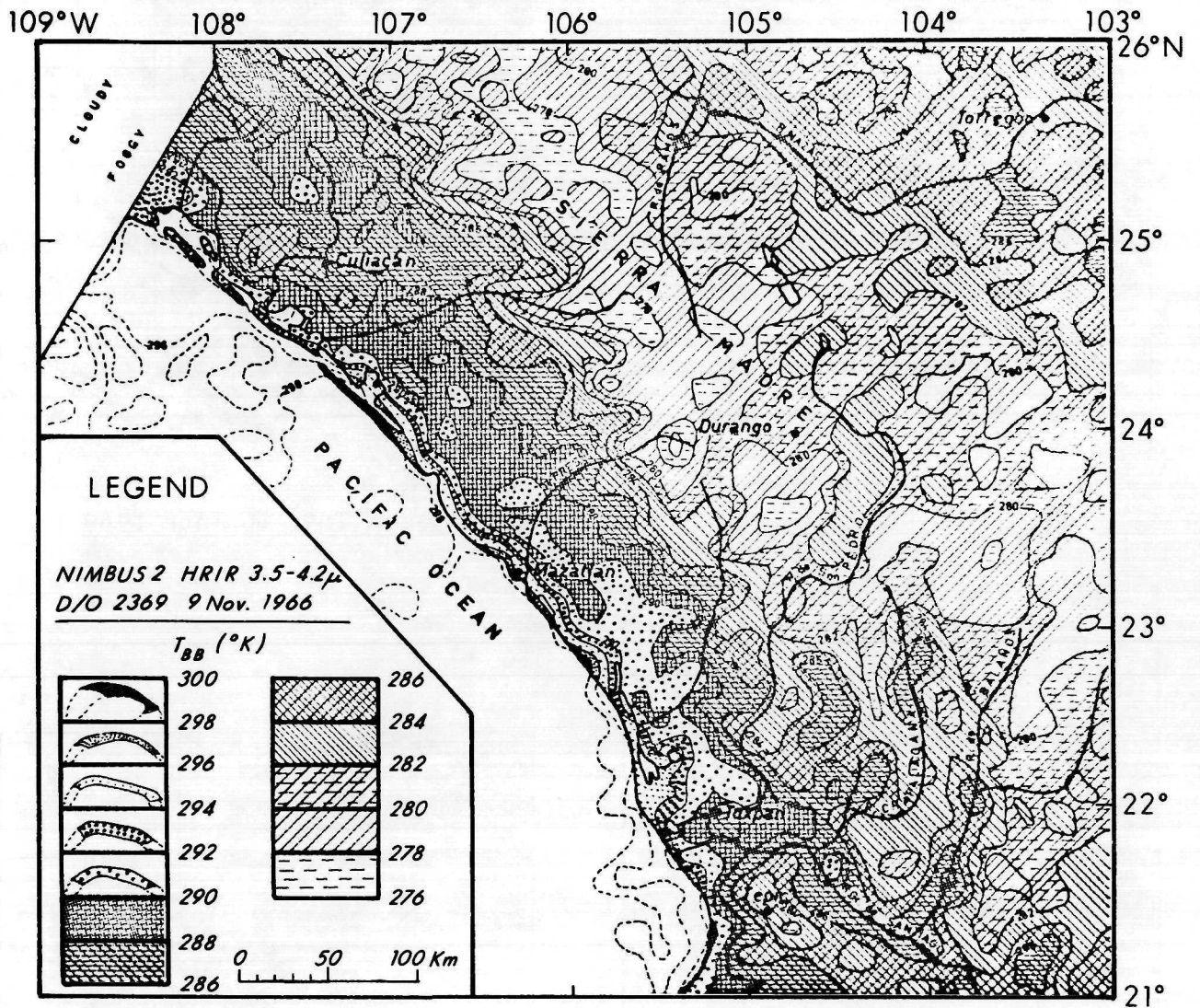


Figure 2-12 Nimbus 2 nighttime HRIR equivalent blackbody temperature map of the Mexican Tuxpan-Culiacan coast (Pouquet, 1969). The position of a former sea level along the northwest Mexican coast is indicated by the 290°K isotherm.

Nimbus data have been partly described in Section 2.2.3; the effect of weathering has been described in Sections 2.2.1 and 2.2.4. The effect of volcanism may not be observed in detail, but detection of volcanic activity is, at times, possible and will be described in Section 2.4. Individual glaciers, sand dunes, waves and currents, and ground-water may not be observed with certainty, although the combined regional effects of these geomorphic agents may be inferred.

Eolian processes of erosion and deposition, and associated landforms, have not been studied with the aid of Nimbus data, although arid regions have been described from Nimbus imagery in various publications. Nonetheless, pertinent information exists on Nimbus imagery. Individual sand dunes cannot be seen since they are smaller than the resolution of the Nimbus imagery; however, sand dune fields have been recorded (Figure 2-13), and at times even dust storms. Figure 2-14 shows the migration of a dust storm across western Africa and the Atlantic. It is possible from this sequence of photographs to plot the path and areal distribution of the storm, and to calculate its velocity.

Coastal sedimentation is another process that reshapes the surficial configuration of coastal landforms and can, at times, be detected by Nimbus imagery. Figure 2-15 shows sedimentation plumes in the Persian Gulf off the Tigris-Euphrates delta. The complexity of the delta itself is evident, including the river channels, wetlands and playas. With proper photographic enhancement or a false color technique, such as the color displays described in Section 3.3, it may be possible to infer the relative mass and distribution of the suspended sediment, direction of sediment transport, submarine channels and the relative depth of the coastal waters. Additional Nimbus imagery illustrating coastal sedimentation processes is available, but has not been reviewed for this publication. One purpose of this report is to stimulate interest in these areas among geoscientists.

As the distribution and behavior of meteorological events often correlate with regional geomorphic provinces and large landforms, geomorphology cannot be studied without some understanding of atmosphere-ground interaction. The Nimbus satellites are specially designed to provide information in this area. Figure 2-16 is a small sampling of Nimbus photographs illustrating the effect of landform on cloud cover conditions. Note, for example, the wake clouds forming in the lee of the Canary Islands near the upper center of Figure 2-16c.

2.3 Regional Geology

Synoptic, small-scale/large-view Nimbus imagery is of value in illustrating large, conspicuous terrestrial features; in providing low-resolution images of high-latitude areas for which no other high-resolution satellite coverage is available; and possibly in detecting unmapped lineaments in mountainous areas where

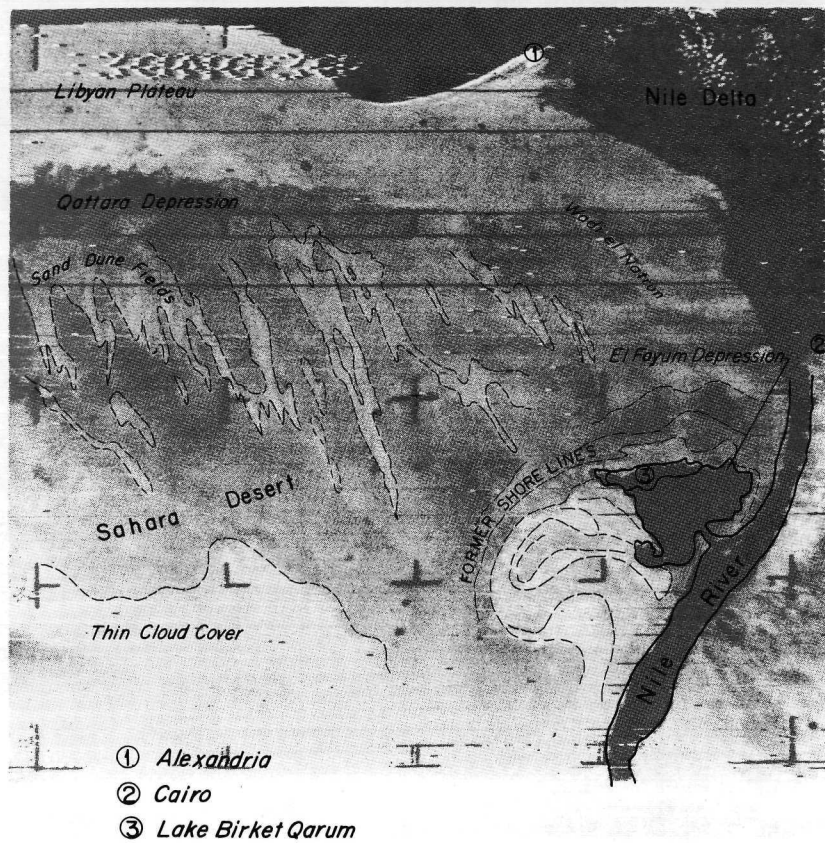
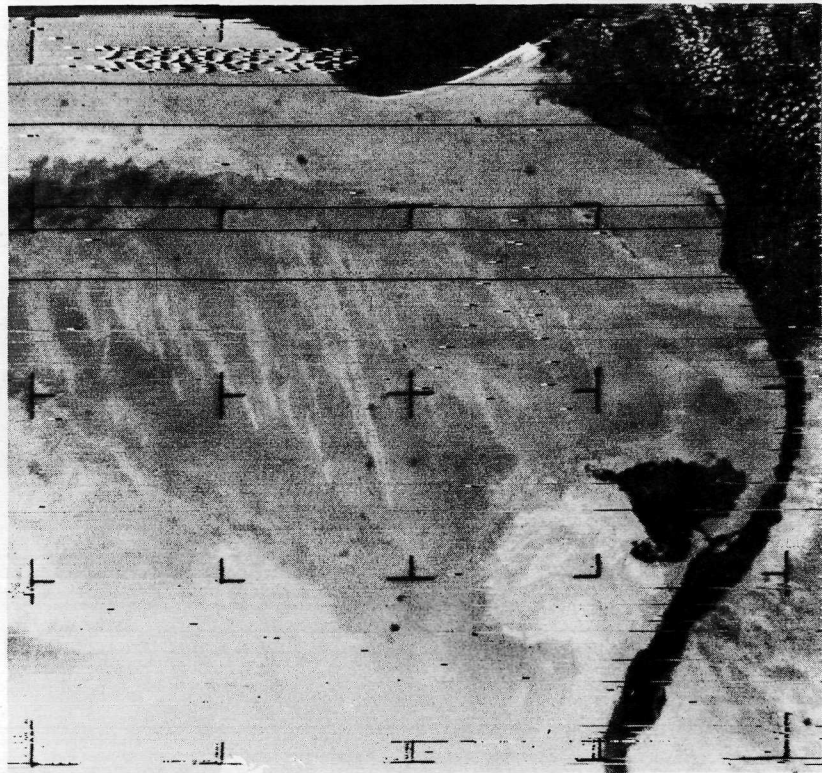
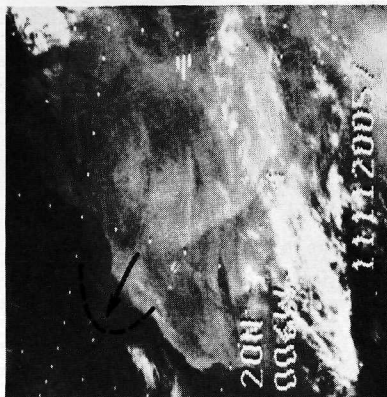


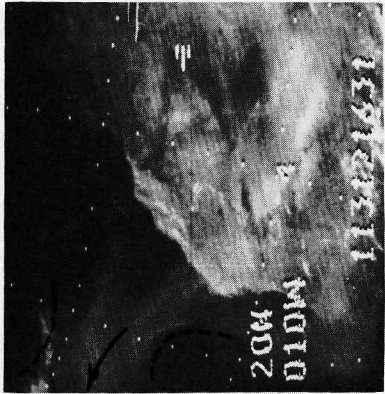
Figure 2-13 Nimbus 1 AVCS photograph of northwestern Egypt taken on orbit 323, 19 September 1964, showing the distribution of sand dune fields and the positions of former shorelines in the vicinity of the El Fayum Depression.



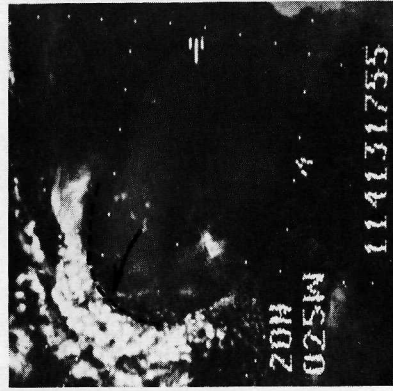
Orbit 177, 21 April



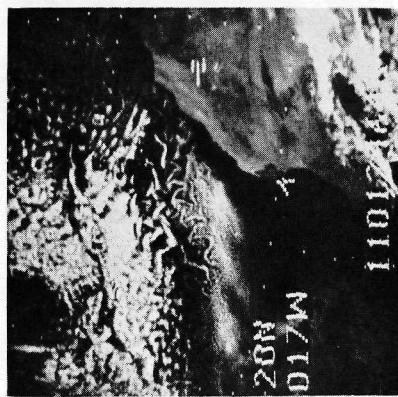
Orbit 191, 22 April



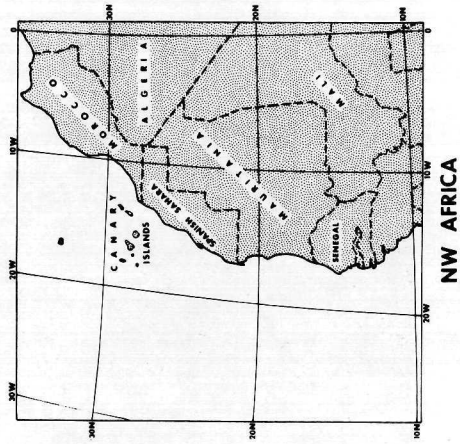
Orbit 204, 23 April



Orbit 218, 24 April

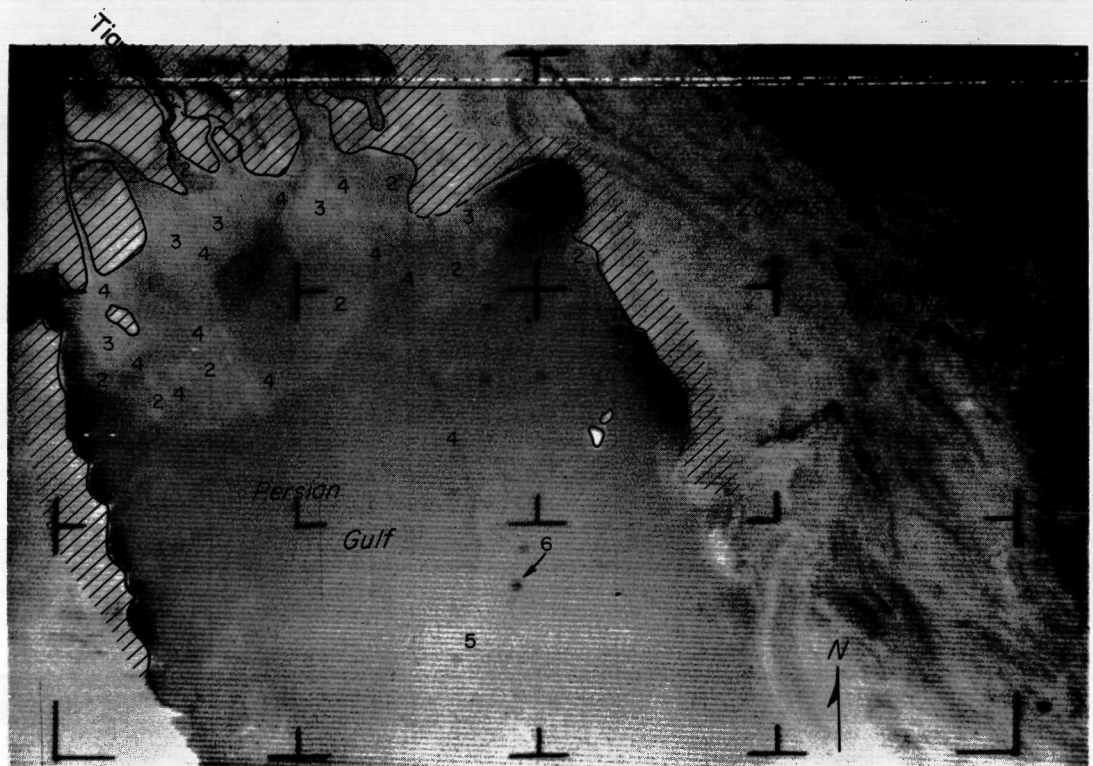
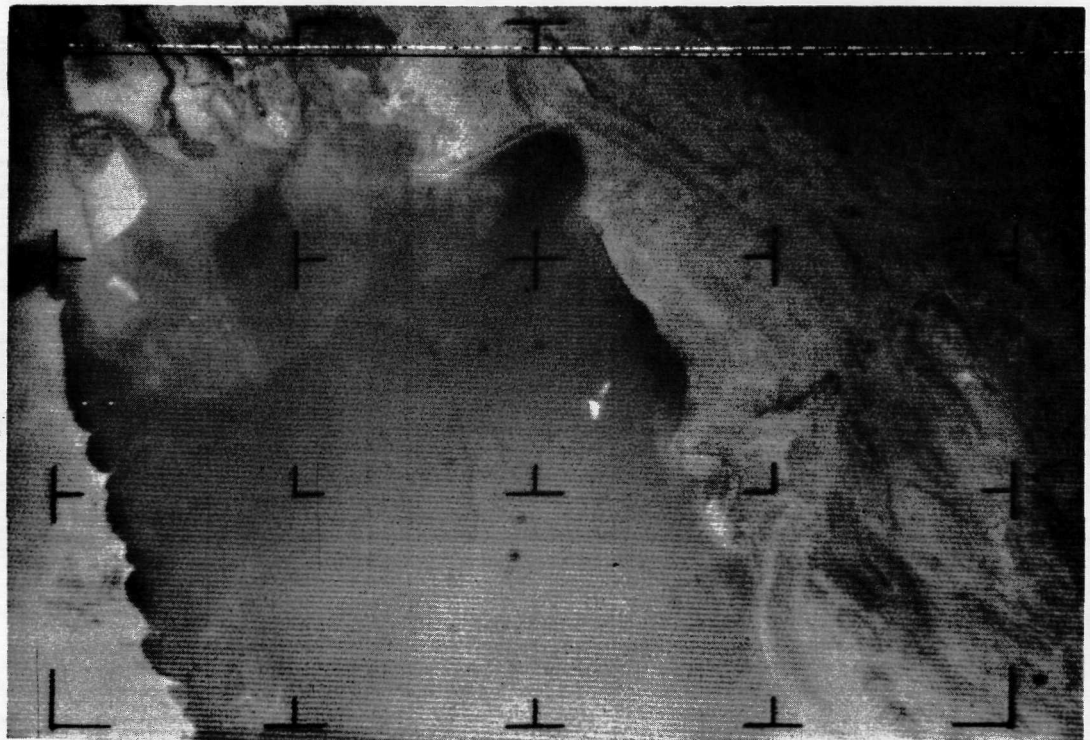


Orbit 164, 20 April

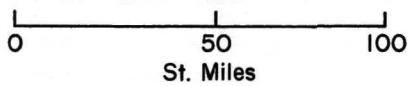


Orbit 231, 25 April

Figure 2-14 Nimbus 4 IDCs photographs showing the migration of a Sahara dust storm across western Africa and the Atlantic during April 1970.

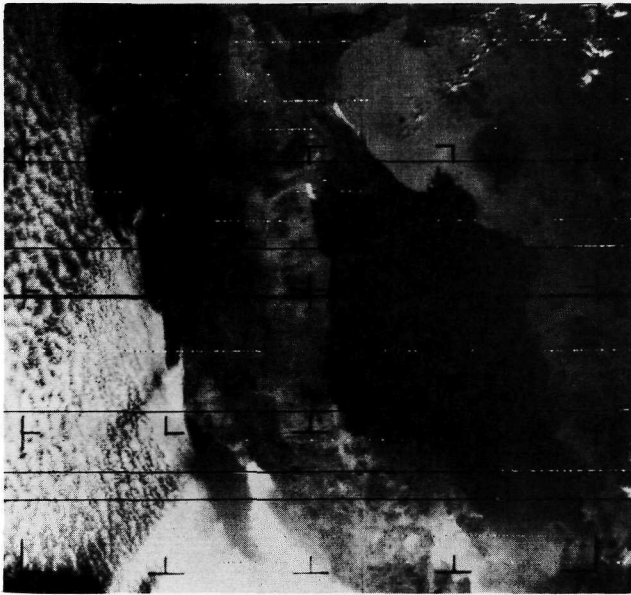


Land Area

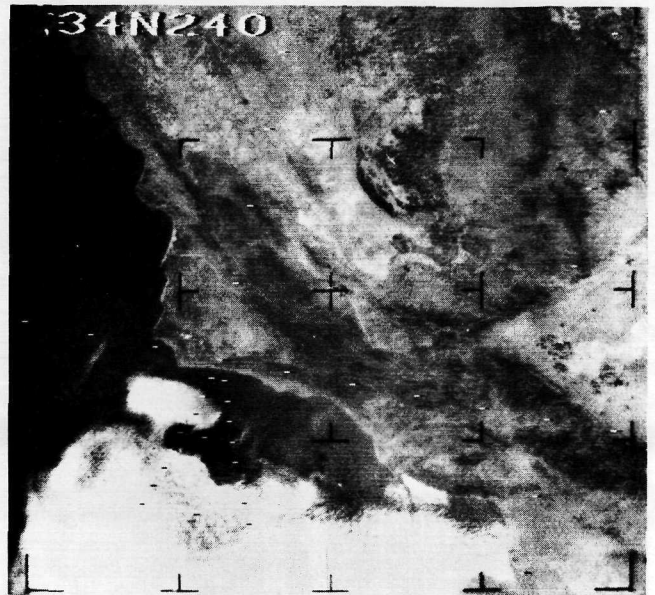


- 1 - Relatively clear water
- 2 - Suspended sediment - low concentration
- 3 - Suspended sediment - high concentration
- 4 - Submarine channels
- 5 - Sunlint
- 6 - Noise

Figure 2-15 Nimbus 1 AVCS photograph of the Persian Gulf and the Tigris-Euphrates River delta taken on orbit 249, 14 September 1964.



a. Lower California, Nimbus 1 AVCS
Orbit 124, 5 September 1964



b. Islands off Santa Barbara, California
Nimbus 1 AVCS, Orbit 329, 19 September 1964



c. Canary Islands, Nimbus 3 IDCS
Orbit 995, 27 June 1969

Figure 2-16 A selection of Nimbus photographs illustrating the effects of landforms on cloud patterns and distributions.

the topography is outlined by snow (Lowman, personal communication, 1971). The interrelationships between the various tectonic elements can at times be easily seen on Nimbus imagery, and correlation from region to region, and even continent to continent, becomes possible. Figure 2-17 shows a few examples (Lowman, 1971) of geologic features of extremely large areas which can be well illustrated with the aid of Nimbus imagery.

Only a few Nimbus data have been used for regional geologic studies, considering the vast amount of data available. Factors limiting the application of Nimbus data to geology may be their small scale and unfamiliarity of geoscientists with satellite data, especially the infrared and near infrared HRIR and THIR.

2.3.1 Regional Outcrop Patterns and Provinces

Usefulness of Nimbus photographs for delineation of regional outcrop patterns and provinces is discussed in various reports, some of which will be covered in this section. It is hard to claim any direct correlation between the outcrop patterns, lithology, and the gray tones visible on Nimbus photographs. However, the drainage patterns shown by the Nimbus images may sometimes be indicative of the rock types (sedimentary, metamorphic, or igneous).

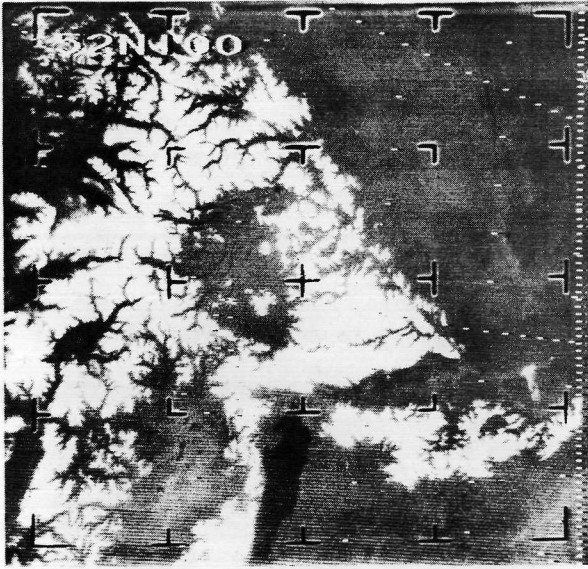
The Nimbus 1 image of the Canadian Rockies (Figure 2-4) also discussed in Section 2.2.3 is a good illustration of one such case. The map (Figure 2-18) showing the drainage systems and fault distribution in this region illustrates the lithologic and structural dependence of two different geologic provinces. The predominant NW-SE striking faults east of the Fraser-Columbia Rivers are generated in sedimentary beds of the same trend, while the irregular distribution of faults west of the Fraser-Columbia Rivers is due to igneous intrusion and repeated orogenic activity and metamorphism (Rabchevsky, 1970b). Most of the NW-SE trending streams in the eastern portion of the photograph and the Fraser-Columbia Rivers follow the strike of the easily eroded sedimentary formations and the strike-slip fault lines. The Fraser and Columbia Rivers, of course, follow the Rocky Mountain Trench, which shows as a prominent snowless lineament running from the top left to the bottom right of Figure 2-4.

Figure 2-19 shows the complex patterns of the folded Appalachian Mountains in the Pennsylvania region. Taggart (1965) compared the geologic map of Pennsylvania to the tonal patterns on this Nimbus 1 AVCS photograph and concluded that these patterns easily correlated with the general geology of the region and, to some extent, even with the lithology.

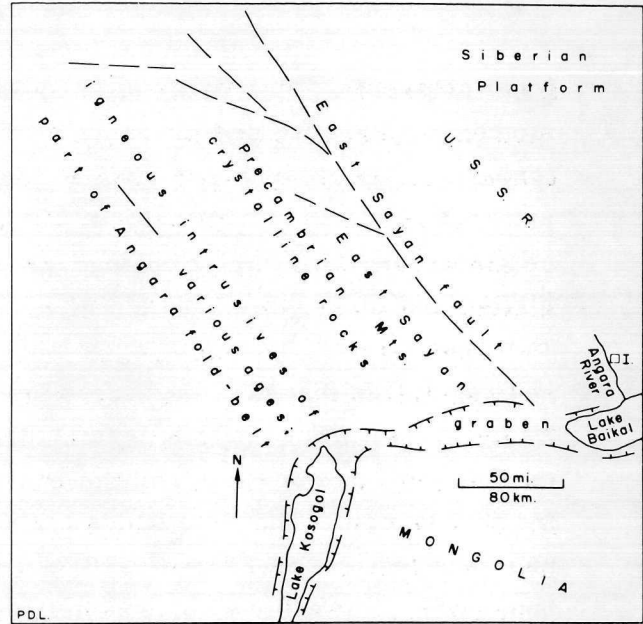
Figure 2-20 shows the Chesapeake Bay region and Piedmont area of Virginia and surrounding area. The Chesapeake Bay region is characterized by numerous rivers, bays, marshes and lack of distinct tonal lineaments, textures or extreme

tonal contrasts. The Piedmont province on this photograph is characterized by its mottled appearance and presence of distinct NE-SW trending lineaments (light gray tones). After referring to ground truth (see Rabchevsky, 1970), the lineament patterns in the Piedmont portion of this photograph were correlated with lineaments on the ground (see aerial photograph, Figure 2-21). The lineaments may be due to a combination of effects including the regional strike of the Precambrian and lower Paleozoic strata, bedrock edges of the tilted Triassic sandstones and intrusives, and vegetation (darker tones) growing in the areas of more fertile soil (Lewis and Davis, 1966). The complementary dark gray persistent SE-NW lineaments transecting the Coastal Plain and the Piedmont correspond to the major systems draining this region. The Blue Ridge (point 6 on Figure 2-20) and the Valley and Ridge province (point 4 on Figure 2-20) are characterized by distinctly patterned tonal boundaries. The Blue Ridge is defined by a dark tone as a consequence of dense vegetation. The higher albedo of the Great Valley, on the other hand, is generated by a thinner vegetal cover, crop fields, and possibly haze collected in the trough of the Valley. The major ridges of the Valley and Ridge province (west of point 4, Figure 2-20) stand out as light-gray tones and are recognized by their typical zig-zag patterns. These patterns reflect the underlying geology and topography of the province and on the AVCS photographs are also accentuated by the vegetation cover. As can be seen on Figure 2-22, the slopes of the Shenandoah Mountains, besides differing in lithologic composition, are also more densely forested than the valley floors below.

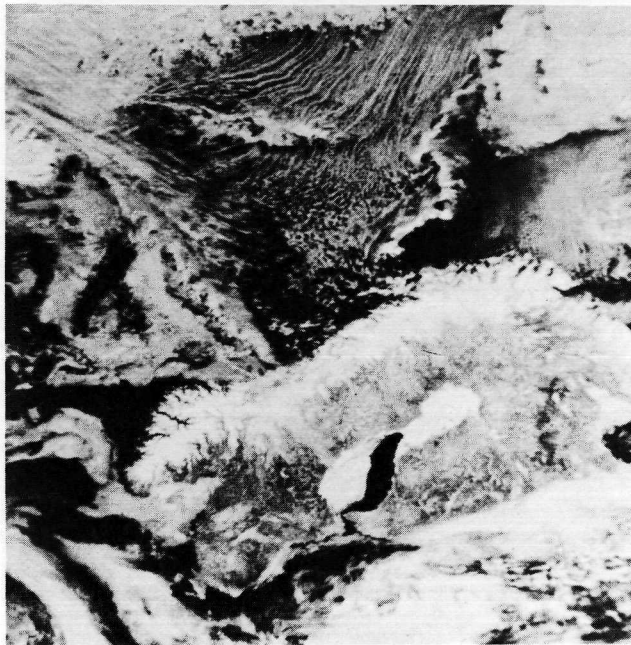
A Nimbus 1 AVCS photograph which included southwestern Wyoming, northwestern Colorado, and northeast Utah was compared by Short (1971) to topographic, geologic, and soil maps of the region (Figure 2-23). The topographic map clearly shows a relation between highlands and darker areas on the photo largely because of the association of Douglas fir and spruce with the higher elevations. Grasslands, appearing as intermediate gray tones, occur in the higher parts of the basins. Within the lower basin the prevailing vegetation is sage, saltbrush, and greasewood, spatially distributed in densities too low to be a major influence on the more highly reflective soils, alluvium, and sedimentary rocks responsible for the lighter gray tones. When comparing the Nimbus photo with the geologic map one can easily recognize the folded Wyoming, Hoback, and northern Wasatch ranges because of their forest cover. The string of small dark patches extending south of the Sweetwater arch are block-faulted and folded mountains which rise enough above the basins to develop thick stands of deciduous and coniferous trees. In general, very different rock types, such as the granites of the Wind River and Uinta Mountains, and the sediments in the basin, have albedoes so similar that they cannot be differentiated by tone alone. Note, however, that bands of intermediate gray (see arrows) broadly correspond to upper Cretaceous rocks. These units are generally sandy



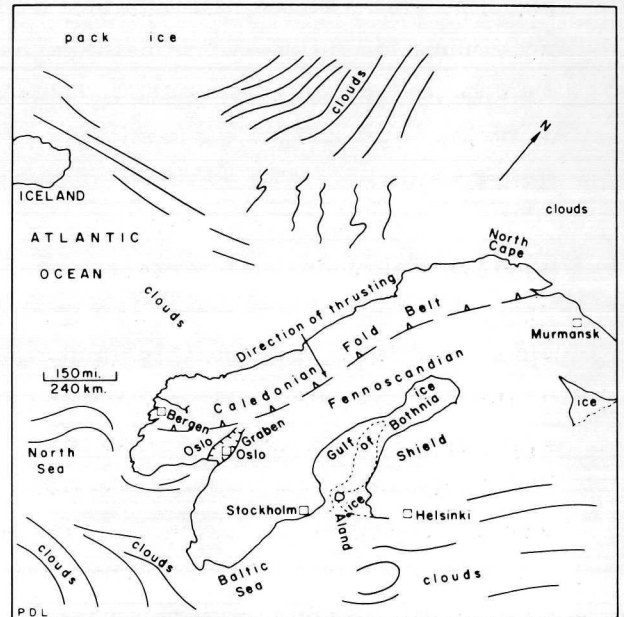
Nimbus 1 AVCS photograph taken on orbit 320, 19 September 1964



Geologic index map based on a Nimbus 1 AVCS photograph taken on orbit 320, 19 September 1964.

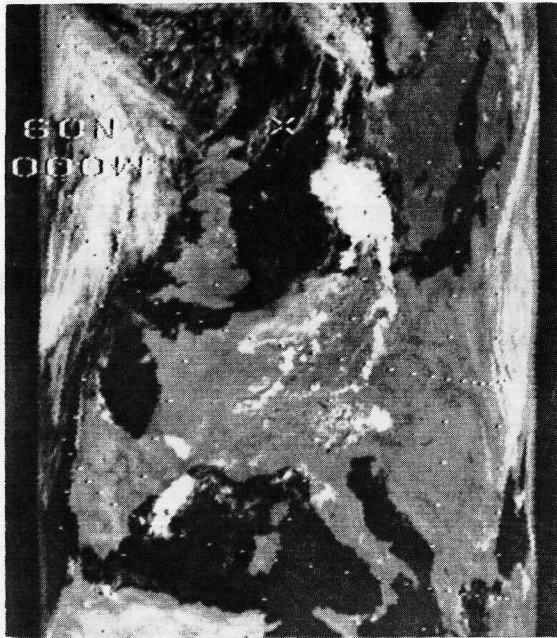


Nimbus 4 IDCS image taken on orbit 68, 13 April 1969

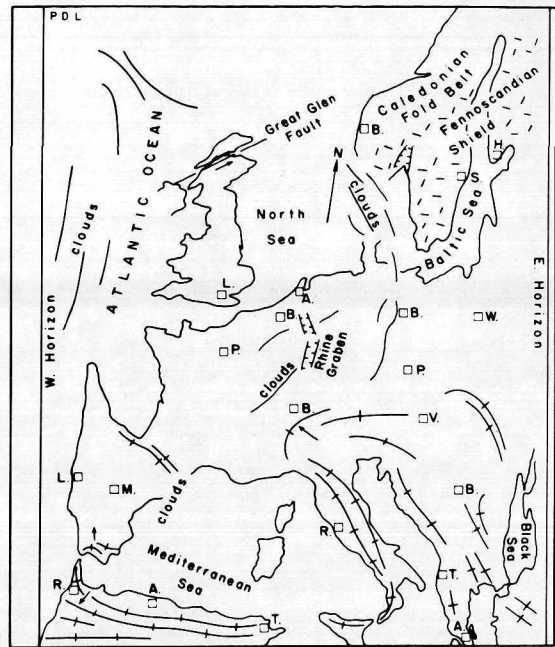


Geologic index map based on a Nimbus 4 IDCS image taken on orbit 68, 13 April 1969.

Figure 2-17 Analyses of Nimbus images showing mesoscale geologic features. (Lowman, 1971)



Nimbus 3 daytime HRIR taken on orbit 1530, 6 August 1969



Tectonic index map of western Europe based on Nimbus 3 daytime HRIR taken on orbit 1530, 6 August 1969.

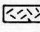


-  Precambrian Shield
-  Rift Valley
-  Cenozoic Fold trend

Figure 2-17 Cont'd

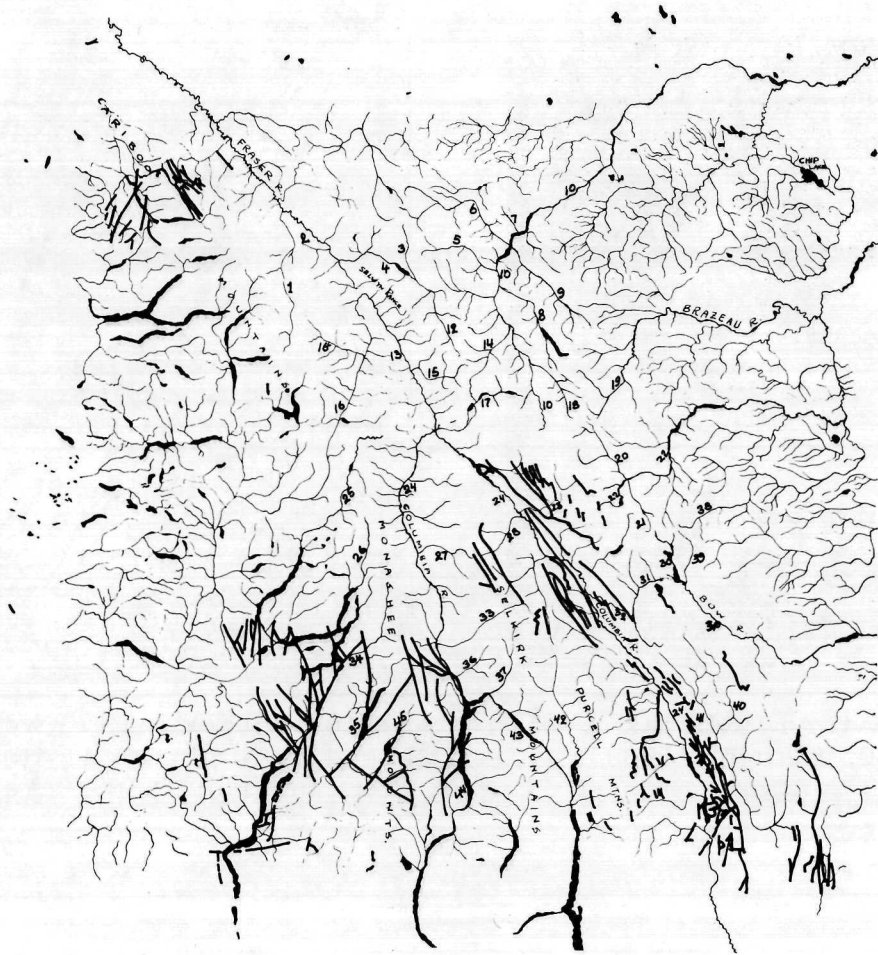
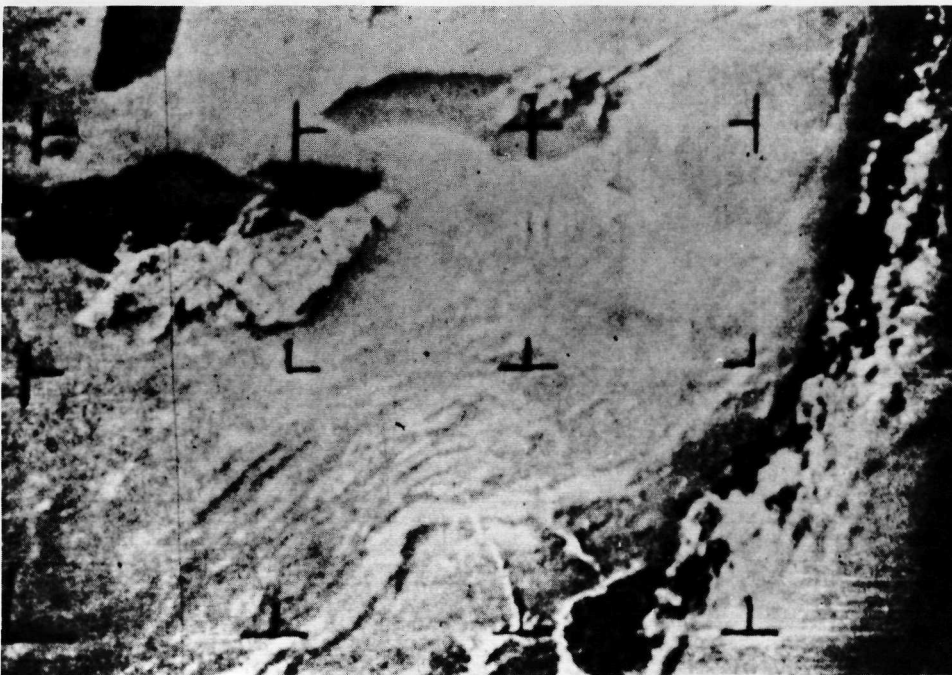
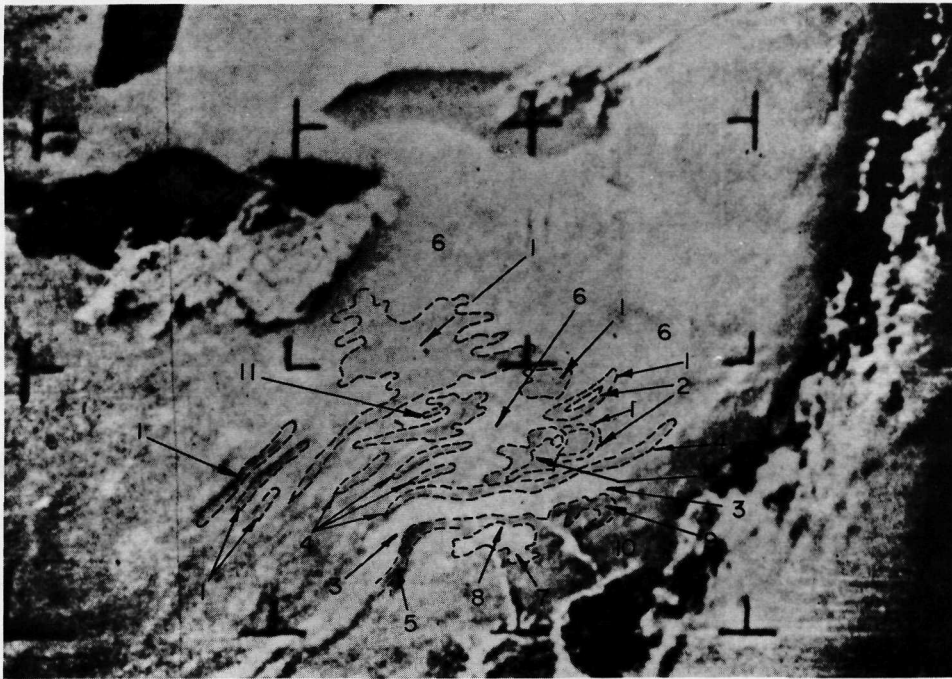
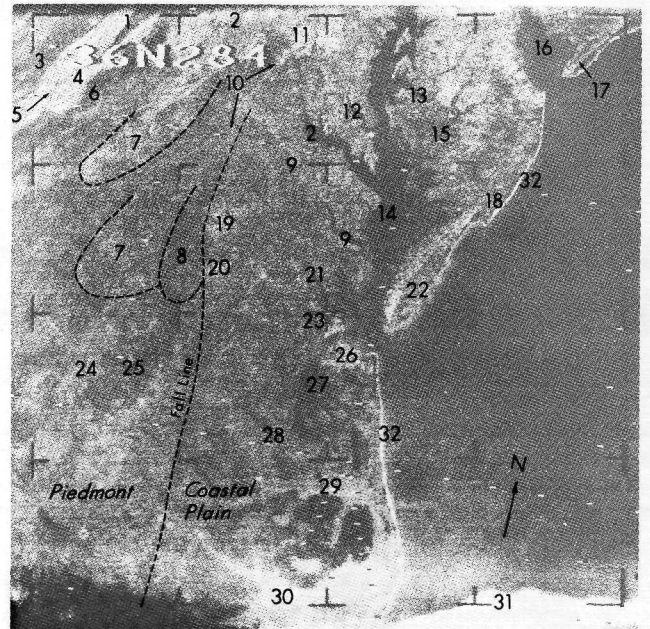
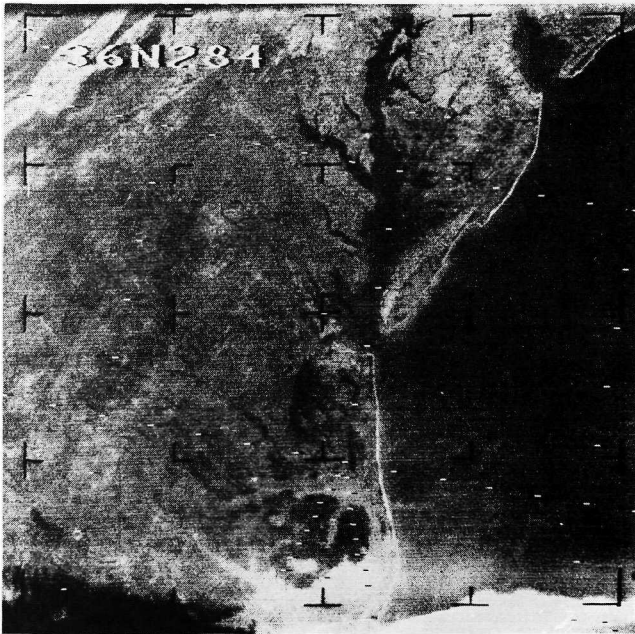


Figure 2-18 Map of major drainage and fault lines in the Canadian Rockies. (Numbers on map correspond to geographic features identified on the photograph shown in Figure 2-4.)



Dark-toned features due mainly to denser vegetation: (1) Mississippian-Pocono Group. (4) Silurian-Shawangunk and Tuscarora Formations. (5) Ordovician-Beekmantown Group. (9) Pre-Cambrian-Granite gneiss. (10) Triassic-Brunswick, Locketong and Stockton. (12) Ordovician-Juniata, Bald Eagle Formations. Light-toned features: (2) Pennsylvanian-Post-Pottsville Group. (3) Ordovician-Martinsburg Formation. (6) Devonian-Susquehanna Group. (7) Ordovician-Conestoga Formation. (8) Ordovician-Cocalico Formation. (11) Pennsylvanian-Conemaugh Formation.

Figure 2-19 Nimbus 1 APT view of the complexly folded Appalachian Mountains in the Pennsylvania region taken on orbit 254, 14 September 1964. (Taggart, 1965)



- | | | | |
|-----|----------------------------|-----|---------------------------|
| 1. | Massanutten Mountains | 17. | Garden State Parkway |
| 2. | Potomac River | 18. | Chincoteague Bay |
| 3. | Shenandoah Mountains | 19. | Richmond |
| 4. | Great Valley | 20. | Petersburg |
| 5. | Noise in recording | 21. | York River |
| 6. | Blue Ridge Mountains | 22. | Hog Island and South Bays |
| 7. | Triassic sedimentary rocks | 23. | James River |
| 8. | Paleozoic granite rocks | 24. | Roanoke River |
| 9. | Rappahannock River | 25. | Meherrin River |
| 10. | Interstate Route 95 | 26. | Norfolk and Portsmouth |
| 11. | Washington D. C. | 27. | Dismal Swamp |
| 12. | Patuxent River | 28. | Chowan River |
| 13. | Choptank River | 29. | Albemarle Sound |
| 14. | Chesapeake Bay | 30. | Pamlico Sound |
| 15. | Nanticoke River | 31. | Clouds |
| 16. | Delaware Bay | 32. | Beach |

Figure 2-20 Nimbus 1 AVCS photograph of the Chesapeake Bay region and vicinity taken on orbit 137, 6 September 1964.

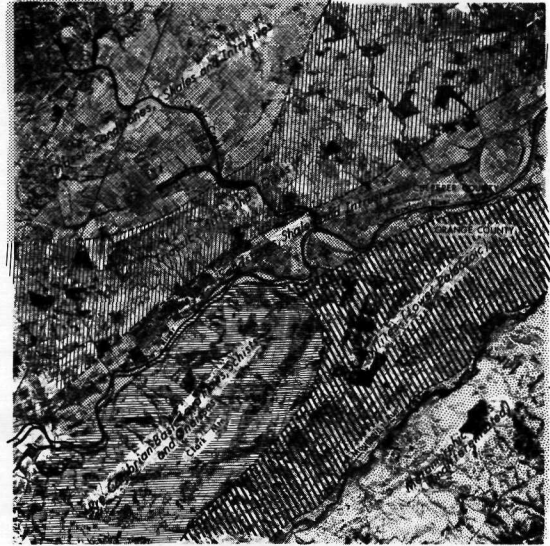
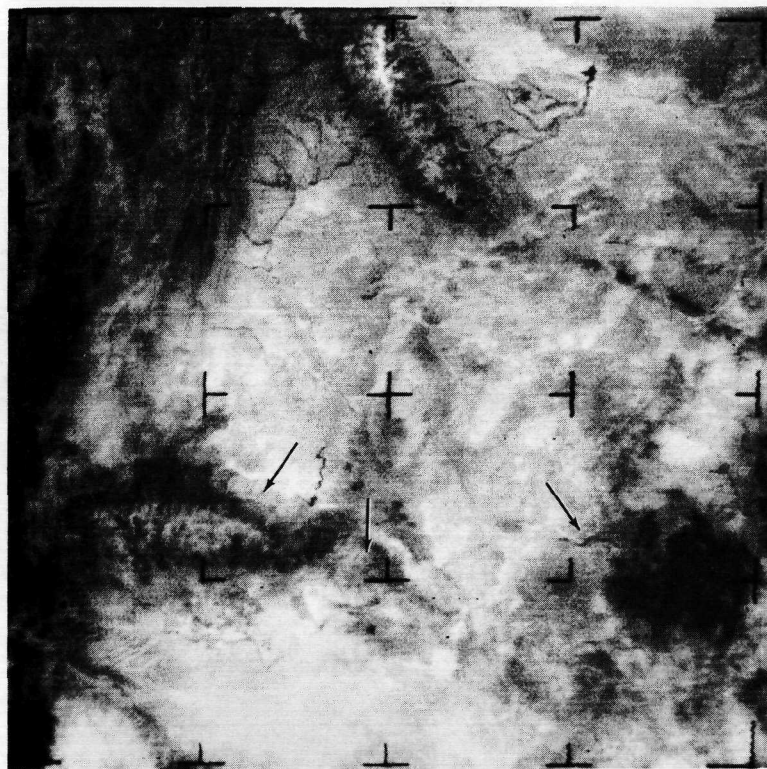


Figure 2-21 USGS aerial photograph of a portion of the Piedmont approximately 30 miles west of Fredericksburg, Virginia taken on 20 February 1960 from 30,000 ft.



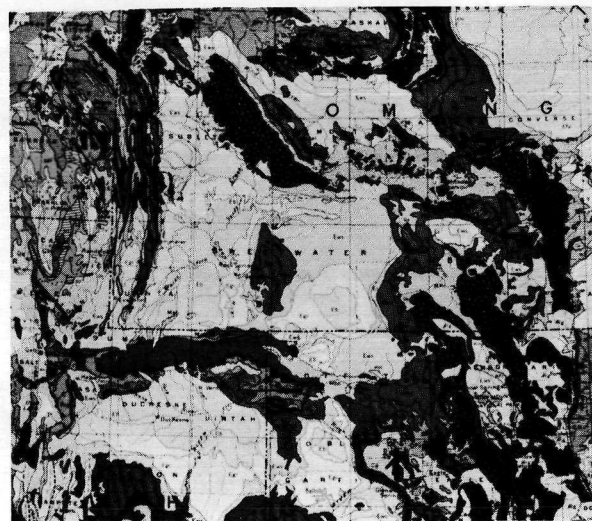
Figure 2-22 Panoramic view of the Shenandoah Mountains, Pendleton County, West Virginia. (Note the sharp contrast in vegetation and elevation between the Moorefield River Valley (foreground) and the ridges of the Appalachian Ridge and Valley Province.)



Nimbus 1 AVCS photograph



Topographic map



Geologic map

Figure 2-23 Nimbus 1 AVCS photograph of southwestern Wyoming northwestern Colorado, and northeast Utah taken on orbit 109, 4 September 1964 as compared to topographic and geologic maps of the region. (Short, 1971)

and foster growth of grass, sage, and small cedars in denser clusters. It is this effect that allows the Rock Springs uplift to be seen. Short (1971) compared gray patterns with a soil map for the Green River basin and found crude matches between soil types and tonal patterns in several places, but little correlation of soils and tonal patterns in others. He concluded that in a semi-arid region, high topographic relief shows good co-association with exposed geology and with vegetation (and, to a lesser degree, with soil types). This results in strong correlations between photographic tonal patterns and ground truth. In the lower, flatter basins, most tonal patterns are related to the subtle variations in soil color and to the amount of vegetation.

Outcrop patterns, like drainage systems, are enhanced by either snow-fall or vegetation. Figure 2-5 of the Paris Basin illustrated the application of Nimbus photographs for the delineation of geomorphic provinces. The same frame also shows distinct outcrop patterns which correlate with the general bedrock geology of the Paris Basin (Figure 2-24), the vegetation playing an important role in the delineation of the various formations. The light Cretaceous chalk formations, for example, do not support a dense vegetal growth and stand out as light tones on the photograph. On the other hand, the Quaternary alluvium and soil developed on highlands underlain by Jurassic strata, have a dark tone due to heavy vegetation and dark soil. Vinogradov (1969), using published maps of geology and vegetation, was able to delineate lithological boundaries on this photograph (Figure 2-33), as will be described in Section 2.3.3.

2.3.2 Tectonic and Structural Features

The detection of tectonic or structural features is another area where Nimbus imagery has been of use. Although the satellite cannot locate sills and dikes, or volcanic necks, it has at times shown joints, folds, faults, and large lava flows. Under special circumstances, it has even detected volcanic activity; this last subject will be discussed in Section 2.4.

One of the first Nimbus 1 AVCS photographs to be interpreted for its structural geology content is presented in Figure 2-25. According to Woloshin (1965), the lineaments traced on this photograph match reasonably well with the published geological maps. All the major mapped faults are clearly discernible on the photograph as the lithologic and/or vegetative differences in the landscape cause marked tonal contrasts. Another geologically interesting Nimbus 1 AVCS photograph of the same area is shown in Figure 2-26. The effect of the strike-slip displacement of the San Bernardino and San Gabriel Mountains along the San Andreas Fault is clearly visible. Two faults, one along the Santa Ynez Mountains and the other along a line connecting the Santa Rosa and Santa Cruz Islands and Santa Monica Mountains,

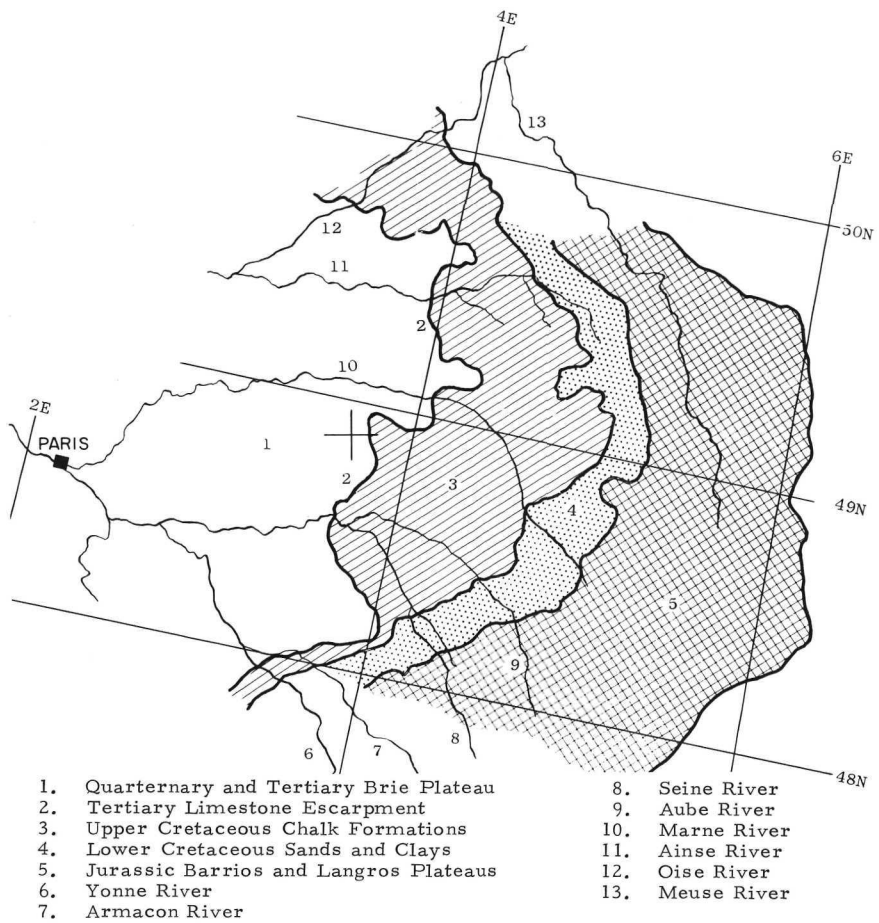
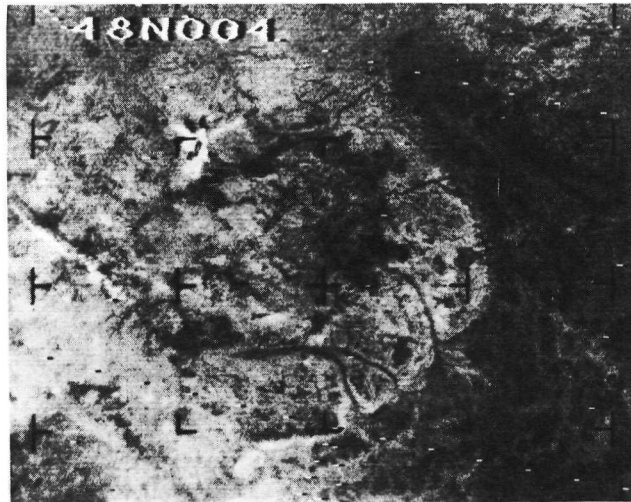


Figure 2-24 General geologic map of central France and corresponding Nimbus 1 AVCS photograph taken on orbit 236, 13 September 1964. (See also Figures 2-5 and 2-6.)



Overlay is slightly offset so that geologic features may be seen.

Figure 2-25 Geologic interpretation of Nimbus 1 AVCS photograph of southern California taken on orbit 285, 16 September 1964. (Woloshin, 1965)

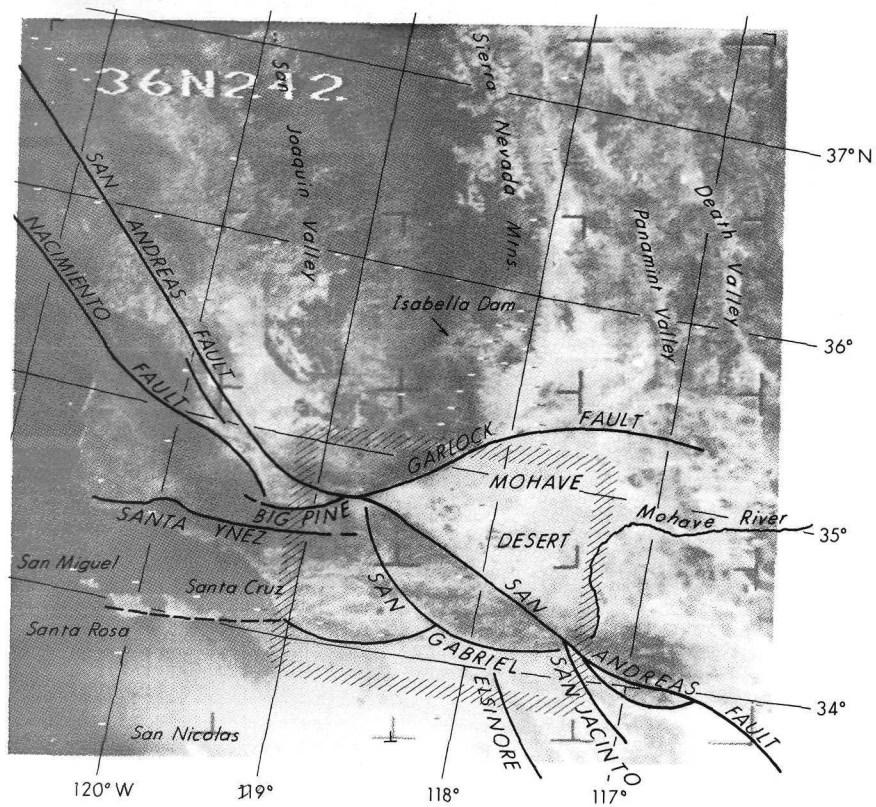
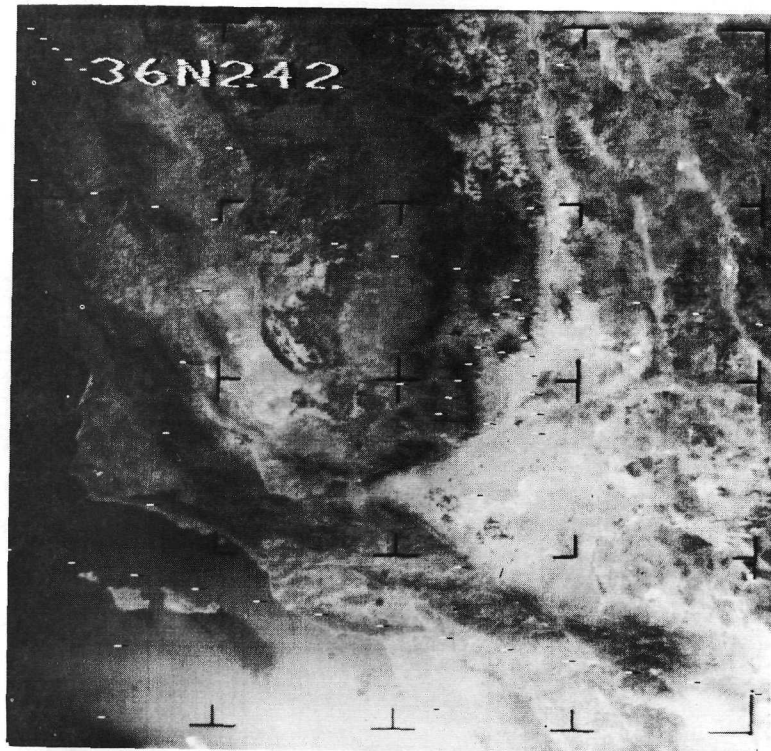
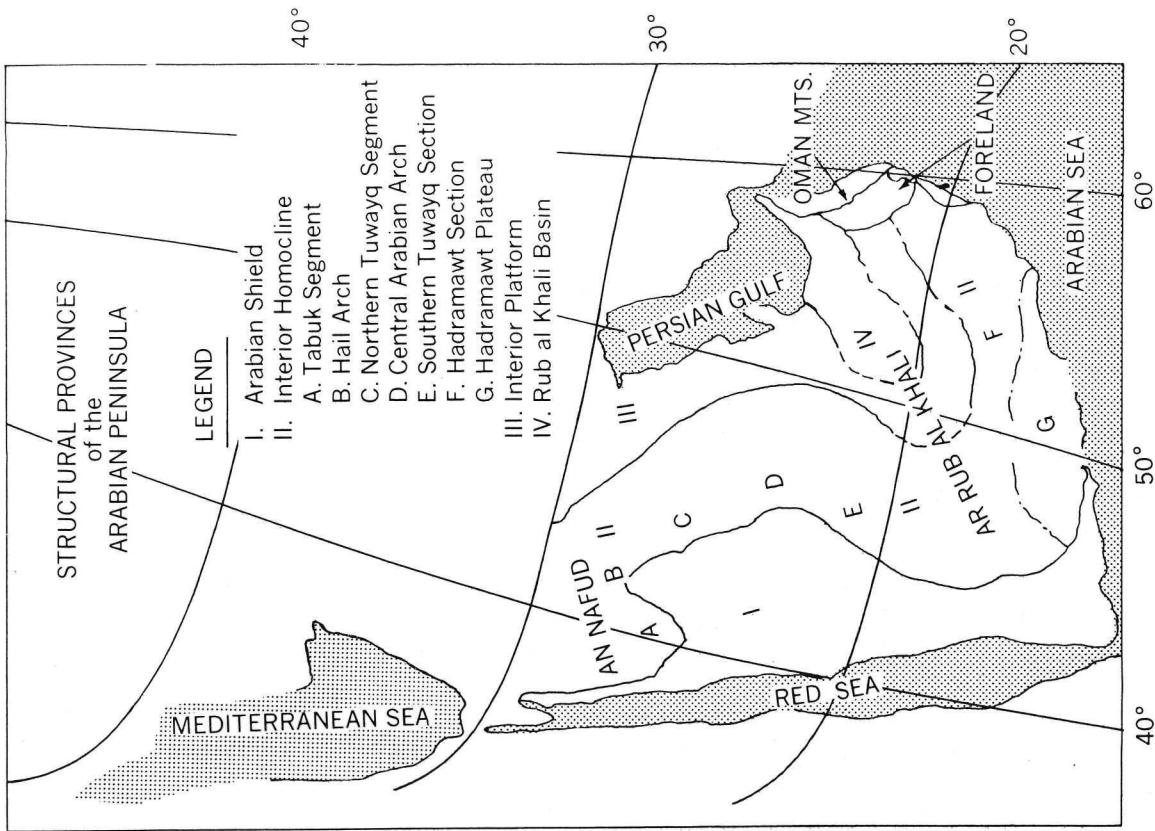
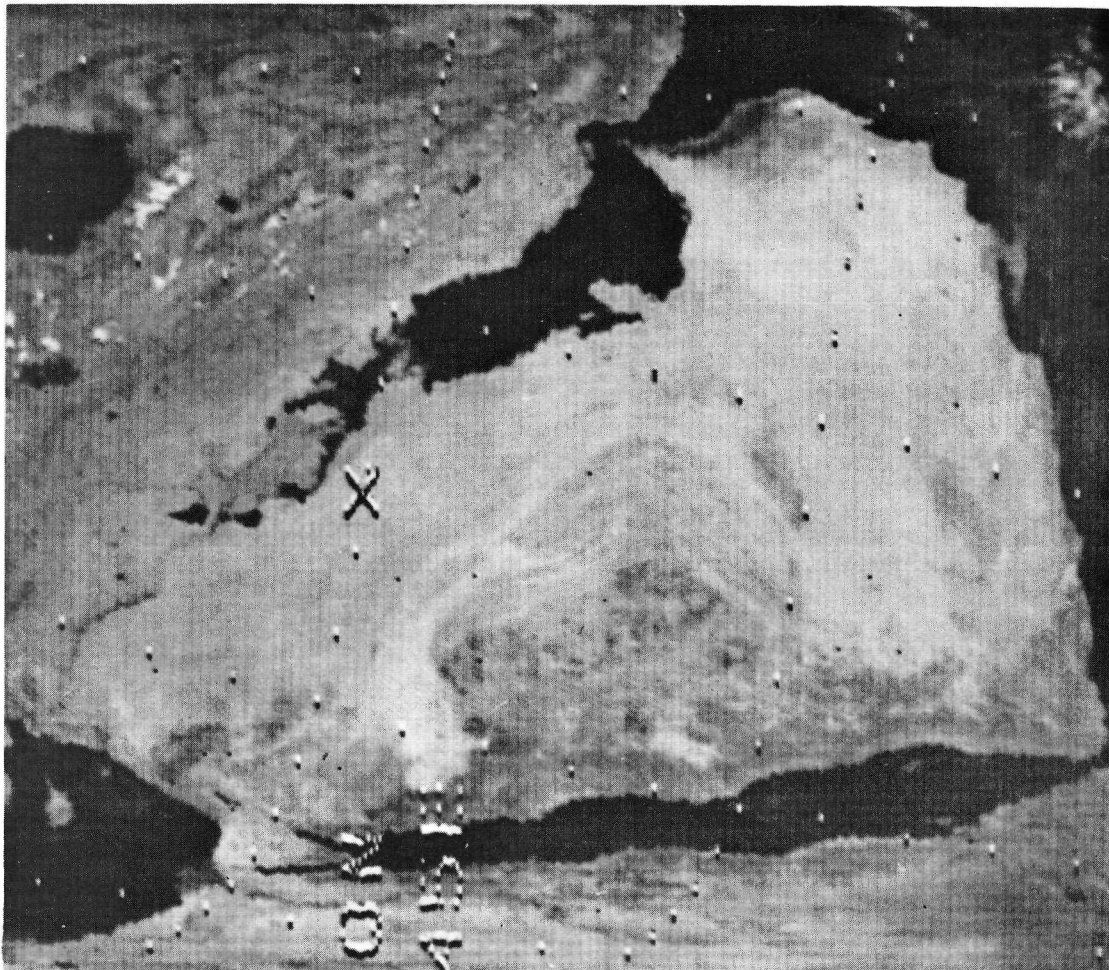


Figure 2-26 Nimbus 1 AVCS photograph of southern California taken on orbit 168, 8 September 1964 showing the distribution of major fault lines. The outlined area is enlarged in Figure 1-4.

also become more readily apparent as possible extensions of the oceanic Murray Fracture Zones as hypothesized by Reed and Hollister (1968).

Blodget (1971) used Nimbus 3 HRIR daytime imagery (Figure 2-27) to illustrate the major geologic structural provinces of the Arabian peninsula and the following description of the provinces is abridged from that report. On Figure 2-27 the Arabian shield forms the dark mottled tones of the western third of the peninsula. This extensive area consists mainly of igneous and metamorphic rocks which are locally overlain by Cenozoic volcanics and Quaternary alluvial and eolian sediments (Anon, 1963). Some of the larger volcanic and sedimentary surfaces can be distinguished on the basis of their respective dark and light tones. The shield area is bordered by the interior homocline, a wide belt of sedimentary strata consisting variously of limestone, shale, and sandstone beds (Powers et al, 1966, pp. 20-91). Differential erosion and subsequent deposition of alluvial and eolian sediments in the topographically lower areas has produced the stripe-like pattern which can best be recognized in the area of the central Arabian arch. In the north and south, the homocline is partially covered by the extensive windblown sands of the An Nafud and Ar Rub al Khali, respectively. The southern-most unit of the homocline, the Hadramawt plateau, consists of limestone, shale and marl strata (Greenwood and Bleackley, 1963, pp. 50-53), and is characterized by medium gray hues on the imagery. The interior homocline is bordered by the interior platform. The division between these two structural units is marked by the hinge line created by a break in slope between the slightly dipping strata of the homocline and the nearly flat-lying beds of the platform. The Ar Rub al Khali basin is characterized by the light-toned areas of eolian and alluvial materials deposited on the topographically low, flat surfaces. Neither the structure of this basin, nor its precise boundaries, can be determined by Nimbus. Blodget concludes that "... major structural provinces can be recognized at the small scale of the Nimbus 3 imagery. ... The scale and resolution of the HRIR imagery is, however, much too small to be used in general mapping, but does provide a valuable supplement to standard geologic mapping techniques, for it shows how the structure mapped at larger scales fits into the regional tectonic system. "

The effect of seasonal snow cover in geologic interpretation was used by Woloshin (1965) and Lowman (1967) to detect the extension of a fault (Figure 2-28) in the East Sayan Mountains of the USSR. The difference in the elevation on the two sides of the fault with a corresponding difference in snow accumulation and reflectivity along the fault made it possible to locate this fault zone. As stated by Sabatini and Sissala (1968), the fact that a few weeks earlier or later this pattern may have been obscured by lack of snow or too much of it reveals how unusual and unexpected may be the benefits from analysis of these satellite photographs.



Nimbus 3 daytime HRIR image

Figure 2-27 Comparison between Nimbus 3 daytime HRIR image, orbit 711, 6 June 1969 and structural provinces map of Saudi Arabia. (Blodget, 1971)

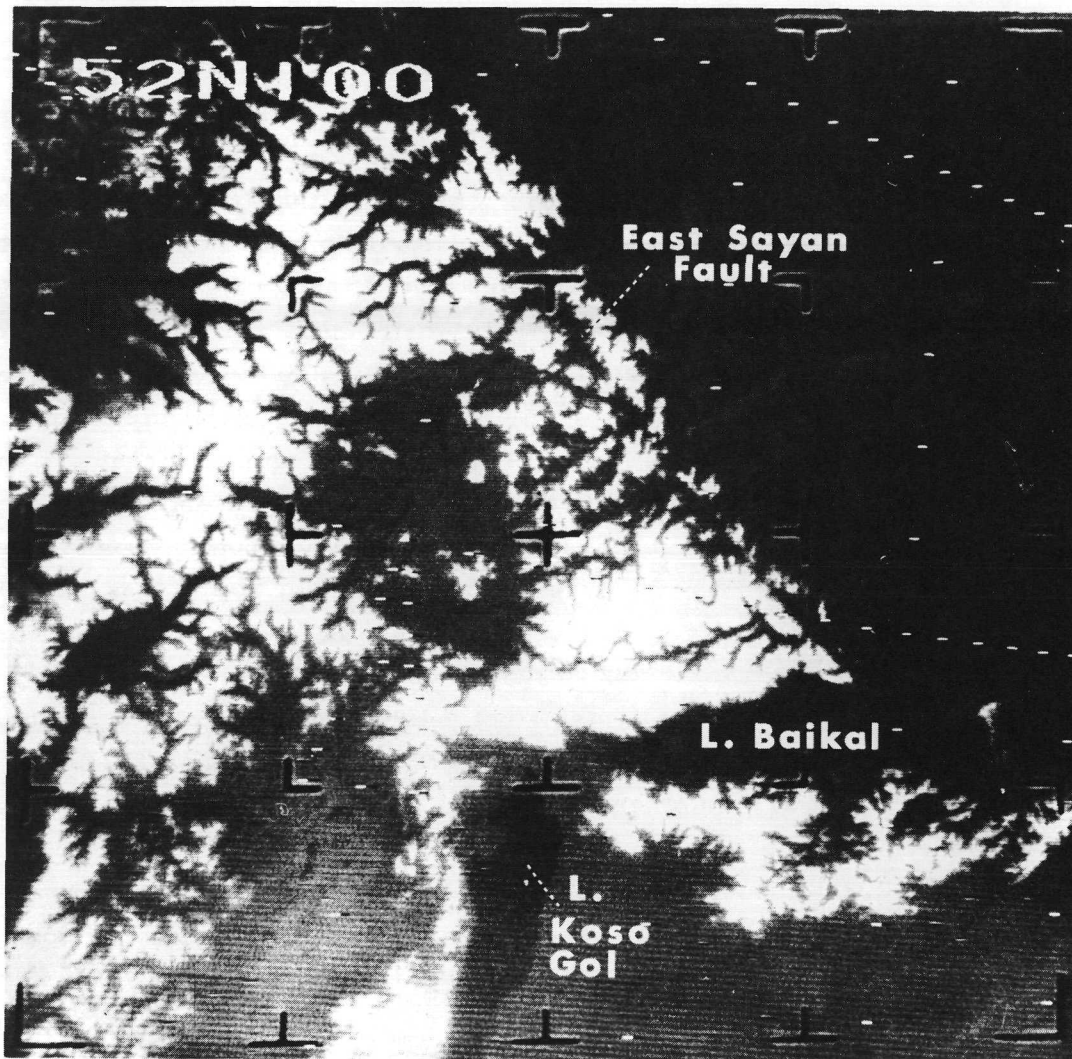


Figure 2-28 Nimbus 1 AVCS photograph of the Sayan Mountains and vicinity, USSR taken on orbit 320, 19 September 1964. (The east Sayan Fault is revealed by a new snowfall pattern.)

Figure 2-1, described in Section 2.2.1 of Regional Geomorphology, was also used for structural analysis of the Columbia River Basin. Griggs (1967) adds that the west-northwest lineaments reflect anticlinal arching of the basalt plateau and may also reflect displacements in the basement rocks.

The HRIR and THIR data can be formatted into digitized grid-print maps which show quantitative values of temperatures or reflectances. This presentation is especially useful for research, although not as easy to interpret as the AVCS or IDCS photography. Pouquet (1968a, 1968b) was among the first to apply digitized Nimbus HRIR maps to geological studies. In his works he presents examples of HRIR digital maps of the southwestern United States and northeast Africa in which known positions of many faults correlate with warm areas and with steep gradients of temperature. The ability of the fault areas to store moisture, which raises the heat capacity of the ground, is responsible for the warmer nighttime temperatures.

Additional Nimbus AVCS, IDCS, HRIR and THIR data exist that are appropriate to structural geologic background studies. Below are presented brief comments on several Nimbus AVCS photographs of regions which are not only geologically complex but also poorly known. Figure 2-4, for example, was discussed in Section 2.3.1. A more in-depth analysis of the regional drainage pattern on this Nimbus 1 AVCS photograph (Figures 2-4 and 2-18) could uncover additional lineations that may correlate with fault or joint systems not yet recorded on existing geologic maps. It is interesting to note that some of the snow bands in the northeast corner of the photograph are wider (a) than others (b). The wider snow bands at (a) correspond to the higher elevations of the Big Horn and Brazeau Ranges. A ground photograph of the Canadian Rockies published in the July-August 1967 issue of Geotimes shows the city of Calgary with the Front Ranges in the background. A light veneer of snow blankets the hilltops (upthrust blocks) along the eastern slope of the Ranges and brings out the locations of the fault scarps (McConnell thrust) facing Calgary.

Another example of the utility of Nimbus photographs in structural geology appears in Figure 2-29. The geology of Ellesmere Island has been discussed in various reports; detailed geographical, geological and structural maps, however, are incomplete. Figure 2-29 shows the geology of the Island as it appears on the most recent (1969) U. S. Geological Survey Tectonic Map of North America (King, 1969). Interpretation of the Nimbus 1 AVCS photographs provides a new look at the complex hydrological and geological setting of this area (Figure 2-29). The regional NE-SW strike of the sedimentary formations stands out clearly, and the complex fault and drainage patterns provide indirect information on the distribution of the lithological types. It is possible to trace out on this photograph the general distribution of lineations, although precise distinction between the strike of beds, faults, joints, and even valleys, is not always feasible.

2.3.3 Discrimination of Lithologies

Discrimination between different lithologies or surface compositions using remote sensor data is, at best, very difficult. Although many promising laboratory and field experiments have been conducted on the identification of various surficial covers, rocks, and minerals, from their spectral characteristics, an operational system does not yet exist that can remotely identify rock types. At times, it is possible on Nimbus imagery to infer rock types from indirect indicators. For example, as discussed previously, the geomorphology, the structural geology, the hydrology and the vegetation cover all provide clues to the recognition of the underlying lithologies. This section shall examine the possibility of lithologic discrimination from HRIR and THIR surface temperatures, and shall review a few lithological interpretations from Nimbus data.

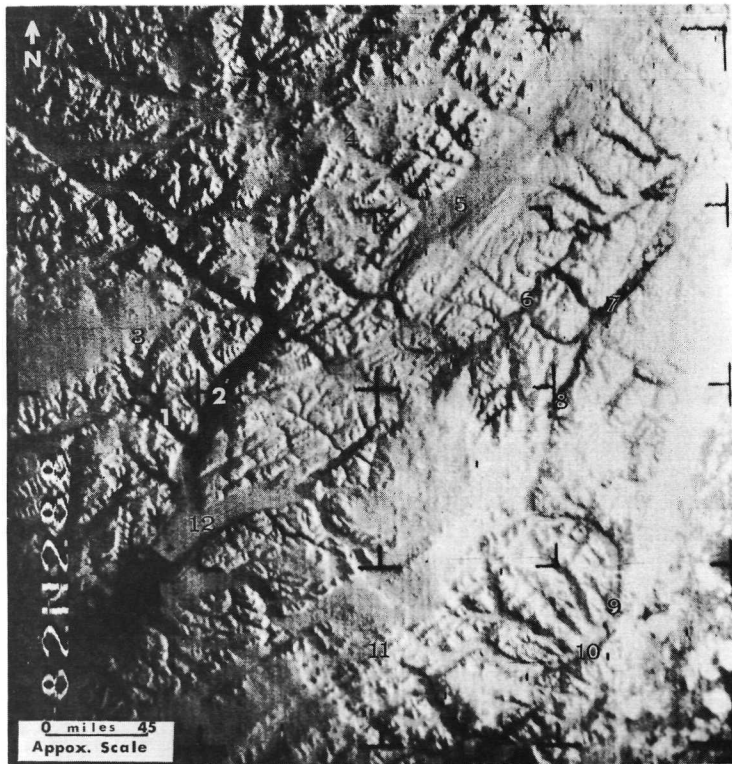
2.3.3.1 Surface Discrimination Consideration from Nimbus HRIR and THIR Data

An understanding of the factors influencing surface temperatures and their variations is necessary to relate spatial and temporal temperature differences to surface and subsurface properties. For example, in an arid region of low relief with a cloudless uniform atmosphere, surface temperature variations are due to the differences in the response of the surface to heating and/or cooling by:

- 1) Solar radiation
- 2) Infrared radiation
- 3) Conduction (the flux of sensible heat within the soil)
- 4) Convection (the flux of sensible heat to and from the atmosphere)
- 5) Latent heat of phase transformation of water

A quantitative evaluation of all of the above factors to determine the surface temperature distribution is extremely complex and only possible under ideal and simplified conditions. If we make the assumptions that the surface is completely dry (so that there is no phase transformation of water), and that there is no wind (and therefore no gains or losses by convection), then spatial differences of surface temperatures may be attributed to differences in surface properties influencing the gains or losses of energy by solar and infrared radiation and by conduction. Briefly, these properties are:

- 1) Surface albedo which controls the solar radiation absorbed by the surface. Dark areas (low albedo) absorb more solar radiation than light areas (high albedo) and, therefore, generally show higher daytime temperatures. Diurnal temperature variations are also greater for dark areas.



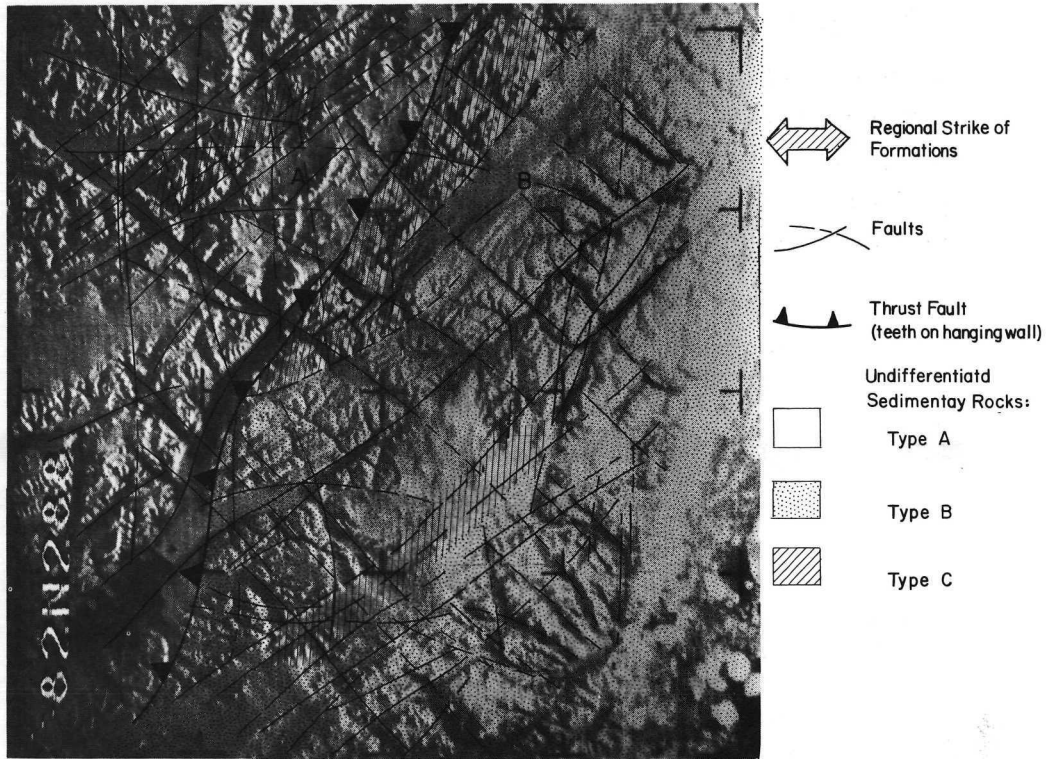
- 1 Borup Fjord
- 2 Tanquary Fjord
- 3 Conger Range
- 4 U. S. Range
- 5 Lake Hazen
- 6 Musk-ox Valley
- 7 Archer Fjord
- 8 Ella Bay
- 9 Rawlings Bay
- 10 John Richardson Bay
- 11 Albert and Victoria Mountains
- 12 Greely Fjord

Nimbus 1 AVCS photograph

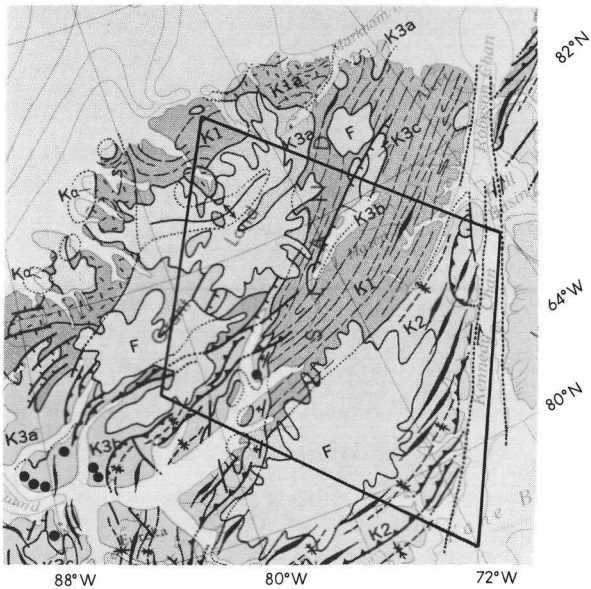


Hydrologic interpretation

Figure 2-29 Hydrologic and geologic interpretations of Nimbus 1 AVCS photograph of a portion of Ellesmere Island taken on orbit 207, 11 September 1964.



Geologic interpretation



Tectonic map (USGS, 1967)

- F = Ice Caps of Quaternary Age on Pre-Cambrian to Cenozoic Basement
- K1, K1a = Eugeosynclinal Deposits
- K2, K2a = Miogeosynclinal Deposits
- K3a, K3b, K3c = Deposits of Successor Basins
- K3a = Pennsylvanian and Permian
- K3b = Mesozoic
- K3c = Early Tertiary

- Anticlines
- Synclinal Axis
- Thrust Fault
- Sub-Sea Area
- Normal Fault
- Anticlinal Axis
- Dip of Beds
- Buried Fault

Figure 2-29 Cont'd

2) Surface emissivity which controls infrared radiation lost by the surface to the atmosphere. Surfaces with low emissivity lose heat by radiation more slowly than a surface with high emissivity at the same temperature. Surfaces of low emissivity in the HRIR and THIR spectral bands show lower temperatures than the actual surface temperature because of the blackbody assumption (emissivity = 1) in the derivation of HRIR and THIR temperatures (see Appendix B).

3) Surface thermal properties, such as specific heat, which control the conduction losses or gains.

This section deals mainly with the effects of the surface thermal properties, since these have the greatest influence on temperature variations of bare desert level surfaces.

Conduction, or the flux of sensible heat near the surface, is controlled by the thermal properties of the surface and subsurface. A natural parameter which expresses the thermal properties of substances composing the earth's surface is $(\rho c \lambda)^{1/2}$, the thermal inertia, with ρ , c , λ , being the density, specific heat, and thermal conductivity of the substance. This thermal property depends on the condition and composition of the soil, on its structure and, most important, on its moisture content. Table 2-2 (from Lettau, 1951) lists the thermal inertia for some typical surface covers and lithologies. Note the dramatic increase of the thermal inertia of sand with increased moisture. The thermal inertia of the surface has a substantial control on the fluxes of heat between the ground and the air. If the thermal inertia is large, the subsurface absorbs a great amount of heat during the day and then conducts a great amount of heat to the radiating ground surface during the night. Temperature variations of the surface and the air layer near the surface are consequently moderate. Soils of poor thermal inertia conduct little heat to the subsurface, and accordingly, the surface transmits much heat to the air during the day and receives little heat from the subsurface at night. Thus, the surface attains high temperatures in the daytime and low temperatures at night.

At night over calm desert areas the only effects on the temperatures are conduction and longwave radiation. Brunt (1932) has analyzed this simplified situation and derived the following equation for surface temperature $T_o(t)$ at time t after sunset:

$$T_o(t) - T_{oo} = \frac{-2 R_{oo}}{(\rho c \lambda)^{1/2}} \left(\frac{t}{\pi}\right)^{1/2} \quad (2-1)$$

where

t = time after sunset

T_{oo} is the surface temperature at time $t = 0$ (at sunset)

R_{oo} is the infrared radiation lost by the surface at sunset

TABLE 2-2
THERMAL INERTIA $(\rho c \lambda)^{1/2}$ FOR VARIOUS SURFACES

Surface	$(\rho c \lambda)^{1/2}$
Quartz Sand (Medium Fine) Dry	.014
8% Moisture	.030
10% Moisture	.034
22% Moisture	.047
Sandy Clay 15% Moisture	.036
Basalt	.046
Sandstone	.050
Granite	.057
Concrete	.056

Furthermore, Brunt shows that R_{oo} can be derived from T_{oo} and the surface vapor pressure. The variability of the surface vapor pressure over deserts is small and may be adequately established from climatological data. Eq. (2-1) shows that the nocturnal drop in surface temperatures can be used to evaluate $(\rho c \lambda)^{1/2}$, a parameter characteristic of the surface. For given initial conditions, the greater the drop in temperature with time, the smaller the value of $(\rho c \lambda)^{1/2}$. Thus, sand cools rapidly after sunset and becomes colder than the hard rock formations which are able to retain the heat of the day for a much longer time. Nimbus HRIR or THIR, unfortunately, do not provide continuous temperature records of any area for direct application of Eq. (2-1). However, Brunt's analysis, when modified, is applicable to the derivation of thermal inertia from spatial measurements of surface temperature.

At a particular time of night, under similar atmospheric conditions, the temperature would be lower over surfaces with low values of the thermal inertia than over surfaces with high values of the thermal inertia. If it can be assumed that the temperatures at sunset are the same for all points in the area under study (and, therefore, R_{oo} is also the same if differences in surface emissivity are small), then at time t after sunset the difference in temperature $\Delta T_{1,2}$ between any two points is, from Eq. (2-1),

$$\Delta T_{1,2} = T_o(t)_1 - T_o(t)_2 = K \left[\frac{1}{(\rho c \lambda)_1^{1/2}} - \frac{1}{(\rho c \lambda)_2^{1/2}} \right] \quad (2-2)$$

where

$$K = -2R_{oo} \left(\frac{t}{\pi} \right)^{1/2}.$$

The adjective "equivalent" has been chosen to modify this remotely obtained thermal inertia since the assumptions made in the derivation of Eq. (2-2) (no convection losses, no latent heat of phase transformation, no differences in sunset surface temperatures) preclude the determination of the real thermal inertia. If the area under study contains two surfaces of known thermal inertia, then Eq. (2-2) will yield a value of K for the area, which can be used to calculate absolute values of an "equivalent thermal inertia" for unknown surfaces.

In applying Eq. (2-2) to actual data, it should be noted that variations in surface emissivities may cause HRIR and THIR temperature variations as large as a few degrees (see Appendix B). These emissivity effects cannot be differentiated from the thermal inertia effects unless the surface emissivity is known and, therefore, may have to be incorporated in the calculations of the "equivalent thermal inertia." Also, in applying THIR or HRIR grid-print map data to studies of surface lithology, it is best to work with filtered data and consider average temperatures for fairly large areas (of the order of hundreds of square miles) so that uncertainties in the data are smoothed out (see Appendix C for a discussion of the noise problem).

Up to this point we have only considered the application of nocturnal synoptic temperature variations over a desert surface. Nimbus 4 THIR 11.5 μm channel is unaffected by solar radiation and provides additional daytime measurements of surface temperature which, in conjunction with nighttime measurements, may yield more information about the surface. Brunt (1932) showed that the diurnal temperature change of a bare surface, assuming no convection or phase change, varies approximately sinusoidally, the amplitude being a function of the thermal inertia $(\rho c \lambda)^{1/2}$. A sandy surface of low thermal inertia would show a larger difference between peak daytime and nighttime temperature than would a rock surface of higher thermal inertia. Of course, moisture which raises the thermal inertia of a surface would decrease the amplitude of the diurnal temperature curve. Jaeger and Johnson (1953) generalized Brunt's equation for the diurnal temperature curve of such a surface at the equinox to any latitude and season, and expressed the surface temperature variation, v_s , from the mean by

$$v_s = \frac{F_o}{(\rho c \lambda)^{1/2} \omega^{1/2}} \cos \lambda \cos \delta \phi(t) \quad (2-3)$$

where

$$\phi(t) = \sum_{n=1}^{\infty} \frac{2 (\sin n h \cos h - n \cos n h \sin h)}{\pi n^{3/2} (n^2 - 1)} \cos (n\omega t - \frac{\pi}{4})$$

and

λ is latitude

δ (declination of earth's axis) = 23.5° at summer solstice
 = 0 at equinoxes
 = -23.5° at winter solstice

$$\cos h = -\tan \lambda \tan \delta$$

F_o is the incident solar radiation absorbed by the surface
 $\approx 0.010 \text{ cal cm}^{-2} \text{ sec}^{-1}$

ω (angular velocity of earth) = $\frac{2\pi}{p}$ ($p = 24 \text{ hours} = 86,400 \text{ seconds}$)

t is time after local noon

$n > 1$

Figure 2-30 is a plot of Eq. (2-3) for the equinox at $\lambda = 30^\circ$ and for three different surfaces: quartz sand, sandstone and granite.

The above equation was applied to the analysis of HRIR surface temperature differences for selected uniform areas of sand, sandstone and granite in the Nafud desert area of Saudi Arabia (see Figure 2-31). Specifically, Eq. (2-3) was modified as follows:

$$\Delta T_{1,2} = v_{s1} - v_{s2} = K \left[\frac{1}{(\rho c \lambda)_1^{1/2}} - \frac{1}{(\rho c \lambda)_2^{1/2}} \right] \quad (2-4)$$

where

$$K = \frac{F_o \cos \lambda \cos \delta}{\omega^{1/2}} \phi(t).$$

In the HRIR grid print analysis, the sand areas of the Nafud Desert showed the lowest nighttime HRIR temperatures. The 292° isotherm delineated fairly well the extent of the sand. Other lithologies could not be delineated by any particular isotherm although average temperatures for sand, sandstone and granite showed

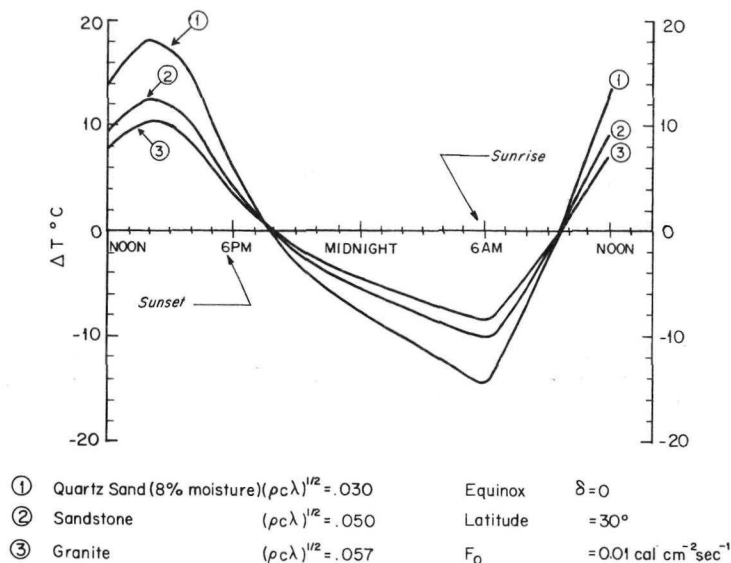


Figure 2-30 Diurnal variation in temperature at the equinox and at 30° (north or south) derived using Eq. 2-4 for surfaces of quartz sand, sandstone, and granite.

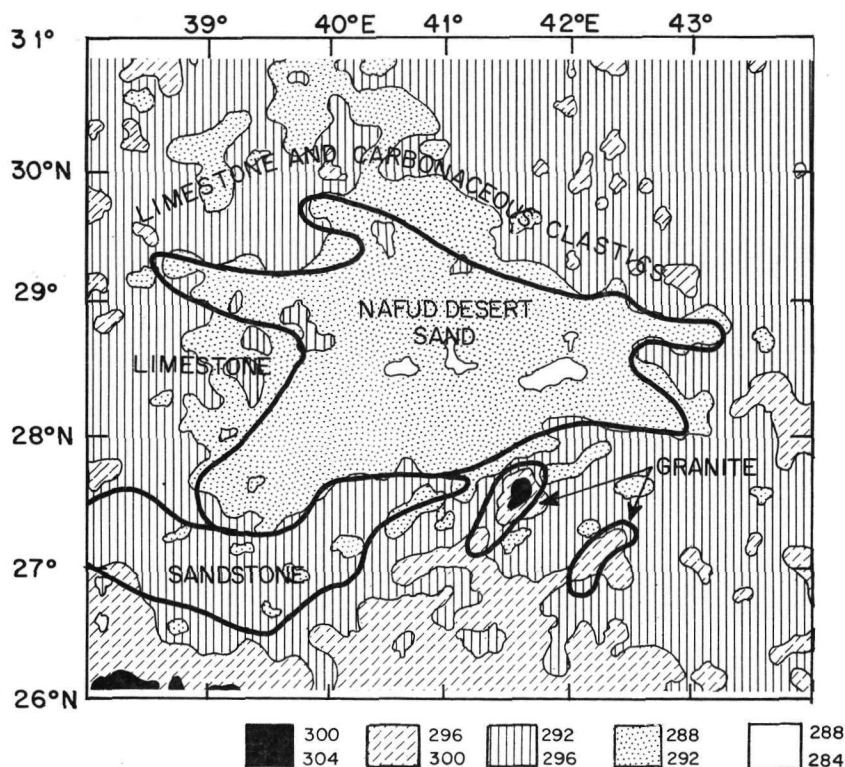


Figure 2-31 Nimbus 2 nighttime HRIR temperature map of the Nafud Desert area of Saudi Arabia taken on orbit 846, 17 July 1966. (The areas of sand, sandstone, and granite were delineated with the aid of the 1963 geologic map of Saudi Arabia (1:2,000,000) compiled by the U. S. Geological Survey and the Arabian Oil Company.)

the expected differences, with sand and granite showing the coldest and warmest averages, respectively. No marked distinction was shown by the temperature averages for the undifferentiated limestones and carbonaceous clastics north of the Nafud Desert, nor for the sandstones in the deserts south and west. The resulting averages and the theoretical surface temperature differences obtained by Eq. (2-4) for the three surfaces for the time and date of the HRIR map (11:30 PM, 24 July) are compared in Table 2-3.

TABLE 2-3
THEORETICAL AND HRIR AVERAGE SURFACE TEMPERATURE DIFFERENCES FOR THE NAFUD DESERT AREA IN SAUDI ARABIA

Type of Surface	Average HRIR Temperature (K°)	$\Delta T_{1,2}^{HRIR}$	ΔT from Equation (2-4)
Sand (8% moisture)	289.6	} 3.8	5.7
Sandstone	293.4		
Granite	296.6	} 3.2	1.2
Sand (8% moisture)	289.6		
		} 7.0	6.9

Since Eq. (2-4) is based on simplifying assumptions, it cannot be expected to provide values precisely comparable to values derived from experimental data or satellite measurements. The results are therefore encouraging, although further studies are needed to establish the usefulness of Eq. (2-4).

It may also be possible to estimate an "equivalent thermal inertia" from the HRIR and THIR temperatures with the aid of Eq. (2-3). Using Eq. (2-3) the difference in temperature between daytime and nighttime, $\Delta T_{d,n}$, is measured by

$$\Delta T_{d,n} = v_s(\text{day}) - v_s(\text{night}) = \frac{F_o \cos \lambda \cos \delta}{(\rho c \lambda)^{1/2} \omega^{1/2}} \left[\phi(t_{\text{day}}) - \phi(t_{\text{night}}) \right] \quad (2-5)$$

where the only unknown is $(\rho c \lambda)^{1/2}$, the thermal inertia. $\phi(t_{\text{day}})$ and $\phi(t_{\text{night}})$ are calculated for the time of the THIR observations (11:30 AM and 11:30 PM, respectively). The "equivalent thermal inertia" calculated by Eq. (2-5) would contain undetermined convection and latent heat of condensation effects, but would not be affected by emissivity effects since we are using temperature differences. This method of computation and the significance of the calculated "equivalent thermal inertia" are currently being investigated by ARA.

THIR temperatures can also be used to derive purely empirical relationships between diurnal temperature differences and types of surfaces. Such empirical relationships may aid in defining surfaces of unknown composition and need not necessarily be limited to unvegetated areas. For example, the THIR and HRIR data may be used to analyze the seasonal trend of temperature (time-temperature signature) for a particular area. The shape of the curve and its amplitude might be related to the type of surface and subsurface materials and the moisture content. An initial catalog of time-temperature signatures compiled for various well-known surfaces of the earth may aid in the study of poorly known regions. It is doubtful that such seasonal temperature curves will distinguish types of vegetation; nevertheless, the signature should at least be indicative of thickness of vegetation cover and should distinguish cultivated from bare land.

2.3.3.2 Existing Lithological Interpretation from Nimbus Data

Figure 2-32 is a Nimbus 1 HRIR nighttime infrared image of a portion of western South America obtained on 14 September 1964. The crescent-shaped feature near 23°S is the Salar de Atacama playa in northern Chile. The temperature of the inner region of the playa is colder (light tone $\approx 263^{\circ}\text{K}$) than the area surrounding it (dark tone $\approx 273^{\circ}\text{K}$). The entire playa covers a region of fairly uniform altitude, so that differences between the center and the rim of this salt flat are small. Based on topographic considerations and on earlier laboratory spectral measurements of minerals performed by Hovis (published in 1966), Nordberg and Samuelson (1965) attributed this 10°K difference to the spectral response of the salt. Unerring discrimination of salt flats, however, cannot be performed with Nimbus 1 radiometer data. Gawarecki et al (1965), for example, presented three possible explanations for the Atacama anomaly:

- 1) An inversion, or reversal, in the normal temperature lapse rate due to differences in relief. In this the authors differ substantially from Nordberg and Samuelson in the estimation of the significance of the altitude difference between the playa and the surrounding rim.
- 2) Relatively warm springs near the base of the mountains surrounding the Atacama playa.
- 3) Emittance and, therefore, temperature differences between the mountains and the playa fill (detritus and evaporites).

More laboratory and field checks with natural covers and materials are obviously necessary for acceptable correlation of Nimbus HRIR and THIR data to lithologies.

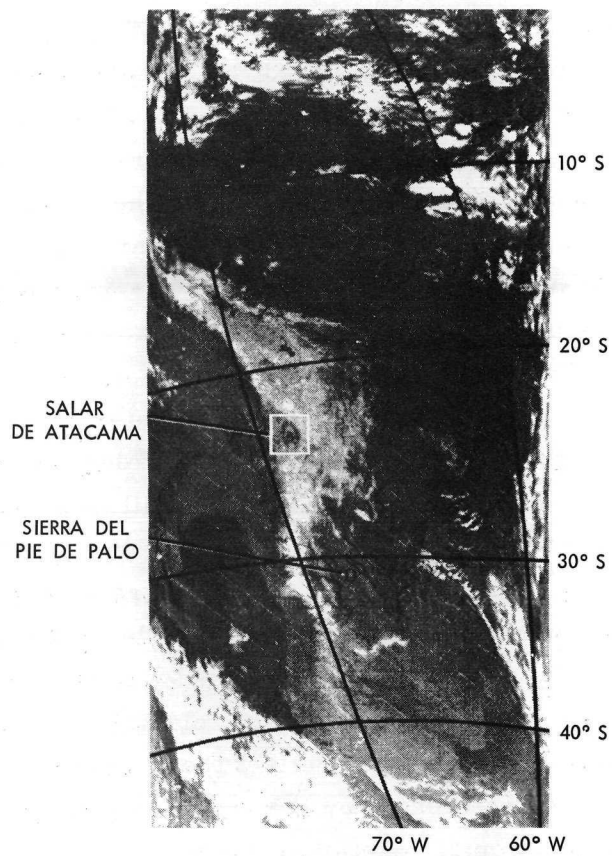


Figure 2-32 Nimbus 1 HRIR photofacsimile taken over South America near midnight on orbit 246, 14 September 1964. Dark shades represent warm surfaces, light shades represent cold surfaces. (Nordberg and Samuelson, 1965)

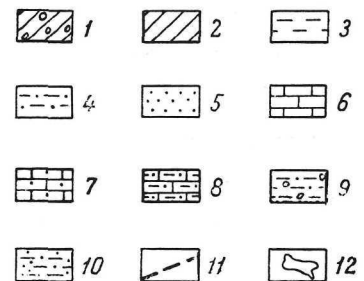
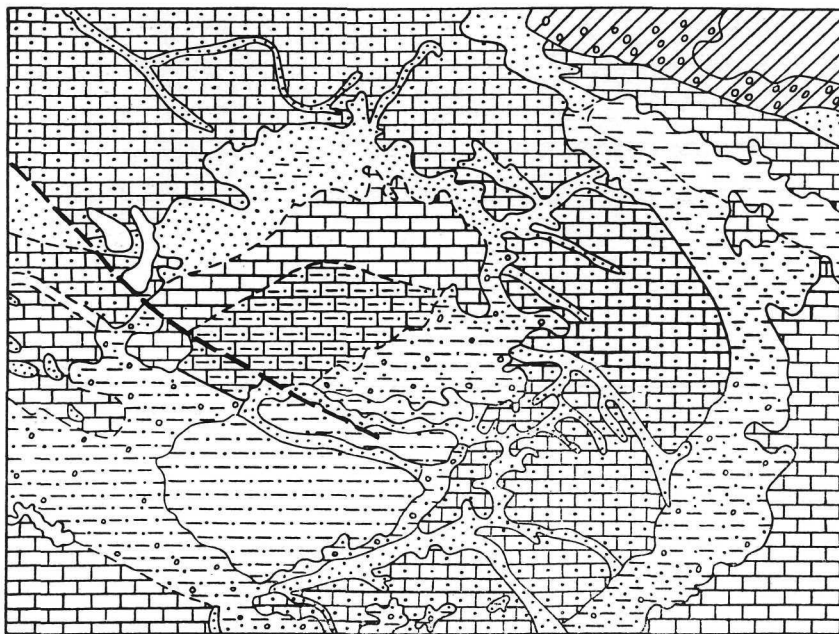
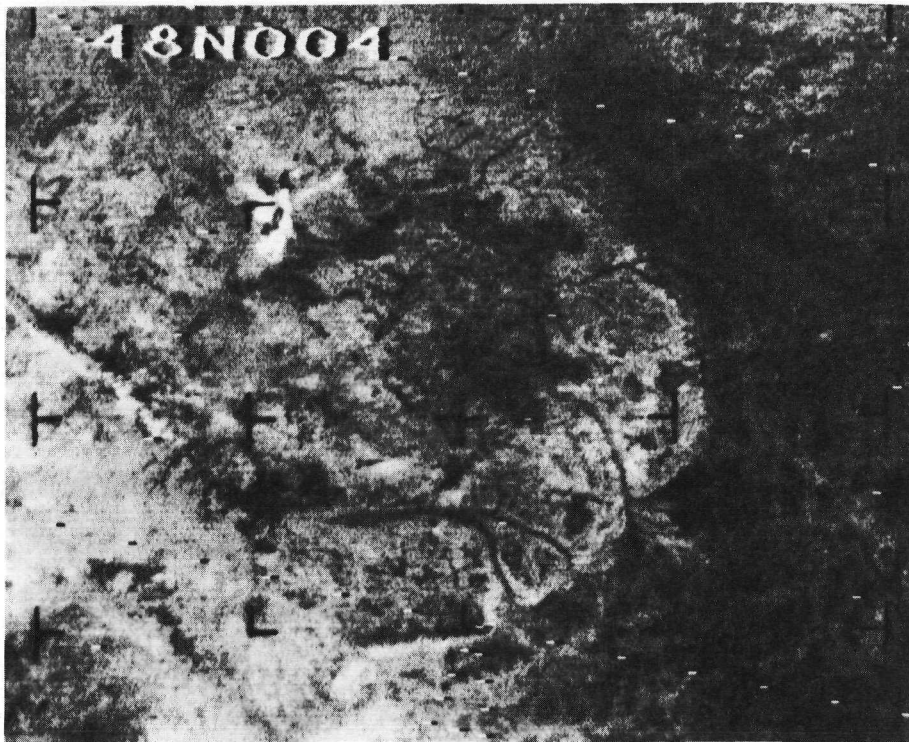
As mentioned previously, most of the so-called identifications of lithologies from remote sensing data are done by references to existing information or personal familiarity with the region. Thus the delineation of boundaries that may correlate with the various known lithologic types is possible, but the remote identification of the bedrock geology underlying the patterns is not.

Taggart (1965), for example, outlined the complex outcrop patterns of the Appalachian Mountains in the Pennsylvania region on a Nimbus 1 AVCS photograph (Figure 2-19). According to his interpretation, patterns on the photograph correlated closely with the rock-type units as depicted on the geological map of Pennsylvania. It may be more appropriate to state that the patterns coincide with regional topographic landforms, supported by lithologies of varying weathering and erosional resistances. It is improbable that shales, sandstones, conglomerates or coal beds could be identified or differentiated on that Nimbus photograph from tones of gray, since most of this Appalachian region is densely forested.

A more cautious correlation of patterns to lithologies was presented by Lewis and Davis (1966). The general distribution of lithologies in the Chesapeake Bay region (Figure 2-20) did, more or less, coincide with tonal patterns present on the Nimbus 1 AVCS photograph. That same photograph was later discussed by Rabchevsky (1970) who agreed with the comments made by Lewis and Davis on the lithologic discriminations. The conclusion reached was that major topographic forms and outcrop patterns identified in Nimbus television pictures correlate with published geological data. The patterns reflect the underlying geology and topography of a region and are accentuated by the vegetation cover. Without any ground truth, however, discrimination of vegetation from rock types, or even, at times, from water bodies, is not as yet possible.

Vinogradov's (1969) interpretation of the Paris Basin photographed by the Nimbus 1 AVCS camera was partly discussed in Section 2.2.3. Besides analyzing geomorphic and vegetation boundaries, Vinogradov commented on the discrimination of lithologies on Nimbus photography. Comparing the tones on the photograph with the geological map of France, and noting the correspondence of the outcrop patterns with vegetation boundaries and geomorphic provinces, he concluded that 60% of known lithological contacts could be drawn on this Nimbus 1 photograph (Figure 2-33). Vinogradov also stated that if the riverine Quaternary alluvial sands (30% on photograph) were excluded from photographic identification, then lithologic boundary discrimination on this photograph would rise to 75%. However, approximately 10% of the lithological boundaries were drawn tentatively, without any regard to detailed patterns, and 15% of tonal boundaries present on the photograph were not identified.

The determination of the geologic age of formation (or the detection of geologic time boundaries) is not possible with Nimbus imagery unless the time



1. Silurian and Cambrian shales
2. Lower Carboniferous and Devonian shales
3. Lower Jurassic clays
4. Tertiary marls
5. Lower Cretaceous, Upper Cretaceous, Tertiary and Quaternary sandstones
6. Lower Cretaceous chalks
8. Tertiary Calcareous limestones
9. Lower and Upper Cretaceous marls and sandstones
10. Lower and Upper Cretaceous clays and sandstones
11. Faults
12. Clouds

Figure 2-33 Lithological interpretation of the Paris Basin as compared to a Nimbus 1 AVCS photograph taken on orbit 236, 13 September 1964. (Vinogradov, 1969) (See also Figures, 2-5, 2-6 and 2-24.)

boundaries coincide with lithological boundaries. As lithological contacts do not necessarily agree with geological formations, Vinogradov (1969) states that the discrimination of formation boundaries on Nimbus imagery is 50% less probable than the identification of lithological contacts.

2.4 Volcanic and Hydrothermal Activity

The intensity of volcanic eruptions and hydrothermal emanations is variable. Although such activities tend to be confined to specific geological structures and regions, their detection on Nimbus imagery is difficult because of their relatively small size. The resolution elements of the AVCS, IDCS, HRIR and THIR data are larger than the size of most active volcanic vents or hydrothermal sources. Nevertheless, as pointed out in Section 1.2, a very high temperature contrast and, at times, a smoke plume, may make an eruption detectable by the Nimbus thermal sensors (HRIR, THIR) and television cameras (AVCS, IDCS).

The feasibility of locating and identifying hydrothermal sources on Nimbus imagery has not been fully investigated. The only published example on this subject is the brief note by Gawarecki et al (1965) on the Salar de Atacama to which reference was made in Section 2.3.3.2. The relatively warm springs surrounding the Atacama Basin, however, are not very hot and, even if they are of hydrothermal origin, their source is located in the surrounding mountains far from the playa. The question then arises whether even this one instance represents the identification of hydrothermal activity on Nimbus imagery. Regardless of the interpretation, it is interesting to note that the thermal halo feature in the HRIR around the center of the playa has no visual counterpart in the Nimbus AVCS imagery (Conti, 1967). More investigations are obviously necessary.

The effects of volcanic activity on the surrounding surface and atmosphere facilitate its identification. For example, an oceanic volcano or a volcano erupting on an oceanic island may be located easier than a similar continental eruption. The heat of the oceanic eruption and light albedo of the associated smoke plume contrast sharply with the uniformly colder and darker waters, thus enhancing its detection. Similar eruptions on land may be hidden by the less uniform surface temperatures and reflectances in the area surrounding the volcanic vents or thermal spring sources.

On IDCS images the possibility of an eruption is indicated by the presence of a plume formed by smoke, ash, and steam discharge. An eruption of the Beerenberg volcano on Jan Mayen Island was reported on 20 September 1970 by the Smithsonian Center for Short-Lived Phenomena (Smithsonian Institution, 1970). A plume resulting from this eruption was observed by the Nimbus IDCS camera and daytime HRIR system beginning on 21 September (Figure 2-34). The white plume,

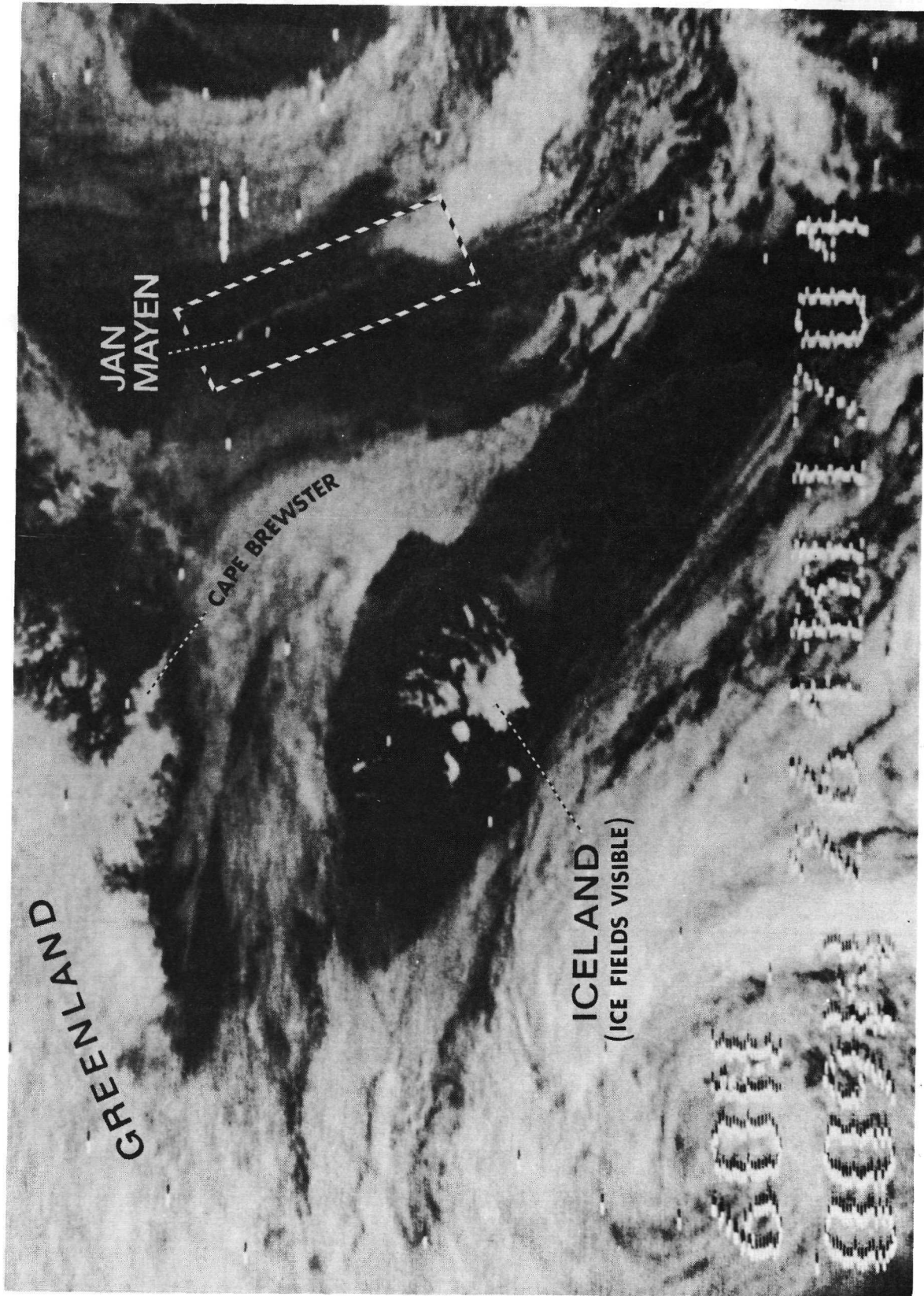


Figure 2-34 Nimbus 4 IDCs photograph of an ash plume from Beerenberg volcano, taken on orbit 2231, 21 September 1970.

extending south-southeast from the glacier-covered island, measured some 200 miles in length before it met the cloudy area. Although the plume formed from ash particles, Merritt (1970) suggested that its presence was enhanced by the formation of a contrail from the condensation of the ejected water vapor (steam) on the ash particles.

Since the launch of the first Nimbus satellite in 1964, only four other instances of volcanic detection on Nimbus imagery have been published in reports: the Kilauea and Mauna Loa volcanoes on the island of Hawaii, Mount Etna in Sicily, the Hekla volcano in Iceland, and the Surtsey volcano in the Vestmannaeyjar Archipelago. It may be that, with a properly oriented search, other volcanic eruptions could be located; this, however, requires more than just a casual survey of the available Nimbus imagery.

The first volcanic observations by the Nimbus 1 satellite were the volcanic craters Mauna Loa and Kilauea in Hawaii. According to Gawarecki et al (1965), a small thermal anomaly corresponding to the summit crater is visible in the HRIR as a dark spot atop Mauna Loa (Figure 2-35), the highest volcano in the Hawaiian island chain. The more active Kilauea volcano on the east side also shows a strong thermal anomaly, whereas Mauna Kea on the north, which is inactive, shows no thermal difference. The thermal zonation of the Mauna Loa and Kilauea craters is also accentuated by the elevation differences. The flanks of these volcanoes become cooler with increasing altitude so that the hot vent at the top contrasts sharply with the cooler surrounding temperatures. Inasmuch as the craters are somewhat smaller than the minimal HRIR resolution (3.3 km) at subpoint perigee, this example once more indicates that subresolution features may show up in the HRIR, or THIR, if they contrast sharply in temperature with their surroundings.

Friedman and Williams (1968) have mentioned Nimbus observations of Mount Etna (Sicily), but have not described the appearance of these eruptions or illustrated them with Nimbus imagery.

Another instance of volcanic activity observed by a Nimbus satellite sensor was mentioned in a paper presented at the 1970 annual Geological Society of America meeting by Friedman (1970). He discussed thermal emission from Hekla volcano, Iceland, before its eruption on 5 May 1970. In that presentation, Friedman noted that thermal emission from the lava-fountain phase was recorded by the Nimbus 4 THIR radiometer beginning 6 May. More recently the eruption of Mount Etna which started on 6 April 1971, was detected by the Nimbus 4 THIR (Friedman, 1971).

The classic case for the feasibility of detection of volcanic activity by Nimbus satellite sensors is the Surtsey volcano eruption which is described in several papers by Friedman and Williams (1968), Friedman et al (1969) and

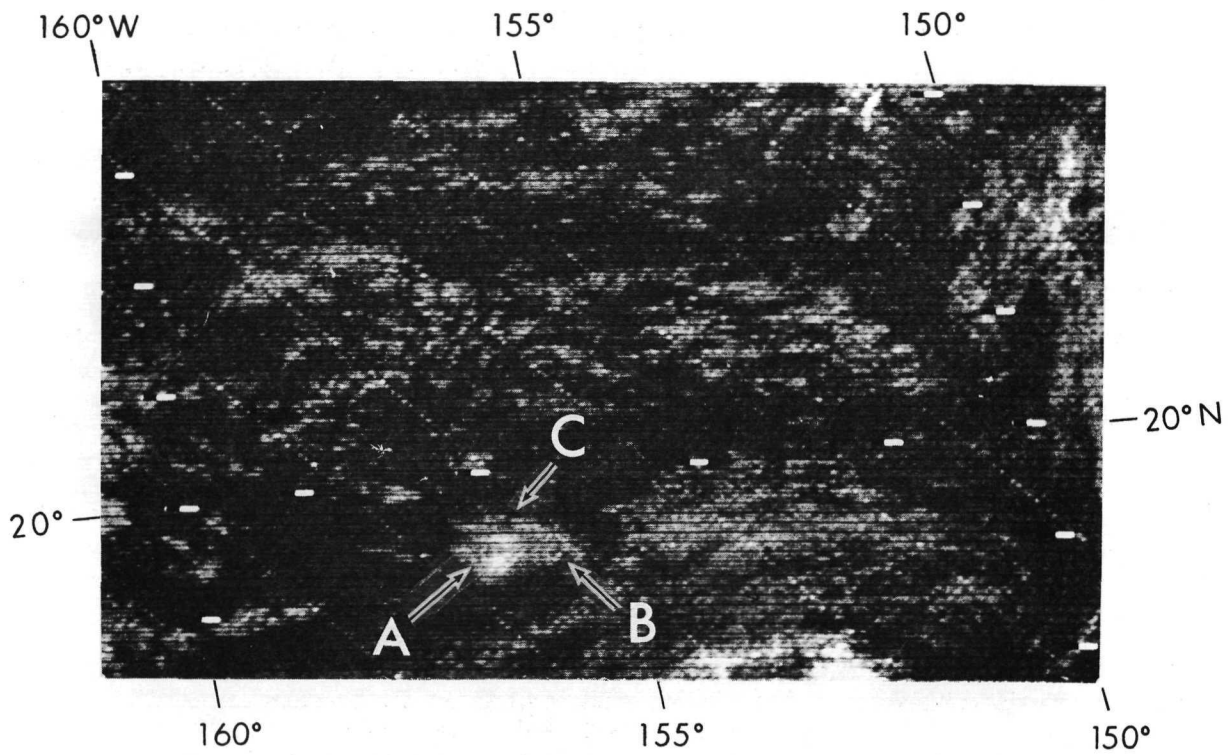


Figure 2-35 Nimbus 1 HRIR image of Hawaiian Islands and vicinity taken on orbit 250, 14 September 1964. Light shades are cold surfaces. Mauna Loa (A) and Kilauea (B) volcanoes have thermal activity as indicated by dark spots. Mauna Kea (C) is inactive. Clouds (light shades) are present in much of the image. (Gawarecki et al, 1965)

Williams (1970). The island of Surtsey lies in the Vestmannaeyjar Archipelago off the southern coast of Iceland. Surtsey's eruptive history has been discontinuous, complex and unpredictable. Summaries of the history of Surtsey are given by Thorarinsson (1966, 1967), Norrmann (1970), and the four volumes of the Surtsey Research Progress Reports (1965-1968).

On 19 August 1966 an effusive fissure eruption began at Surtsey, following two and a half years of inactivity in the Surtur I crater, and fifteen months of inactivity in the Surtur II crater. Infrared emission from the Surtsey volcano, between 19 August and 3 October 1966, was recorded concurrently by an airborne scanning radiometer and the Nimbus 2 HRIR system. This marked the first time concurrent observations by satellite and airborne instruments yielded data on infrared emission from an erupting volcano. On Nimbus 2 infrared imagery, the Surtsey eruption appeared as a small black dot,* of one or two resolution elements (Figure 2-36), on at least seven separate orbital passes (Friedman and Williams, 1968). The first appearance was on orbit 1288, 12:27:29 UT, 20 August 1966, 12 hours after the first extrusion from the eruption fissure, and the spot definitely was present as late as 3 October 1966. The anomaly is clearly visible on Nimbus 2 imagery from the orbits given in Table 2-4.

TABLE 2-4
NIMBUS 2 ORBITS ON WHICH THE SURTSEY VOLCANIC ERUPTION
APPEARS AS A DARK SPOT ANOMALY ON THE HRIR IMAGERY
(from Friedman and Williams, 1968)

Orbit No.	Date
1288	20 August 1966
1315	22 August 1966
1541	8 September 1966
1648	16 September 1966
1701	20 September 1966
1774	21 September 1966
1874	3 October 1966

The effusive eruption on Surtsey was detectable from orbital altitude because the spectral sensitivity of the HRIR instrument in the 3.4 μm to 4.2 μm atmospheric transmission window was near the peak wavelength emittance of the incandescent lava. A contrasting cold ocean also facilitated the observations.

Further confirmation that the Nimbus HRIR system did, indeed, record the Surtsey anomaly, is provided by a positive spike at the correct geographic

*The higher the surface temperature (or infrared emission), the darker the area on an HRIR or THIR positive image.

position for Surtsey on scan line analog profiles (visicorder oscillograph records). The visicorder oscillograph records, when properly calibrated, permit measurement of radiance and temperature as a function of time and sensor scan angle. Figure 2-37b shows the effective radiance (N) and the equivalent blackbody temperatures (T_{bb}) from the earth's surface along a profile from Greenland to Great Britain, 22 August 1966, recorded at an altitude of 1114 km by the Nimbus 2 HRIR. The highest positive spike on this analog profile represents infrared radiation in the 3.4 μm to 4.2 μm wavelength band emitted by lava craters and incandescent flows in Surtur I on Surtsey, integrated with infrared radiation from the remainder of the island (total island area is 2.35 km^2) and the 61.65 km^2 area of surrounding ocean surface.

Detection of the Surtsey anomaly on Nimbus HRIR imagery demonstrates that effusive volcanic events of this magnitude, involving major convective heat loss, can undoubtedly be detected and monitored from orbiting infrared scanning radiometers (Friedman et al, 1967, 1969; Williams et al, 1968, 1970).

2.5 Regional Hydrology

The Nimbus television and infrared imaging sensors have the capacity to monitor some of the hydrologically significant parameters. The visible spectrum sensors (AVCS and IDCS) are suited for snow and ice surveillance, and for viewing the extent of inland water bodies and inundated land. The near-infrared reflectance sensor (the Nimbus 3 HRIR 0.7 μm to 1.3 μm channel) is sensitive to variations in surface moisture and extent of water bodies. The HRIR (3.4 μm to 4.2 μm) and THIR (10.5 μm to 12.5 μm) infrared sensors measure surface temperatures which are related to soil moisture content and evaporation rates. Table 2-1 in Section 2.1 lists the possible hydrological applications of Nimbus data. This section documents some of these applications.

2.5.1 Surface Moisture and Surface Water Identification

Nimbus HRIR and THIR temperature and reflectance measurements can yield valuable information about soil moisture and surface water conditions. Soil moisture strongly influences surface temperatures because it controls the surface thermal inertia (see Section 2.3.3.1). A dry surface has a lower thermal inertia than a similar wet surface; this lower thermal inertia implies poorer retention of daytime heat and greater cooling at night. During the day, especially in arid and semiarid regions, solar heat dries the upper A-horizon of the soil and the moisture migrates downward toward the cooler B and C soil horizons. The uniformly heated soil thus does not reveal possible humidity underneath.

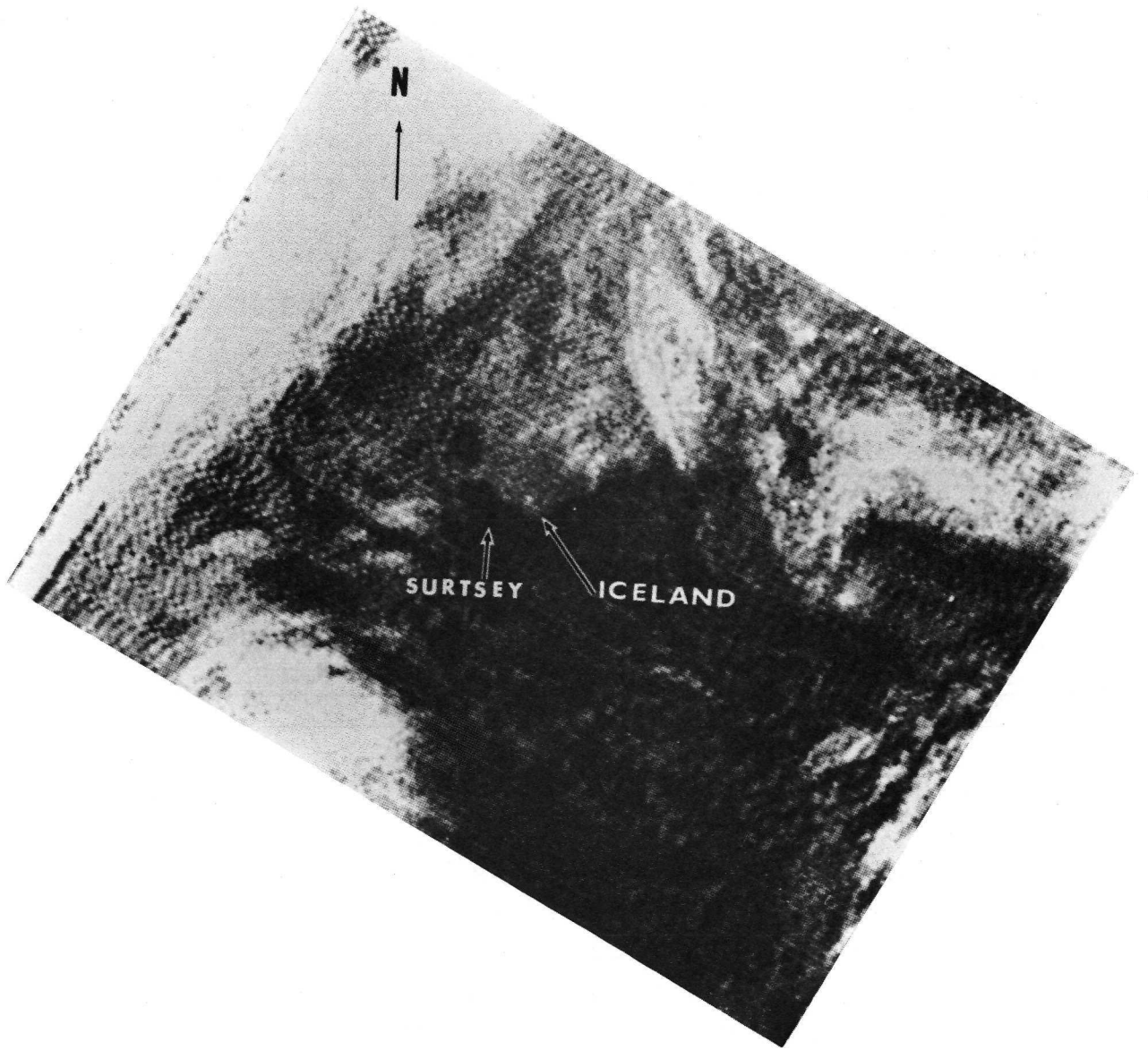
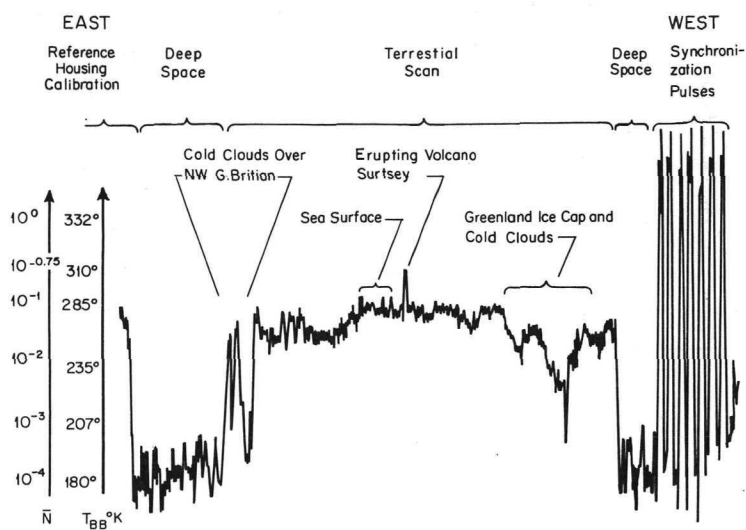
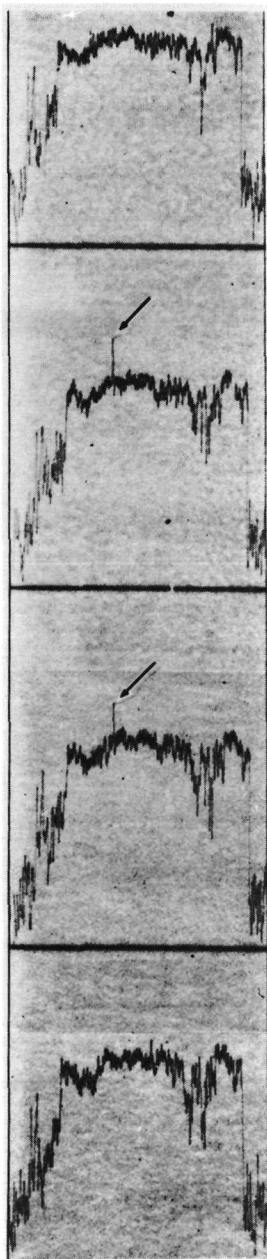


Figure 2-36 Nimbus 2 nighttime HRIR photofacsimile observation of Surtsey taken on orbit 1541, 8 September 1966.



a) Portions of four consecutive analog traces across the Surtsey area taken on orbit 1541, 8 September 1966.

b) Calibrated visicorder analog trace of one scan taken on orbit 1315, 22 August 1966 (after Friedman and Williams, 1968).

Figure 2-37 Analog traces of Nimbus 2 HRIR data.

But at night, any moisture stored below the A horizon migrates by capillary action toward the surface (which is being cooled by radiative processes) bringing the heat of the day with it. Thus, in regions of constant surface elevation and constant soil composition, nocturnal surface temperature gradients over unvegetated areas may be related to soil moisture.

The following equation

$$\Delta T_{2,1} = T_2 - T_1 = K \left[\frac{1}{(\rho c \lambda)_1^{1/2}} - \frac{1}{(\rho c \lambda)_2^{1/2}} \right] \quad (2-6)$$

also discussed in Section 2.3.3.1, shows the relationship between an "equivalent" surface thermal inertia $(\rho c \lambda)^{1/2}$ and surface temperature differences $(\Delta T_{2,1})$, obtained from the HRIR or THIR. Ground-truth observations of moisture, concurrent with satellite observations of surface temperatures, may yield a knowledge of how this "equivalent" thermal inertia from satellite temperature observations is related to soil moisture. So far, Nimbus radiation data have been related to surface moisture only qualitatively. In a series of studies, Pouquet (1968a, 1968b, 1969a, 1969b) analyzed nighttime HRIR temperature maps of arid and subarid regions in various parts of the world, and was able to associate higher nocturnal temperatures to areas of higher surface moisture content. Usually these areas are alluvial deposits of former river and lake beds, depressions, and hidden fault lines. He states (1969a) that the delineation of these areas in subarid lands is most valuable for agricultural purposes since a minimum of irrigation would be necessary to support agricultural activity. In an analysis of a region of the north-eastern Sahara, Pouquet (1968a) finds that maps drawn with the HRIR radiometric measurements allow a good, even a precise preselection of the spots suitable for agriculture. In another study involving the analysis of all available Nimbus 2 HRIR data over the southwestern United States, Pouquet (1968b) concludes that with little irrigation most of the empty lands between the Colorado River and Salton Sea could be drastically changed, converted into "luxuriant gardens". Similarly, the land south of Tucson to Nogales could be reclaimed to agriculture with a minimum of irrigation because of the quasi-permanent soil moisture. Pouquet and Raschke (1968) emphasize, though, that the satellite data are no substitute for field work. "Satellite measurements must be considered only as a tool ... used to select in advance, with a precision unknown in the past, areas of interest which can then be investigated on the ground more carefully than would have been possible without the spacecraft."

Surface moisture, especially surface water changes due to flooding, may sometimes be detected by the Nimbus 3 HRIR daytime reflectance measurements. Reflectance changes due to flooding and surface moisture in many river basins of the world are discussed by Pouquet and Rabchevsky (1970a, 1970b), Sissala and

Rabchevsky (1970), Rabchevsky (1970, 1971), and MacLeod (1970a, 1970b). As illustrated in the following examples, reflectances are usually low in the spring or rainy season and increase during the dry summer months.

2.5.1.1 Lower Mississippi River Region

Examination of the Nimbus 3 daytime HRIR (0.7 μm to 1.3 μm) reflectance data in the Lower Mississippi River Valley during the period April-September 1969 revealed the presence of significant variations in tonal patterns. Investigations of the possible causes of the changes by MacLeod (1970a) and by Sissala and Rabchevsky (1970) suggest that the changes in reflectivity observed on the successive photofacsimiles (Figure 2-38) and the computer-produced grid-print maps* (Figure 2-39) correspond primarily to decreases in soil moisture during the dry (1969) summer season. The moisture decrease, from 22 May to 9 August, resulting from a decrease in rainfall, affected the vegetal cover (wilted vegetation, poor crop yield) and soil texture; the radiometer, in turn, integrated those changes as higher reflectances. Similarly, a reversal to a lower relative reflectance by 12 September was a response to moisture added to the ground by increased rainfall.

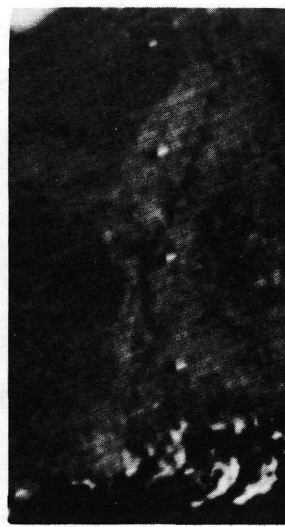
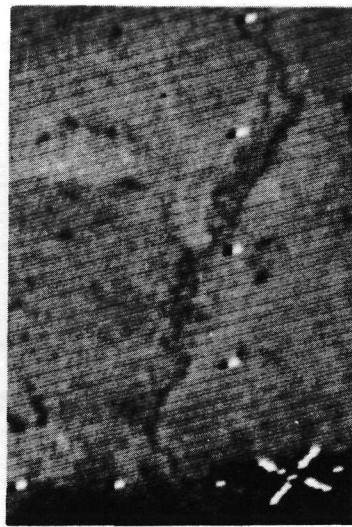
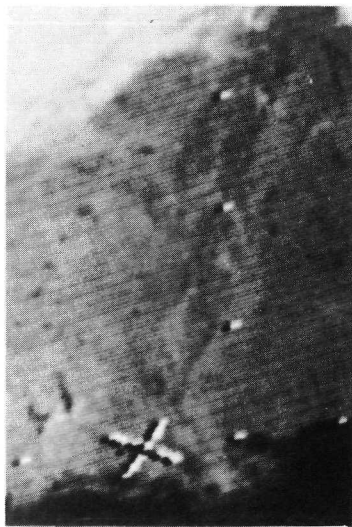
Figure 2-40 provides another example of reflectance changes in the Mississippi Valley associated with the surface moisture. MacLeod (1970a) pointed out that the 20 May photofacsimile shows dark areas around the Mississippi not present in the 15 May photofacsimile. In fact, heavy precipitation (with some flooding) recorded in the area between 15 May and 20 May accounts for the drastic increase in soil moisture. Two days later the decrease in surface moisture and flooded areas shows up as a general relative increase in reflectance.

In another analysis of the same general region (Figure 2-41), north-south low reflectance contours are evident along the course of the White River in Arkansas. The low reflectances near the bottom of the map area follow the trend of the Mississippi River. No similar pattern, however, is evident for the Arkansas River, in the lower left, where it enters the Mississippi River. This lack of pattern associated with a river is not unique. The satellite does not see the river as such; rather it detects the thick vegetation which characterizes many river beds.

2.5.1.2 Ouachita River

The effects of a spring flood of the Ouachita River (near the Louisiana-Arkansas border) have been detected by Nimbus HRIR sensors (Figure 2-42). An Apollo 9

*Appendix B, Section B.4, contains a discussion on the significance of the reflectances plotted on the grid-print maps from the Nimbus 3 daytime radiation measurements.



0.57

0.47

0.27

0.29

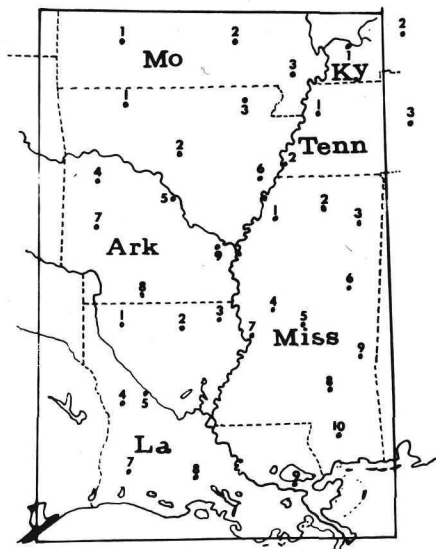
Orbit 515,
22 May

Orbit 716,
6 June

Orbit 1574,
9 August

Orbit 2030,
12 September

Horizontal bars represent rainfall averages in inches for the week prior to image acquisition. 22 May - rainfall of 0.5 to 2 inches on 18 May; 6 June - rainfall 0.2 to 1.2 inches in Louisiana and Mississippi on 2 June. Light and scattered rainfall elsewhere since 22 May; 9 August - almost no rainfall since 28 July; 12 September - generally heavy rainfall 1 through 12 September. No rainfall from 9 through 12 September



Index map of the imaged area. Numbers represent rainfall gauging station from which information was collected.

ARKANSAS

1. Harrison
2. Greers Ferry
3. Walnut Ridge
4. Blue Mts. Dam
5. Little Rock
6. Forrest City
7. Narrows Dam
8. El Dorado
9. Dumas

KENTUCKY

1. Paducah
2. Madisonville

LOUISIANA

1. Minden
2. Calhoun Exp. Sta.
3. Epps 6 W
4. Leesville
5. Alexandria
6. Baton Rouge
7. Lake Charles
8. Lafayette
9. New Orleans

MISSISSIPPI

1. Clarksdale
2. University
3. Tupelo
4. Yazoo City
5. Canton
6. Louisville
7. Vicksburg
8. Collins
9. Meridian
10. Wiggins

MISSOURI

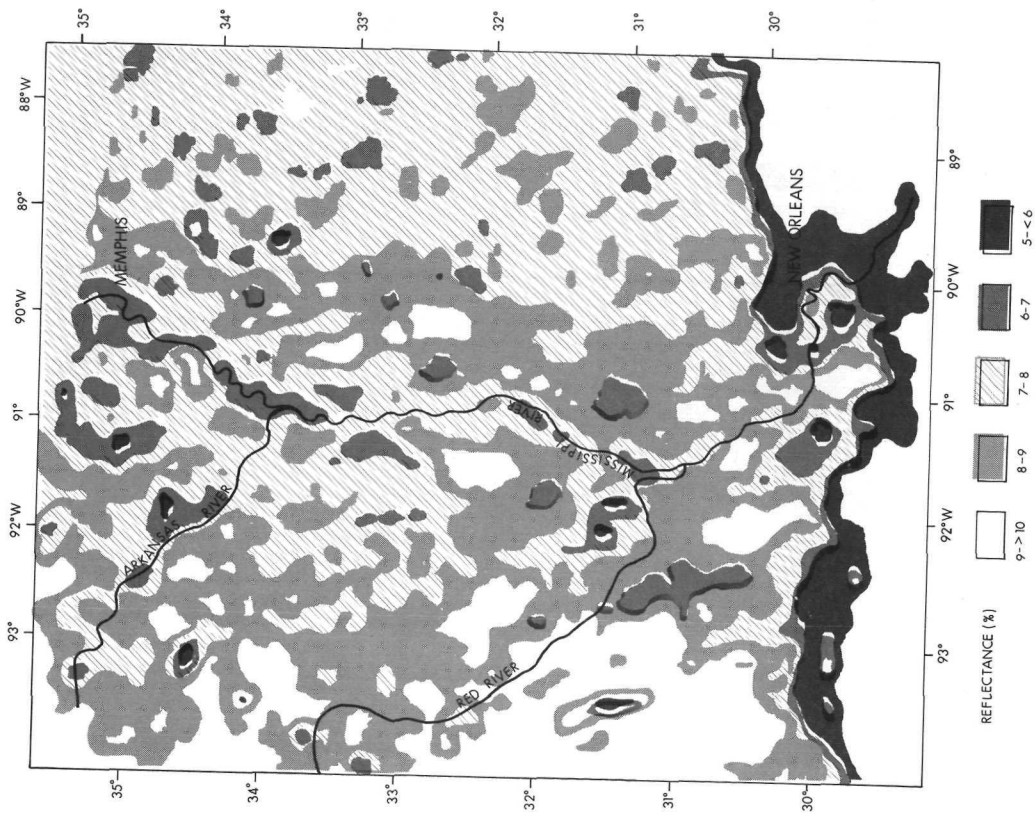
1. Springfield
2. Ellington
3. Malden

TENNESSEE

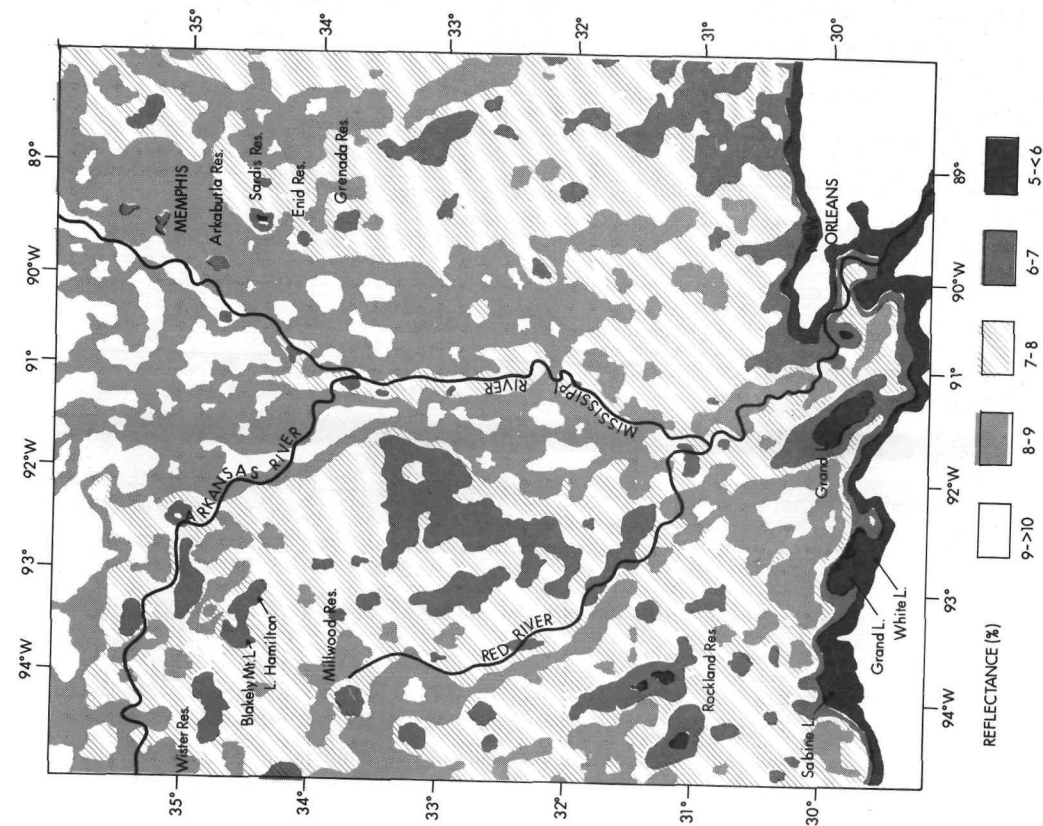
1. Dyersburg
2. Memphis
3. Centerville

Gauging stations from which rainfall information was collected.

Figure 2-38 Changing near-infrared (0.7 to 1.3 μm) reflectance patterns in the lower Mississippi Valley recorded by the Nimbus 3 day-time HRIR during 1969.

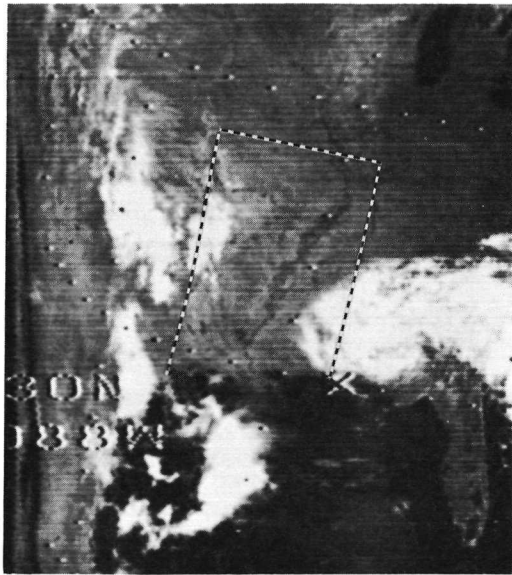


a) Reflectance values along the river are 6 to 8%. Orbit 515, 22 May 1969.



b) Reflectance values along the river are about 8 to 10%. Orbit 2030, 12 September 1969.

Figure 2-39 Analyses of computer-produced Nimbus 3 daytime HRIR (0.7 to 1.3 μm) reflectance maps of the Mississippi River Valley area.



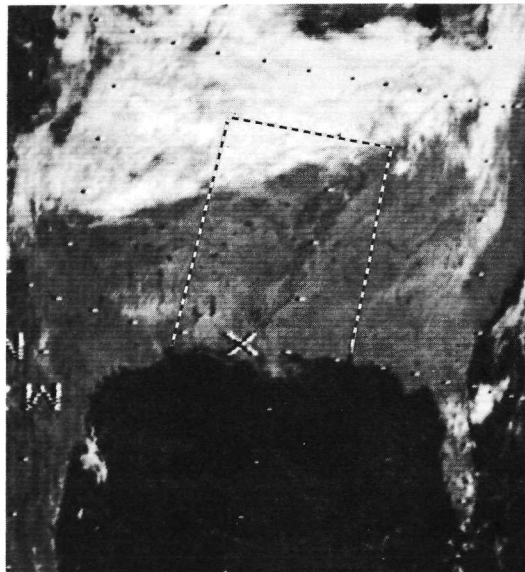
Orbit 421, 15 May

Area rainfall averaged less than .01 inch per day for each of the preceding four days.



Orbit 488, 20 May

Area rainfall averaged 0.24 inch per day for each of the preceding four days. Most light tones within the area are caused by cumulus clouds.



Orbit 515, 22 May

No rainfall within the area on May 20 and 21. Some cumulus clouds are within the area.

Figure 2-40 Rapid reflectance changes of the lower Mississippi Valley as recorded by Nimbus 3 daytime HRIR during May 1969. (MacLeod, 1970a)

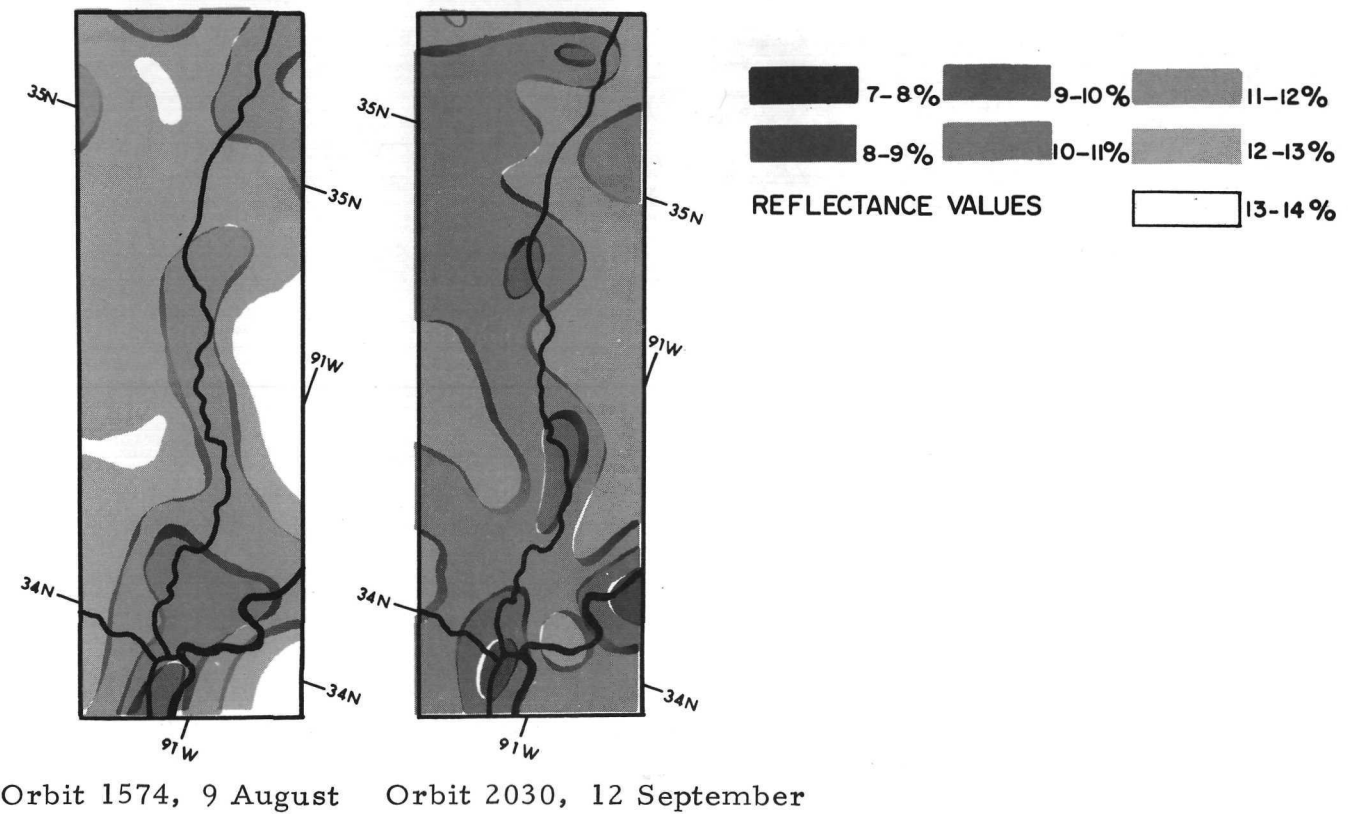
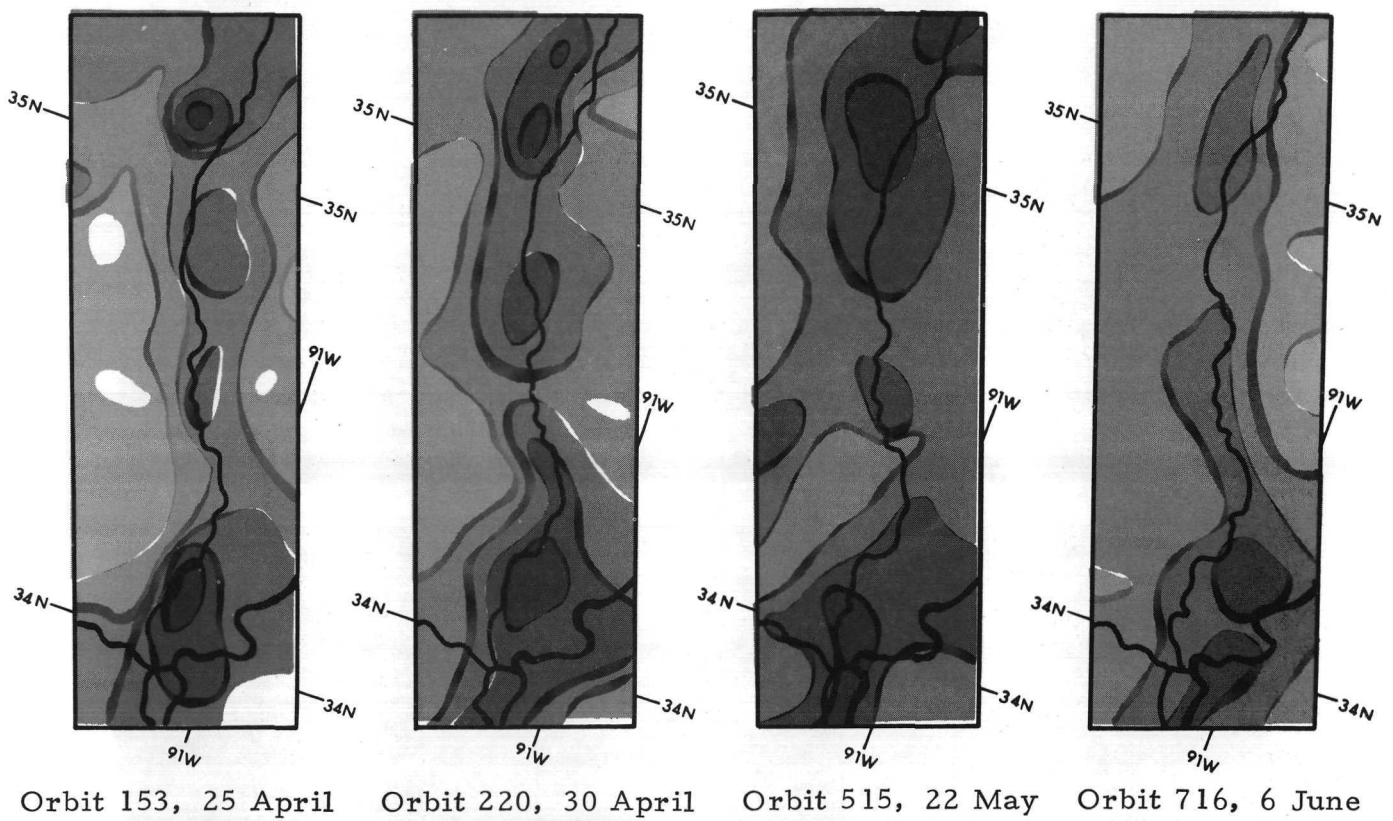


Figure 2-41 Temporal sequence of Nimbus 3 daytime HRIR reflectance patterns along the White River in Arkansas during 1969.

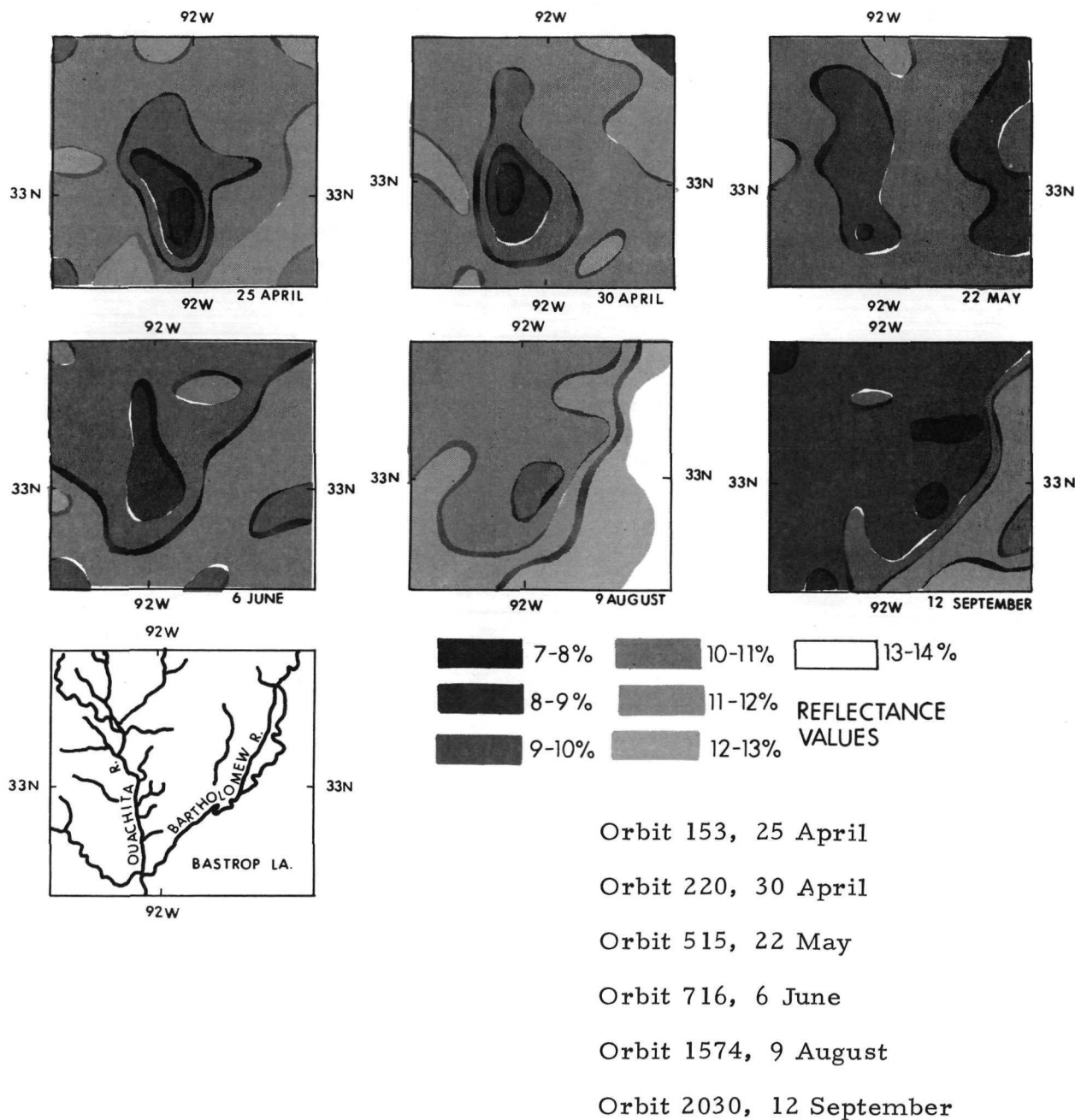


Figure 2-42 Analyses of computer-produced Nimbus 3 daytime HRIR (0.7 to 1.3 μm) reflectance maps of the Ouachita River during 1969. (Changing reflectance values and patterns are related to a 1969 spring flood along the Ouachita River at the Louisiana-Arkansas border.)

near-infrared image of the area taken on 9 March 1969 (Figure 2-43) shows this area at the height of the flood when about 165 sq. mi. were inundated (NASA, 1970). Analysis by Sissala and Rabchevsky (1970) of Nimbus 3 HRIR grid-print reflectance maps for 25 and 30 April 1969 (Figure 2-42) shows a low reflectance pattern in the flood area one and one-half months after the Apollo picture was taken. By 6 June, a weak northeast-southwest tonal gradient corresponding to the two major vegetation types (visible in the Apollo picture) has now appeared. By 9 August, there is a marked reflectance increase in the eastern half of the picture (no rain has fallen in this area in over two weeks). This drought seems to have had a pronounced effect on reflectance in the intensively cultivated area along the Mississippi River with a lesser effect on the different vegetation in the western half of the map.

2.5.1.3 Paraguay-Parana Rivers Floodplain, South America

A series of daytime HRIR photofacsimiles, presented in Figure 2-44, depicts temporal surface moisture and flood conditions of the Paraguay-Parana Rivers floodplain. The circled area focuses on a region where reflectances decrease from June to November because of the increased surface moisture and flooding associated with the rainy season. A comparison with digitized grid-print maps (Figure 2-11, also discussed in an earlier section of the report) affords quantitative evaluation of reflectances at the height of the flooding, the period when the streams and swamps of this huge floodplain merge in places to form larger water bodies, thus contributing to the capacity of the Parana River. The United Nations has launched a series of studies (Cordeiro, 1967) to determine the hydrologic regime of this region; HRIR and THIR information could complement data gathered from aircraft and ground surveys, both in assessing overall flood conditions and in estimating soil moisture and evaporation rates.

2.5.1.4 Lake Chad and Niger River Region, Africa

Two regions in Africa, the Lake Chad Basin and the Niger River Valley, have also been investigated, as reported in the previously cited references. Since the Lake Chad Basin is another area where the United Nations has undertaken an extensive hydrologic survey (Gisler, 1967; UNESCO, 1970), the application of satellite-acquired data could be particularly beneficial. Figure 2-45 is a sequence of daytime HRIR photofacsimiles showing the seasonal reflectance changes in the Chad area which are thought to be associated with the changes in soil moisture and flood conditions. Lake Chad itself undergoes a noticeable seasonal change in surface area.

Seasonal soil moisture changes and flooding are believed to account for most of the reflectance variations of the Niger River inland "delta" in the Nimbus 3 daytime HRIR images (Figure 2-46). Rainfall increases from May through August and then decreases to a negligible amount by November. Delta reflectances appear to

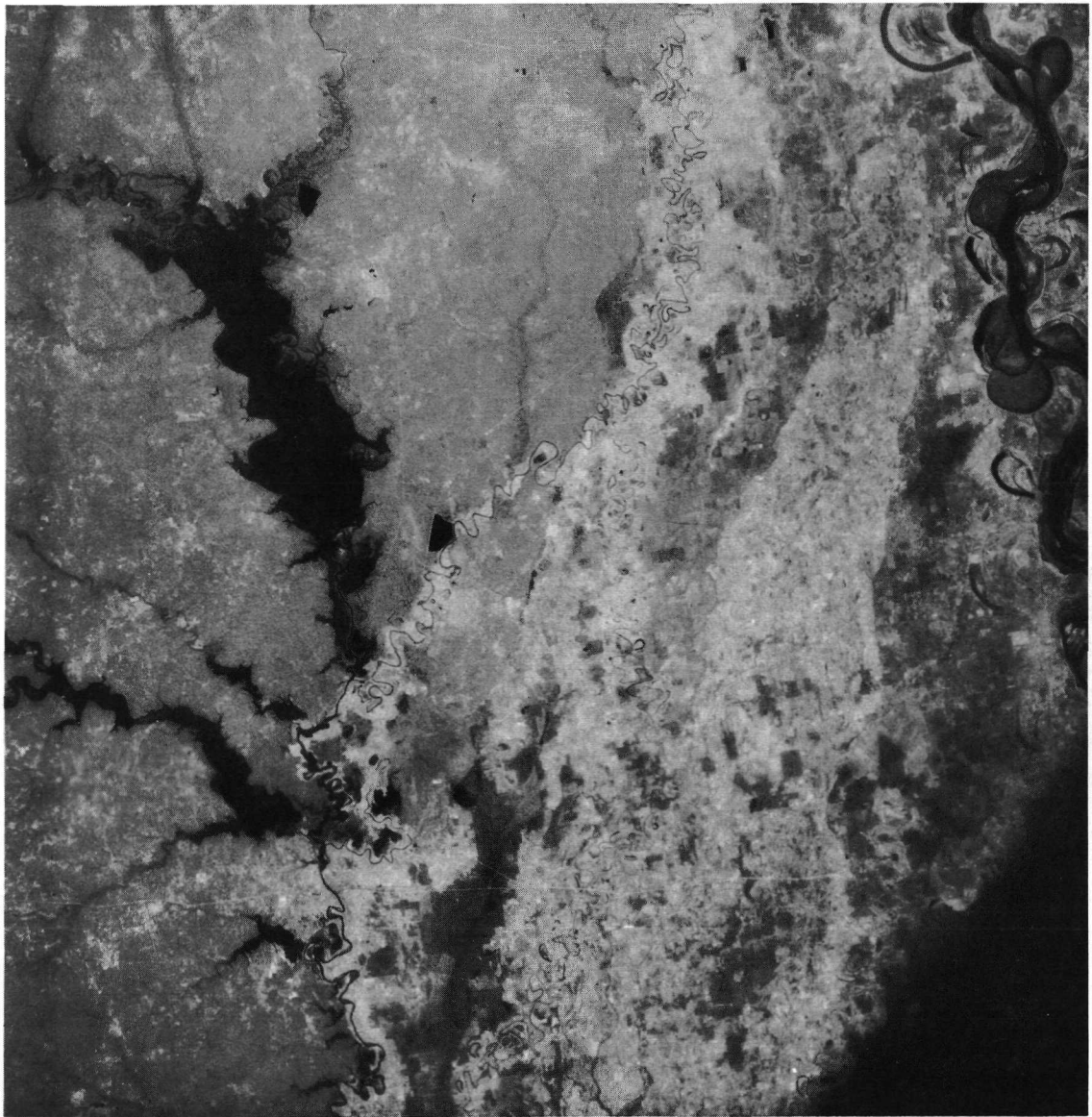
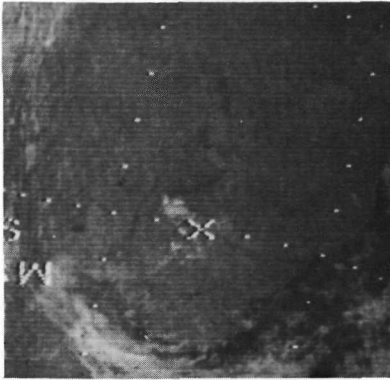
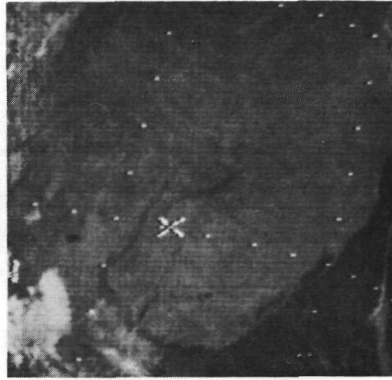


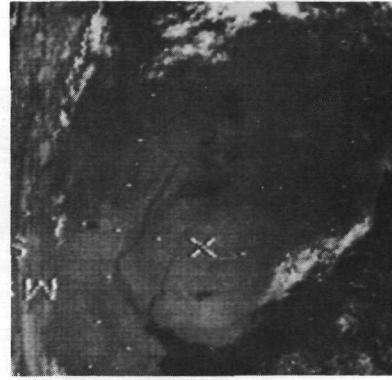
Figure 2-43 An Apollo 9 near-infrared (0.68 to 0.89 μm) picture taken on 9 March 1969 showing the Ouachita River flood that was later recorded by Nimbus 3 daytime HRIR (see Figure 2-42). (The Mississippi River is at the extreme right. The wide light swath running from top to bottom is agricultural land on a former plain of the Mississippi River.)



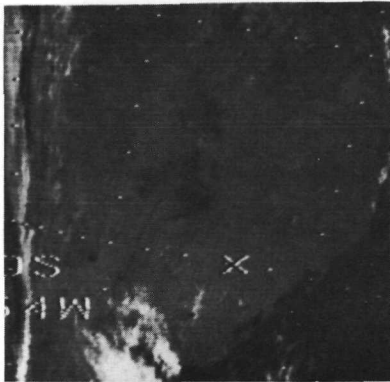
Orbit 769
10 June 1969



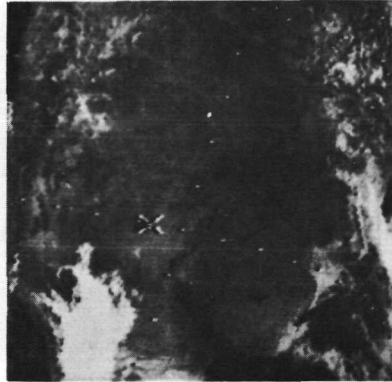
Orbit 1426
29 July 1969



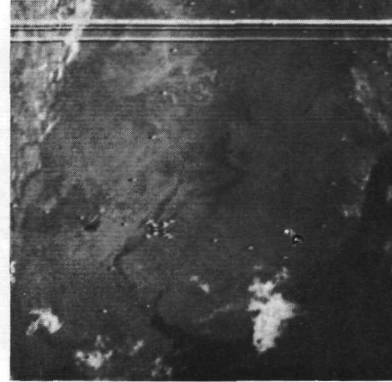
Orbit 2418
11 October 1969



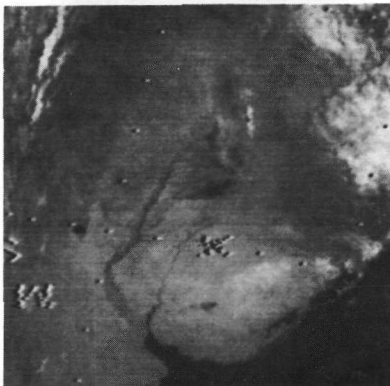
Orbit 2619
26 October 1969



Orbit 2874
14 November 1969



Orbit 3142
4 December 1969

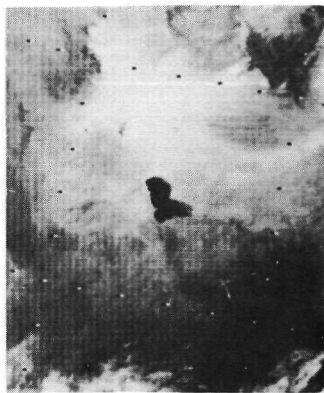


Orbit 3410
24 December 1969

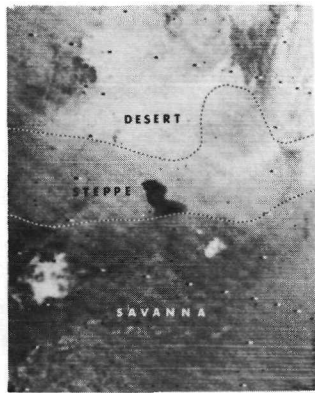


APPROXIMATE AREA COVERAGE OF EACH PICTURE

Figure 2-44 Temporal surface moisture and flood conditions of the Paraguay-Parana Rivers flood plain as imaged by Nimbus 3 daytime HRIR during 1969.



Orbit 176
27 April 1969



Orbit 270
4 May 1969



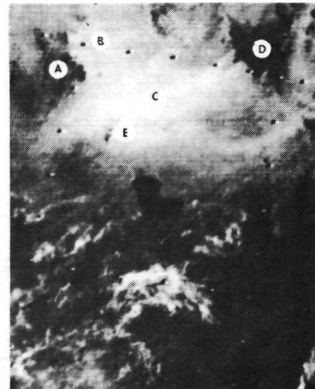
Orbit 833
15 June 1969



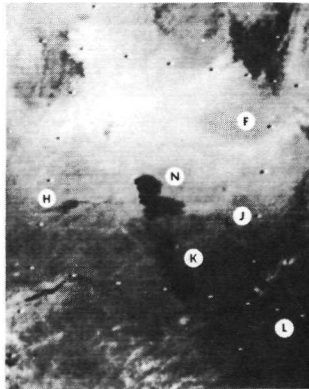
Orbit 1329
22 July 1969



Orbit 1691
18 August 1969



Orbit 1986
9 September 1969



Orbit 2415
11 October 1969



Orbit 2911
17 November 1969



Orbit 3340
19 December 1969



Orbit 3608
8 January 1970

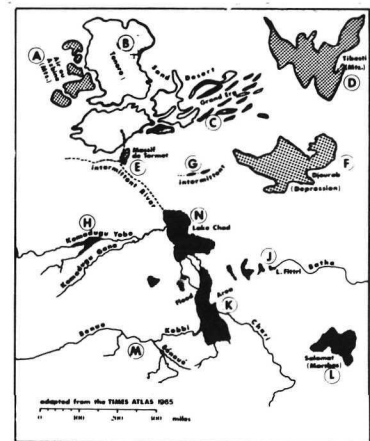


Figure 2-45 Seasonal changes in the Lake Chad region recorded by the Nimbus 3 daytime HRIR. Winter and spring reflectances are relatively high because of very low rainfall. During the summer rain period, and immediately after, reflectances decrease with an increase in soil moisture. Some hydrological features, the Komadugu Rivers (H), Salamat Marsh (L) and flood area (K) are accentuated by the increased surficial water. The Djourab depression (F) maintains a uniform tonal appearance throughout the year.

decrease from July through November. Concurrent with a lack of rainfall from November through January is a dramatic increase in the delta reflectance. The reflectance changes are illustrated quantitatively in the grid-print maps given in the earlier Figures 2-9 and 2-10. The 7 to 9% reflectance values are indicative of "normal" vegetation, while reflectances below 5 to 6% are interpreted as water bodies or extremely moist soils. Sands and clouds usually respond with reflectances above the 10 to 12% values.

Reflectance changes observed in the three Nimbus 3 daytime HRIR images (Figure 2-47) of Western Africa roughly correlate with the broad vegetation zones of the tropical forest, savannah forest, and savannah grasslands that belt the West African continent south of the Sahara Desert. These regional vegetation boundaries, in turn, correspond to seasonal changes in soil moisture.

These examples of reflectance changes observed in the 0.7 to 1.3 μm HRIR data correlate with seasonal rainfall patterns. Reflectances decrease during the rainy season, persist at low levels for one to two months after the end of the rains and then increase. It seems probable, therefore, that these reflectance changes are related to changing soil moisture, flooded areas, and seasonal vegetation growth patterns. A quantitative correlation of satellite-observed reflectance changes with soil moisture, vegetation conditions or amount of flooding has yet to be established. When, by means of concurrent ground-truth observations, correlations are established, the hydrologist will have a powerful tool to help him evaluate the ever-changing, yet repetitive, hydrologic cycle for large areas of the world.

2.5.2 Snow Surveillance

Areas of snow cover can be delineated and mapped in Nimbus imagery. The percentage snow cover of river basins can be calculated, therefore, and used in flood prediction and water management programs. The identification of snow in satellite photographs also helps to identify vegetation and land use boundaries, accentuates some geologic and geomorphic features such as fault lines, and highlights thin ice (on water bodies) which would otherwise be invisible. Although only limited snow-depth information can be derived from Nimbus AVCS and IDCS pictorial data, depths up to about 4 inches can be estimated in non-forested areas because of an increase in reflectance as snow accumulates. Figure 2-48 is an example of a changing winter snow cover pattern along the east coast of the United States as recorded by the Nimbus IDCS Real Time Transmission System.



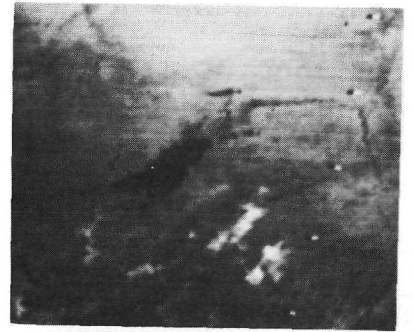
Orbit 847
16 June 1969



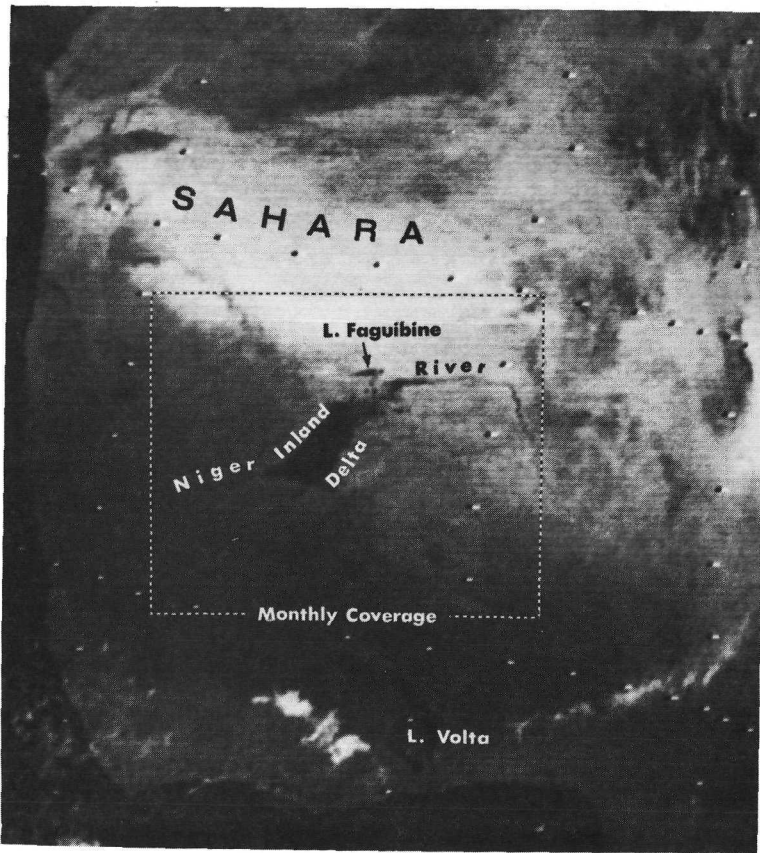
Orbit 1209
13 July 1969



Orbit 2067
15 September 1969



Orbit 2429
12 October 1969



Orbit 2925
18 November 1969



Orbit 3421
25 December 1969



Orbit 3917
31 January 1970

Figure 2-46 Seasonal soil moisture and vegetation changes in the Niger Inland Delta area recorded by the Nimbus 3 daytime HRIR.

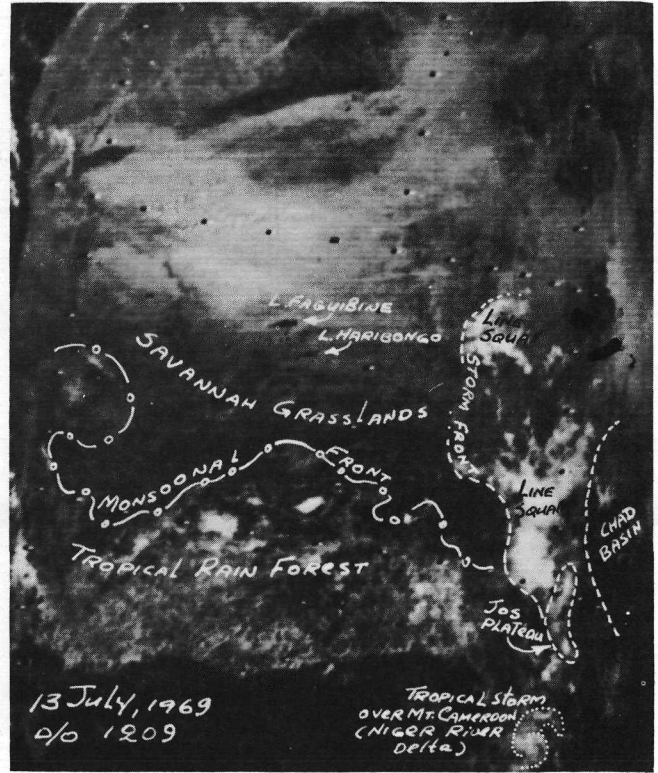
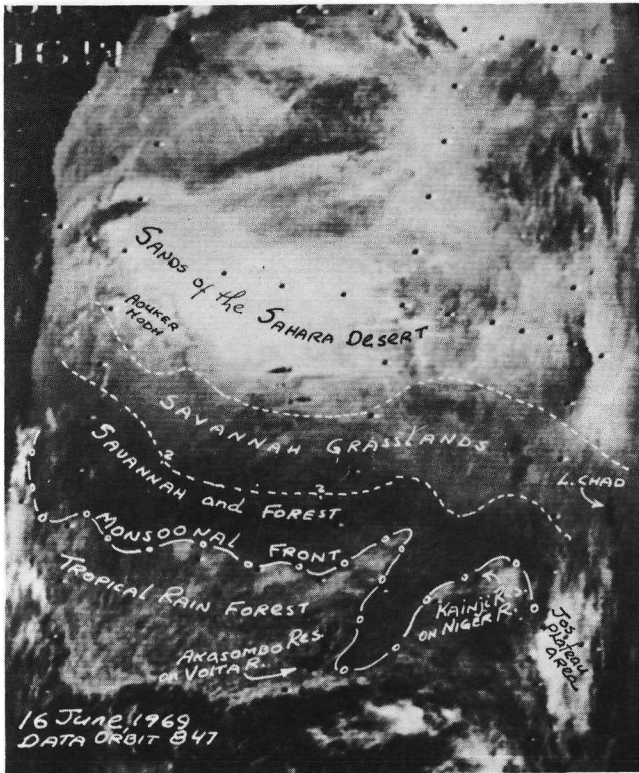
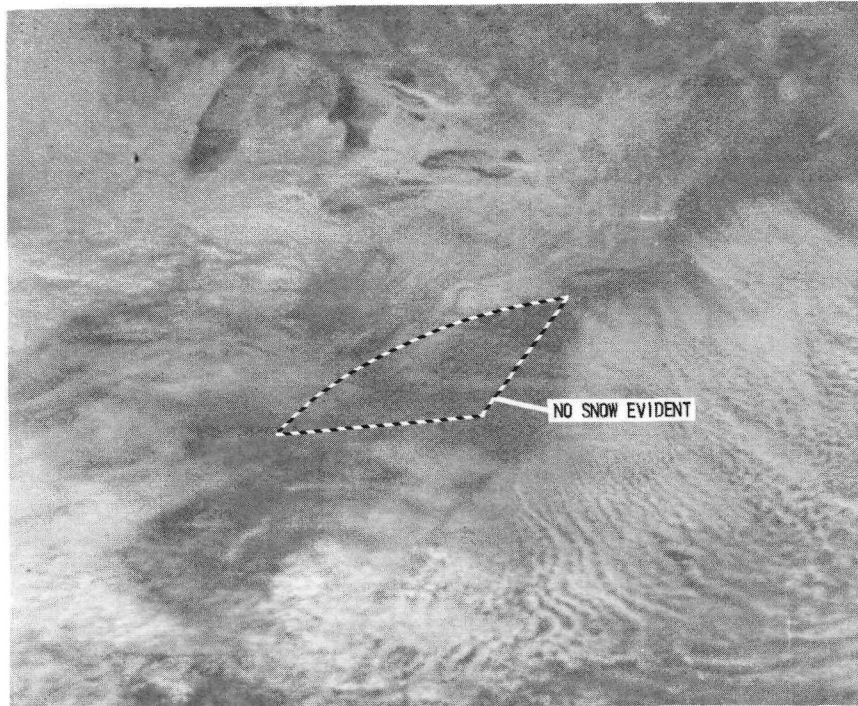
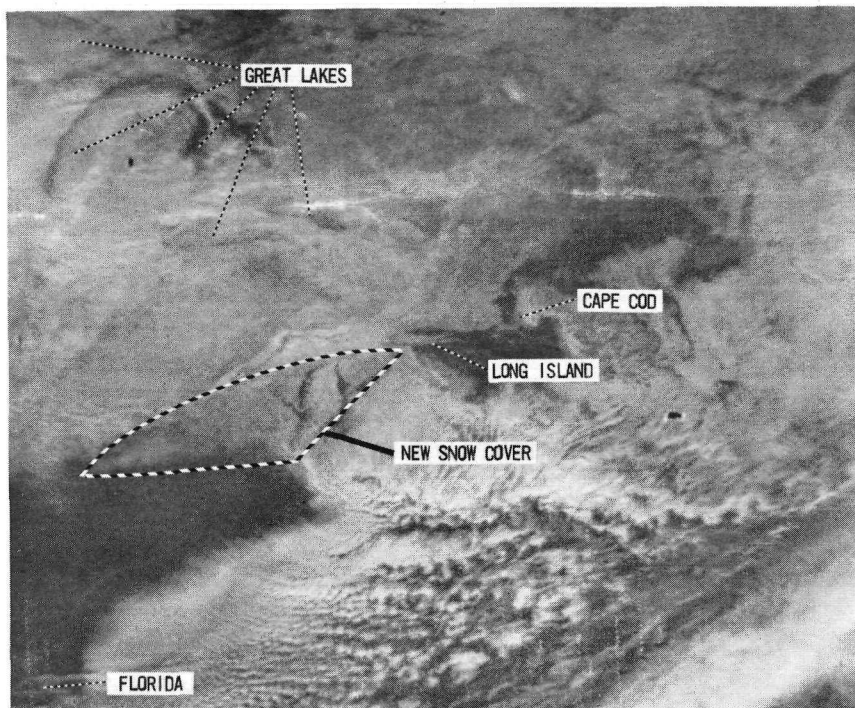


Figure 2-47 Temporal sequence of Nimbus 3 daytime HRIR showing western Africa-Niger River area. Dashed lines were subjectively drawn on these images to divide different gray level areas which roughly correspond to the savannah - forest and savannah grasslands of western Africa. The dashed-dot lines define the tropical monsoonal cloud areas.



a) Orbit 3571, 5 January 1970



b) Orbit 3611, 8 January 1970

Figure 2-48 Changing winter snow cover pattern along the east coast of the United States as recorded by the Nimbus 3 DRID.

2.5.2.1 Techniques for Differentiating Snow from Cloud

Since snow and cloud can have nearly identical reflectances in the visible, differentiation between the two can be a serious problem when analyzing satellite photography. Barnes and Bowley (1968, 1969, 1970) have performed the most thorough documentation of techniques for differentiating snow from clouds in both flat and mountainous terrain. Their techniques are: (1) referencing of satellite imagery with concurrent cloud observations on weather charts to determine when major cloud systems cover an area of interest, (2) recognition (and base mapping) of terrestrial features, such as coastlines, lakes, rivers, and forest/non-forest boundaries, which are apparent in the absence of clouds; (3) identification of stable reflectance patterns over a period of two days or more; and (4) examination of pattern appearance (clouds often have a rough texture due to the shadows of higher clouds on lower clouds; snow surfaces are generally smoother).

Although MRIR data are of marginal utility for snow cover studies because of their low resolution, Hauth and Weissman (1968), using Nimbus 2 MRIR measurements over the Greenland ice cap, found that snow cover can be differentiated from clouds by its reflectance characteristics. Solar radiation reflected from a snow surface did not vary as markedly as that reflected from a cloud surface when the angle of observation changed. Thus, consecutive MRIR observations of the same areas at different viewing angles permitted differentiation of snow from cloud cover.

2.5.2.2 Effects of Vegetation and Snow Depth on Snow Identification

Barnes and Bowley (1968) found that in non-forested areas, brightness can be qualitatively related to snow depths for accumulations up to four inches (Figure 2-49). For accumulations greater than four inches no further brightness change is normally detectable. The relationship between brightness and snow depth can, however, be affected by several factors; to evaluate snow depth properly, one must consider snow age, rainfall, terrain, vegetation, camera characteristics, and solar angle. Figure 2-50 is a Nimbus 2 APT image of the east coast of the United States; here the extreme brightness of the Delaware-Maryland-Virginia peninsula corresponds to eight inches of fresh snow. The rest of Maryland and Virginia contrasts sharply; these areas had received only a trace to four inches of snow, and their reflectances are consequently much lower.

In forested areas little variation in brightness occurs with increasing snow depth. In deciduous forest, all snow depths greater than about one to two inches appear approximately the same tone of gray. Thus, although satellite photography can distinguish snow covered forests, it can give little information on snow depths in the forest. Likewise, since mountain snow depths are normally much greater than four inches, little snow depth information can be derived there.

Brightness Level	Snow Depth (inches)								
	0	T	1	2	3	4	5	6	>6
Dark	▨								
Gray			▨						
Bright						▨			

Figure 2-49 Relationship between snow brightness on satellite imaging and snow depth for non-forested area.

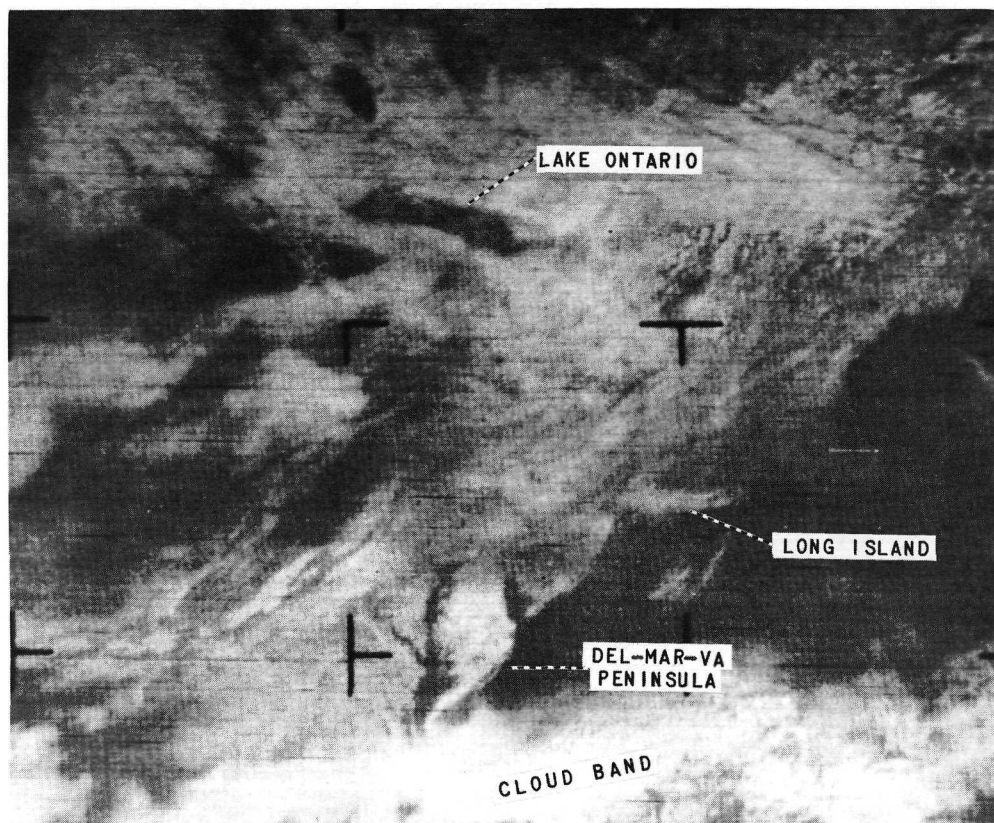


Figure 2-50 Nimbus 2 APT picture of the eastern United States taken on orbit 3333, 20 January 1967.

Since reflectances from snow covered forests decrease as tree density increases, areas of dense coniferous forest cover, such as the Adirondacks in New York, are distinctly identified during winter. In a study based on reflectance variations, Aldrich et al (1969) established a 30% tree density boundary across Canada from satellite APT pictures (Figure 2-51). In another study, Kuusela and Poso (1970) of the Forest Research Institute of Finland used an ESSA 8 satellite APT picture (similar to a Nimbus AVCS) to relate, by a regression equation, gray tones of snow covered forest areas to the volume of growing timber as obtained from a forest inventory of Finland. A high correlation coefficient of 0.84 indicates that in the presence of snow cover, a satellite picture can be used to estimate timber volumes. Of course, control measurements in the field are necessary for reliability. Nimbus provides excellent pictures of snow-covered forest land which can be used for similar studies in other parts of the world. For example, in Figures 2-52 and 2-53, showing snow-covered Alaska and Siberia, the gray tones correlate well with the distribution and density of forested areas.

2.5.2.3 Mapping Snow Cover

Cloud-free areas with a continuous brightness distinctively greater than the normal dark background, can be mapped as being snow covered. As reported in the Barnes and Bowley studies, the snow line enclosing such areas will normally represent the limit of a snow accumulation of one inch or more in relatively flat terrain. In mountainous regions, because of the roughness of the terrain and the rapid build-up of snow with elevation, the snow line probably represents an accumulation of several inches. In flat terrain snow lines can be positioned with an accuracy of ± 10 n.mi. In mountainous terrain, where landmarks can often be used to establish geographic referencing more accurately than is possible in flat terrain, the snow line can be monitored with an accuracy well within 10 n.mi.

Snow cover in selected mountain river basins has been accurately mapped from meteorological satellite imagery (Barnes and Bowley, 1970). For the river basins of the southern Sierras the percent snow cover of basins was mapped with an accuracy to within $\pm 5\%$ of that obtained from aerial survey observations. Moreover, the rates of snow decrease in these basins derived from ESSA and Nimbus pictures were very similar to those derived from the aerial survey data.

In a pilot study, as yet unpublished, conducted by Salomonson of NASA/LMES, and Barnes of ARA, Nimbus IDCS pictures were also used to demonstrate the feasibility of relating satellite-viewed snow cover to basin runoff. Figure 2-54 shows the seasonal area extent of snow cover in the Himalaya Mountains as depicted by Nimbus 3 IDCS. These photographs were used to measure the snow cover extent in the Indus River watershed; Figure 2-55 shows that this snow cover correlates

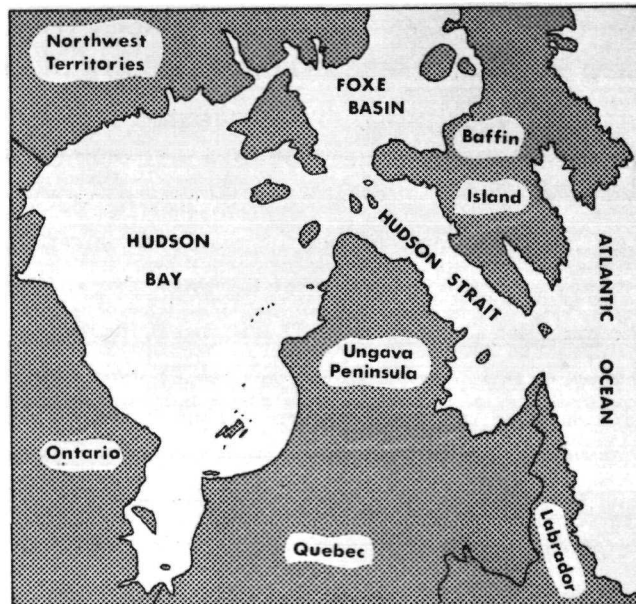
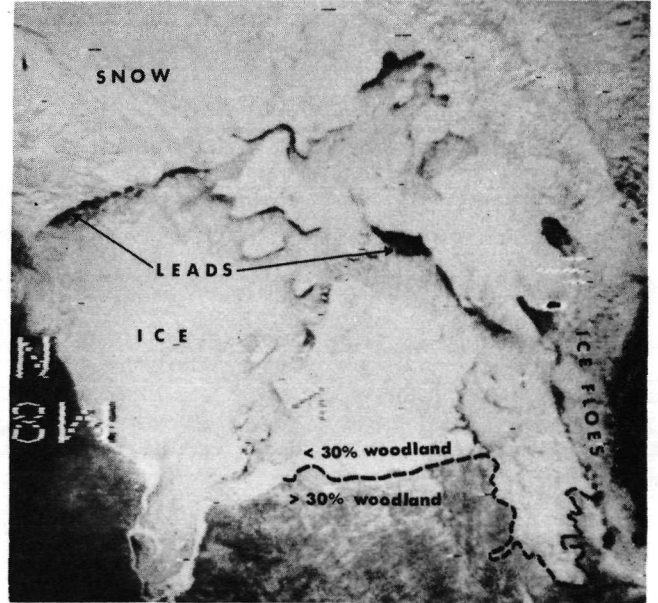
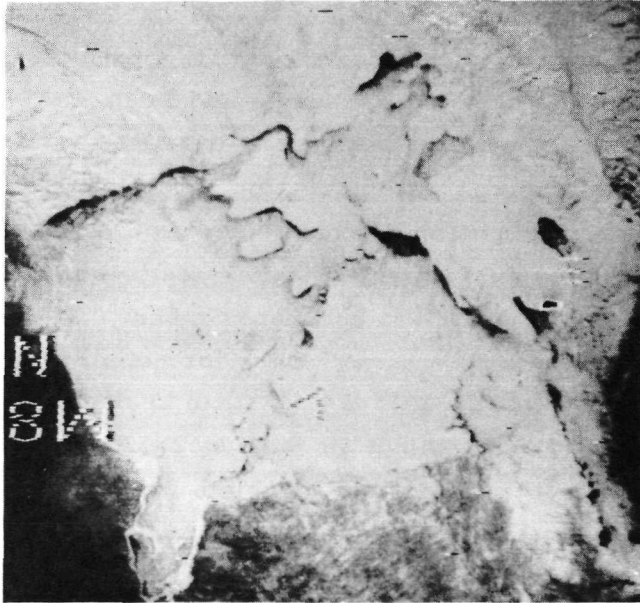


Figure 2-51 Nimbus 3 IDCS observation of the Hudson Bay area showing a vegetation boundary accentuated by snow cover, taken on orbit 219, 30 April 1969.

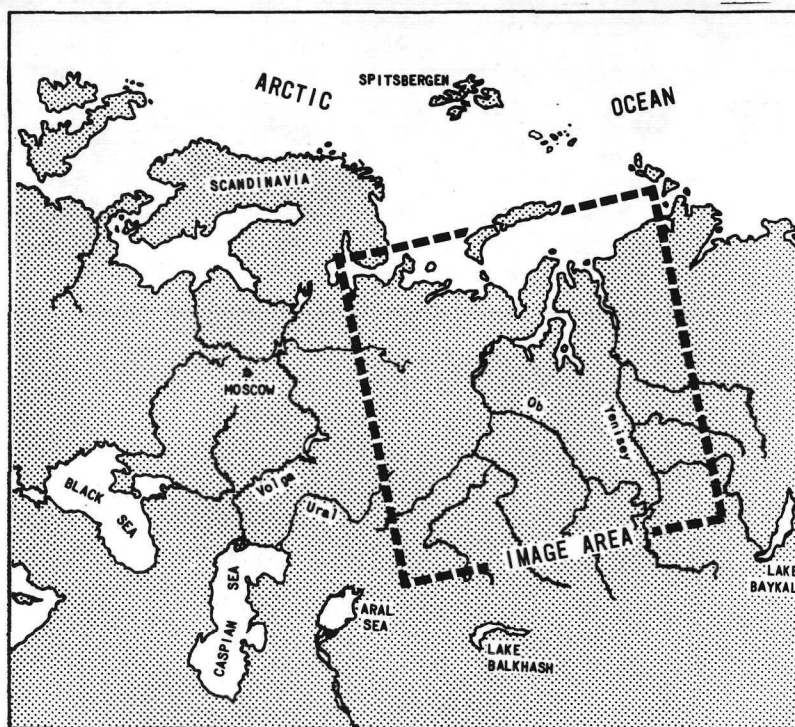
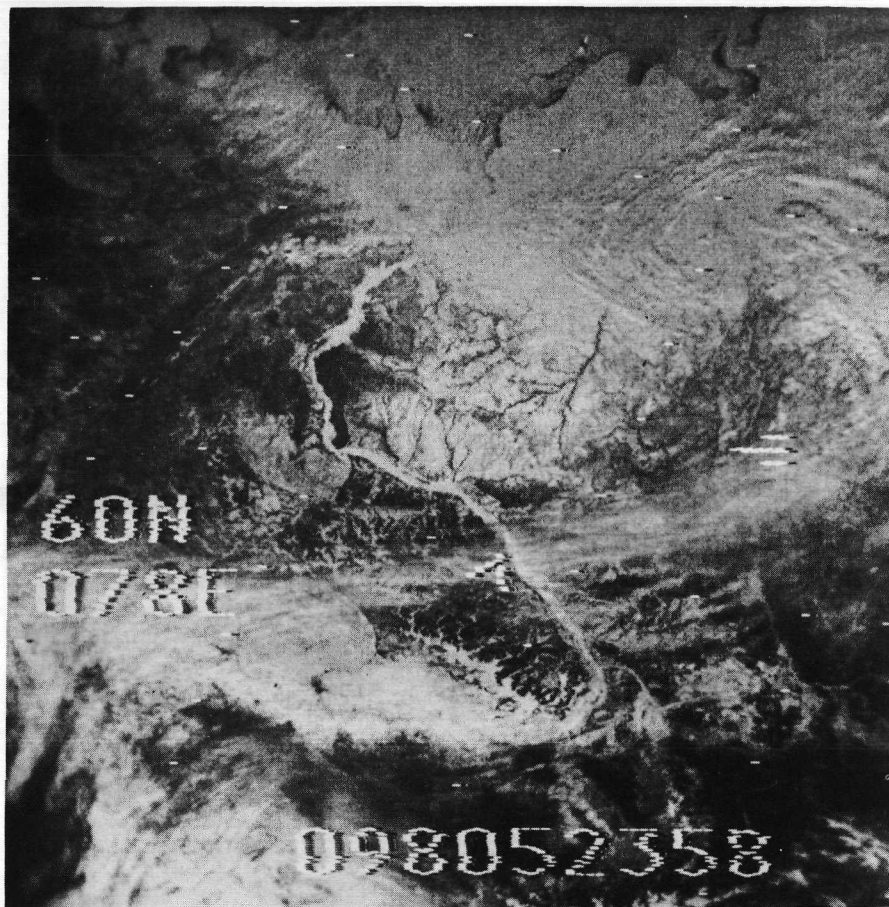


Figure 2-52 Nimbus 4 IDCS observation of snow and ice over Siberia and the Arctic Ocean, taken on orbit 4900, 8 April 1971.

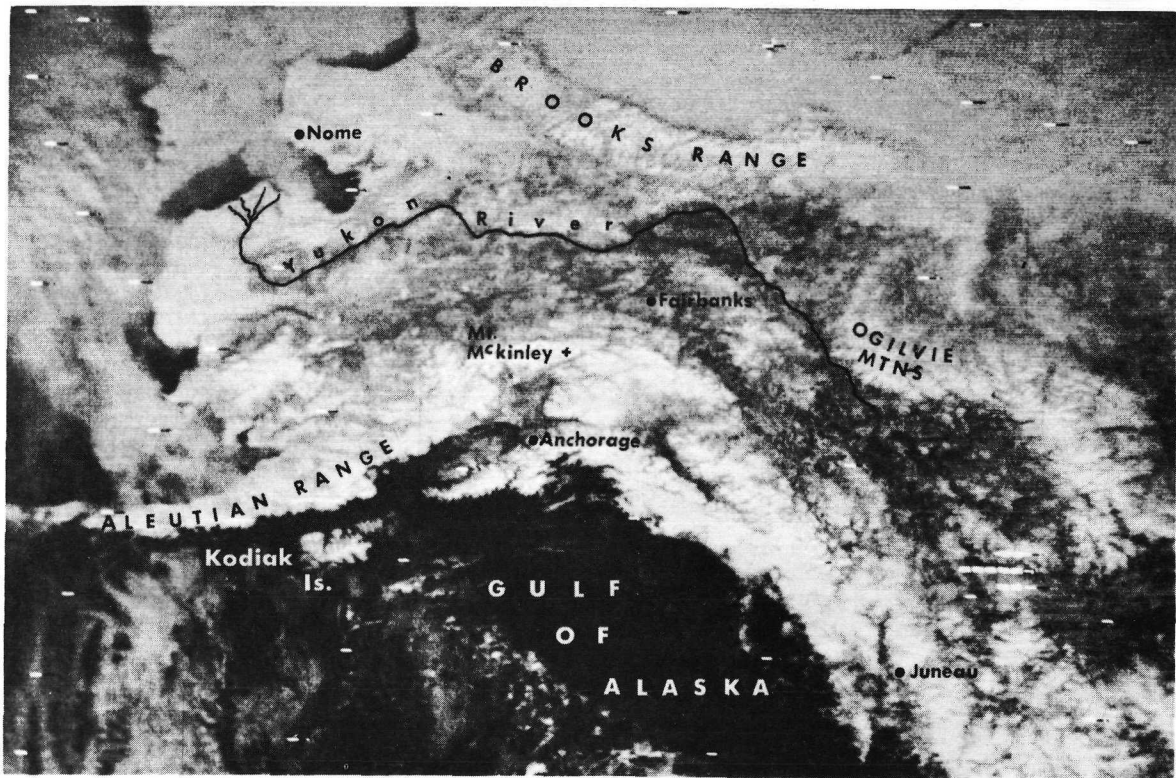
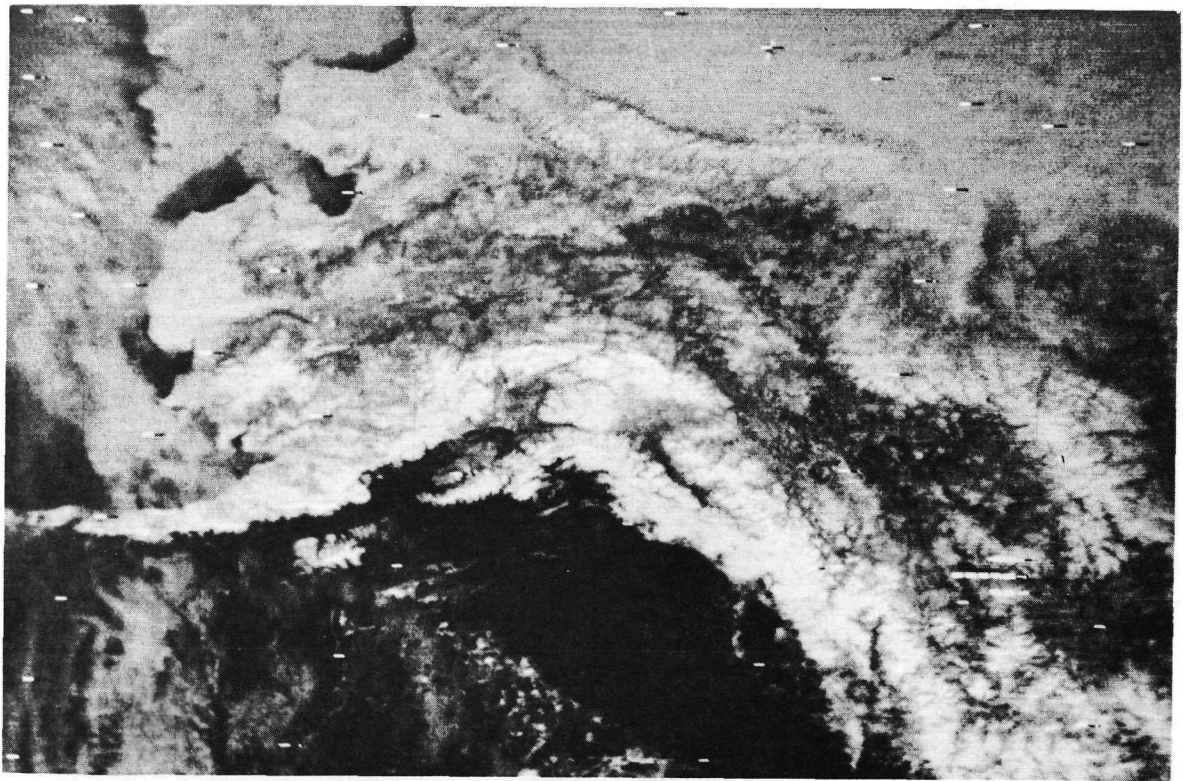
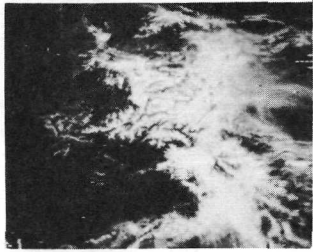
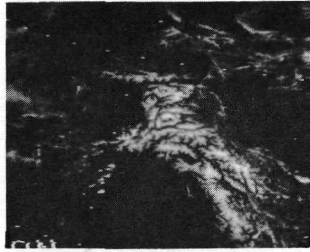


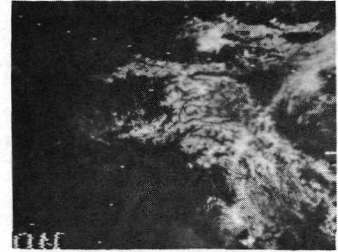
Figure 2-53 Nimbus 4 IDCS observation of snow and ice over Alaska and the Bering Straits area, taken on orbit 4774, 29 March 1971.



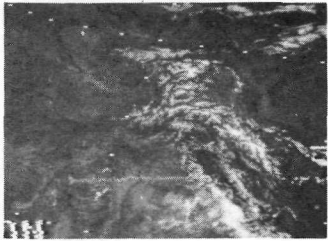
Orbit 187
28 April 1969



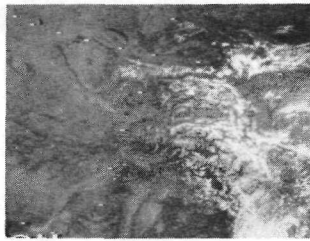
Orbit 616
30 May 1969



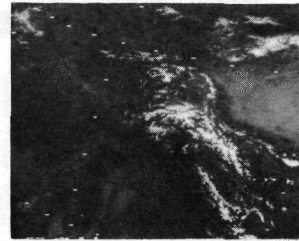
Orbit 911
21 June 1969



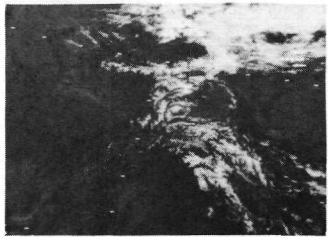
Orbit 1273
18 July 1969



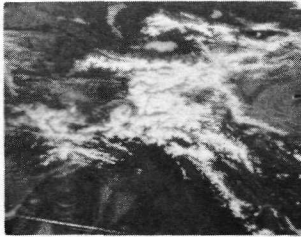
Orbit 1769
24 August 1969



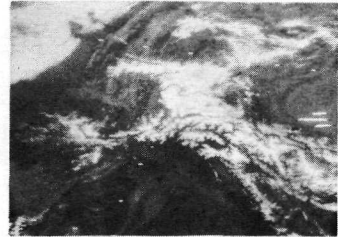
Orbit 2104
18 September 1969



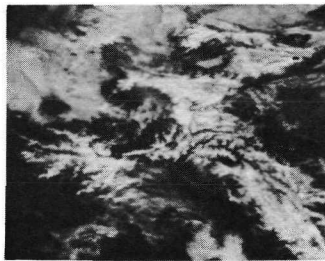
Orbit 2426
12 October 1969



Orbit 3056
28 November 1969



Orbit 3351
20 December 1969



Orbit 3780
21 January 1970



Figure 2-54 Seasonal area extent of snow cover in the Himalayas as recorded by Nimbus 3 IDCS.

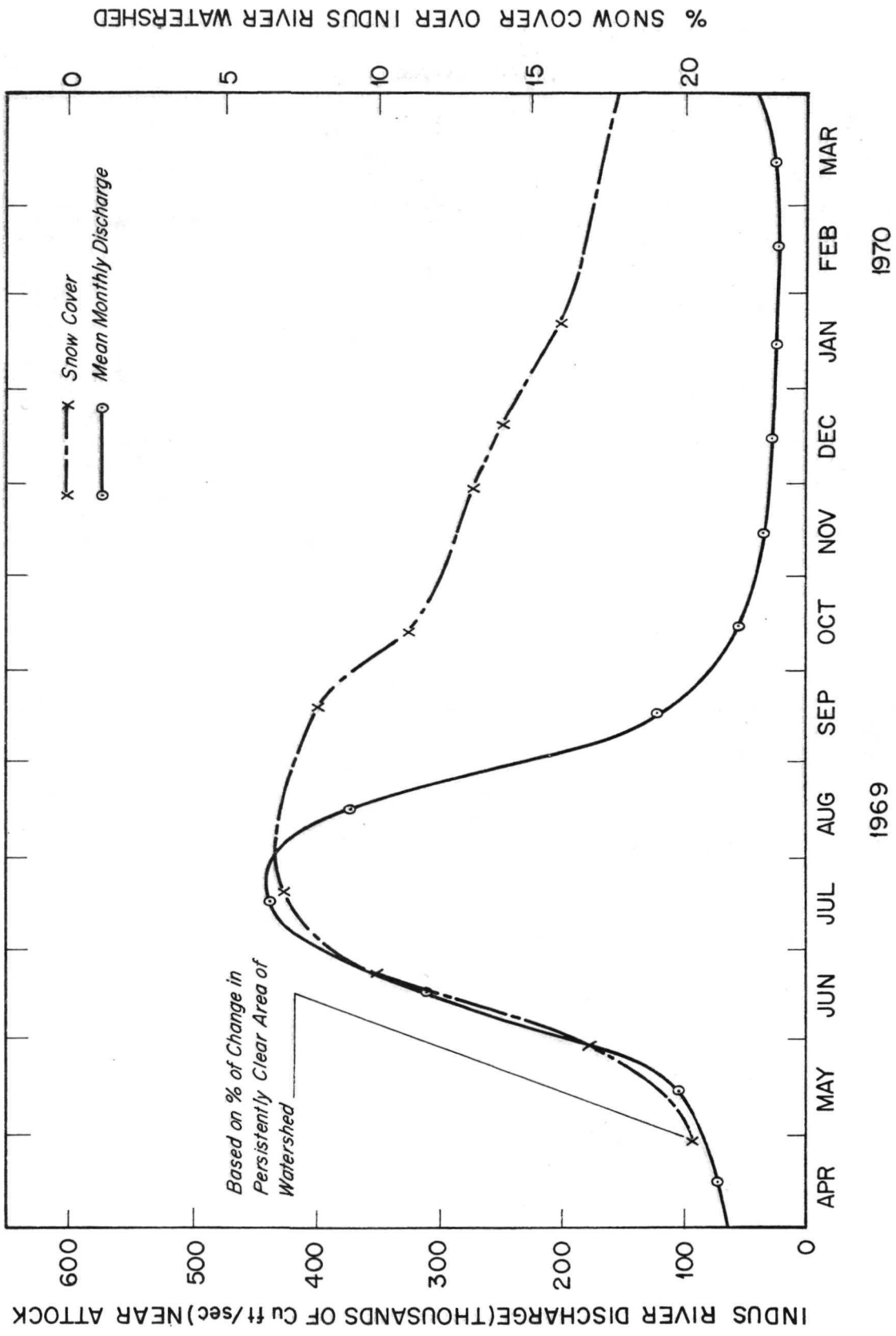


Figure 2-55 Snow cover extent over the Indus River watershed from April 1969 to March 1970 compared with the mean monthly discharge of the Indus River near Attock, northern West Pakistan.

well with the Indus River discharge rates. Another study by Barnes and Palgen (1971) discusses the use of satellite data, including Nimbus, for predicting Mekong River floods by measuring snow cover in the Upper Mekong River Basin.

An automated technique to determine snow-covered areas in satellite pictures has also been developed (McClain and Baker, 1969). For a selected time interval (usually five days), the lowest reflectance value for each data point is stored in a computer. Upon command, an array of these values is displayed as a Composite Minimum Brightness (CMB) Chart. Snow and ice boundaries are readily apparent as the transient cloud patterns are eliminated by this procedure.

2.5.2.4 Application of HRIR and THIR Data to Snow Mapping

Snow surface temperatures, a significant parameter for predicting snow-melt, can also be measured from Nimbus infrared sensors. Furthermore, since snow reflects a large amount of incident solar radiation during daytime, a snow-covered surface will presumably be colder than adjacent non-snow-covered terrain. It should be possible, therefore, to map snow boundaries from THIR and HRIR window channel (10.5 to 12.5 μm and 3.4 to 4.2 μm) measurements. Although studies to determine the utility of these data in snow hydrology are in progress, at present there are no published results of such applications. In the future, in addition to visual and infrared measurements, microwave sensors (see Appendix A) may provide quantitative snow depth information.

In the study by Barnes and Bowley (1970), a sample of Nimbus 3 daytime HRIR (0.7 to 1.3 μm) data in the pictorial format was also examined to determine whether mountain snow could be detected. Because of the lack of complete coverage over the western United States and problems with noisy data, the sample available was rather limited. The results indicated, however, that whereas water bodies, such as Great Salt Lake, Salton Sea, and Lake Tahoe, could be easily identified, mountain-snow patterns were essentially undetectable. In the daytime HRIR data, therefore, contrast between snow and bare ground is apparently less than the contrast between water and ground.

Although other characteristics of the systems undoubtedly have some influence, the major influence on the detection of snow and water appears to be the difference in the spectral intervals of the Nimbus 3 daytime HRIR sensor and IDCS camera. In the IDCS pictures contrast between snow and ground is very high, but water bodies are difficult to detect. Thus, it appears that camera systems with a peak spectral response at about 0.5 to 0.7 μm are the most useful for snow detection. Sensors with a peak response at slightly longer wavelengths (0.7 to 1.3 μm), although not as good for snow detection, may be more useful for hydrologic purposes such as flood surveillance.

In another study, Pouquet (1969a) found that the Nimbus 3 daytime HRIR sometimes reveals a "peculiar" dark reflectance for surfaces that show up white (snow covered) in the visible IDCS pictures. One such occurrence is in an April 1969 daytime HRIR photofacsimile covering the Sierra Nevada of the southwestern United States. Pouquet explains the low near-infrared reflectances of snow, hence the darker shades on the photofacsimile, by the presence of melted waters on the snow surface.

2.5.3 Lake Surveillance Studies

2.5.3.1 Surface Temperature of Lakes

Surface temperature patterns of large lakes such as the Great Lakes, and average surface temperatures of smaller lakes, can be obtained from Nimbus HRIR and THIR. These values have many uses, one of which is the estimation of evaporation rates. Spatial and seasonal variations of surface temperatures provide a guide to different biological zones; these zones may then be used to infer the distribution of fish. Furthermore, successive maps of lake surface temperatures may yield information on water currents and the lake's general circulation. This information is needed for an understanding of lake dynamics, and is especially critical in combatting water pollution.

Although Nimbus data have not been used extensively for lake surface temperature studies, investigators have presented maps showing the surface temperatures of Lake Michigan (Strong, 1967; Sabatini and Sissala, 1968; Warnecke et al, 1969; Noble and Wilkerson, 1970). All point out the difficulties of analyzing the HRIR temperature fields for the relatively small area of Lake Michigan. The main difficulties are noise and misplacement of data by the mapping program. Noise in the data can be attenuated by passing the data through filter programs (see Appendix C), but the misplacement of data is inherent in the way the mapping program positions each scan line. During the mapping program, the center of each scan is determined from the occurrence of the horizon on either side. Uncertainties in the definition of the actual horizon cause errors in the location of the scan on the order of 10 km. These location errors are most evident at temperature discontinuities outlining coastlines normal or nearly normal to the scan. Thus the meanders in the apparent position of the coastline of Lake Michigan (see Figure C-3, Appendix C) are thought to be caused by this mapping error. The noise and location errors can be attenuated by choosing a map size of 1:2,000,000 or smaller and/or by judicious smoothing of the isotherms.

In spite of these difficulties, meaningful surface temperature patterns of relatively large lakes can be derived from Nimbus HRIR. Strong (1967) discusses

Lake Michigan, and an example for this same lake (Sabatini, 1971) is shown in Figure 2-56. (Temperatures in this example have not been corrected for noise or atmospheric effects.) A plot of the average temperatures from Nimbus 2 HRIR is compared with averages from ship observations and an airborne radiation thermometer (ART)* in Figure 2-57. The Nimbus derived temperatures consistently averaged 2° to 4°K colder than the other observations; atmospheric absorption effects probably explain the differences. For actual comparison of areal distribution, the 18 October 1966 ART temperature map from Noble and Wilkerson (1970) is presented in Figure 2-58 to be used with the HRIR map of 25 October 1966 (Figure 2-56). Both maps show relatively warmer temperatures near the eastern shore and colder temperatures on the western shore.

Figure 2-59 is another example of lake surface temperatures derived from Nimbus 2 HRIR (Sabatini and Sissala, 1968) showing the western section of Lake Erie, a lake where the ever increasing eutrophication is of great concern. Temperature maps such as this will help establish circulation patterns and may eventually be used to identify areas of thermal pollution.

2.5.3.2 Lake Conditions

Continuous surveillance of lake ice conditions, important for navigation, is possible by means of satellite observation. The National Weather Service is operationally using satellite photographs to monitor ice conditions on the Great Lakes, and issues periodic ice maps derived from satellite photographs.

Ferguson et al (1969) have utilized ESSA and Nimbus APT to monitor ice conditions in Canadian lakes. Satellite photographs of large lakes show day to day changes in the ice cover during breakup (see, for example, Figure 2-60). Smaller lakes merely show a condition of "all ice" or "no ice." These investigators found good agreement between satellite and surface observation of ice breakup, but freezeup dates from satellite observations averaged about 10 days later than the conventional dates. They believe that in many cases black ice** forming first on the lake surface cannot be distinguished from water in satellite photographs, and that the apparent freezeup is actually the first snow covering on top of the ice.

*The ship observation averages were obtained from weekly and biweekly average temperature maps compiled by the Great Lakes Research Division of the University of Michigan (Strong, 1969 personal communication). The ART measurements were obtained from temperature maps presented by Noble and Wilkerson (1970).

** Thin, new ice on fresh or salt water, appearing dark in color because of its transparency.

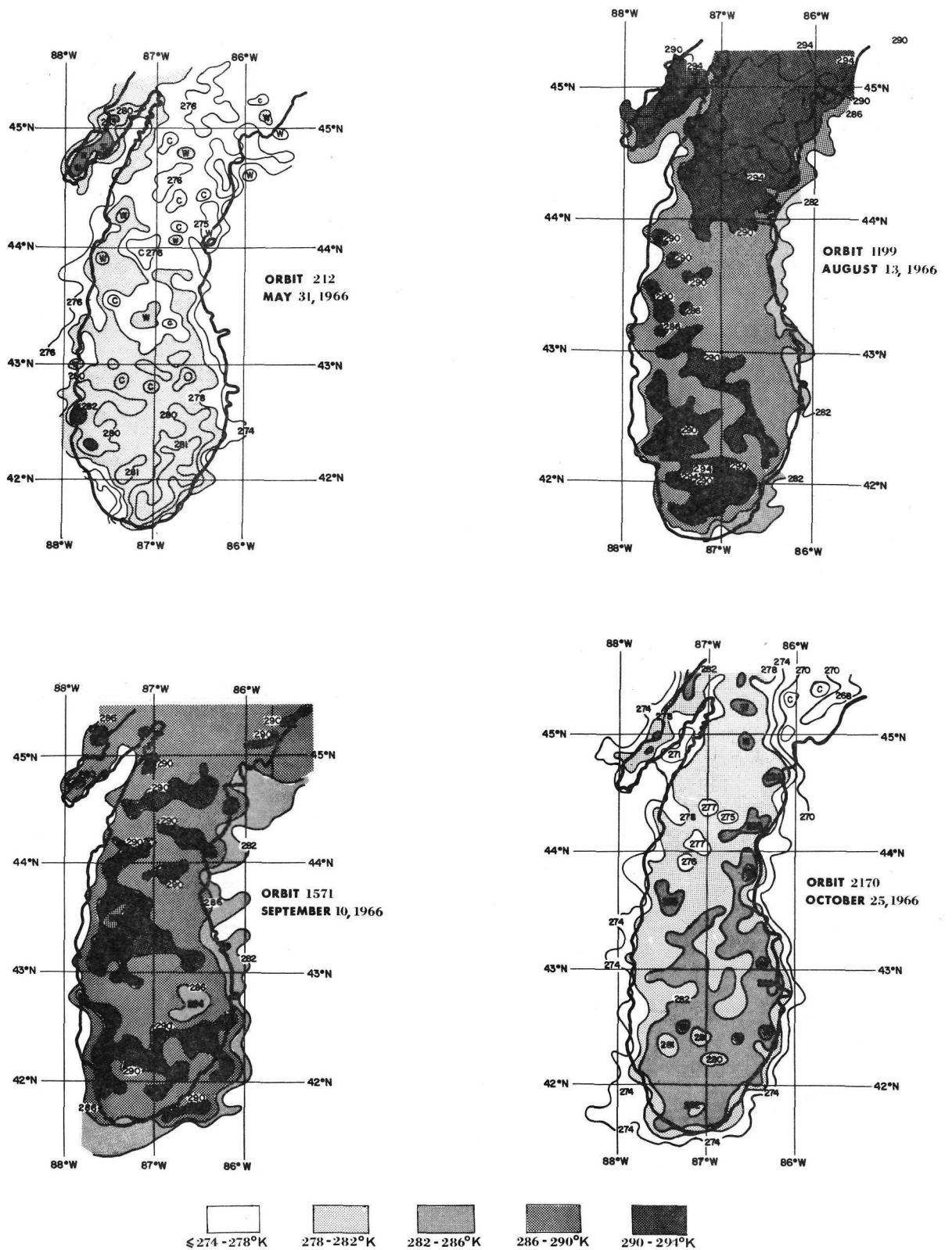


Figure 2-56 Nimbus 2 HRIR temperature maps of Lake Michigan derived from digitized data.

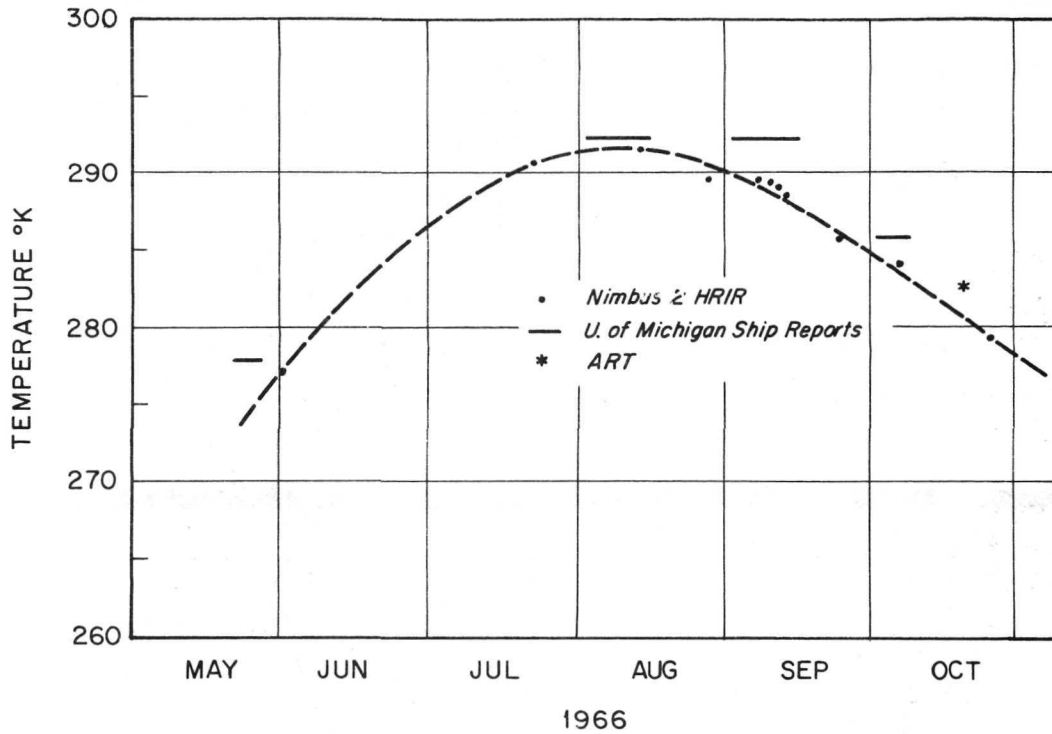


Figure 2-57 Comparison of average temperatures of Lake Michigan obtained from Nimbus 2 HRIR, ship reports compiled by the University of Michigan and infrared airborne radiometer thermometer flights.

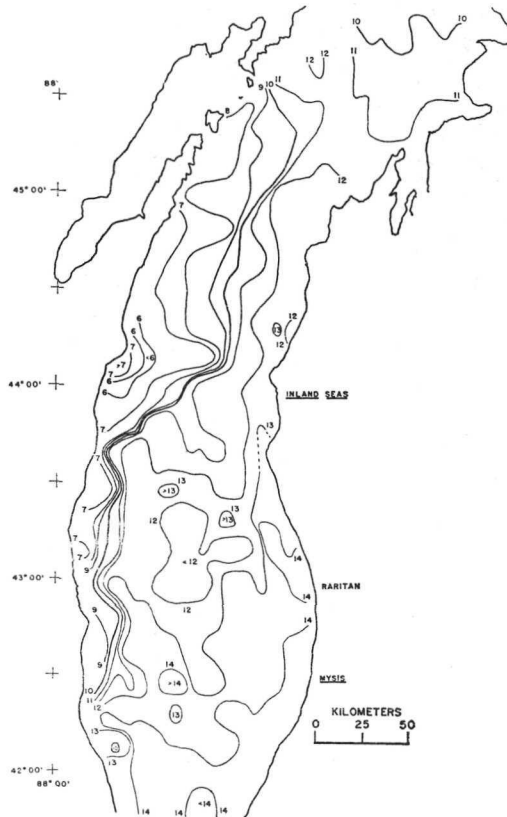


Figure 2-58 Surface temperatures of Lake Michigan from an infrared airborne radiometer thermometer flight, 18 October 1966. (Noble and Wilkerson, 1970)

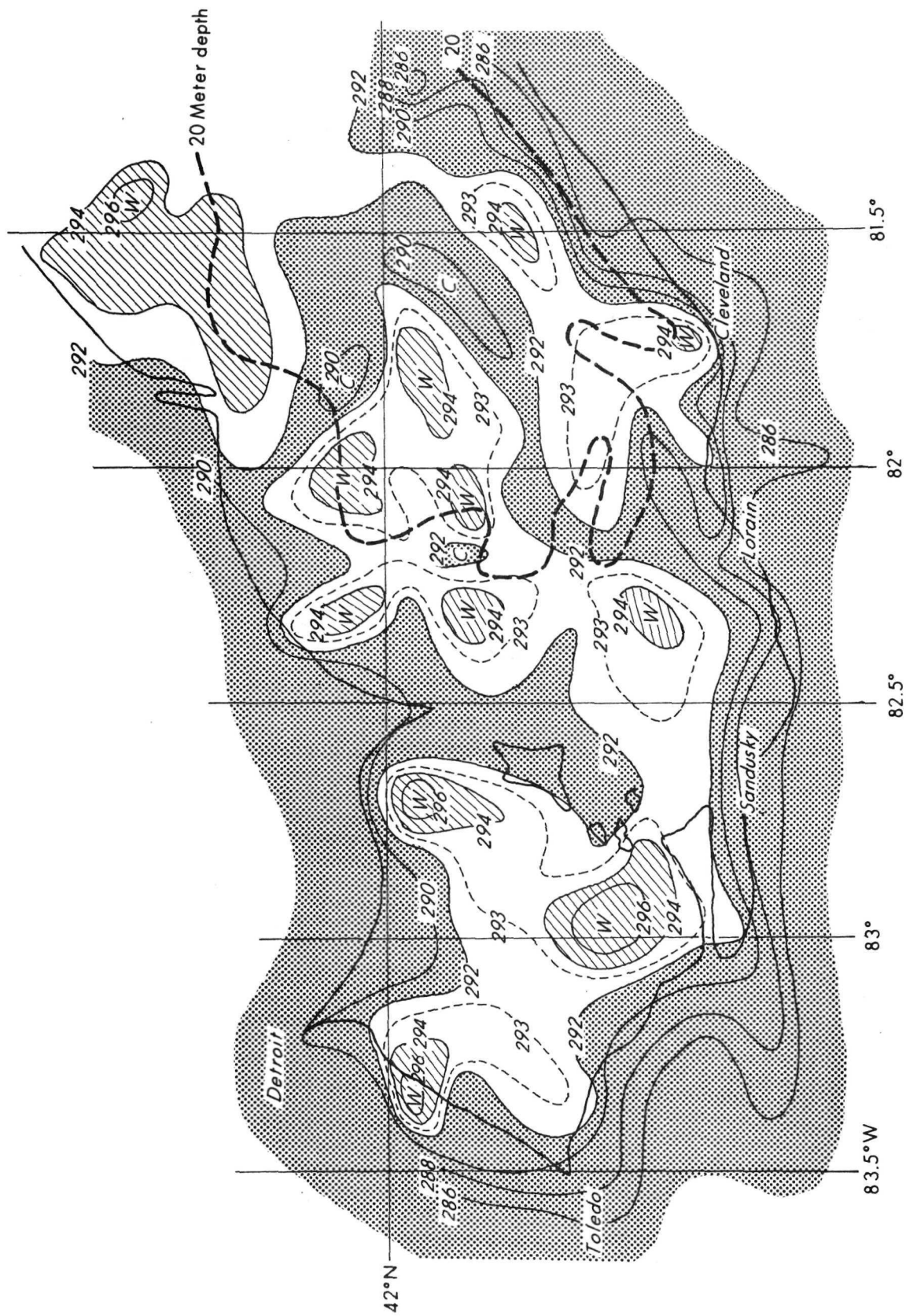
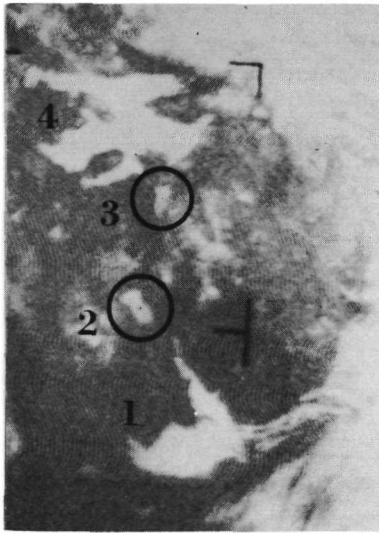
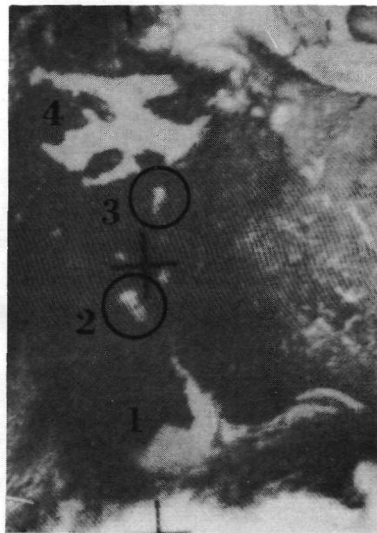


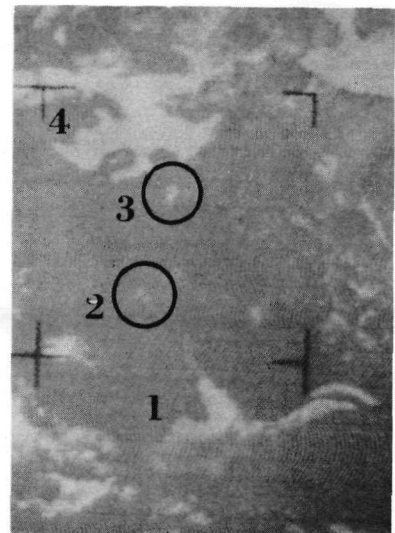
Figure 2-59 Portion of an analysis of Lake Erie surface temperatures based on digitized Nimbus 2 nighttime HRIR data taken on orbit 1290, 20 August 1966.



Orbit 219
31 May 1966



Orbit 272
4 June 1966



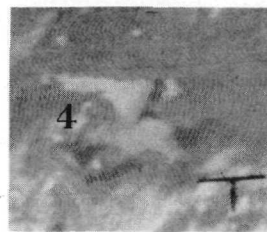
Orbit 392
13 June 1966



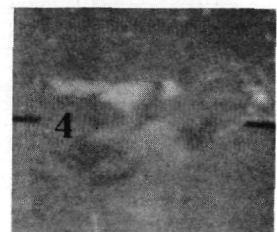
Orbit 538
24 June 1966



Orbit 592
28 June 1966



Orbit 618
30 June 1966



Orbit 645
2 July 1966

ICE MELT OF 4 LAKES IN NORTHERN CANADA MONITORED BY THE NIMBUS 2 APT SYSTEM
DURING THE SPRING OF 1966.

LAKES: 1. GREAT SLAVE LAKE 2. LAC LA MARTRE 3. HOTTAH LAKE 4. GREAT BEAR LAKE

Figure 2-60 Ice melt conditions of four lakes in northern Canada as observed by Nimbus 2 APT system during the 1966 breakup period.

The authors further hope to relate the time of freezeup to lake depths and eventually estimate unsurveyed lake depths using satellite data.

2.5.3.3 Man-Made Lakes

The resolution of the Nimbus sensors permits gross area or temperature surveys of only the largest man-made lakes. The accidental low orbit of Nimbus 1 (perigee of 423 km) provided resolutions that adequately measured the areal extent of the large Fort Peck Reservoir in Montana (Figure 2-61, Ackermann and Rabchevsky, 1971); in fact, the 360 sq. mi. area derived from the AVCS image compares favorably with the area derived from a U. S. Geological Survey map (340 sq. mi.).

Nimbus imagery has shown the effect of the Aswan High Dam on the Nile River (Figure 2-62). A Nimbus picture taken in September 1964 while the Aswan High Dam was under construction shows no evidence of Lake Nasser, but five years later, Lake Nasser is clearly visible in the September 1969 Nimbus 3 day-time data.

Even the gross resolutions of the Nimbus HRIR and THIR may yield the surface temperature regime and local climatology of large man-made lakes such as Lake Volta (Figure 2-63), Lake Nasser (Figure 2-62), or Lake Kariba in the Okavango Basin of South Africa (Figure 2-64, Ackermann and Rabchevsky, 1970). The temperature information may be utilized to calculate evaporation rates, an important term of the hydrological budget of these lakes, especially when the lakes are in arid or semiarid regions.

2.5.3.4 Intermittent Lakes and Playas

Neal (1968) has used Nimbus 1 AVCS pictures to study the surface conditions of intermittent lakes and playas. Playas (or salinas), situated in arid regions of the world, are useful as indicators of the hydrologic environment. Reflectance changes indicating soil moisture variations of playa surfaces have been observed in Nimbus 1 AVCS imagery since the reflectance of the hard, dry clay crust typical of playas is reduced by 20 to 30% when moistened. In addition, the increased moisture content increases the thermal property of the surface and, therefore, playa moisture changes can be monitored by nocturnal temperature variations measurable by the HRIR and THIR radiometers.

Figure 2-65 from Neal (1968), taken over northwestern Nevada, shows a variety of playa surface conditions ranging from hard, dry crusts (locations 2, 3, 6, 7, 16, and 19) to soft, dry, friable surfaces (locations 5, 8, 10, 14, and 15). The latter frequently contain moist surfaces with accumulations of salt (see, for

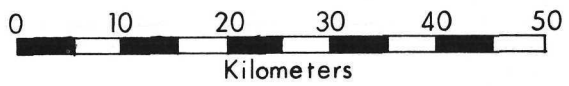
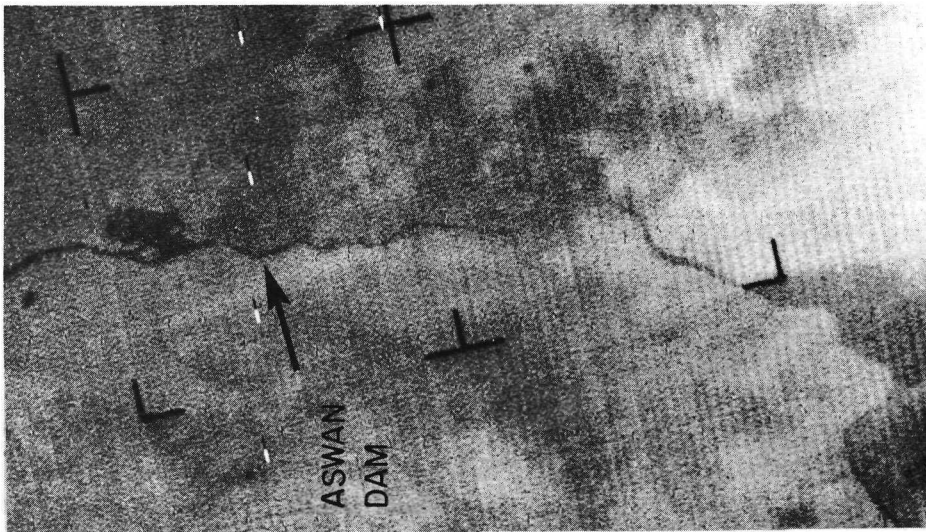
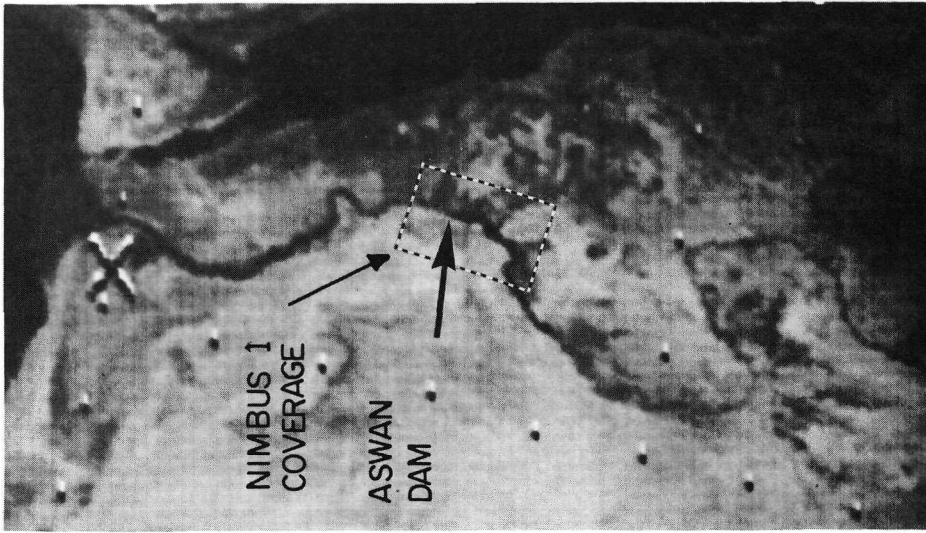
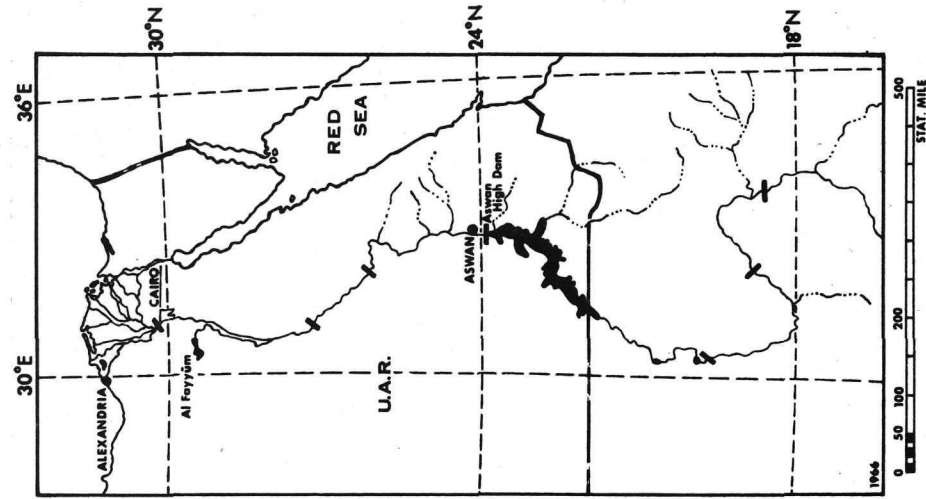


Figure 2-61 Fort Peck Reservoir, Montana as viewed by Nimbus 1 AVCS photograph taken on orbit 299, 17 September 1964.



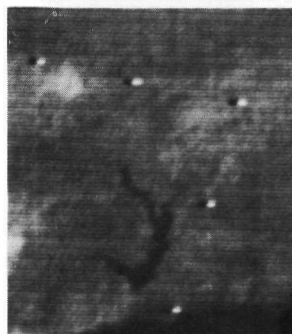
Nimbus 1 AVCS
Orbit 279, 16 September 1964



Nimbus 3 daytime HRIR
Orbit 2012, 11 September 1969

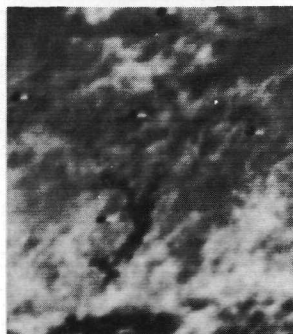
Figure 2--62 Growth of Lake Nasser formed by the Aswan High Dam on the Nile River as recorded by Nimbus imagery.

Orbit 619



30 MAY

Orbit 1343



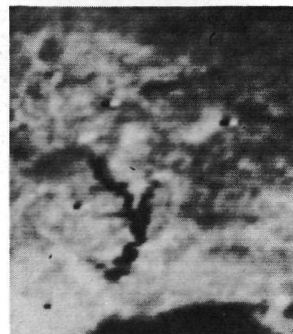
23 JUL - CLOUDINESS SIGNIFIES THE ADVANCE OF THE ITC (INTERTROPICAL CONVERGENCE) AND THE RAINY SEASON

Orbit 1705



19 AUG - INCREASED CLOUDCOVER AND CONVECTION CONTRIBUTES TO THE 20-40 INCH RAINFALL

Orbit 1772



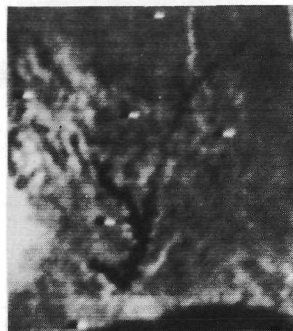
24 AUG - WITH VERY LITTLE CONVECTION OVER THE WATER, L. VOLTA CAN BE SEEN THROUGH THE ELSEWHERE HEAVY CLOUDCOVER

Orbit 2040



13 SEP - PEAK OF RAINY SEASON

Orbit 2295



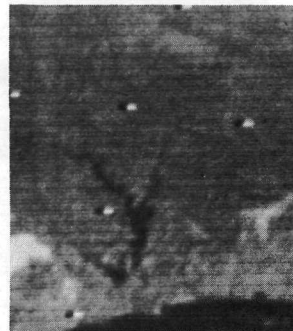
2 OCT - LARGELY FLOODED, THE RIVER SYSTEM BECOMES MORE DISTINCT AS COMPARED TO THE 30 MAY PHOTO

Orbit 2496



17 OCT - LESS CLOUDINESS SIGNIFIES THE END OF THE RAINY SEASON

Orbit 2925



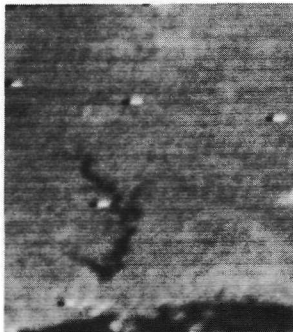
18 NOV - WITH THE ITC MIGRATED, THE DRIER PARTS OF THE TRADES TAKE OVER

Orbit 2992



23 NOV - SUBTROPICAL ANTICYCLONES NOW DOMINATE THE LAKE VOLTA REGION

Orbit 3059



28 NOV - WITH LESS CONVECTION IN THE ATMOSPHERE DROUGHT-LIKE CONDITIONS EXIST

Orbit 3421



25 DEC - A CLOUDFREE DAY DURING THE WINTER OF LAKE VOLTA

Orbit 3555



4 JAN - NEARING END OF DRY SEASON

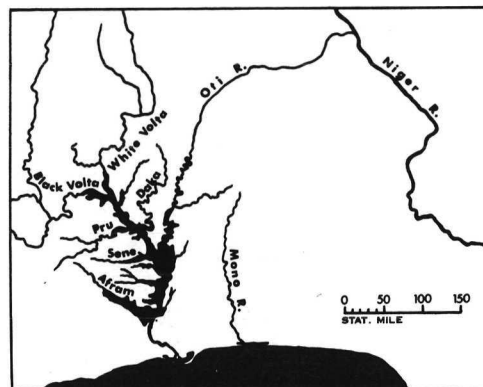
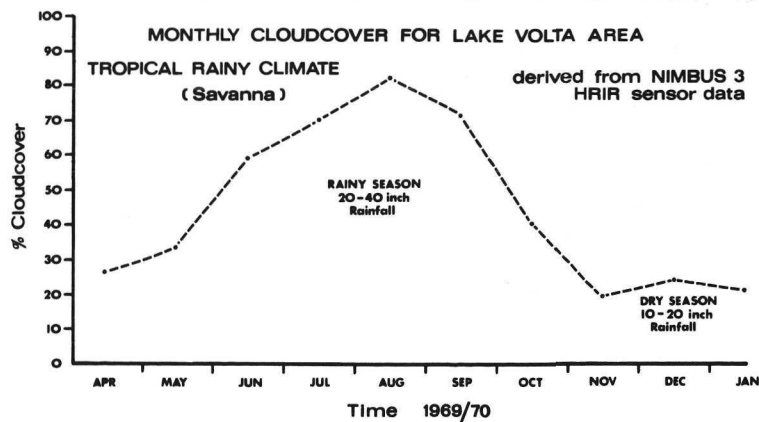
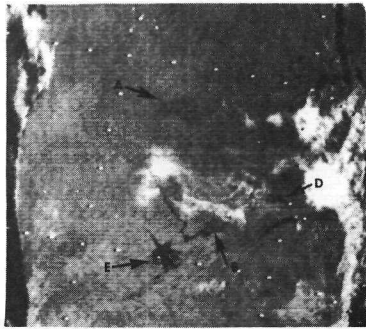


Figure 2-63 Monitoring of Lake Volta, Africa by Nimbus 3 daytime HRIR

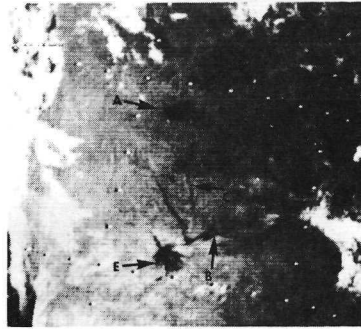
END OF DRY SEASON, CLOUDCOVER INCREASES FROM DAY TO DAY



Orbit 1329
22 July 1969

DRY SEASON, LUETE R. AND NYENGO SWAMPS ALMOST INDISTINCT

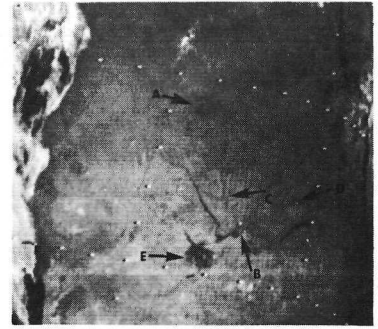
SHORT SECONDARY RAINSEASON SHOWS TERRESTRIAL CHANGES



Orbit 1758
23 August 1969

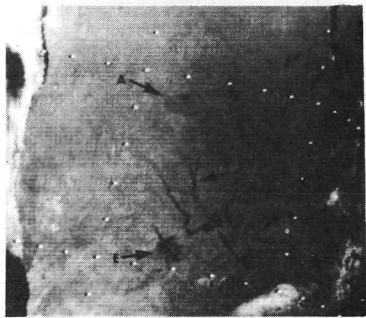
NEAR PEAK OF PRIMARY RAINY SEASON, AREA IS PARTLY CLOUDCOVERED

DRY SEASON ONCE AGAIN, RIVER SYSTEM BECOMES LESS DISTINCT



Orbit 1986
9 September 1969

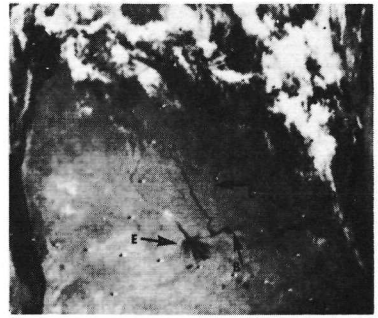
THE OKAVANGO BASIN AFTER FIRST NOTABLE PRECIPITATION



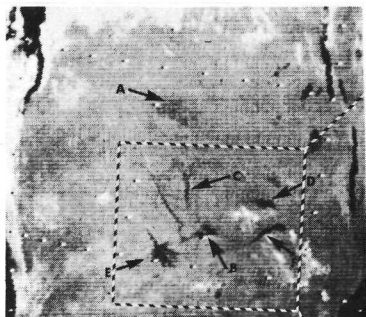
Orbit 900
20 June 1969



Orbit 2911
17 November 1969

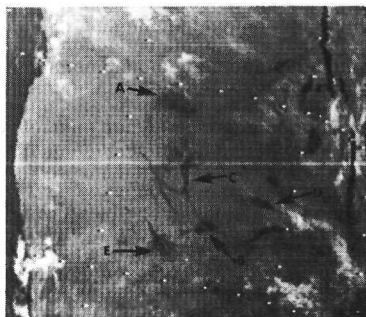


Orbit 2415
11 October 1969

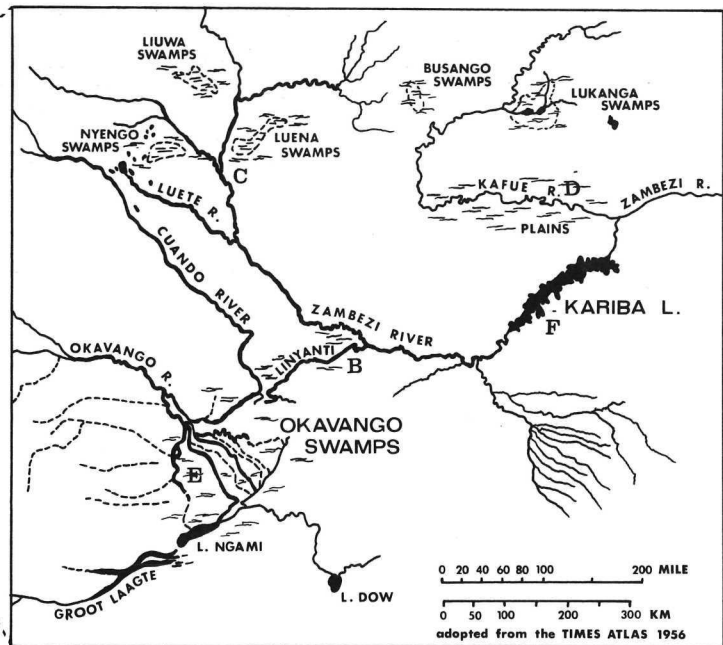


Orbit 538
24 May 1969

FLOODED CONDITIONS DURING SECONDARY RAIN MAX.



Orbit 176
27 April 1969



A = an area located in eastern Angola near the source of the Zambezi River

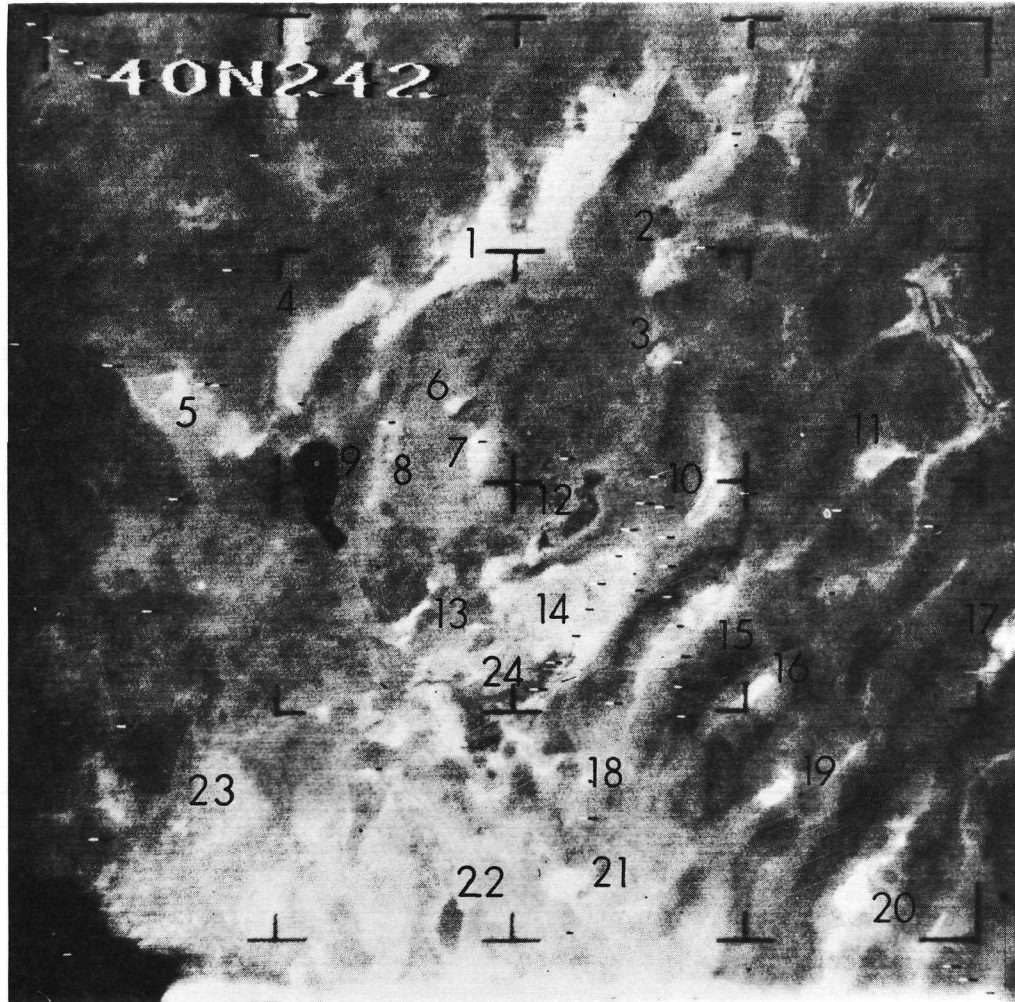
B - F are shown on the map above

Figure 2-64 Monitoring of the Okavango Basin, Africa by Nimbus 3 daytime HRIR

example, the central portion of the Humboldt Salt Marsh, point 15 on Figure 2-65). Without prior knowledge of surface conditions, it would be difficult to identify the type of surface that exists on these playas. For example, the gray-tone level of the hard, dry clay crust at Smith Creek Valley (point 19) is the same as the central salt core of the Humboldt Salt Marsh. However, it is known that these two playas change little from year to year, so that any pronounced change in the reflectance level of these surfaces would probably indicate a change in moisture, or surface flooding.

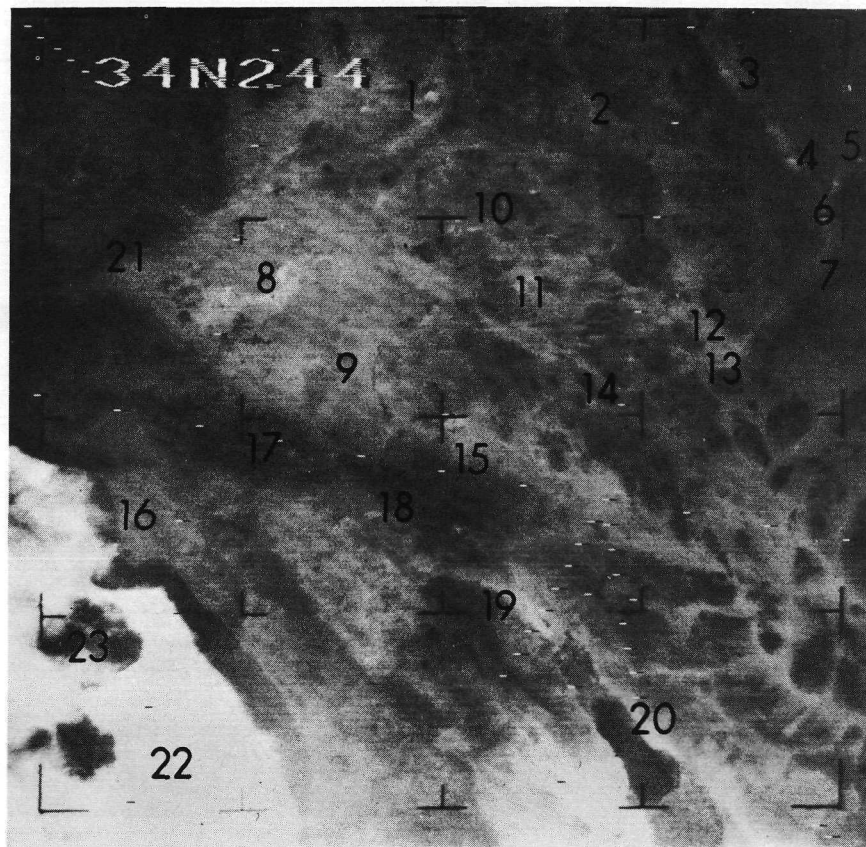
Neal (1968) also described two other Nimbus 1 AVCS photographs that contain playas. On Figure 2-66 the low contrast between lake beds and the surrounding terrain in the Mojave Desert makes the lake beds difficult to see. The increase in average regional albedo from Figure 2-65 to Figure 2-66 is due to the lesser overall relief and to the sparser vegetation cover in the second picture. The relative position of playas, however, is easily located. Figure 2-67, taken over southern Iran, again shows the playas as the brightest terrain features with the highly reflective white zones indicating salt on the surface. Lavar Maidan (1) and Sirjan Kavir (playa) (7) contain mixed surfaces; the brightest zones are salt, and the adjacent lighter gray zones are clayey silts with lesser amounts of salt (Neal, 1968). Maidan-I-Gil (6) is a predominantly soft, dry, friable-surfaced playa and is considerably less reflective than the salt surfaces. Lavar Maidan, Daryacheh-I-Tasht and Daryacheh-I-Bakhtigan were photographed one year later on the Gemini 5 mission and are shown for comparison (Figures 2-68 and 2-69). Analysis of the reflectance levels of playa and its adjacent terrain on both the Gemini photographs and the AVCS image reveals that the Daryacheh-I-Bakhtigan and Daryacheh-I-Tasht were largely free of water in 1964 during the Nimbus 1 mission, whereas during the Gemini 5 mission they were largely flooded. The value of using the two contrasting types of data is apparent. Neal concludes that the utility of Nimbus 1 AVCS images in playa studies is limited, but that the images can provide considerable information when used with other data.

Figure 2-70 is an enlarged portion of a Nimbus 1 AVCS picture showing the Great Salt Lake area in Utah. The size of the Great Salt Lake varies from about 1000 to 1500 sq. mi. depending on the season (Greer, 1971); in this September 1964 view of the lake, the water level was at its yearly minimum, and the lake surface was calculated to be 1005 sq. mi. (Ackermann, 1971; personal communication). Surrounding the lake are many highly reflective salt flats and basins, some of which are covered when the lake reaches maximum water level in late winter or spring. This picture demonstrates the excellent resolution and gray scale dynamic range of the Nimbus 1 AVCS; Stansbury Spit, an arm of land 500 meters wide, is clearly visible at the southern end of the lake. Seasonal observations at this resolution can provide enough detail to monitor areal changes of this large Plei-



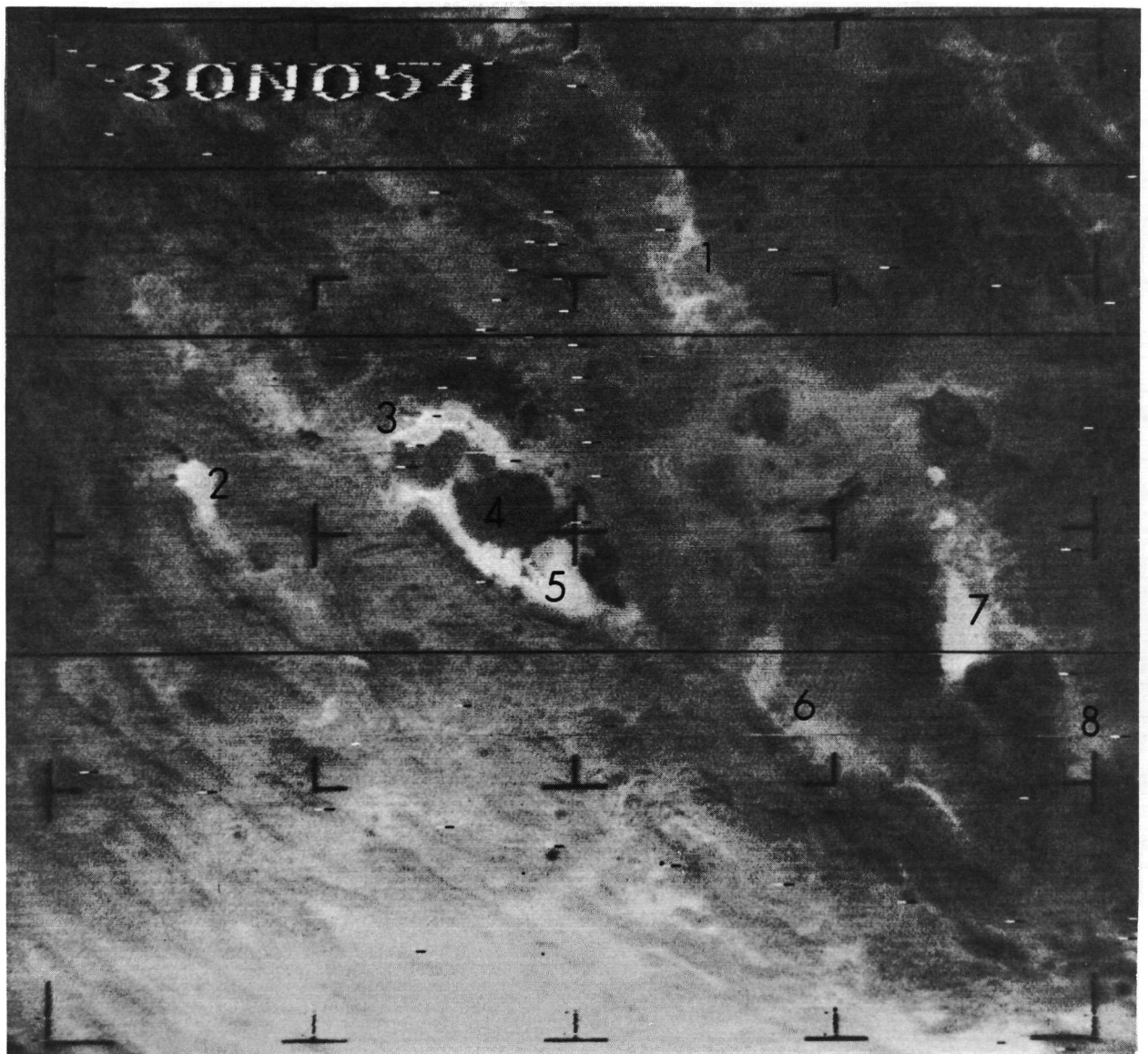
- | | |
|--|----------------------------------|
| 1 - Black Rock Desert (playa) | 13 - Brady Playa |
| 2 - Jungo Flats (playa) | 14 - Carson Sink (playa) |
| 3 - Pit-Taylor Reservoir (playa) | 15 - Humboldt Salt Marsh (playa) |
| 4 - Smoke Creek Desert (playa) | 16 - Edwards Creek Playa |
| 5 - Honey Lake Valley (2 playas) | 17 - Grass Playa |
| 6 - Bluewing Playa | 18 - Labou Flat (playa) |
| 7 - Adobe Flat (playa) | 19 - Smith Creek Playa |
| 8 - Winnemucca Lake (playa) | 20 - Big Smoky Playa |
| 9 - Pyramid Lake | 21 - Gabbs Playa |
| 10 - Buena Vista Playa | 22 - Walker Lake |
| 11 - Buffalo Playa | 23 - Lake Tahoe |
| 12 - Farmlands in lacustrine sediments | 24 - Marshland (dark gray area) |

Figure 2-65 Nimbus 1 AVCS image of northwestern Nevada showing good contrast separation between lake beds (white and light gray), alluvium (intermediate gray), forested mountains (dark gray), and lakes (black) taken on orbit 285, 16 September 1964. (Neal, 1968)



- | | |
|---------------------------------|--------------------------------------|
| 1 - Searles Lake (playa) | 13 - Devil's Playground (sand dunes) |
| 2 - Southern Death Valley | 14 - Lavic Playa (light) and |
| 3 - Pahrump Valley | Mt. Pisgah (dark) |
| 4 - Mesquite Playa | 15 - Lucerne Playa |
| 5 - Jean Playa | 16 - Los Angeles |
| 6 - Roach Playa | 17 - San Gabriel Mountains |
| 7 - Ivanpah Playa | 18 - San Bernardino Mountains |
| 8 - Rogers Playa | 19 - San Jacinto Mountains |
| 9 - El Mirage Playa | 20 - Salton Sea |
| 10 - Superior Valley Playas (3) | 21 - Tehachapi Mountains |
| 11 - Coyote Playa | 22 - Clouds over Pacific Ocean |
| 12 - Soda Playa | 23 - Open water, Pacific Ocean |

Figure 2-66 Nimbus 1 AVCS image of the Mojave Desert, California taken on orbit 285, 16 September 1964. V-shaped pattern at left center of image outlines the Garlock and San Andreas Faults. (Neal, 1968)



- | | |
|---------------------------------|-----------------------------------|
| 1 - Lavar Maidan (playa) | 5 - Daryacheh-I-Bakhtigan (playa) |
| 2 - Daryacheh-I-Maharly (playa) | 6 - Maidan-I-Gil (playa) |
| 3 - Daryacheh-I-Tasht (playa) | 7 - Sirjan Kavir (playa) |
| 4 - Volcanic mountains | 8 - Ibrahimabad Kavir (playa) |

Figure 2-67 Nimbus 1 AVCS image of southern Iran, orbit 323, 19 September 1964, showing terrain features. (Neal, 1968)

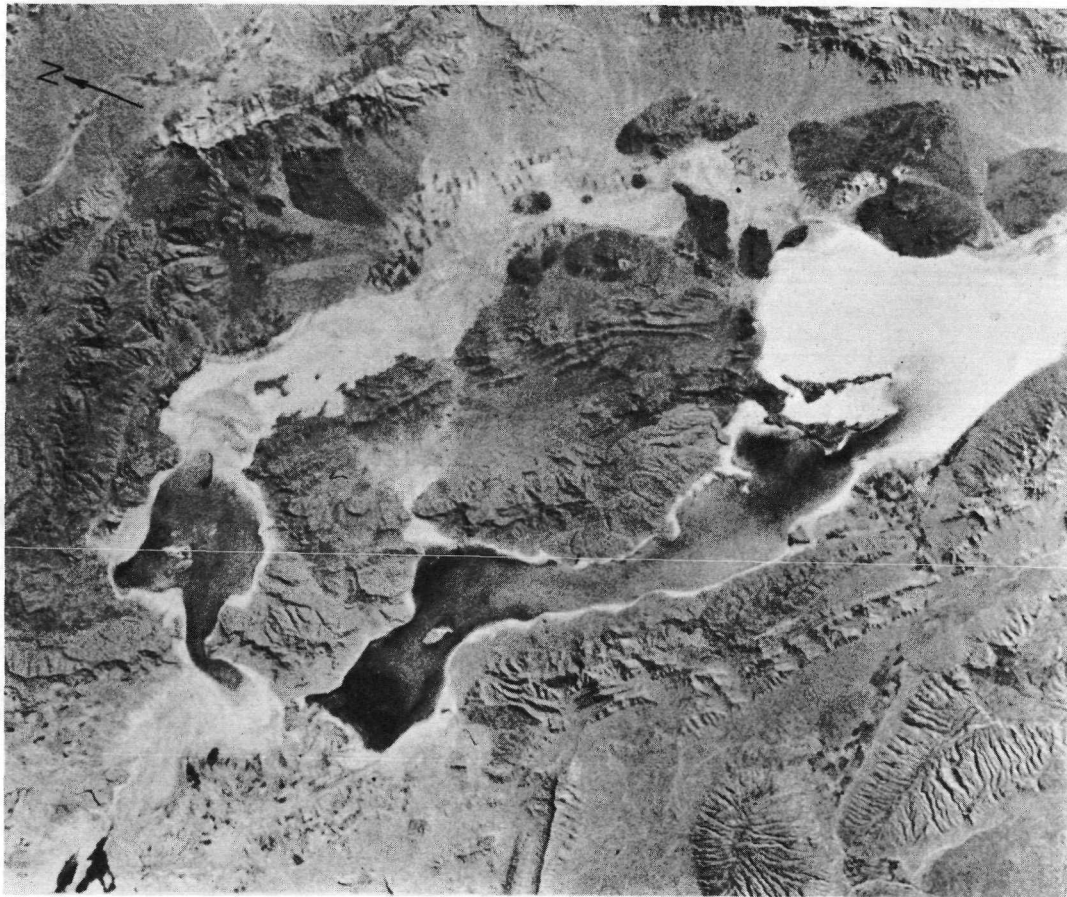


Figure 2-68 Gemini 5 photograph of southern Iran, 22 August 1965. (Compare with Figures 2-67 and 2-69.)



Figure 2-69 Gemini 5 photograph of Lavar Maidan (left center) in southern Iran, 22 August 1965.

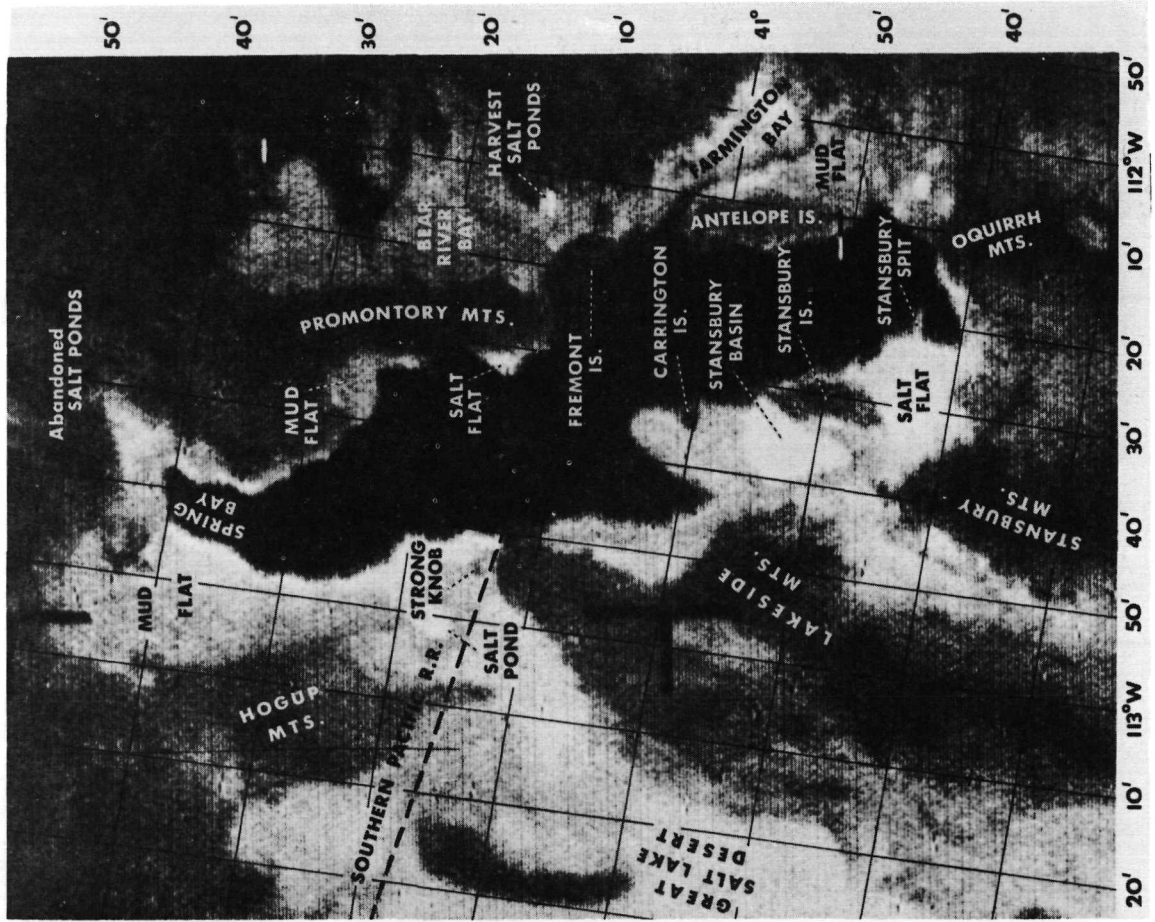
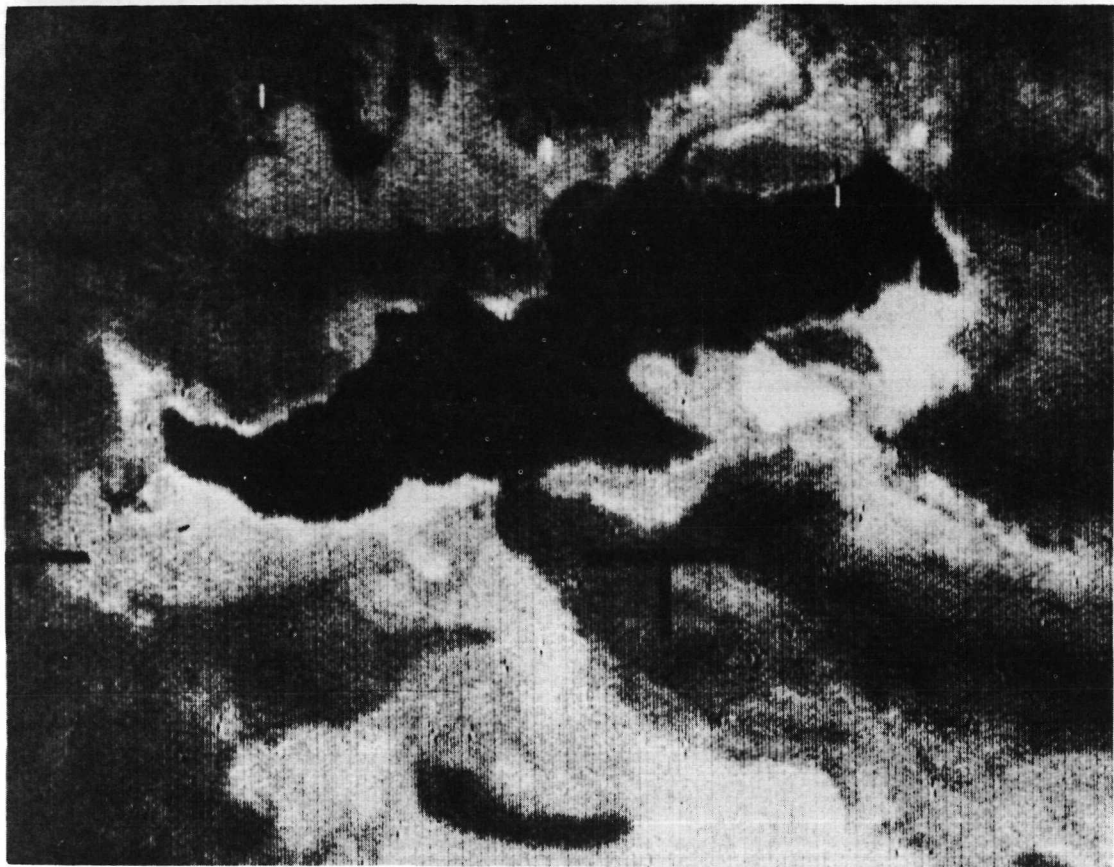


Figure 2-70 Enlargement of a Nimbus 1 AVCS image of the Great Salt Lake area, Utah, taken on orbit 197, 10 September 1964. Identification of surface features was made with the aid of a map of the Great Salt Lake, Utah. Scale 1:125,000. (Greer, 1971)

stocene lake. Hahl and Handy (1966) interpreted the same Nimbus I AVCS picture of the Great Salt Lake region, and indicated that detection of submerged features may be possible from this picture. However, no subaqueous features are visible in this photograph, other than a gray band zone along most of the shoreline, probably representing bottom reflection from shallow waters.

Page Intentionally Left Blank

3. OCEANOGRAPHIC APPLICATIONS OF NIMBUS DATA

3.1 Introduction

In its report to NASA, the Oceanography Panel of the National Academy of Sciences Summer Study on Space Applications (1969) summarized the importance of oceanography as follows:

"The oceans affect the lives of all mankind in three important ways: through weather, transportation, and food. Nearly all the moisture in rain clouds and the energy of tropical storms originate in the sea. More than 95% of the tonnage of commerce transported abroad goes by ship. The ocean is a significant source of food protein, not only for direct human consumption, but for the food of land animals ultimately consumed by people."

The report goes on to point out that although satellites will sample only the top layers of the ocean, this is just the portion that is most important to man in his fishing, shipping, and coastal activities. Partly on the basis of this report, NASA now plans to give the first measurement priority of the Earth Observatory Satellite (EOS)* to global ocean coverage. The assigned oceanographic priorities include:

- High Seas Fisheries
- Pollution (detection and tracking)
- Transportation
- Prediction of Oceanic Phenomena

The candidate observables required to achieve the goals implicit in these oceanographic priorities include:

- Biological phenomena
- Sea surface temperatures
- Sea surface roughness
- Ocean color
- Extent, thickness and structure of sea ice
- Dynamic topography of the ocean surface
- Heat flux across the air/sea surface
- Chemical composition

*The EOS satellite series is currently planned to start in 1975 - 1976, as a follow-on to ERTS-A and B satellites.

Although the monitoring of some of these observables requires the development of instrumentation beyond the current state of the art, many have already been measured by sensors on board the Nimbus satellites.

The purpose of this section is to review those contributions to satellite oceanography which have already been made through the use and analysis of Nimbus data. Table 3-1 correlates the Nimbus observables with the three major man/ocean interface areas delineated in the NAS report. Table 3-2 lists by satellite, the Nimbus sensors capable of oceanographic data acquisition. Each of the Nimbus observables in Table 3-1 will be discussed in turn. The basic achievements and applications within each measurement area will be reviewed. Individual contributions to the field may be found in the references and bibliography included in Section 6.

3.2 Sea Surface Temperature

The sea surface temperature is one of the more important and most readily measured of oceanographic parameters. It can have a direct bearing on the development of ocean weather systems, as well as an influence on the favored breeding grounds of particular fish species. Nimbus infrared observations have been used extensively to measure sea surface temperatures. Unlike the potential all-weather capabilities of the untried microwave sensors, * infrared data is degraded by atmospheric attenuation (see Appendix B) and can be used only in cloud-free areas. Despite these limitations, numerous investigators have demonstrated the ability of the HRIR and MRIR to accurately portray ocean surface thermal patterns on a synoptic scale.

The HRIR experiments on board Nimbus 1, 2, and 3 operated in the 3.4 to 4.2 μm spectral region where contamination by reflected solar radiation limits the use of these data to nighttime temperature measurements. (A near-infrared 0.7 to 1.3 μm channel, was added to the Nimbus 3 experiment for daytime use, but does not furnish any direct sea surface temperature information.) The THIR experiment on board Nimbus 4 operating in the 10.5 to 12.5 μm region and, therefore, unaffected by reflected solar radiation, provides both daytime and nighttime surface temperatures.

The nighttime HRIR data of Nimbus 1 were found (Allison and Kennedy, 1967) to provide sea surface temperatures to within 3^o to 6^oK of aircraft measurements. This study which was conducted over several ocean regions, encountered the greatest difficulty in distinguishing between thin cloudiness and cool surface conditions.

*A microwave experiment, the Electrically Scanning Microwave Radiometer (ESMR) will be flown on Nimbus E in 1972 (see Appendix A). The ESMR will be able to detect sea surface conditions and ice through nonprecipitating clouds with a resolution of 25 km.

TABLE 3-1

NIMBUS OBSERVABLES AND APPLICATIONS

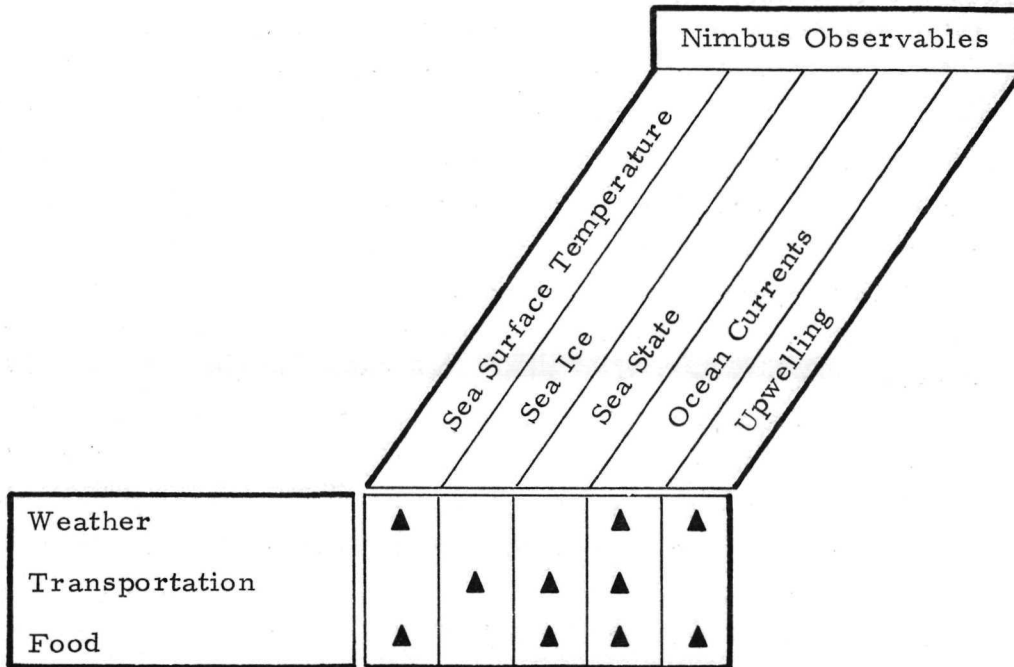


TABLE 3-2

NIMBUS SENSORS CAPABLE OF OCEANOGRAPHIC MEASUREMENTS

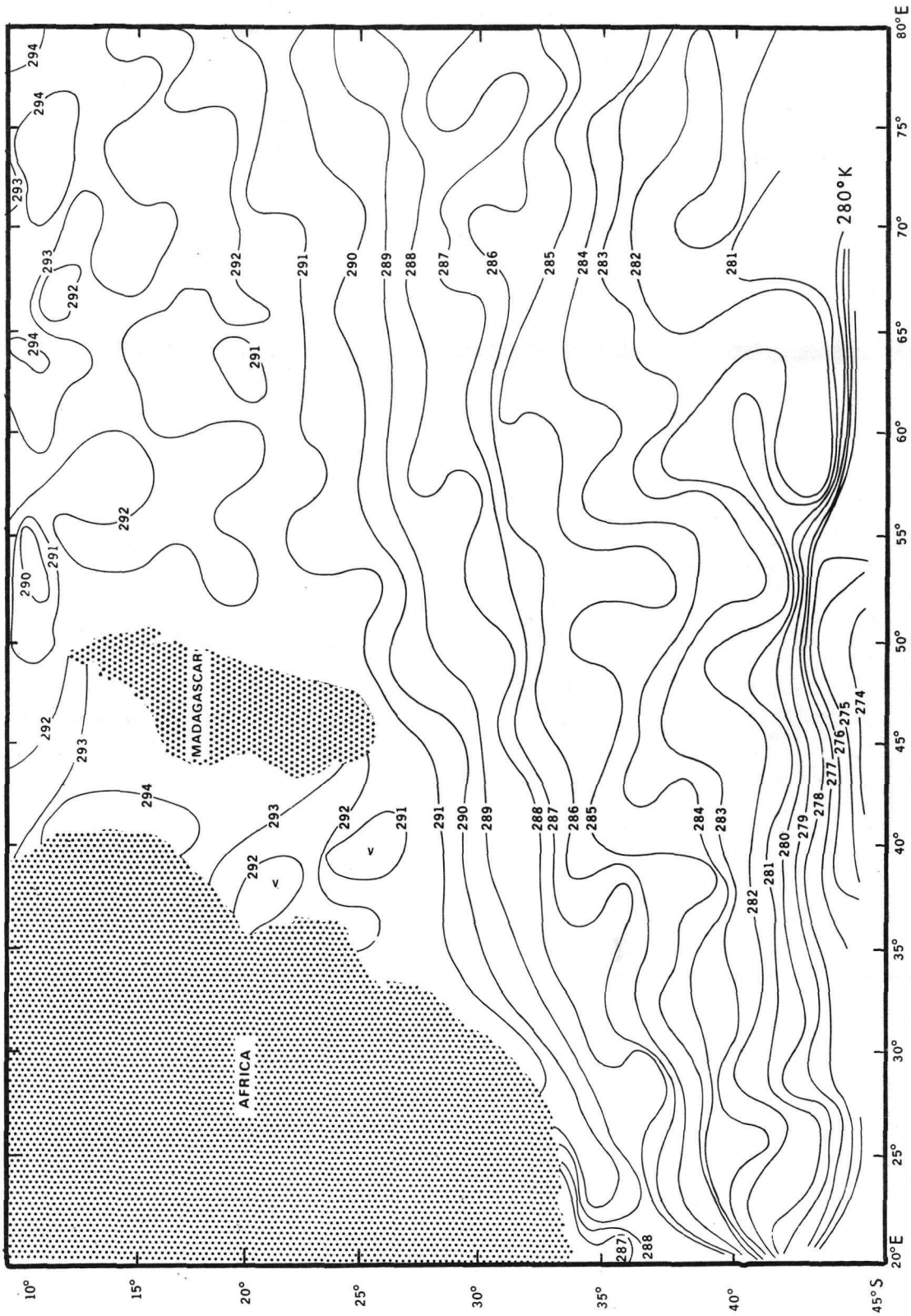
Nimbus	Launch Date	Sensor	Spatial Resolution at SSP (km)	Spectral Interval (μm)	Approximate Operational Period
1	28 Aug 1964	HRIR	3.3 to 7.5	3.5 to 4.1	1 month
		AVCS	0.3 to 0.8	Visible	1 month
		APT	0.8 to 1.8	Visible	1 month
2	15 May 1966	HRIR	9.3	3.5 to 4.1	6 months
		MRIR	60.0	10.0 to 11.0 0.2 to 4.0	2-1/2 months
		AVCS	0.9	Visible	3-1/2 months
		APT	2.2	Visible	23 months
3	14 Apr 1969	HRIR	8.5	3.4 to 4.2 0.7 to 1.3	9-1/2 months
		MRIR	60.0	10.0 to 11.0 0.2 to 4.0	9-1/2 months
		IDCS	3.3	Visible	9-1/2 months
		IRLS	---	---	17 months
4	8 Apr 1970	THIR	7.7	10.5 to 12.5	Operational February 1971
		IDCS	3.3	Visible	Operational Feb 1971
		IRLS	---	---	Operational Feb 1971

LaViolette and Chabot (1969) have had some success in attacking the transitory cloud problem by performing selective five-day composites of the HRIR data. A multispectral approach using MRIR data was taken by Greaves et al (1968). Computer programs were written to reject cloud-contaminated Channel 2 (10 to 11 μm) temperature values on the basis of the albedo levels in the Channel 5 (0.2 to 4 μm) visible data. Shenk and Salomonson (1970) used both the MRIR albedo and water-vapor channels to eliminate cloud-contaminated temperature measurements by the MRIR 10 to 11 μm channel data and obtained excellent correlation (within 1°K) of MRIR sea surface temperatures to ship observations (when corrections were applied for atmospheric effects). Figure 3-1 from Shenk and Szekiolda (1971) shows the average surface temperature of the Indian Ocean from the MRIR 10 to 11 μm channel data obtained by this technique. The average is for the 14 June through 7 July 1966 period and shows temperature gradients rather than the actual sea surface temperatures because no correction for atmospheric effects was applied. The Agulhas Current near the coast of South Africa and especially the oceanic polar front in the South Indian Ocean are well delineated by sharp temperature gradients, even in this three-week average, a good indication of their very stable position. Although these approaches would only work with daytime data, their success suggests that similar procedures could be adopted in a two-channel (IR-window and visible) HRIR experiment.

After examination of the Nimbus 2 HRIR data, Rao (1968), Curtis and Rao (1969), and Blanton and Vukovich (1969) have questioned the authenticity of the fine details which appear in the temperature field. The present ground-truth base is inadequate to either support or refute these small scale patterns. Major features such as the boundaries of major currents are well delineated, however.

Smith et al (1970) used Nimbus 2 and 3 HRIR to develop a statistical histogram method to objectively determine sea-surface temperature from satellite high-resolution window radiation measurements. The blackbody temperatures from $1^{\circ} \times 1^{\circ}$ latitude-longitude square on the ocean are used to construct a statistical histogram. The most probable temperature for the area is taken to be the modal peak of the clear atmosphere observations. The method accounts for atmospheric attenuation and instrumental noise and objectively discriminates cloud-free from cloud-contaminated observations. Comparison with conventional ship observations indicates that both the bias and the random errors of the inferred sea temperatures are less than 1°K . The National Oceanic and Atmospheric Administration (NOAA) is considering this method to obtain sea-surface temperature on a global basis from satellite high-resolution infrared measurements.

With corrections for atmospheric attenuation, it is now felt that in clear-sky areas Nimbus can provide surface temperature measurements to an accuracy of 1°K .



Note: Cloud contaminated measurements were eliminated by discarding those measurements for which concurrent MRIR albedo (0.2 to 4.0 μm) and water vapor (6.4 to 6.9 μm) channels measurements indicated presence of clouds. No corrections were applied for atmospheric absorption effects.

Figure 3-1 Average surface temperature of the south Indian Ocean obtained from the Nimbus 2 MRIR 10 to 11 μm channel for the 14 June - 7 July 1966 period. (Shenk and Szekielda, 1971)

3.3 Sea Surface Current Boundaries

From satellite heights, warm or cold ocean surface currents are detectable only through their temperature contrast with the surrounding water. During the seven years since the launch of Nimbus 1 in 1964, HRIR and THIR data have been used to detect the boundaries of the Gulf Stream, the Peru, Falkland and Brazil Currents, the Agulhas Current, and the Kuroshio.

Nimbus 2 daytime HRIR data also show current boundaries, although the measurements are a combination of solar reflected and thermal energy (see Appendix B), and do not yield temperatures directly. Figures 3-2 through 3-5 show typical ocean current boundaries detected by the Nimbus satellites. The boundaries of the Gulf Stream current are especially visible in the HRIR and THIR. Warnecke et al (1967) have noted that during the 174-day lifetime of the Nimbus 2 HRIR experiment, the north wall of the Gulf Stream could be seen on at least 50 occasions. Using Nimbus 2 data, Greaves et al (1968) developed a time history of Gulf Stream meander movements over a two-month period. Figure 3-6 from Greaves et al (1968) shows the position of the north wall of the Gulf Stream during October 1966. The locations of many of these currents have also been inferred through the analysis of local cloud structure along the current boundaries (LaViolette and Seim, 1968; Seim and LaViolette, 1969; Greaves and Bowley, 1970).

Many investigators (see, for example, Warnecke et al, 1969) have employed color enhancement techniques to bring out sea surface temperature patterns in the HRIR and THIR data. Contrast between chosen temperature intervals or gray levels can be enhanced by the assignment of appropriate colors, thus producing false color pictures which are easier to evaluate. Allison and Kreins (1970) employed the ATS Electronic Image System (EIS) color photorecorder system to produce false color pictures for the enhancement of the Gulf Stream boundaries. They used modified HRIR digital tapes as input to the EIS color photorecorder.

Greaves et al (1968), Warnecke et al (1971), and other researchers have used the Allied Research Associates digital color printer (Demaso et al 1969) to accentuate current boundaries. The ARA color machine takes as input standard computer cards on which the HRIR or THIR temperatures are encoded. The position of the punched holes on the cards controls the color projected on a photographic plate. The cards are an optional output from the GSFC HRIR (or THIR) mapping program.

A third color system, the Spatial Data Systems Data Color Densitometer* has been used successfully to delimit ocean current boundaries from the black and white HRIR and THIR photofacsimile (Szekielda and Mitchell, 1971). The SDS

*Spatial Data Systems, Inc., Goleta, California.

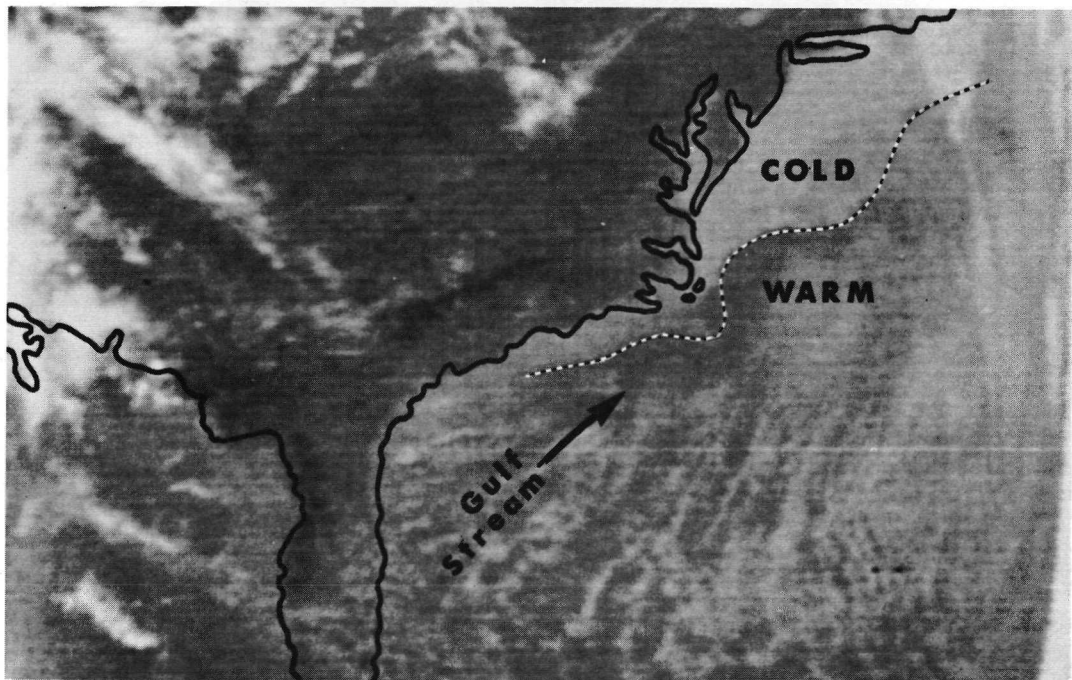
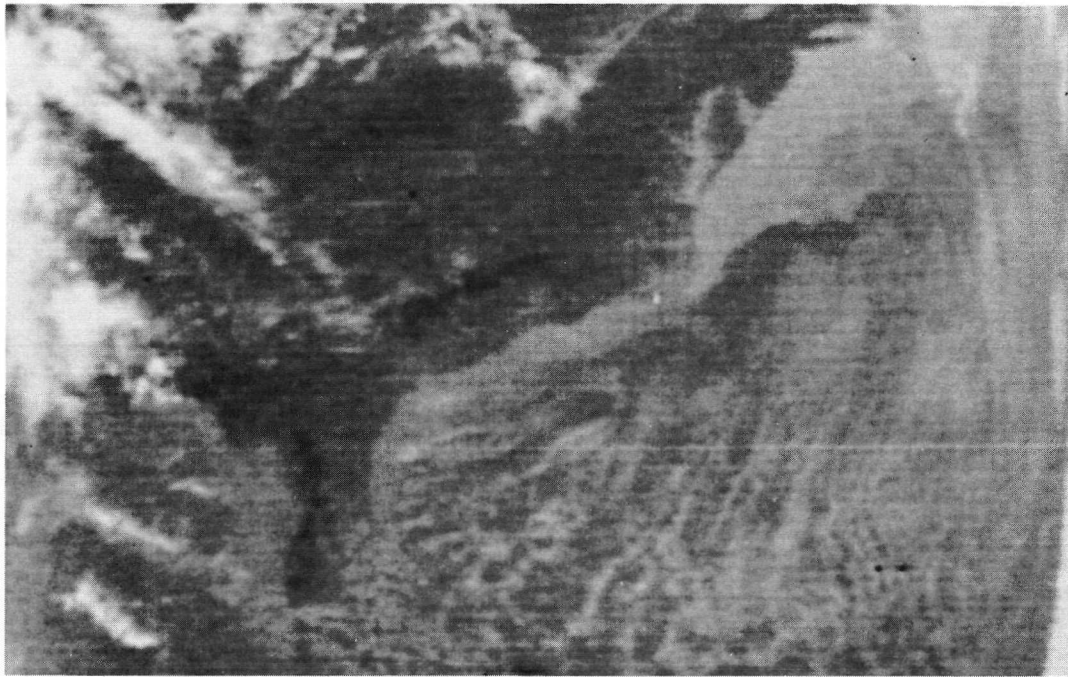


Figure 3-2 Nimbus 4 THIR photofacsimile (11.5 μm channel, daytime) taken on orbit 5, 8 April 1970, showing the Gulf Stream thermal boundary.



Figure 3-3 Nimbus 2 HRIR photofacsimile (3.8 μm channel, nighttime) taken on orbit 1235, 16 August 1966, showing the Falkland-Brazil currents boundary near the Atlantic coast of South America. (Warnecke et al, 1969)

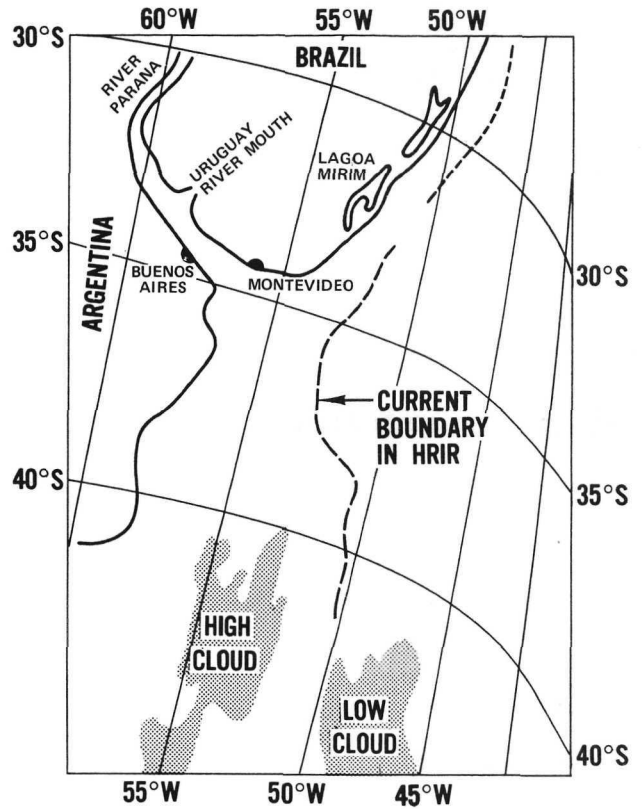
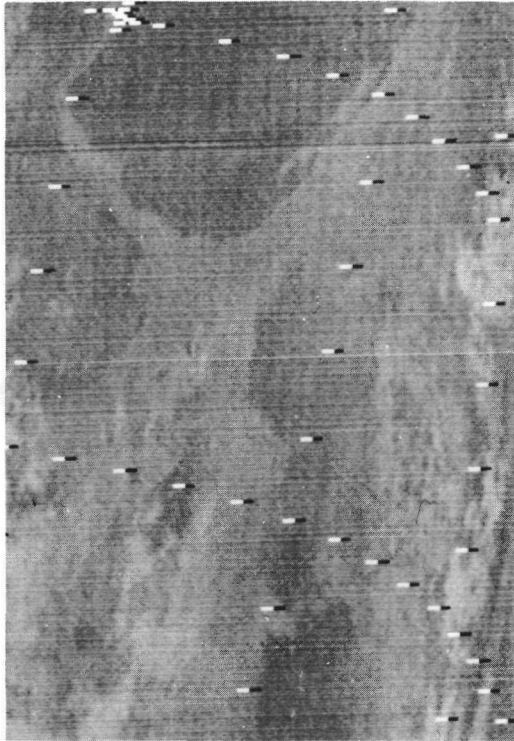


Figure 3-4 Photofacsimile and schematic analysis of Nimbus 2 HRIR daytime measurements (3.4 to 4.2 μm) taken on 25 May 1966, orbit 137 over the south Atlantic Ocean showing the Falkland-Brazil current boundaries. (Warnecke et al, 1969)

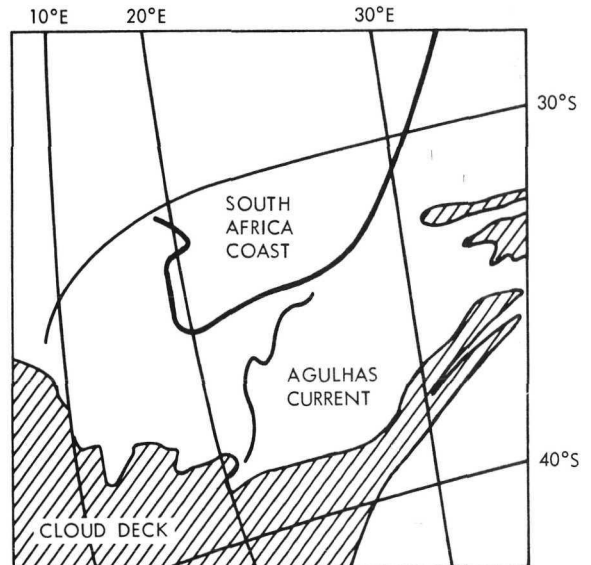


Figure 3-5 Photofacsimile and schematic analysis of Nimbus 2 HRIR nighttime measurements on 19 September 1966, 2130 GMT (orbit 1698), near South Africa. (Warnecke et al, 1969)

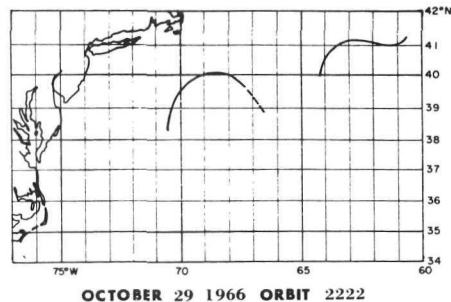
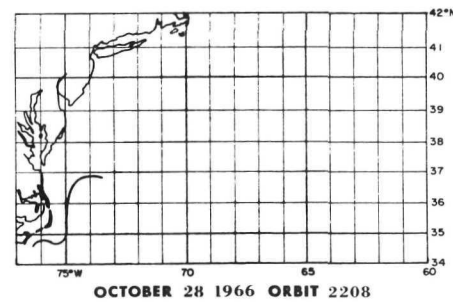
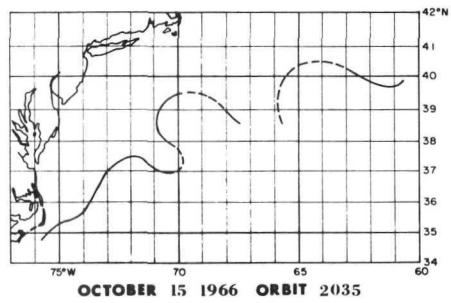
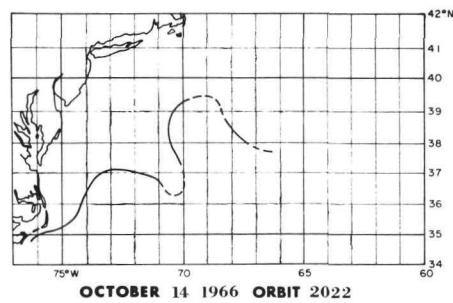
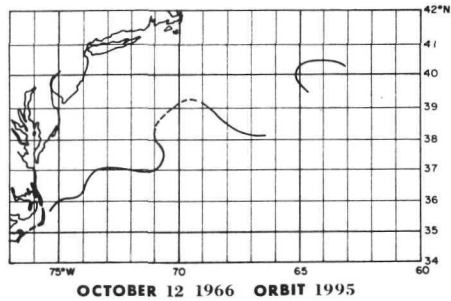
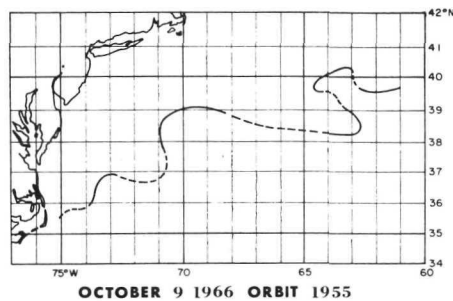
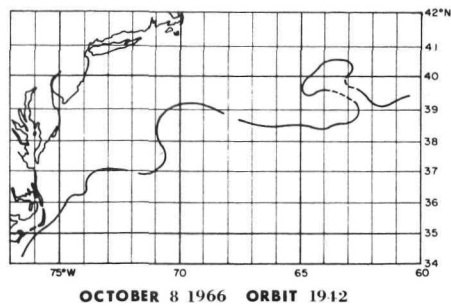
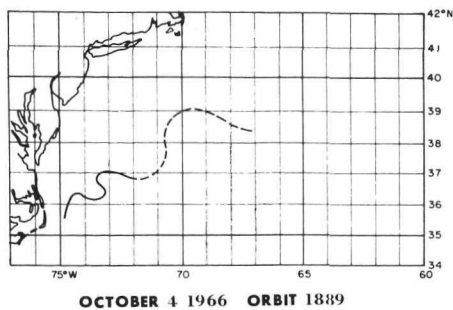


Figure 3-6 Position of the north wall of the Gulf Stream during October 1966 derived from Nimbus 2 HRIR nighttime measurements

system is a television system that converts shades of gray in an image into a wide spectrum of colors and presents the false color image on a computer-type display which can be photographed. The SDS system can take as input photofacsimile transparencies or the equivalent information on computer tape. Both the U. S. Geological Survey and NASA/Laboratory for Meteorology and Earth Sciences are currently experimenting with this system for possible utilization in the analysis of present and future Nimbus and ERTS data.

3.4 Upwelling and Sea State

The mechanism of upwelling brings colder, nutrient-rich water to the ocean's surface. The upwelled water is capable of supporting an abundance of marine life and thus becomes a prime target for exploitation by the fishing industry. Again, the presence of upwelling is currently detectable mainly through its thermal effects. (Eventually, periodic surveillance of phytoplankton chlorophyll through spectrometer measurements near the 6700 Å chlorophyll band may be possible.)

Szekiela (1970a, 1970b) has used Nimbus 2 and 3 HRIR to detect upwelling off the coast of Somali, Africa. Figure 3-7 shows the ocean temperature distribution at the beginning of upwelling. Szekiela (personal communication) is currently using Nimbus data to investigate the occurrence of upwelling near the coast of continents. Studies of upwelling-related cloud patterns using ATS and ESSA data (LaViolette and Seim, 1968; Greaves and Bowley, 1970) show that the Nimbus AVCS or IDCS television data could also be used to detect and monitor the onset or termination of upwelling.

Although side-looking radar seems to offer the most potential for measuring sea state, Duntley and Edgerton (1966) have shown that in the presence of sunglint,* the photographic data of Nimbus or other satellites may be used. In their model, the rate of transition from brightness at the center of the sunglint pattern to darkness at the outer edge is an indicator of sea state. Bowley et al (1969) as well as McClain and Strong (1969) have uncovered a possible link between upwelling centers and areas of lower sea state as observed in satellite photography. Unusual dark patches observed against a brighter sunglint background seem to be due to areas of calm water (associated with wind speeds less than 5 m sec^{-1}) in the midst of rougher sea surfaces. If the sea were perfectly calm, the sunglint would consist of a small, very bright specular-type reflection at a point on the earth determined by the laws of geometric optics. Because the sea is not smooth, sunglint always appears as a larger, more diffuse area. According to this model, an area of calm water not at

*Sunglint is seen when the viewing angle is equal to the angle of incidence of the sun's rays on a wave surface.

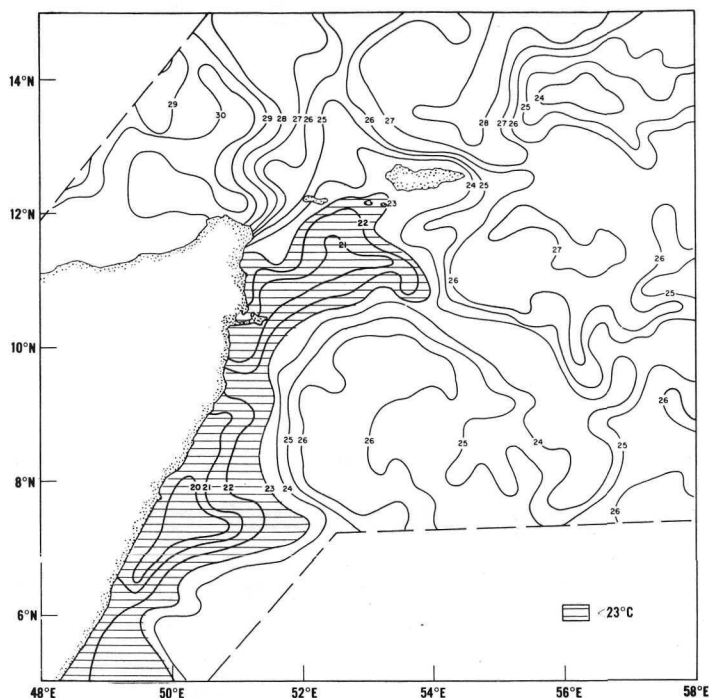
the center of the sunglint pattern would show up as a dark spot against the sunglint background. The phenomenon seems upwelling-related, having been observed in traditional upwelling areas, in the lees of islands, and along diverging wind fields. The reduction of capillary waves in the nutrient-rich upwelled water, plus the relatively calm winds expected in a stable atmosphere overlying a cool ocean surface may account for the calm water conditions. Figure 3-8 presents an example of this sunglint phenomenon as it appeared in a Nimbus 2 AVCS picture. An area of lower reflectivity may be seen extending into a sunglint pattern off the southern tip of Baja, California. If these anomalous dark areas can be directly correlated with upwelling centers, satellite pictures such as those in Figure 3-8 could be of considerable benefit to the fishing industry. Nimbus 4 daytime THIR 11.5 μm channel permits the observation of sea surface temperatures concurrent with anomalous sunglint patterns in the IDCS pictures. Presumably if the dark areas within the sunglint are associated with upwelling, then the THIR would show lower temperatures in these areas.

3.5 Sea Ice

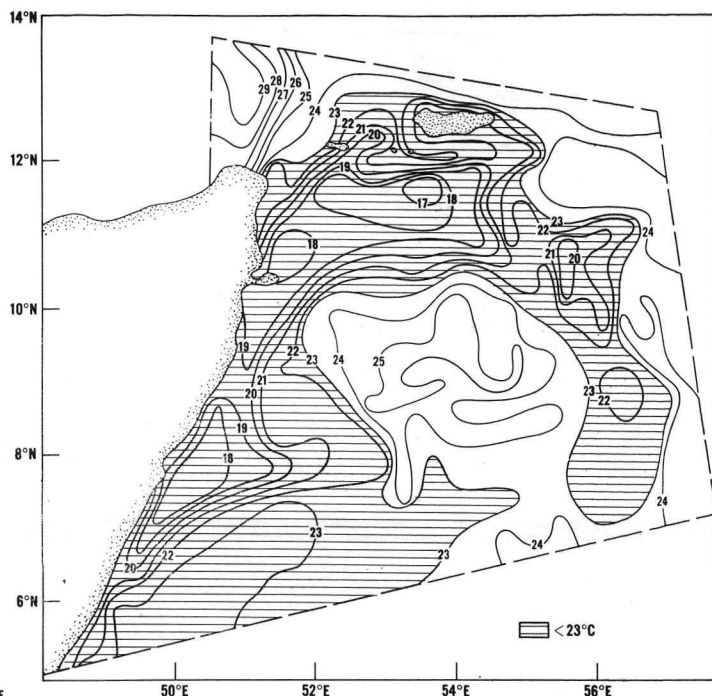
The Arctic and Antarctic regions, which encompass nearly 10% of the earth's surface, are seasonally or perennially ice covered. Conventional means have proved to be inadequate to accurately determine the distribution, variability, and behavior of sea ice in both these areas. The global surveillance capabilities of satellites, however, can offer a major service to shipping by frequent monitoring of ice cover conditions in established sea lanes and by warning of such potential hazards as floating ice. Several studies utilizing the Nimbus television and infrared data have demonstrated the feasibility of an operational satellite ice-reconnaissance system. These data can also be used to study the meteorological and oceanographic conditions related to pack ice distributions.

3.5.1 Ice Concentrations

The Ice Forecast Central of the Canadian Meteorological Service, the U. S. Naval Oceanographic Office, and the U. S. Fleet Weather Facility, Department of the Navy, have used Nimbus photographic data for operational ice surveys. A U. S. Navy report (Operation Deep Freeze, 1970-1971) praised the high quality of the direct readout IDCS pictures received by their APT station at McMurdo, Antarctica. The report states that Nimbus 4 data were found to be "far superior to either ESSA 8 or ITOS 1 for both cloud and ice recognition over and around the Antarctic Continent." The superiority of the Nimbus IDCS for ice and cloud observation is probably due to its higher sensitivity at high surface albedoes. Figure 3-9 from the Antarctic Journal of the United States (March-April 1971) is an example of IDCS direct readout data



Orbit 649, 3 July 1966



Orbit 689, 6 July 1966

Figure 3-7 Changing thermal pattern at the beginning of an upwelling near the Somali Coast as recorded by Nimbus 2 HRIR on 3 and 6 July 1966. (The development of the clockwise circulation pattern was correlated with the bloom of phytoplankton.) (Szekielda, 1970)

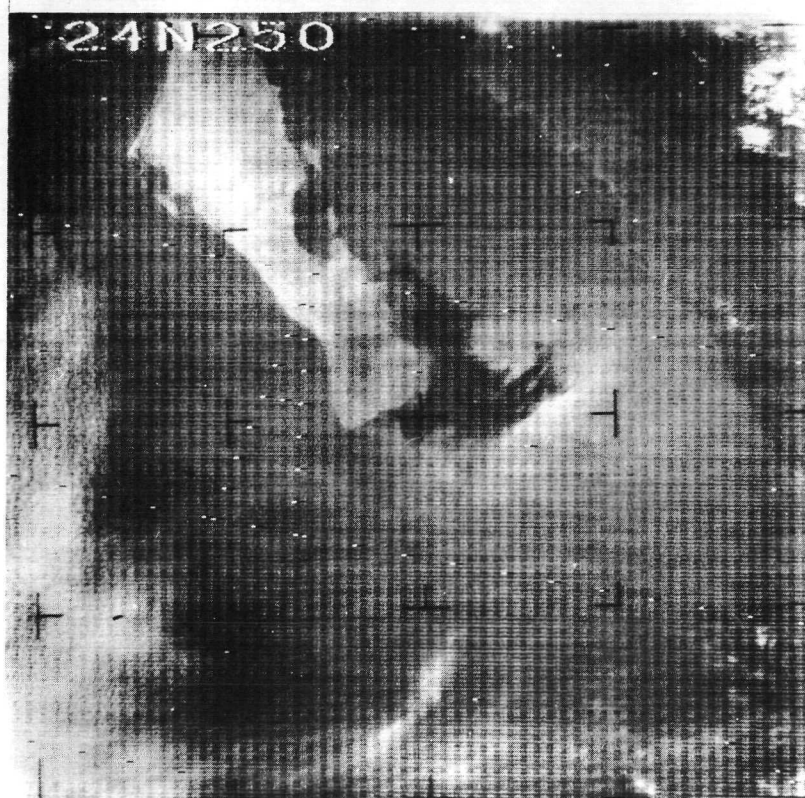
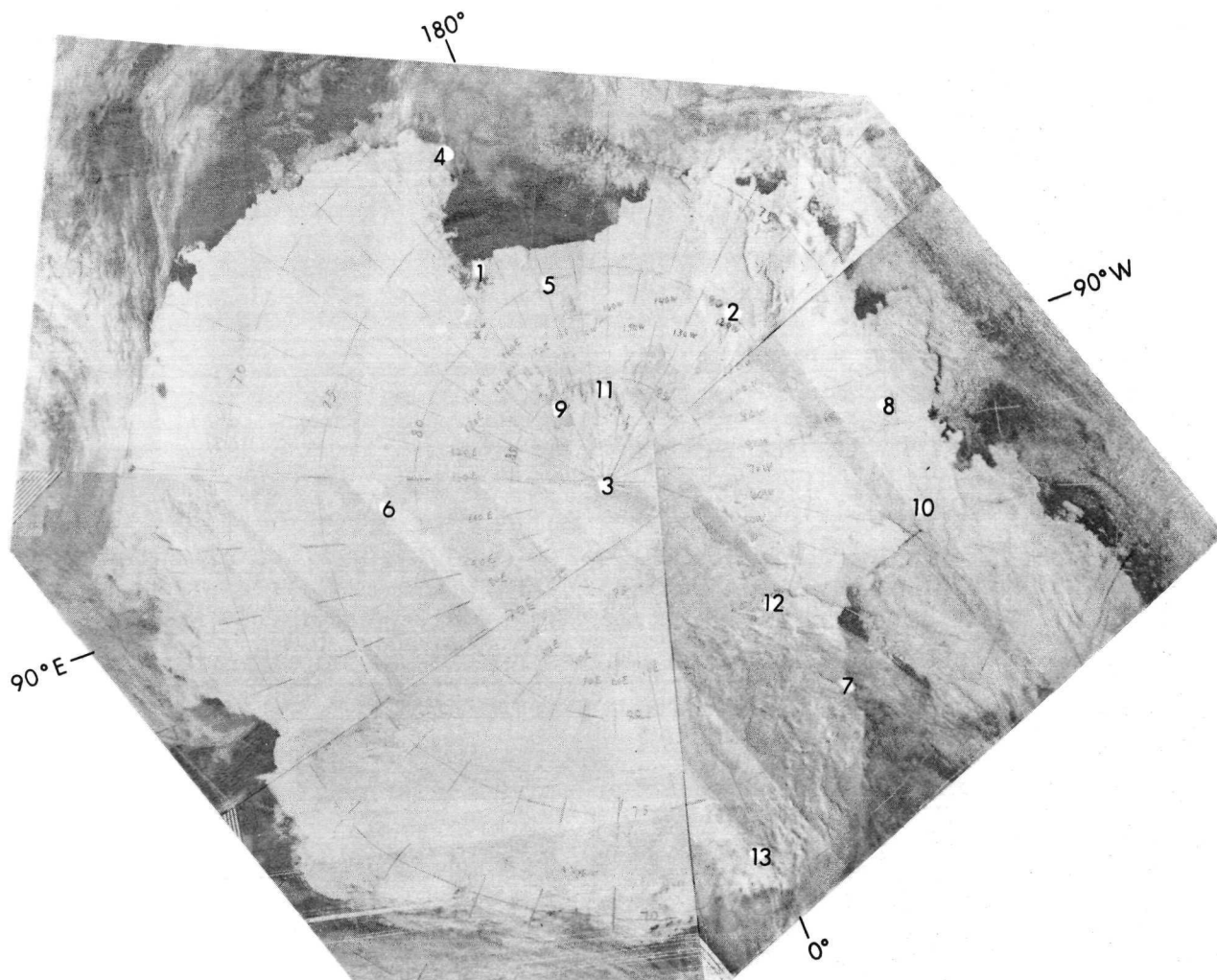


Figure 3-8 Anomalous sun glint pattern in the Gulf of California as recorded by Nimbus 2 AVCS, orbit 126, 24 May 1966



- 1) McMurdo Station (USA) and Scott Base (NZ)
- 2) Byrd Station (USA)
- 3) Pole Station (USA)
- 4) Hallett Station (USA)
- 5) Brockton Station (USA)
- 6) Vostok Station (USSR)
- 7) Halley Bay (UK)
- 8) Siple Camp (USA)
- 9) McGregor Camp (USA)
- 10) Lassiter Camp (USA)
- 11) Amundsen Camp (USA)
- 12) Shackleton Camp (UK)
- 13) Queen Maude Camp (USA)

Figure 3-9 Nimbus 4 Direct Readout IDCS mosaic of Antarctica, January 1971.

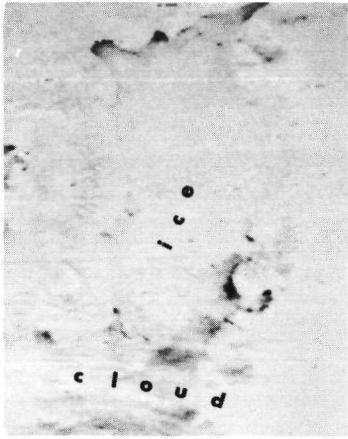
obtained at McMurdo. In the Gulf of St. Lawrence area and in the Arctic Archipelago, ice concentrations determined from APT and IDCS pictures have been found to be in close agreement with aerial survey data. Commander W. E. Willingham, U. S. Navy, reports that "Nimbus data have been an invaluable tool in providing operational sea-ice forecast support in reducing aerial reconnaissance requirements" for the Navy in the eastern Arctic area during the 1970 summer. "Ice boundaries and estimates of concentration were readily determined and in close agreement with aerial reconnaissance data." In fact, based on satellite data alone, ships have been routed through polar ice with excellent results; the ship reports of ice encountered have then been used to evaluate the reliability of the satellite information. A typical Nimbus 4 IDCS picture sequence showing changing ice concentrations in Baffin Bay during the 1970 spring and summer is given in Figure 3-10.

Nelson et al (1970) compared ice amounts from Nimbus 1 AVCS pictures with conventionally gathered ice information at specific locations. They concluded that three classes of ice concentration can be reliably estimated. Ice concentrations from one to three tenths are usually evaluated as ice-free in satellite imagery because of the limitation of resolution in satellite-viewing systems. There is good agreement between satellite and conventional data for ice amounts between four and seven tenths and excellent agreement above seven tenths. Of course, the change of concentration from one class to another can also be noted in the satellite imagery.

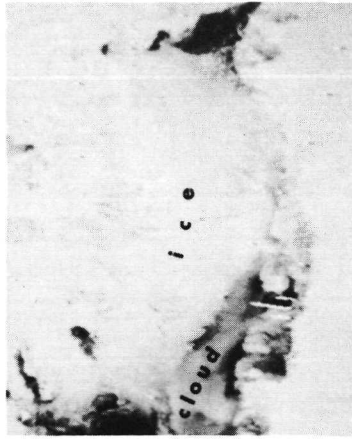
Bowley (1969) examined the breakup of ice in the Hudson Bay area using Nimbus 2 APT data. Accurate evaluation of ice conditions in Hudson Bay is essential for shipping lanes to Churchill, Manitoba, where much of Canada's grain for export is loaded. Bowley concludes ice distribution can, in almost all cases, be distinguished from cloud cover on the basis of concurrent synoptic reports, pattern continuity, recognition of landmarks, and pattern texture. Another approach to the problem of cloud/ice discrimination was taken by Kikuchi and Kasai (1968). Stereoscopic analyses of APT pictures were successfully used to distinguish sea ice from clouds and to estimate the relative height of the cloudiness.

3.5.2 Pack Ice Boundaries

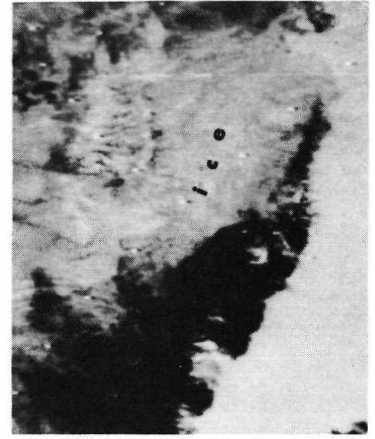
Pack ice boundaries have been established for both polar seas using satellite imagery. Predoehl (1966) was the first to use Nimbus imagery to determine the circumpolar pack ice boundary and area in Antarctica (Figure 3-11). His data sample was limited, however, by the intermittent sensor coverage during the one month lifetime of the first Nimbus. Using larger data samples from Nimbus 2, 3 and 4, Antarctica pack ice boundaries have also been established for July and August 1966, 1969, and 1970 (Figures 3-12 and 3-13, Sissala et al, 1971).



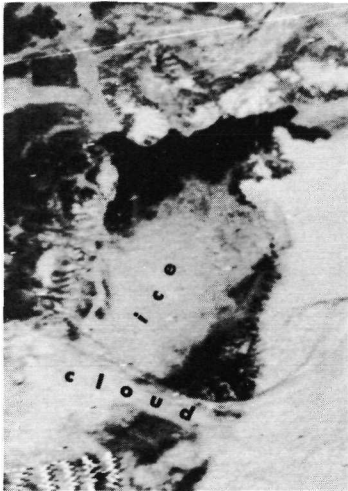
Orbit 245
28 April 1970



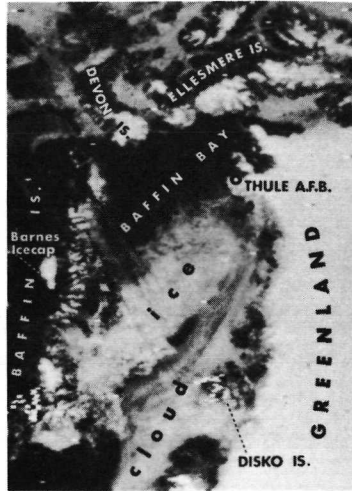
Orbit 635
25 May 1970



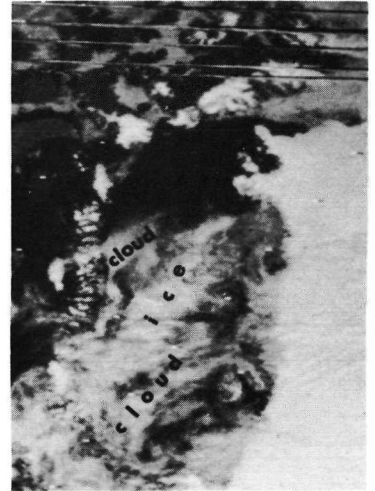
Orbit 1037
24 June 1970



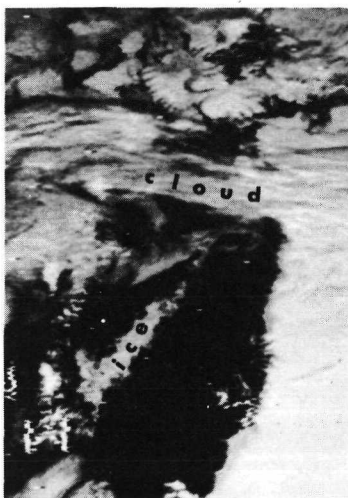
Orbit 1238
9 July 1970



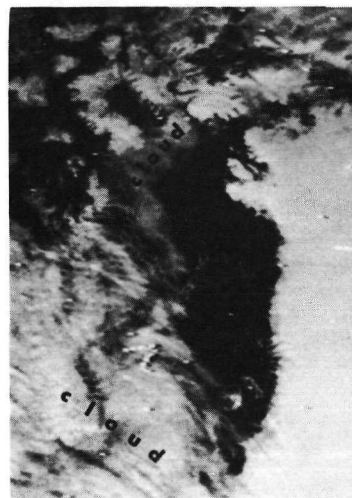
Orbit 1534
31 July 1970



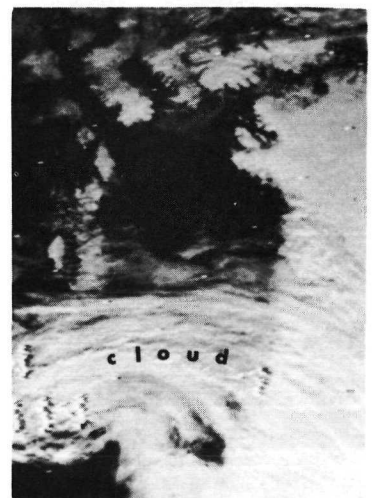
Orbit 1655
9 August 1970



Orbit 1977
2 September 1970



Orbit 2058
8 September 1970



Orbit 2072
9 September 1970

Figure 3-10 Baffin Bay ice survey from Nimbus 4 IDCS pictures. Data such as these have been used by the U. S. Fleet Weather Facility, Department of the Navy, for operational ice surveys.

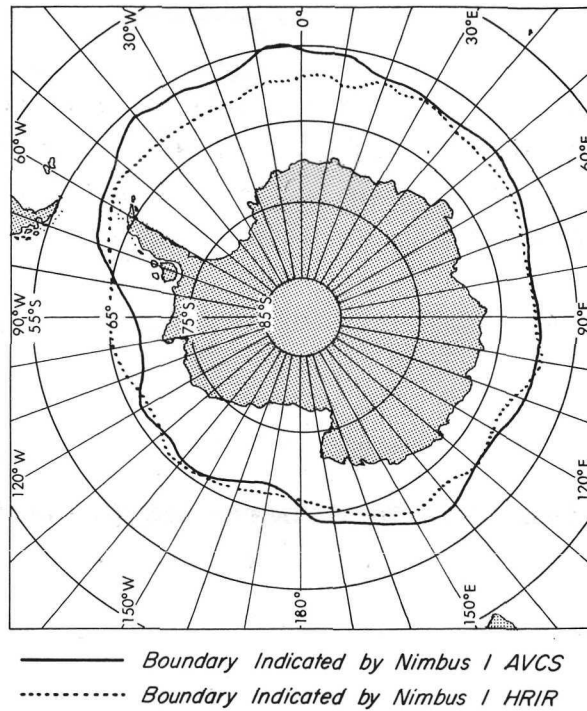


Figure 3-11 Pack-ice boundaries between 28 August and 22 September 1964; solid line is the boundary indicated by Nimbus 1 AVCS pictures; broken line is the boundary derived from Nimbus 1 HRIR pictures. Antarctic pack-ice area is $19.81 \times 10^6 \text{ km}^2$ as calculated from AVCS boundary. (Predoehl, 1966)

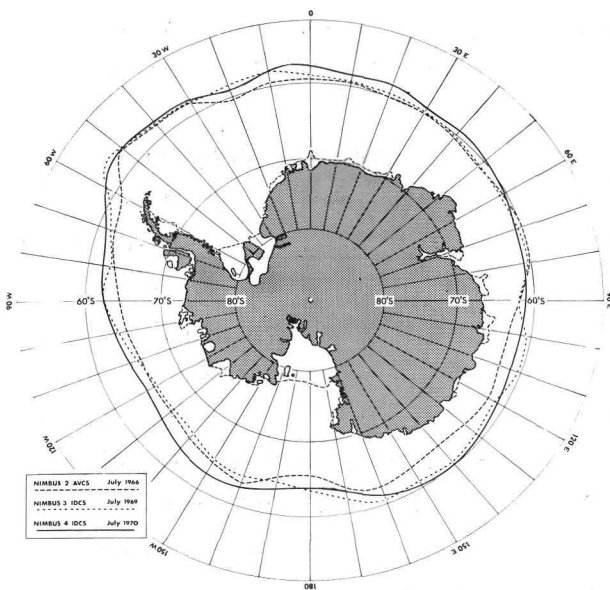


Figure 3-12 Average Antarctic pack-ice boundaries for July 1966, 1969, and 1970 derived from Nimbus data.

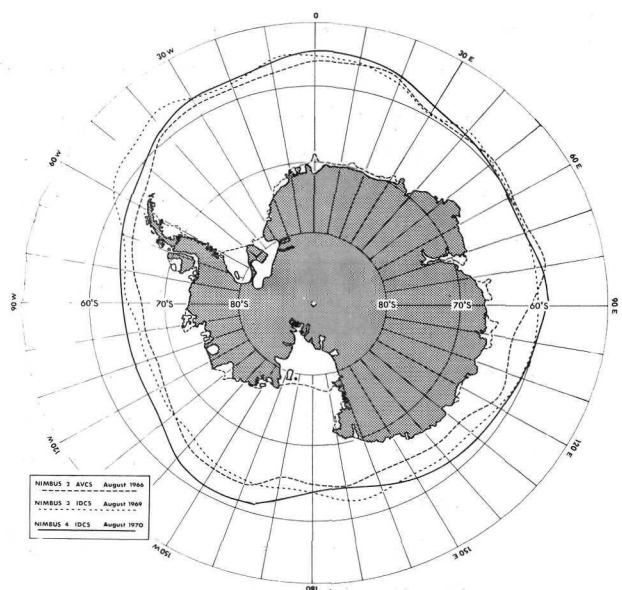


Figure 3-13 Average Antarctic pack-ice boundaries for August 1966, 1969, and 1970 derived from Nimbus data.

Because of clouds, about a week's satellite coverage is needed to establish complete circumpolar pack ice boundaries. When landmarks are available, the ice boundaries can be located with an accuracy to within a few miles. From the satellite-observed boundaries, the total area of polar pack ice, useful in heat budget and ocean current studies, can be computed. Table 3-3 presents the Antarctic pack area calculated by Sissala et al (1971) for the months and areas shown in Figures 3-12 and 3-13.

TABLE 3-3
ANTARCTIC CIRCUMPOLAR PACK ICE AREAS* FOR JULY AND AUGUST
1966, 1969, AND 1970 DERIVED FROM NIMBUS 2 AVCS AND NIMBUS 3 AND 4 IDCS

	July (x 10 ⁶ km ²)	August (x 10 ⁶ km ²)
Nimbus 2 1966	15.26	15.17
Nimbus 3 1969	16.83	17.19
Nimbus 4 1970	17.62	18.55
3 Satellite Average	16.57	16.97

*Does not include Antarctic continent area of 14.24 x 10⁶ km².

Nelson et al (1970) used Nimbus 1 AVCS imagery for a similar study of the Arctic ice boundary. Comparison of satellite boundary position with conventional ice maps was excellent in some areas, but poor in regions not well covered by aircraft survey. Thus, satellite data can provide fairly accurate indications of the boundaries in areas not covered by aircraft survey.

During polar darkness, ice boundaries can also be monitored using Nimbus HRIR and THIR measurements. Studies by Barnes, Chang, and Willand (1970a, 1970b) have shown that principal sea ice boundaries in the Arctic can be identified because of the thermal difference between ice and water. A particularly encouraging result of an analysis of Nimbus 3 HRIR film strips is that ice mapping appears the most reliable during the winter months of December and January, because of the greater occurrence of cloud-free conditions and the accumulation of thicker ice. Since winter is the season of maximum polar darkness, it is the period when other data sources are severely limited. Although the data used in this study were from the Arctic, the results are also applicable to the Antarctic, where winter ice observations can be made during the April through August period.

Even though extremely useful information can be derived from HRIR film strips in their existing format, the authors of the above studies have recognized that limitations do exist. For example, the interpretation of intermediate gray tones can at times be ambiguous. Because of the limiting resolution of the radio-

meter, these tones can be the result of either ten-tenths thin ice cover or open pack. Stratus cloud can also cause misinterpretation, although ice can usually be deduced through the identification of adjacent coastlines, which are obscured when stratus exists. Furthermore, the winter data sample examined in the studies showed that stratus cloud was almost always separated from the ice by a narrow band of open, cloud-free water.

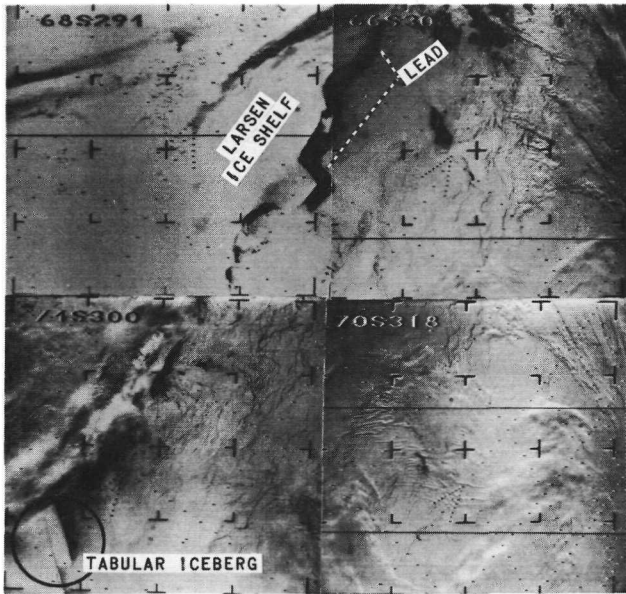
In order to obtain a more objective interpretation of gray-scale variations in the film strips, the above investigators also carried out densitometric measurements. Based on these measurements, experiments were performed to enhance the gray-scale contrast within the temperature range of interest. The results of the experiments show that the present photofacsimile presentations may be improved upon by using discrete steps in the gray-scale and by limiting the number of gray scales used. The gray levels must be readily distinguishable, however, since the purpose of the display is to reduce ambiguity by matching the information content of the display with the information content of the interpretation. In a series of subjective tests, a five gray-level display was found to be optimum in that accurate interpretations of the temperatures could be obtained and significant features of sea ice could be enhanced.

3.5.3 Open Water Areas Within the Polar Pack Ice

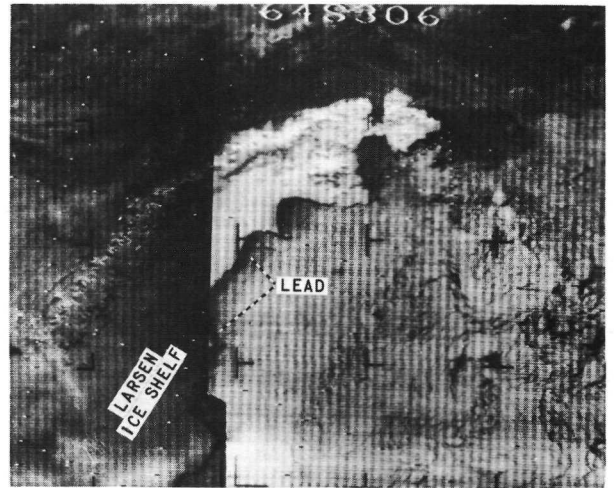
Information about the location and size of polar leads and polynyas (nonlinear ice-free areas within the ice) is valuable for both economic and scientific purposes. Such leads may represent the only corridors available for ship traffic to reach remote scientific stations or an adjoining area of open water, and are extremely important with regard to heat exchange between ocean and atmosphere. Leads greater than about one mile in width are often visible on Nimbus satellite imagery.

One striking example of this feature is a lead that has been observed along the east coast of the Antarctic Peninsula. Pictures from the first three Nimbus satellites, given in Figure 3-14, show that this lead develops at about the same time each year (during late August and early September). The day-by-day development of the lead during the 1969 season is shown in Figure 3-15. Because of the circulation in the Weddell Sea, ice conditions along the Antarctic Peninsula are usually severe; therefore, knowledge of the occurrence of this sizable lead could be vital for ship routing.

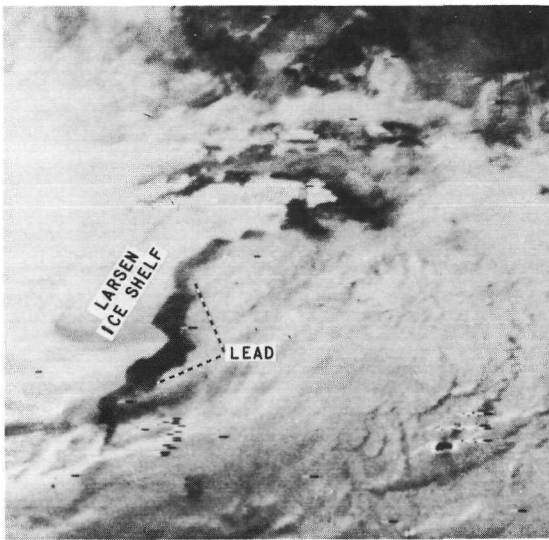
Knapp (1969), using Nimbus television and infrared data to study large Antarctic polynyas, noted that large stationary polynyas are both more numerous and more widely distributed during the winter season than had previously been recognized. The origin of the polynyas, which may cover an area of 5000 km² or more, is primarily due to surface wind stress which removes the annual sea-ice



Nimbus 1 AVCS, Orbit 182,
9 September 1964



Nimbus 2 AVCS, Orbit 1310,
21 August 1966



Nimbus 3 IDCS, Orbit 1923, 4 September 1969

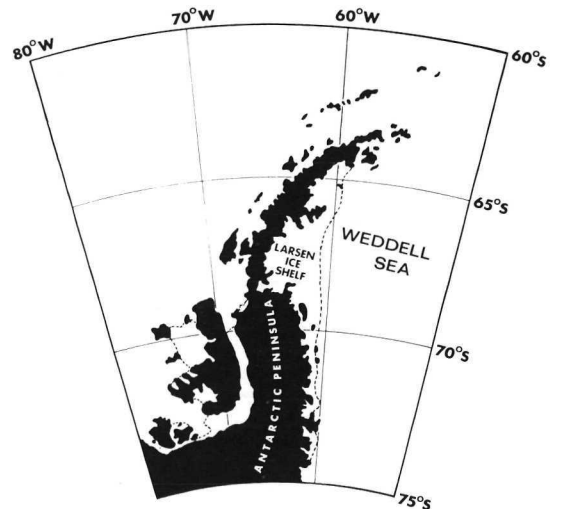
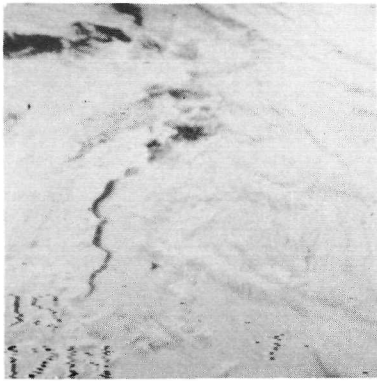
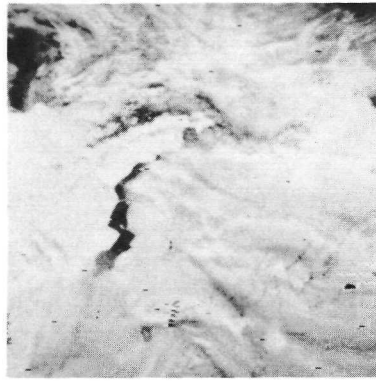


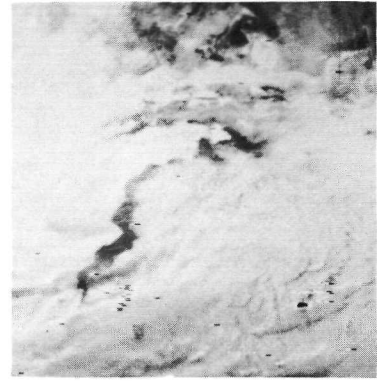
Figure 3-14 Annual development of a lead (long, linear ice-free area) near the Antarctic coast during late August - early September. The lead persists for about two weeks then closes. Also noticeable are some annual changes of the Larsen ice shelf edge.



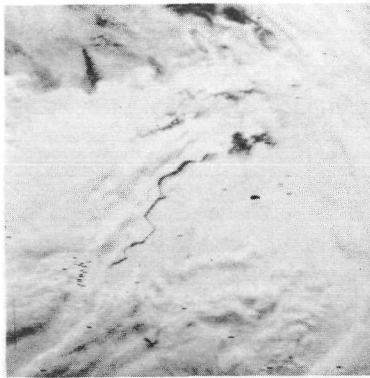
Orbit 1842
29 August



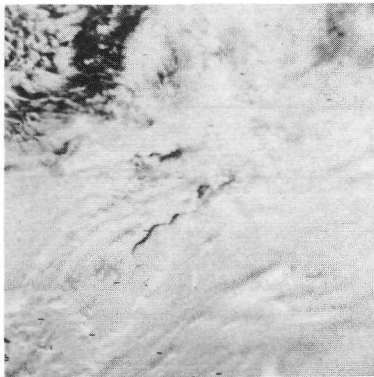
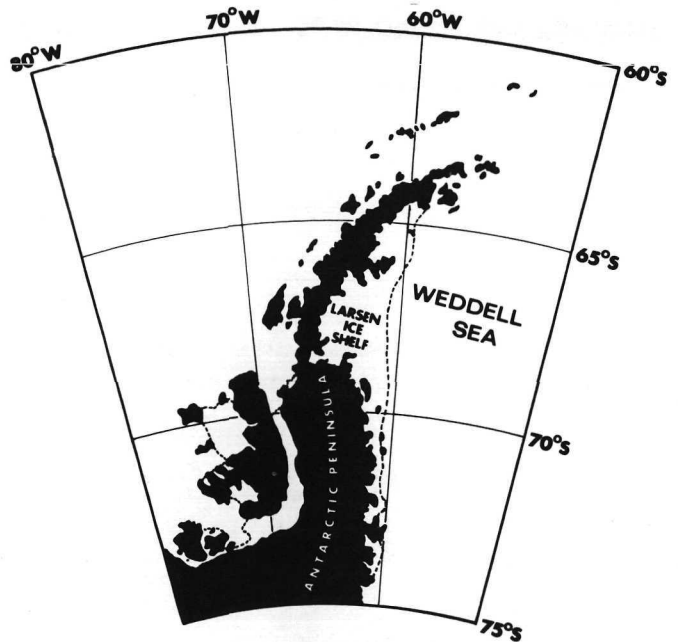
Orbit 1896
2 September



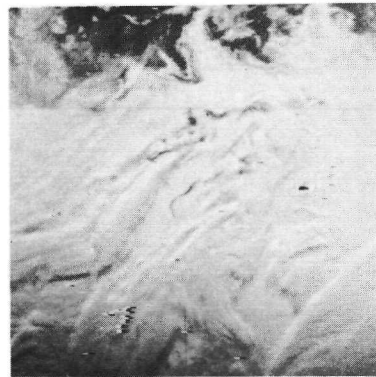
Orbit 1923
4 September



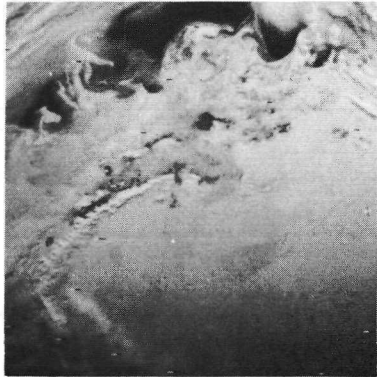
Orbit 1816
27 August



Orbit 1735
21 August



Orbit 1722
20 August



Orbit 1574
9 August

Figure 3-15 Nimbus 3 IDCS pictures recorded during August and September 1969 monitored the development of an offshore lead along the east coast of the Antarctic peninsula. (Westerly winds probably help produce this kind of large lead. Most of the 20 to 30 mile width was produced in a six-day period from 27 August to 2 September. The pack ice boundary can be observed north of the peninsula in several of the images. Such ice information can be useful to ships.)

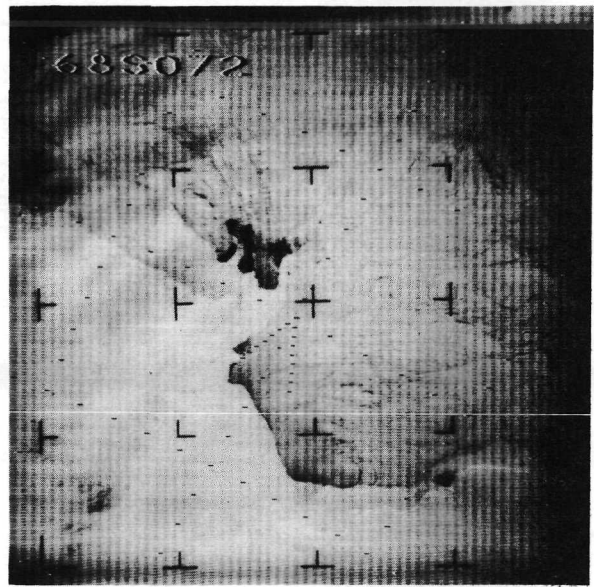
cover from the vicinity of fast-ice, ice-shelf, or continental boundaries. Figure 3-16 from Knapp's report shows an example of the substantial short-term changes that can take place in the size and configuration of the polynyas. The Nimbus 2 AVCS pictures recorded only 25 hours apart reveal dramatic changes in an isolated polynya along the coast of MacRobertson Land in Antarctica. The changes are probably linked to synoptic developments near the Antarctic coastal region.

Open water areas have also been seen in the Arctic. Figure 3-17 is a mosaic of the Arctic area from Iceland to Canada constructed with Nimbus 3 IDCS pictures obtained on three successive orbits on 15 March 1969. Although Baffin Bay is filled with winter ice, Frobisher Bay and Cumberland Sound, off Baffin Island, appear ice-free (probably due to the tremendous tides in these two bays which continually flush any new ice out into Davis Strait). An early spring lead is also evident in this picture off the south shore of Baffin Island in Hudson Strait.

3.5.4 Iceberg Identification and Movement

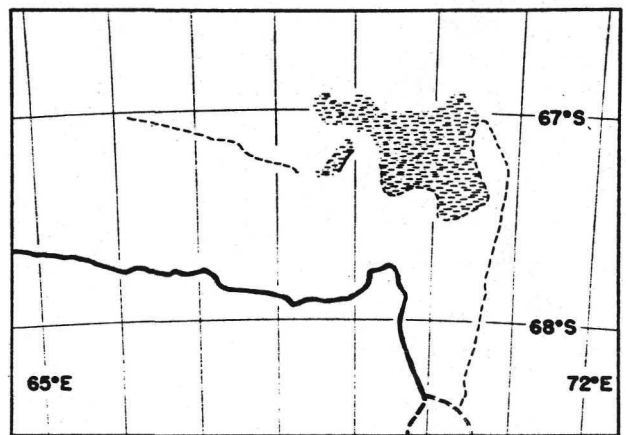
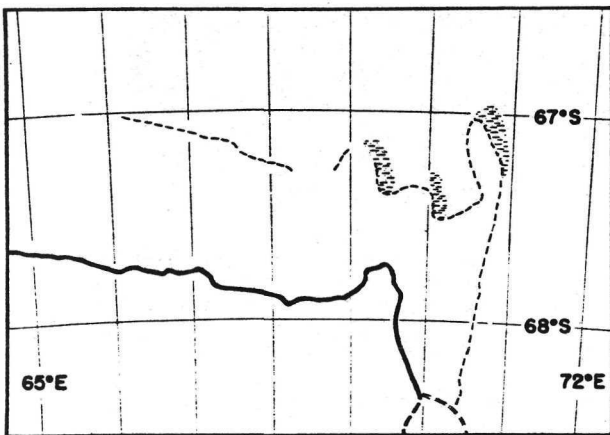
Popham and Samuelson (1965) have analyzed both the AVCS and HRIR data from Nimbus 1 for the Arctic and Antarctic regions. Included in their study was the first known analysis of an iceberg photographed by a satellite (Figure 3-18). The iceberg measured approximately 70 miles long by 15 to 20 miles wide and appeared to have broken off the Filchner ice shelf near the southeastern end of the Antarctic Peninsula. The iceberg did not appear to move during the short Nimbus 1 lifetime (28 August through 22 September 1964). The same area was observed five years later by Nimbus 3 (no observations of this area were made during the Nimbus 2 lifetime in 1966). By October 1969 the iceberg had moved away from the ice shelf and into the pack ice circulation (Figure 3-19).

In a more spectacular case, the drifting of a tabular iceberg in the Antarctic Ocean was monitored over a period of four months using Nimbus 2 AVCS data (Sissala, 1969). The iceberg was partially obscured by clouds in about three-quarters of the sightings; nevertheless, its location and size could be determined even in many pictures contaminated by clouds (Figure 3-20). An ice floe in the Greenland Sea, off the east coast of Greenland, was tracked in a similar manner in Nimbus 2 AVCS pictures (Figure 3-21, Sabatini and Sissala, 1968). The floe movement was calculated to be 0.25 knots, which is in good agreement with the 0.20 knot average current speed for this area given on oceanographic charts. Thus, in some instances, satellite imagery can be used to deduce the speed and direction of currents in remote polar areas and the dissipation of large polar ice objects.



a. Nimbus 2 AVCS, Camera 1
Orbit 1225, 15 August 1966.
Polynya located adjacent to
fast-ice projections in upper
center of picture.

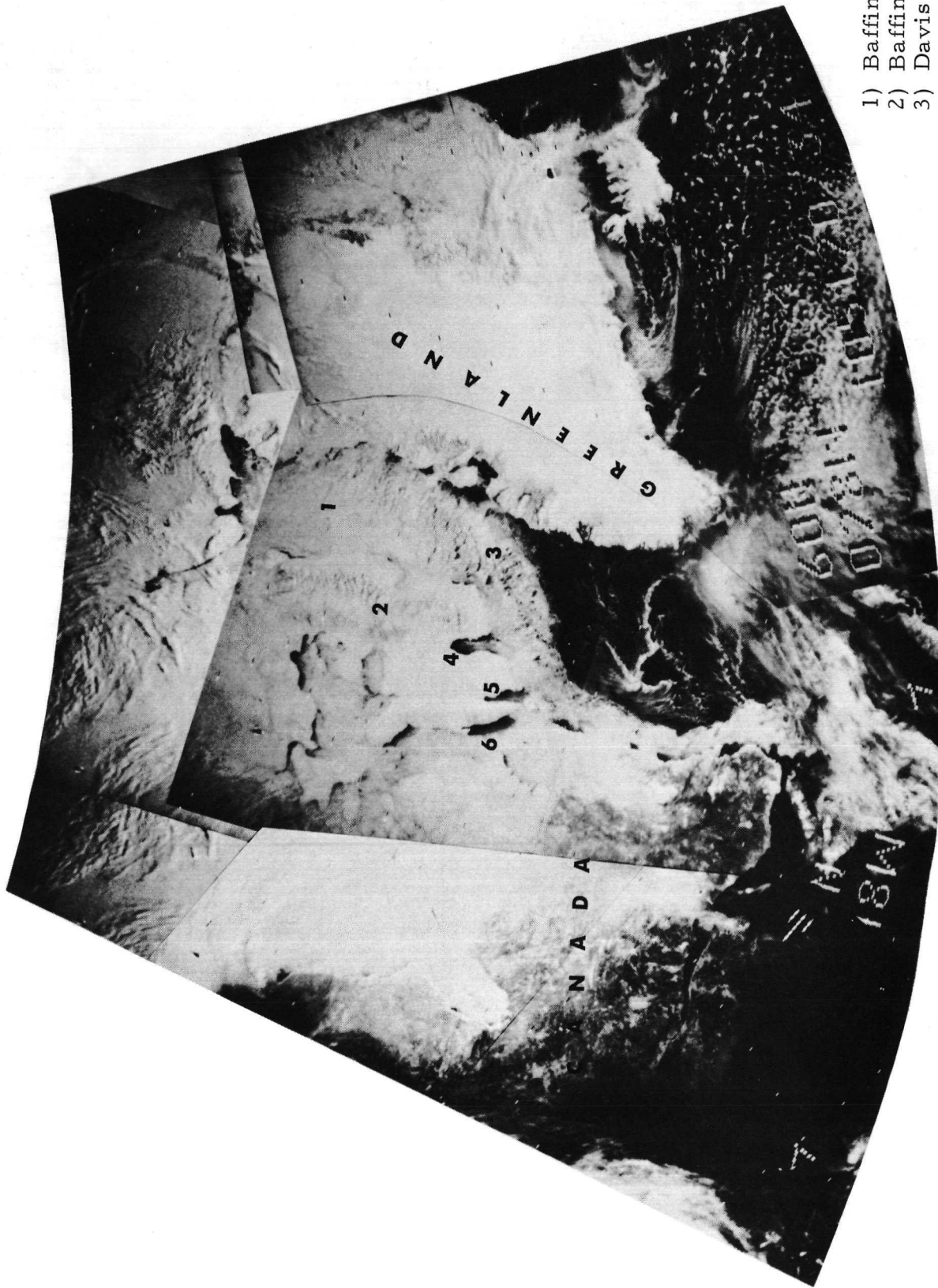
b. Nimbus 2 AVCS, Camera 2,
Orbit 1239, 16 August 1966.
Polynya has increased mark-
edly in size during the preced-
ing 25 hours and is now located
west of the north-south oriented
fast-ice projections.



c. Map of principal ice features
and open water areas seen in
orbit 1225 picture.

d. Map of principal ice features and
open water areas seen in orbit
1239 picture.

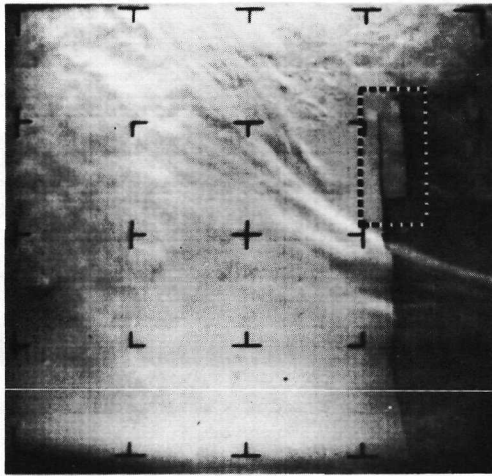
Figure 3-16 Nimbus 2 AVCS observations of short-term changes in the sea-ice regime along the coast of MacRobertson Land, Antarctica. (Knapp, 1968)



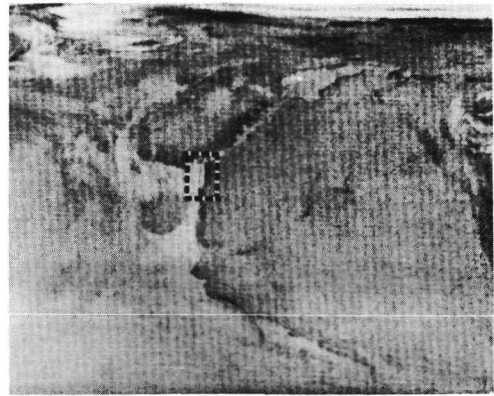
- 1) Baffin Bay
- 2) Baffin Island
- 3) Davis Strait
- 4) Cumberland Sound
- 5) Frobisher Bay
- 6) Hudson Strait

Nimbus 3 IDCS, Orbits 16, 17 and 18.

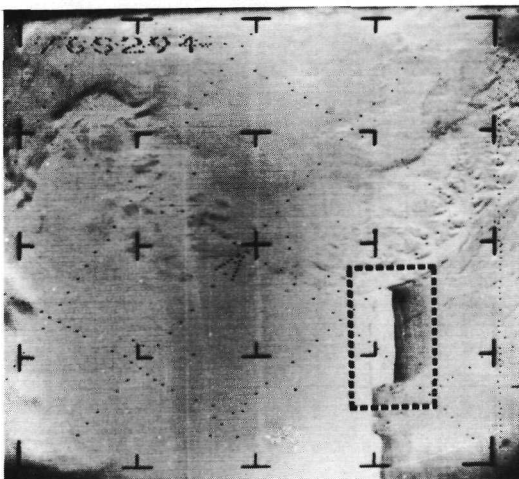
Figure 3-17 Snow and ice conditions from Iceland to Canada on 15 April 1969 as shown by a Nimbus 3 IDCS mosaic.



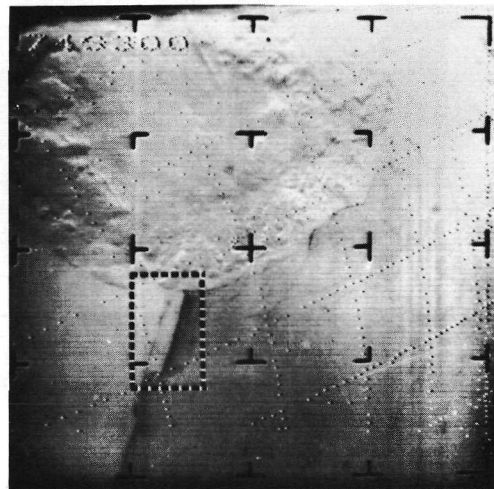
Nimbus AVCS, Orbit 167
8 September 1964



Nimbus 1 HRIR, Orbit 288
16 September 1964



Nimbus AVCS, Orbit 284
16 September 1964



Nimbus AVCS, Orbit 285
16 September 1964

Figure 3-18 Nimbus 1 observations of a tabular iceberg on the eastern coast of the Antarctic peninsula.

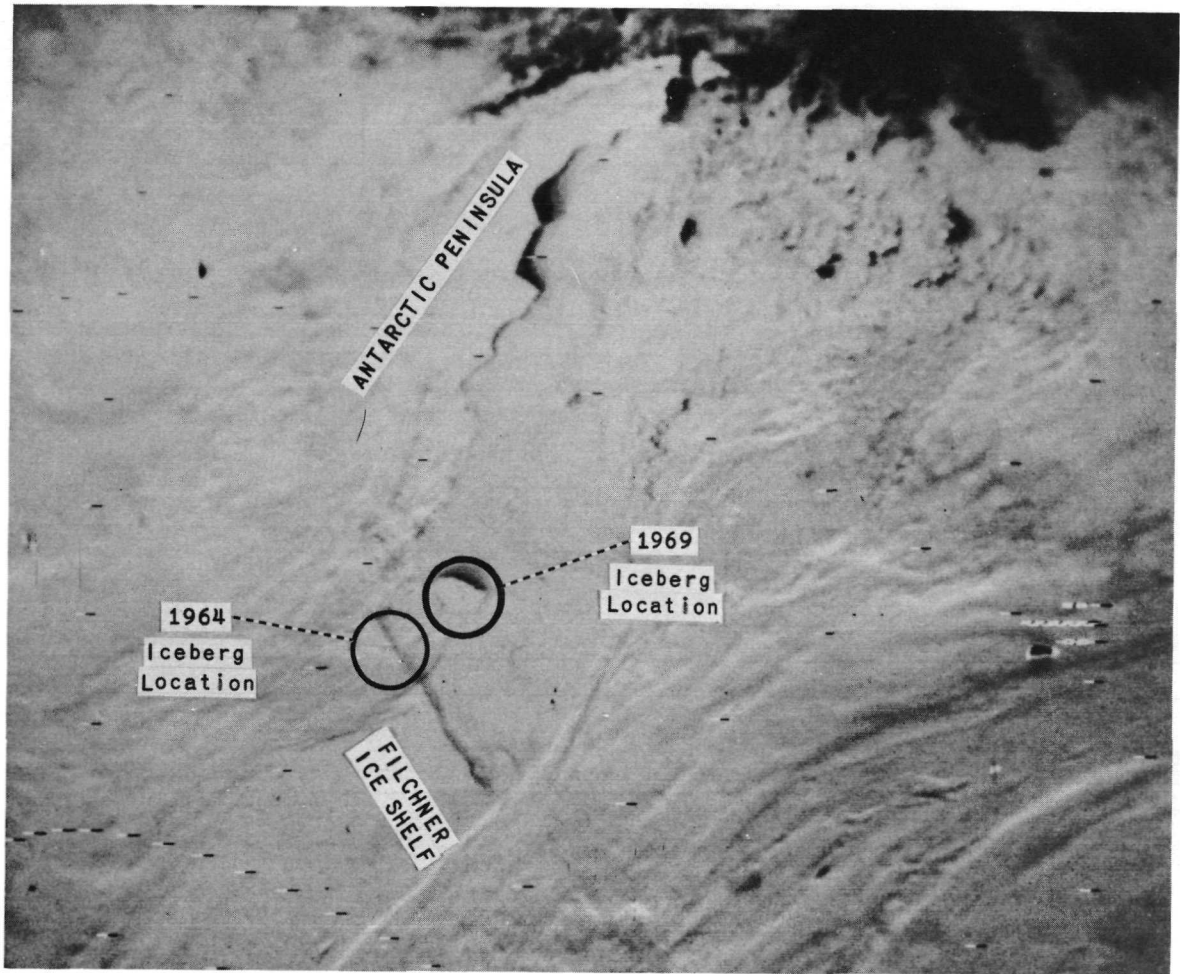
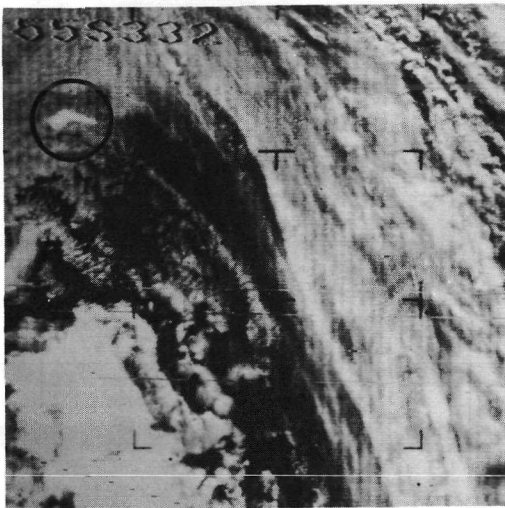
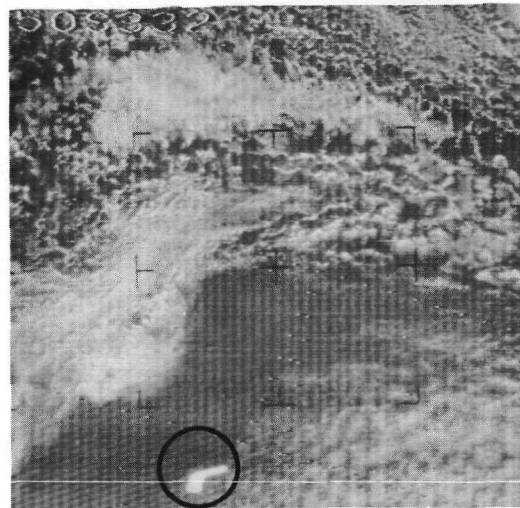


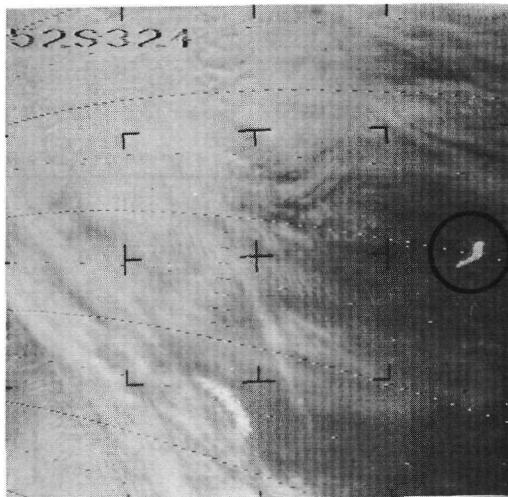
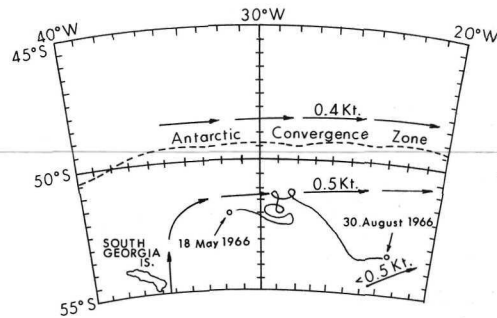
Figure 3-19 Nimbus 3 IDCS picture taken on orbit 2459, 14 October 1969, shows the 1969 location of a tabular iceberg detected in 1964 (see Figure 3-18).



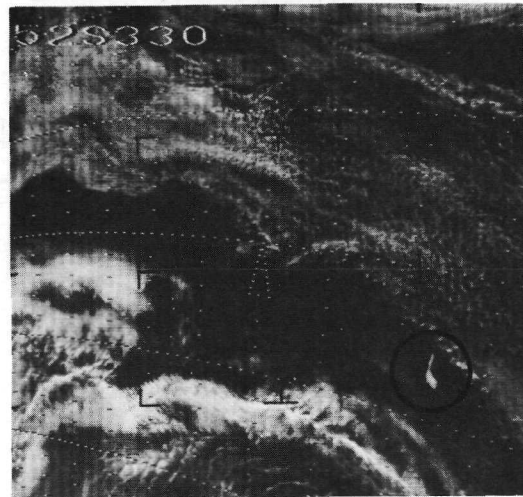
Orbit 44, 17 May



Orbit 470, 19 June

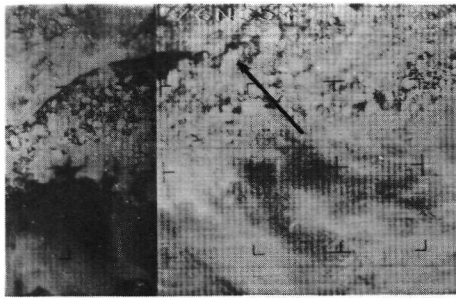


Orbit 776, 12 July

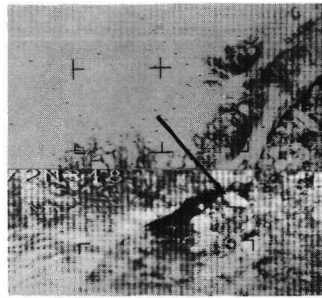


Orbit 1295, 20 August

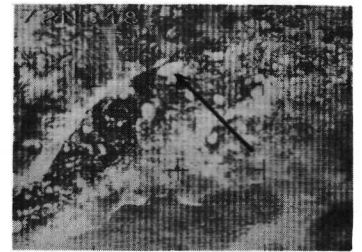
Figure 3-20 Nimbus 2 AVCS observations of a 20-mile long tabular iceberg in the Antarctic Ocean, May-August 1966.



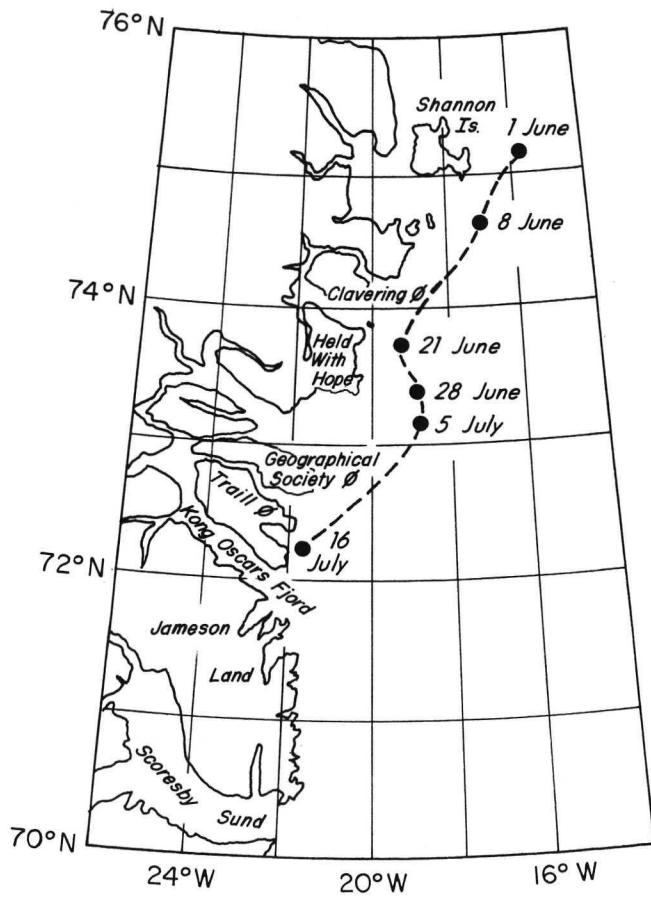
Orbit 227 1 June 1966



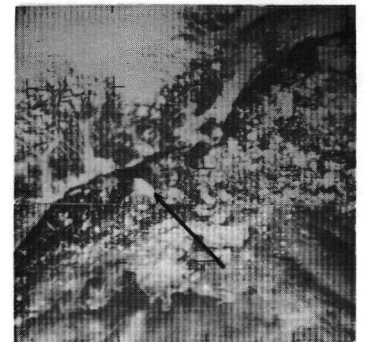
Orbit 321 8 June 1966



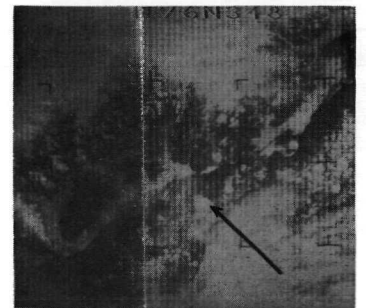
Orbit 494 21 June 1966



East Coast of Greenland from
Shannon Island to Scoresby Sund



Orbit 587 28 June 1966



Orbit 680 5 July 1966



Orbit 827 16 July 1966

Figure 3-21 Nimbus 2 AVCS observations of an ice floe along the east coast of Greenland in 1966.

4. MISCELLANEOUS APPLICATIONS OF NIMBUS DATA

This section discusses those earth resource applications of the Nimbus data that do not logically fall in the Geology and Hydrology or Oceanography categories. These applications include cartography, the interpretation of tonal boundaries, urban analyses, data collection from remote platforms, and the monitoring of such transitory phenomena as brush fires and ship contrails.

4.1 Cartographic and Topographic Revisions in Remote Areas

Major changes in Antarctic ice shelves have been identified from Nimbus imagery. Figure 4-1 shows that an ice tongue, which had persisted for many years, broke off from the continent sometime between the 1966 and 1969 Nimbus observations. Similar observations in other Nimbus imagery have led the U. S. Geological Survey to reconfigure some Antarctic ice shelf boundaries on their 1:10,000,000 plastic relief map (Chief Topographic Engineer, 1965). Figure 4-2 shows significant differences between the Getz Ice Shelf coastline, as presented in a map current in 1964, and the coastline, as viewed in 1964 by Nimbus 1. The American Geographic Society used Nimbus 3 IDCS imagery to update portions of the Caird and Princess Martha Coasts on their 1:5,000,000 Antarctica map (Waugh, 1970).

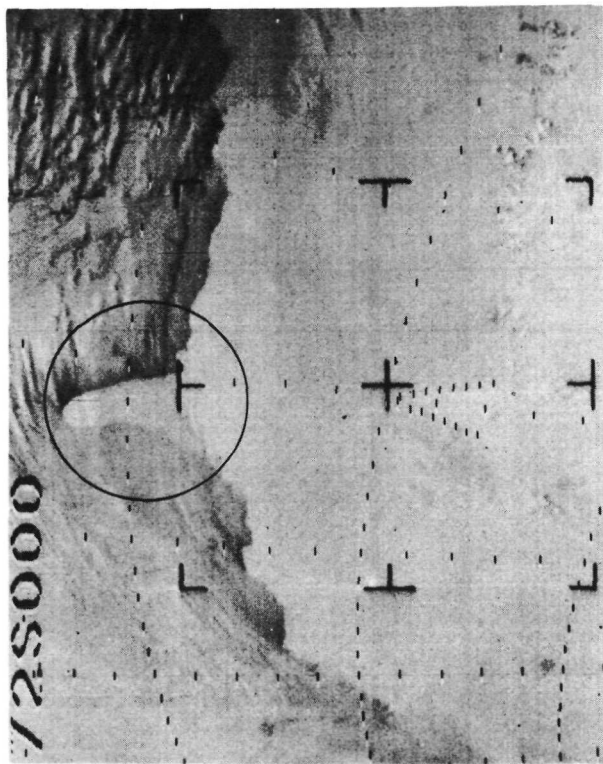
A mountain group in the Kohler Range of Antarctica was eliminated from existing maps after the U. S. Geological Survey analyzed Nimbus 1 imagery of that area. This group evidently was sighted by two expeditions and subsequently positioned by them in two different locations. Nimbus imagery indicated that there was only one group. (Chief Topographic Engineer, 1965.) Also, on the basis of Nimbus data, Mount Siple was repositioned 2° west from the position given on the then existing maps (see Figure 4-2) (Chief Topographic Engineer, 1965). This 3000 meter mountain on the coast is often used as a navigation landmark.

Tibet and China are two other areas where Nimbus 1 and 2 imagery were used to supplement conventional data in the preparation of topographic maps (Norin, 1970).

4.2 Tonal Boundaries in Nimbus Imagery

The repetitive, global coverage of the Nimbus imagery in different visible and infrared spectral bands has provided a wealth of image tonal patterns. Some of these tonal patterns can be recognized at first inspection and mapped for what they represent. For instance, snow fields (Section 2.5.2), changing pack ice boundaries (Section 3.6.2), and major ocean current boundaries (Section 3.3) can

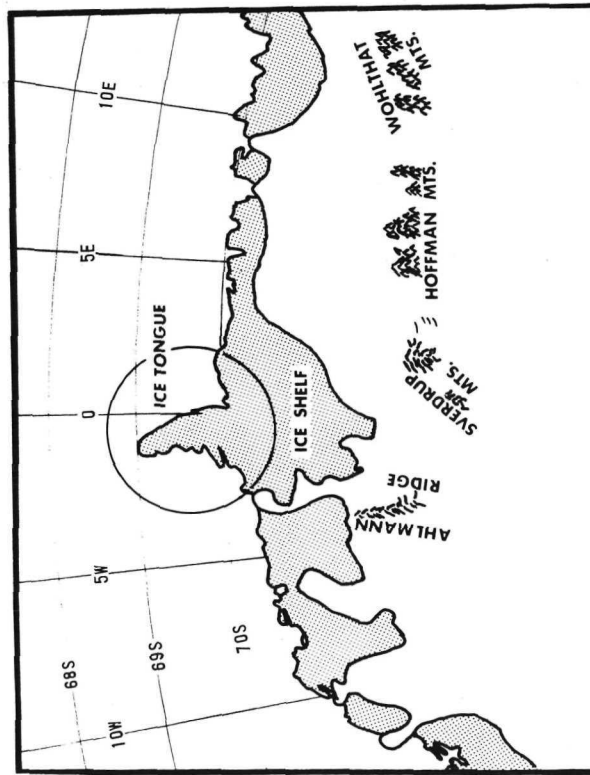
Nimbus AVCS, Orbit 49



NIMBUS 1

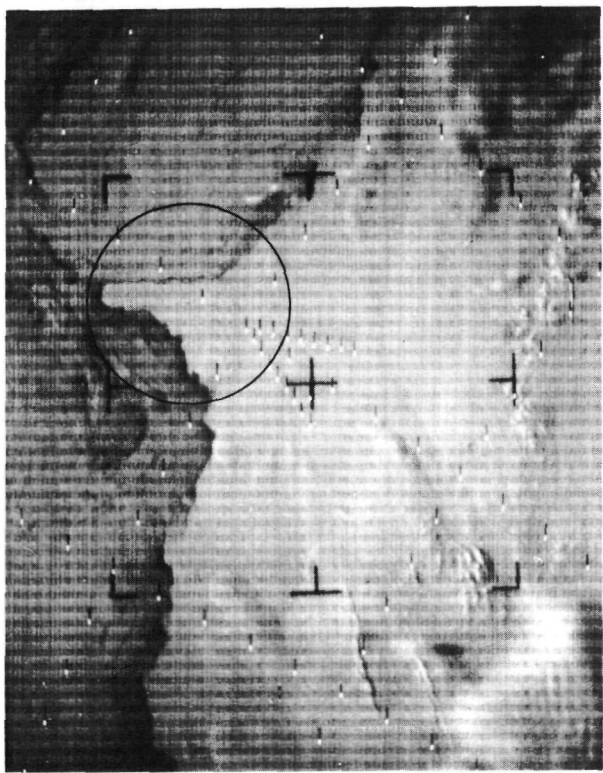
ICE TONGUE

31 AUGUST 1964



GENERAL COVERAGE OF EACH PICTURE

Nimbus AVCS, Orbit 1375

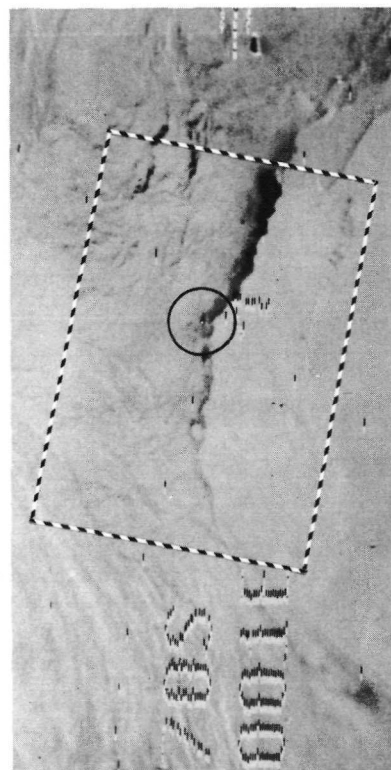


NIMBUS 2

ICE TONGUE - partially cloud obscured

26 AUGUST 1966

Nimbus IDCS, Orbit 2323



NIMBUS 3

NO ICE TONGUE

4 OCTOBER 1969

Figure 4-1 Changing Antarctic coastline observed by Nimbus satellites.

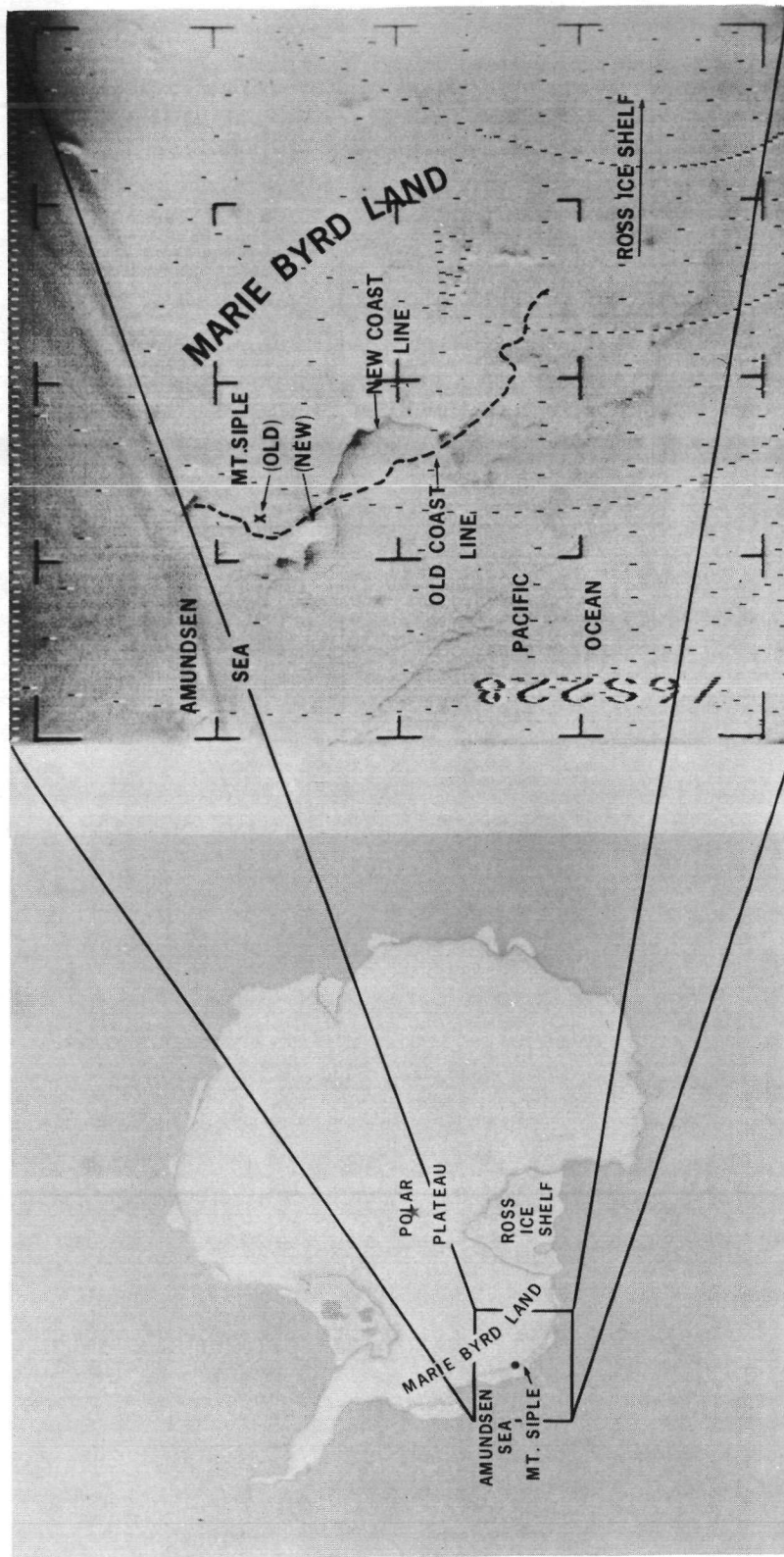


Figure 4-2 Antarctic map revisions derived from a Nimbus 1 AVCS picture recorded on orbit 184, 9 September 1964. (USGS, Chief Topographic Engineer, 1965)

be identified and mapped. Some major soil and vegetation groups can also be reliably identified using conventional thematic maps for correlation. For example, Figures 2-45 and 2-46 (of North Africa) show tonal patterns which correlate with vegetation/climatic types. Some geologic and geomorphic features visible in the imagery can also be identified when compared with conventional map data (Section 2.3). However, there are many tonal patterns which do not seem to correlate with any feature depicted in conventional maps. These patterns should be studied in greater detail.

The Nimbus 3 daytime HRIR imagery in Figure 4-3 illustrates an example of these unidentified patterns. There is a relatively sharp tonal boundary extending across central Canada from Lake Winnipegosis through Cold Lake to the Rocky Mountains. This line appears to represent either a soil or vegetation border between the prairie and coniferous forest, a hypothesis partially confirmed by soil and vegetation maps of the area. A tentative geology contact line drawn on the 1969 Canadian geology map (Geological Survey of Canada, 1969) agrees in part with the image boundary; however, there are significant differences between the boundary location in the imagery and the maps. Thus, the real physical significance of this tonal boundary in the satellite imagery is not readily apparent. More research is required before this feature can be unambiguously defined. When this feature is correctly interpreted, it could revise or add new information to Canadian thematic maps.

Figure 4-4 of Poland, showing the Gulf of Danzig area, is another typical example of the many Nimbus satellite images with a wealth of tonal patterns awaiting interpretation. It is probably impossible to correlate, exactly, all of these patterns and their tonal intensities with features in existing thematic maps. However, the patterns are real and may present a new perspective of the interrelationship of various natural and cultural features. Therefore, new information may be derived from an in-depth analysis of this picture which will improve existing thematic maps and give us a better understanding of the environment.

An example of thematic map information derivable from satellite imagery is shown in Figure 2-51. The tonal boundary is believed to represent the margins of the forest to tundra transition zone in Canada. In the forested region, the reflectance of the snow cover is decreased by the vegetation cover. The lower the reflectance, the greater the vegetation (tree) cover. The area below the boundary line has more than 30% woodland cover while that above it has less than 30% (Aldrich et al, 1969). A similar satellite signature for this kind of transition zone was found in two other Canadian areas. Consequently, this 30% boundary line was extrapolated across Canada using satellite imagery. Further ground checks should establish the reliability of this boundary definition.

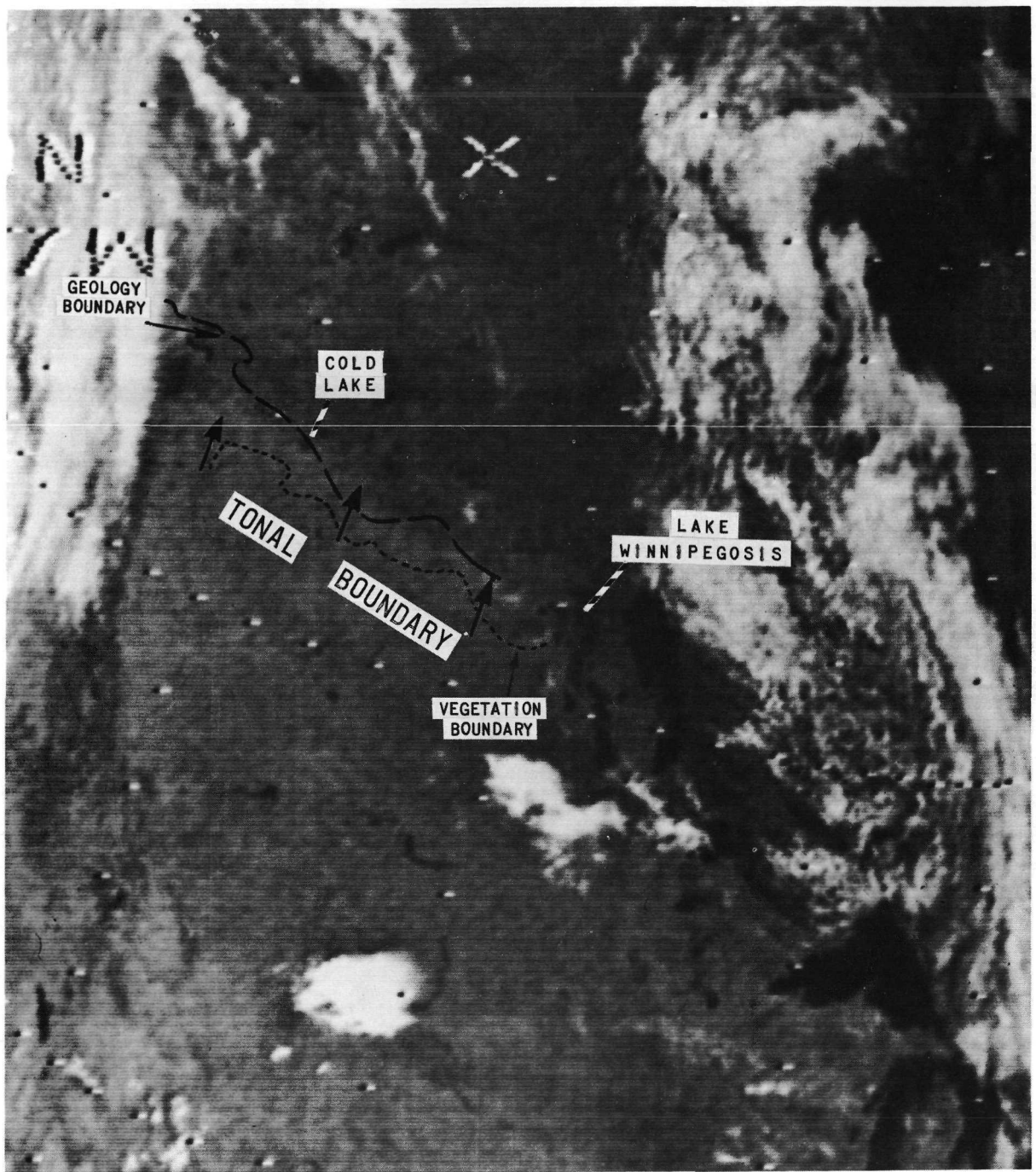


Figure 4-3 Nimbus 3 HRIR daytime image (orbit 1172, 10 July 1969) of northern United States and Canada showing tonal boundary extending across central Canada. The Great Lakes are in the lower right corner. The geology boundary (from map of Geological Survey of Canada, 1969) separates Upper Cretaceous, Cenomanian to Santonian (above) with Upper Cretaceous, early Campanian (below). The vegetation boundary (from vegetation map of Dept. of Interior, Canada, 1930) separates the northwestern coniferous forest (above) from transitional grove belt (below).

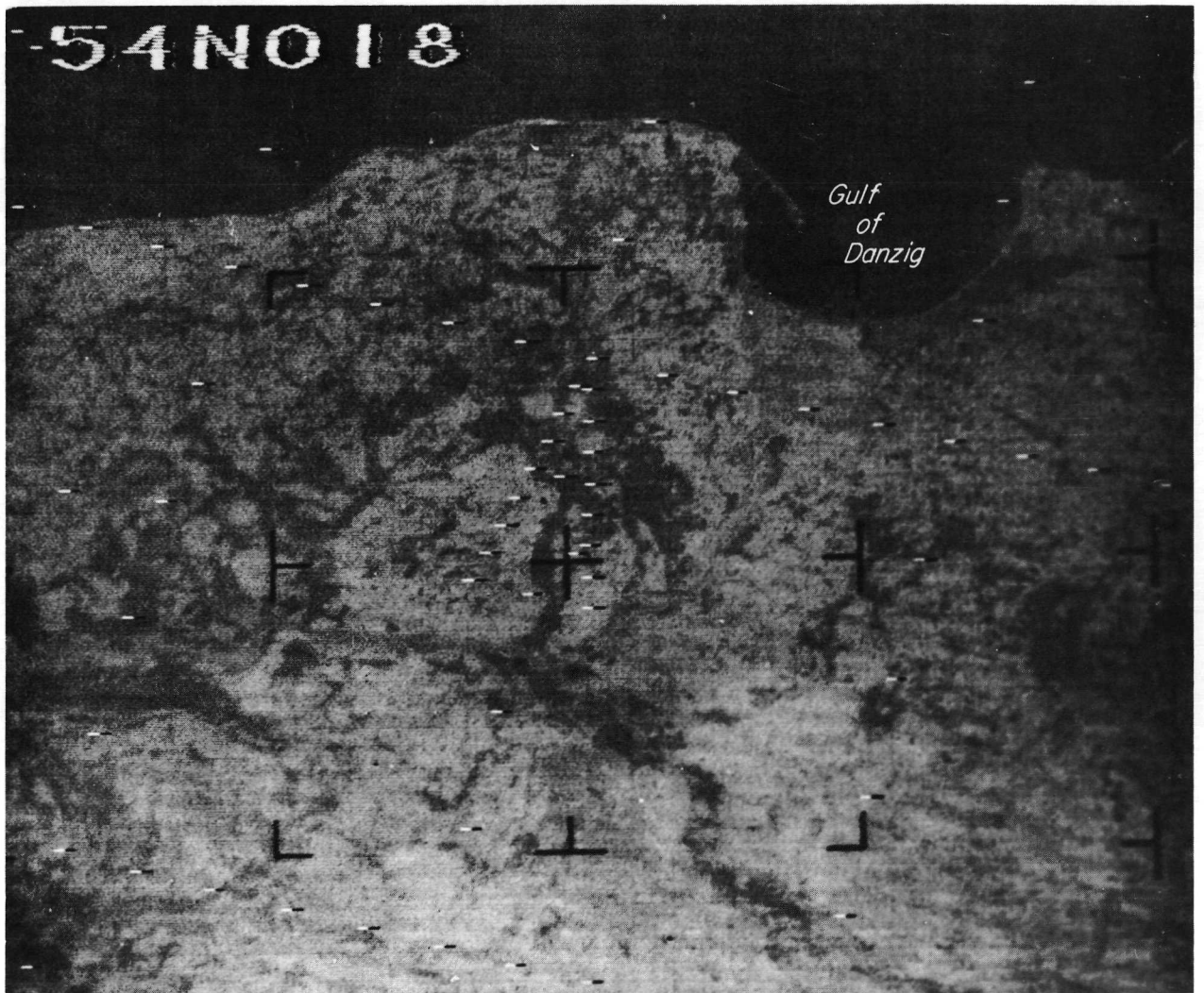


Figure 4-4 Nimbus 1 AVCS photograph of the Gulf of Danzig area, Poland taken on orbit 89, 3 September 1964.

4.3 Urban Analysis

Nimbus was not designed to provide data useful for analysis of urban areas. However, a malfunction during the Nimbus 1 launch resulted in a perigee of 423 km so that AVCS pictures taken at this altitude have a higher than nominal resolution, i. e., 330 meters for high-contrast features. As a result, Nimbus 1 provided photographs in which several major cities, their environs and associated highway systems were identifiable. Two brief analyses of these unique earth views were performed by ARA. The first examined the relationship between the size of urban areas identified in the satellite imagery and the populations of these areas. The second analyzed the ground features associated with certain tonal characteristics in a Nimbus 1 view of the Richmond/Petersburg, Virginia area.

4.3.1 Satellite Estimates of Population

Wellar (1969) examined the possibilities of using space photography in urban analyses. In this study, Wellar provided the following description of a signature for the analysis of urban centers in Gemini photographs:

"The signature of urban centers is similar for all (urban) centers, and is primarily the result of tonal-textural differentiation between the centers and their environs. The urban centers have a lighter tonal appearance and more variegated texture than the surrounding forested and range land areas"

These identification keys developed by Wellar for the Gemini photography should be equally applicable to Nimbus 1 AVCS pictures, with the difference that the Gemini photographs are in color and the Nimbus 1 photographs are not.

In our examination of Nimbus "urban center" signatures, we used Wellar's keys to define and measure the urban areas of six U. S. cities in Nimbus 1 AVCS photographs. Figures 4-5a and 4-5b locate five of these cities on a Nimbus 1 photograph and population map. The size of the measured areas were converted to population estimates using an empirical equation derived by Norbeck (1965) which states that for certain types of U. S. cities the area A (in square miles), is related to the population, P , by the expression $A = 0.00151 P^{0.88}$. Figure 4-6 shows the estimated population plotted against the population of the corresponding city taken from the 1960 census. Note that except for Newport News/Hampton and, to a lesser degree, Fredericksburg, a fairly good linear fit is achieved for the data. One explanation for the Newport News/Hampton anomaly is that there may be a high proportion of high-rise apartment dwellings in the central city; another, that the geographical location constrains the type of normal growth defined by the Norbeck allometric model.

4.3.2 Richmond/Petersburg Evaluation

As defined in the previous section, the urban center signature is based on the tonal-textural differentiation between the centers and their environs. Even at a resolution of 330 meters it is difficult to differentiate light-colored soils from similarly light-colored roof tops. Thus, using Wellar's definition for Nimbus 1 pictures, we are in fact mapping a tonal shape, and to some extent a texture, which corresponds to a complex integration of many surface features.

In the Richmond/Petersburg example (Figure 4-5a) it was first thought that the dark linear area (indicated by arrow) was the James River which flows through the city of Richmond (see Figure 4-7). Careful review of the U. S. Geological Survey 7.5 minute quadrangle maps and other Nimbus photographs for the area showed, however, that the James River is not visible in the center of Richmond. The lineation is, in fact, a rather swampy area traversed by the Chickahominy River. In 1964, around the time of the Nimbus photograph the Richmond area was experiencing an extended drought and, presumably, the only area with green vegetation (low-reflecting in the 0.45 to 0.65 μm spectral interval of the AVCS) would be the damp river area. The surrounding lands should have largely dormant (brown) grasses and perhaps leaves. The dark V-shaped pattern projecting into the western part of the city's tonal pattern corresponds to the approach of the James River.

Using the feature identified as the Chickahominy River, it is a simple task to correctly map the boundaries of the Richmond urban area in the photograph. Comparison between the urban area outlined in the Nimbus photographs (Figure 4-5a) and the 7.5 minute quadrangle (Figure 4-8) areas of Richmond, as shown on the updated 1970 map, indicates that the apparent Nimbus tonal signature defined an area larger in all directions than is indicated in the map. This disparity is reduced by precise density "slicing" of the Nimbus photograph as shown in Figure 4-9a, in which the redefined urban area is outlined. Comparison with the map in Figure 4-7 indicates fairly close correspondence between the area defined by brightness tonal "signature" and the area of major urban center. The less bright areas now correspond to several areas outside the central core area.

The tonal zone which represents the most extensive outline for Richmond probably corresponds to the "tonal-texture differentiation" (Wellar, 1965) between the generally open agricultural lands common to many previous agriculture-centered cities, and the mostly wooded land beyond. If we accept past urban development patterns as a model, the pressure for housing development is most often placed on open farmlands. The rate of expansion into these farmlands is, of course, subject to many factors. However, one may conclude that the largest tonal signature area for Richmond or other cities represents the eventual size of the cities. If the assumptions of the previous paragraph are even grossly valid, then we can specu-

late that Richmond and Petersburg, linked by I-95 highway, will become a single massive city in the long-term future.

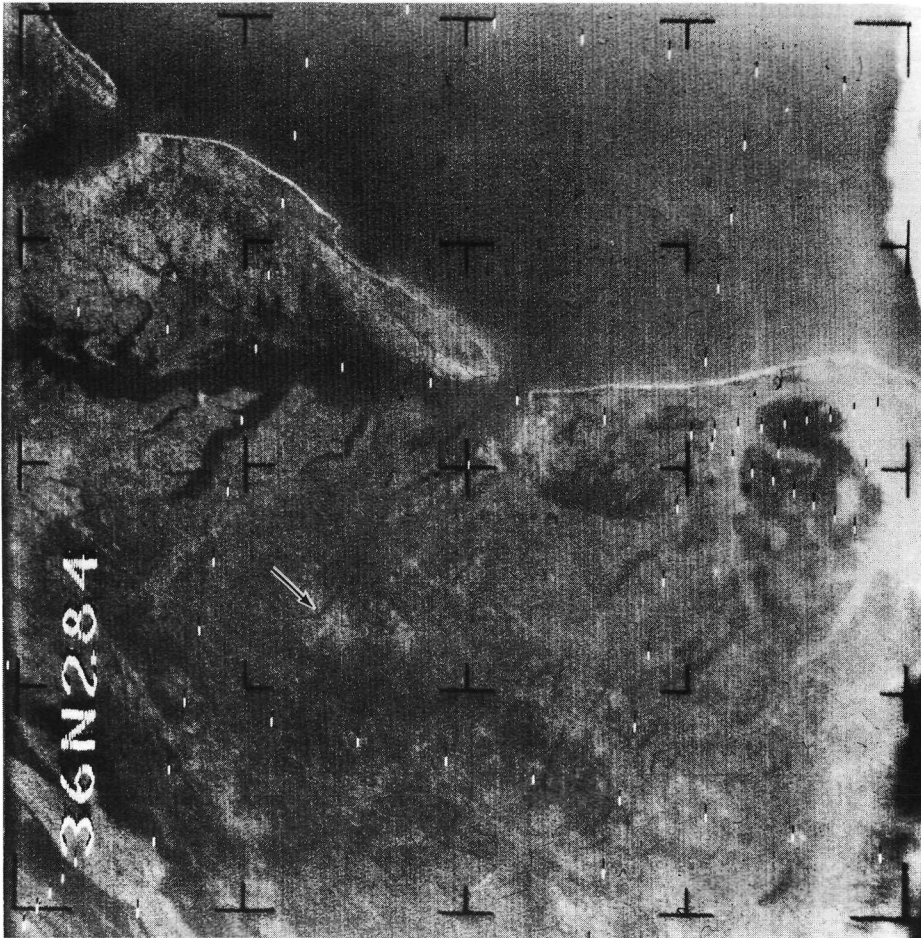
The growth of our urban centers has already led some to speculate that by the year 2000 the area from Boston, Massachusetts, to Washington, D. C., may well be one large megalopolis (Landsberg, 1970). At present, this area is believed to be warmer by 2° to 4° . Infrared sensors such as the HRIR can observe and map such urban heat anomalies. The ITOS scanning radiometer, a device similar to the THIR, has in fact detected this temperature phenomenon. Figure 4-10 (Rao, 1970), shows the warm zone from New York City to Washington, D. C., as observed by the ITOS.

4.4 Data Collection from Remote Platforms

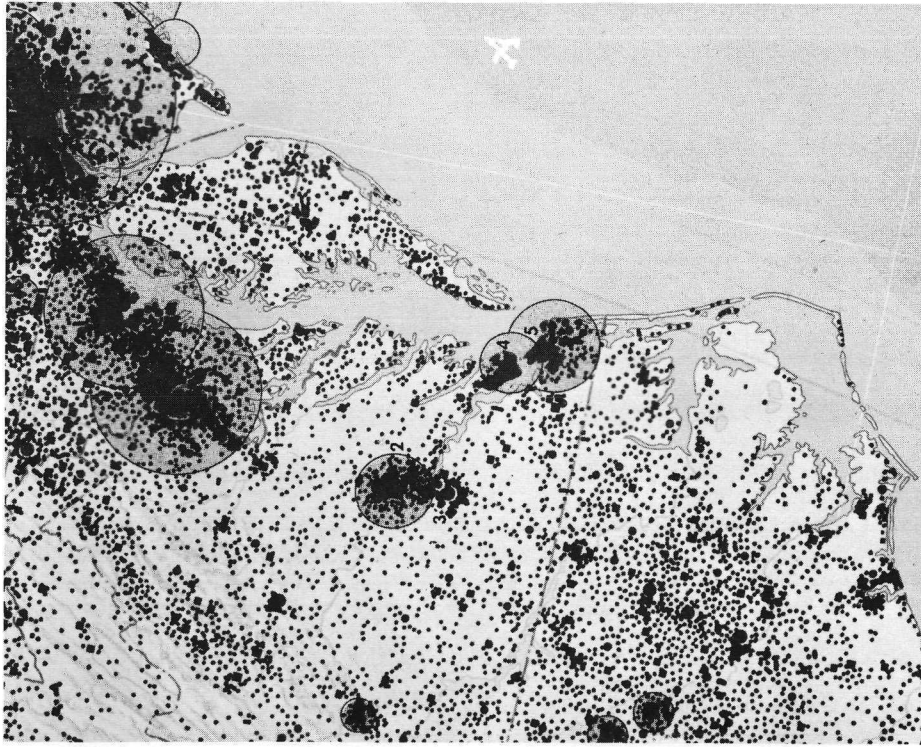
The Interrogation, Recording and Location System (IRLS) flown on Nimbus 3 and 4 represents a departure from the traditional concept of remote sensing. Rather than making the actual observations, the system simply collects the recorded data from various remote platforms. The information is relayed to the receiving site and subsequently distributed to the scientific community for investigation and analysis. Using a range-finding system, platform locations can be determined after two or more interrogations. Such a system is ideal for performing a broad class of measurements which are beyond the capabilities of conventional remote-sensing operations. Some examples include the monitoring of subsurface parameters in ocean regions, measuring precipitation and soil moisture, analyzing air and water pollution concentrations, and tracking wildlife and fish.

Figure 4-11 illustrates a typical IRLS buoy system employed by the Naval Oceanographic Office. Such a system can provide surface and subsurface measurements of temperature, salinity and water productivity. By monitoring the buoy's drift rate, ocean or lake currents can be identified. Figure 4-12 shows the Nimbus 3 tracking of an IRLS buoy off the coast of Puerto Rico. The buoy had broken loose from its original position, but was found a few days later with the aid of the IRLS system. With an increase in platforms and onboard storage, the interrogation capability has increased from 20 per orbit for Nimbus 3 to 370 per orbit for Nimbus 4. As the IRLS system continues to grow, and more experience is gained in processing and disseminating the data, a valuable background of knowledge and skill will be built up. This background would be directly applicable to the development of the oceanography systems of future ERTS missions.

A female elk was tracked by the IRLS experiment on Nimbus 3 in the National Elk Refuge at Jackson Hole, Wyoming, in April 1970. This was the first time that an animal had ever been tracked by satellite (Craighead et al, 1970). The elk was equipped with an instrument collar (Figure 4-13) which transmitted the skin temper-



a) Nimbus I AVCS image

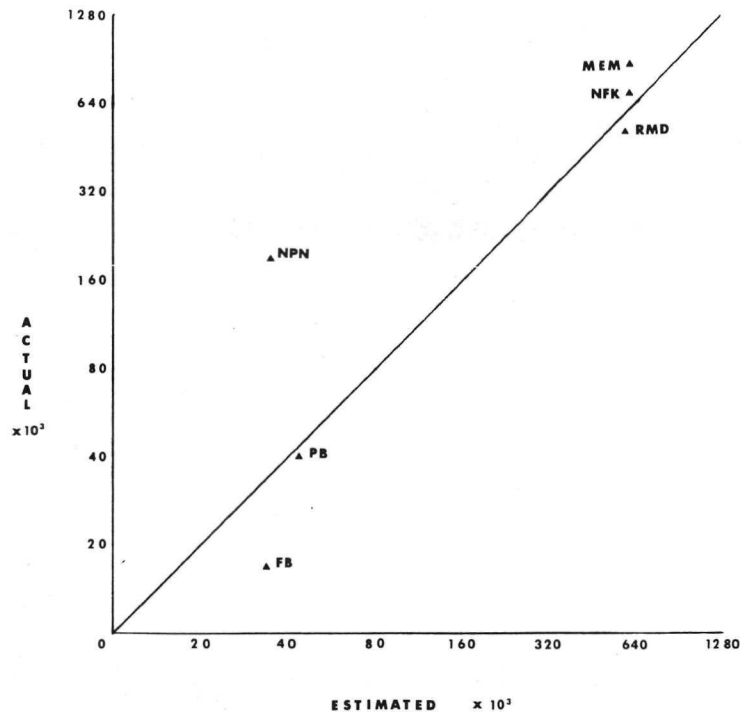


b) Population map

dot concentration is proportional to population density

- 1) Fredericksburg
- 2) Richmond
- 3) Petersburg
- 4) Newport News/Hampton
- 5) Norfolk

Figure 4-5 Nimbus I AVCS photograph of the Chesapeake Bay area taken on orbit 137, 6 September 1964, compared with population map of same area.



NPN = Newport News/Hampton
 MEM = Memphis (not shown on Fig. 4-5)
 NFK = Norfolk
 RMD = Richmond
 PB = Petersburg
 FB = Fredericksburg

Figure 4-6 Actual (U. S. Census Bureau, 1960) vs Nimbus estimated population measurements. The Nimbus estimates were calculated from an empirical equation derived by Norbeck (1965).

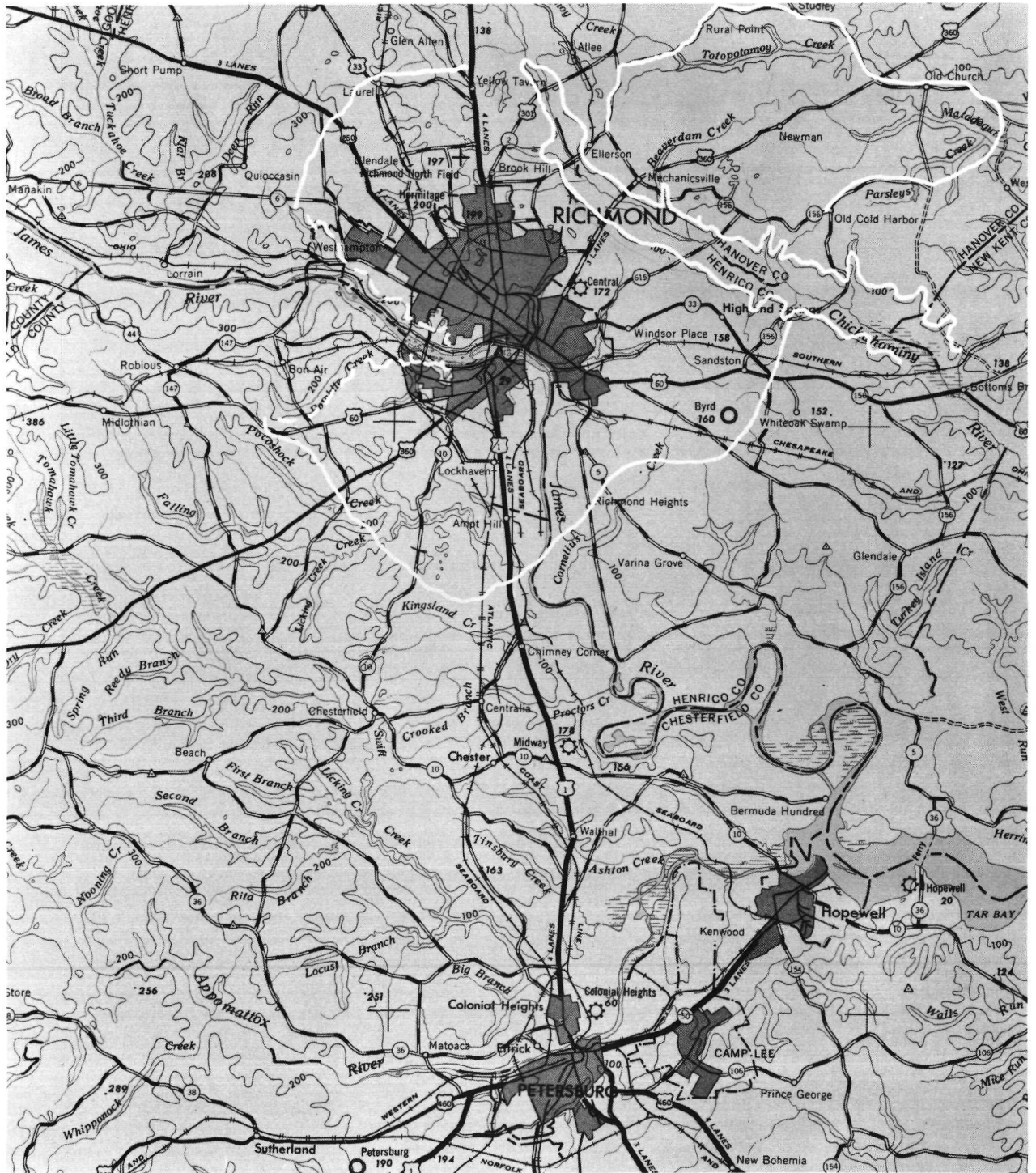
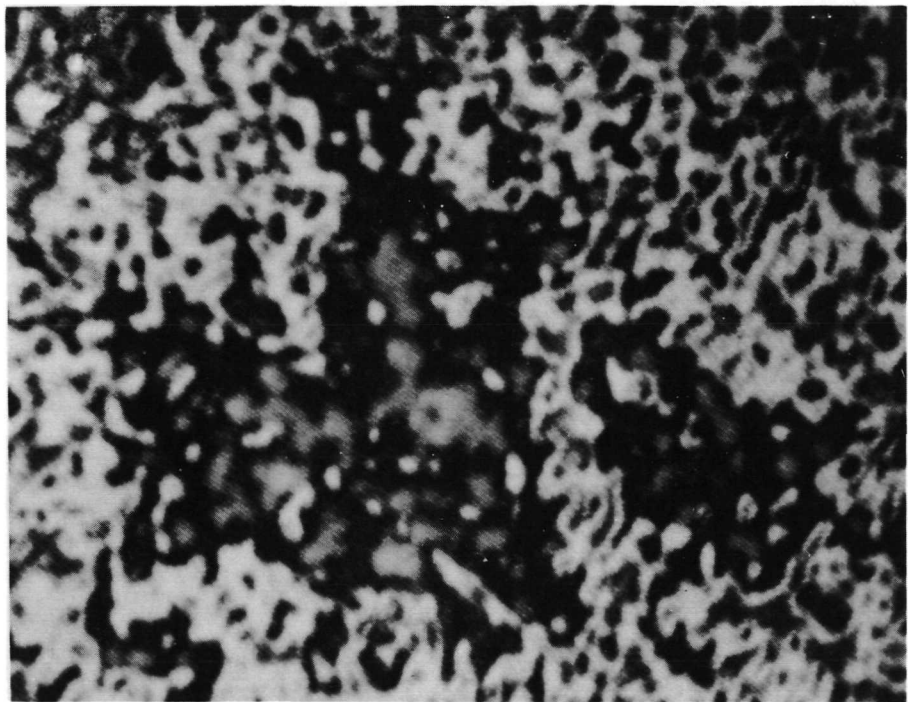


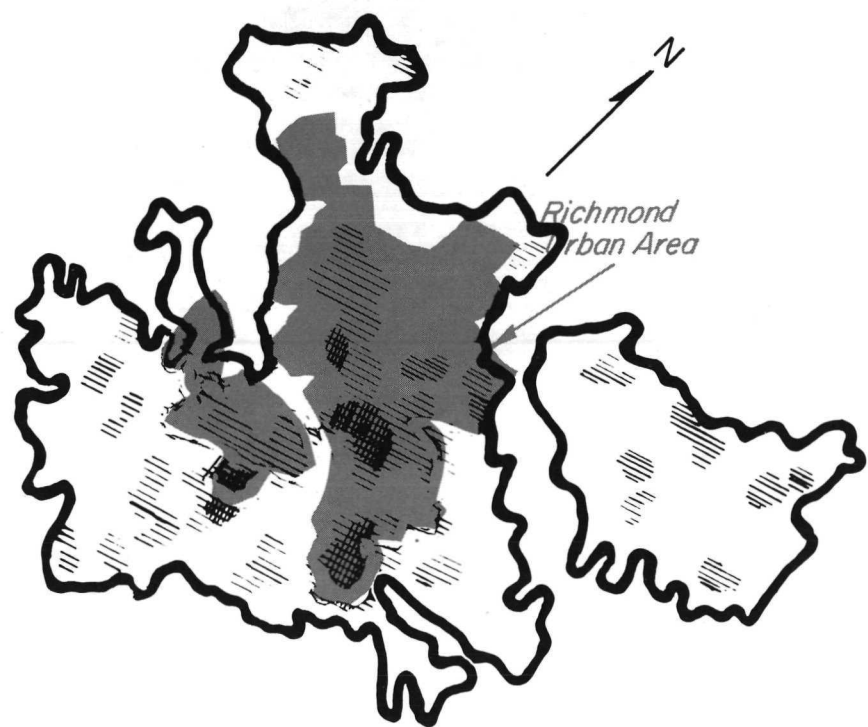
Figure 4-7 Richmond/Petersburg area map (from U. S. Geological Survey 1:250,000 map, Richmond, Virginia Quadrangle, 1964). The area delineated in white is the urban tonal outline measured from the Nimbus photograph of Figure 4-5a.



Figure 4-8 Richmond area map (from U. S. Geological Survey 7.5 Minute Quadrangle Map, 1964). The area enclosed shows the urban tonal outline measured from the Nimbus photograph of Figure 4-5a.



a) "Density Slicing" display originally prepared in color with the Spatial Data System's color densitometer.



b) Outlines of the density area in (a) superimposed on the urban area of Richmond (shaded areas represent higher densities on the image).

Figure 4-9 Comparison of "Density Slicing" display of the Richmond area in Figure 4-5a and the urban area of Richmond as shown in Figure 4-7.



- 1) New York metropolitan area
- 2) Philadelphia/Trenton metropolitan area
- 3) Baltimore metropolitan area
- 4) Washington, D.C. metropolitan area

Figure 4-10 Computer-produced map of the U. S. east coast derived from ITOS Scanning Radiometer data (19 October 1970), showing thermal anomalies correlation with major urban centers. Warmer temperatures are indicated by the horizontal stipple pattern. The warm zones along the coastline represent the smear introduced by the sensor scan over warmer waters. (Rao, 1970)

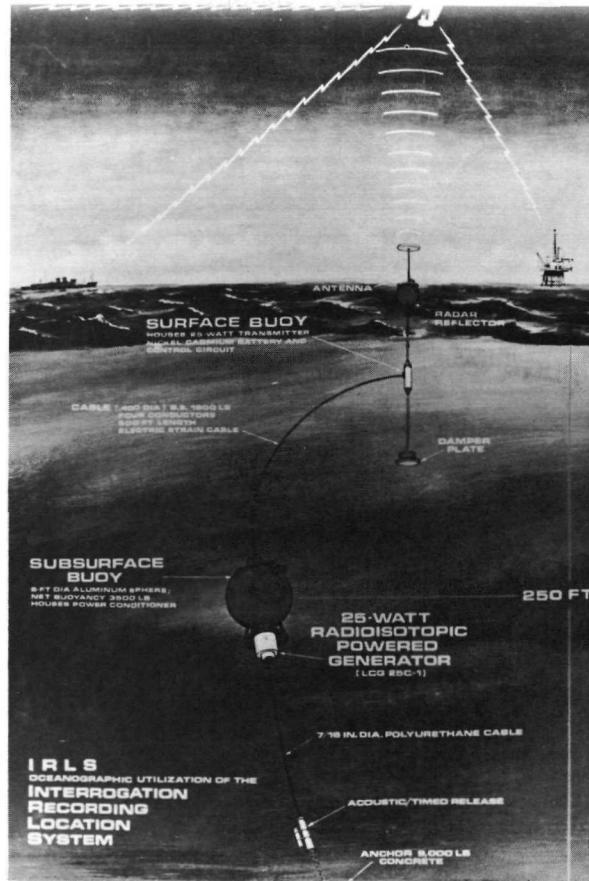


Figure 4-11 Nimbus IRLS oceanographic buoy system

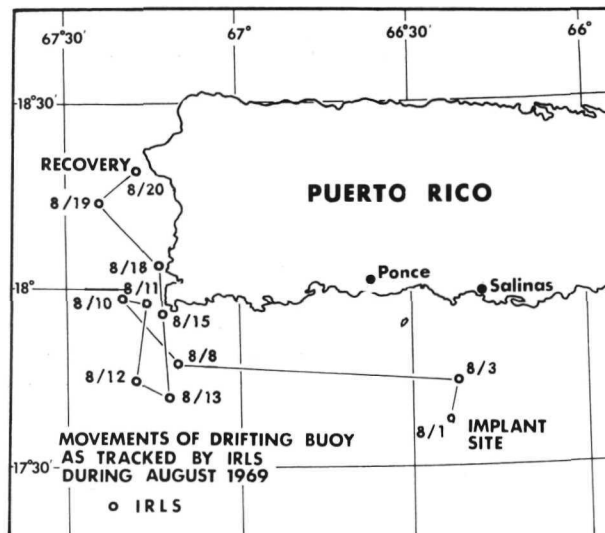


Figure 4-12 Movement of drifting buoy as tracked by Nimbus 3 IRLS during August 1969. (Nimbus III Data Catalog, Vol. 4)



Figure 4-13 Elk tracked by the Nimbus 3 IRLS on the National Elk Refuge, Jackson Hole, Wyoming. The elk is equipped with an instrument collar transmitting skin temperature and light intensity to the interrogating Nimbus satellite.

ature of the animal and the light intensity of the environment to the interrogating Nimbus satellite. Location errors varied from 1 to 15 km. Craighead further comments that the IRLS accuracy of location can be improved to near the theoretical limit of ± 1 km by improved antenna systems, and that the collar weight can be reduced to 50 grams, or less, by microminiaturization of the instruments and use of a doppler-shift satellite tracking system. They conclude that satellite tracking and data collection systems can provide powerful new tools for studying biological phenomena, the uniqueness lying in the ability to combine tracking of animals with simultaneous monitoring of physiological and environmental parameters.

According to the U. S. Geological Survey (Forrester, 1970) the Nimbus 4 satellite is now relaying the temperature of steam emitted from the snow-capped Mt. Rainier volcano in Washington. Eight times each week as the Nimbus satellite passes over the 14,410 ft mountain, the IRLS receives radio signals from a special temperature-monitoring station located at the peak of the mountain (Figure 4-14). The signals are, in turn, relayed to a ground station at Fairbanks, Alaska, and then, by way of land lines, transmitted to National Aeronautics and Space Administration/GSFC. This is the first time that volcanic activity information has been relayed through satellites. Future similar experiments are planned by the Interior Department, Earth Resources Observation System (EROS) program and NASA's Earth Resources Technology Satellite (ERTS) program to begin in 1972.

4.5 Brush and Forest Fire Detection

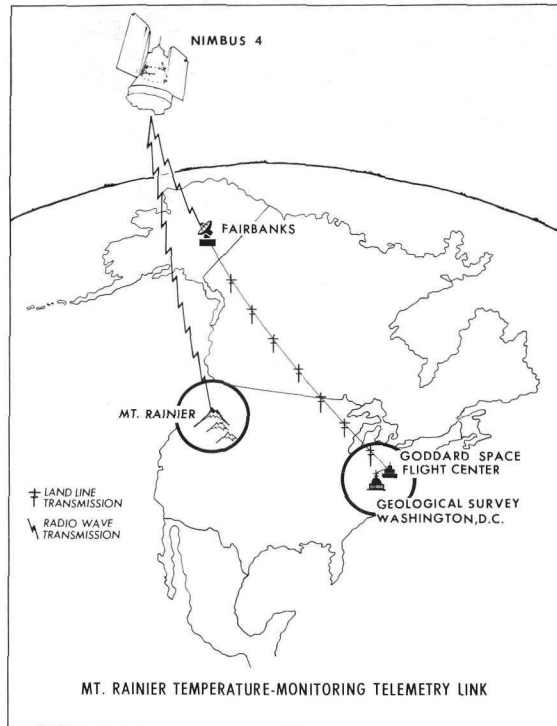
Figure 4-15 from the Nimbus 4 IDCS taken on 27 September 1970, shows smoke plumes from major brush fires in Southern California. Newspaper reports indicated that at the time of the picture 140,000 acres of brush land were burning or had burned in the vicinity of San Diego (1); 105,000 acres had burned in the Los Angeles area (2); and 5000 acres were burning in the Sequoia National Forest (3).

No systematic search has been made of Nimbus data for other brush fires or forest fires. It is probable that a search would locate many more such occurrences.

4.6 Ship Plumes

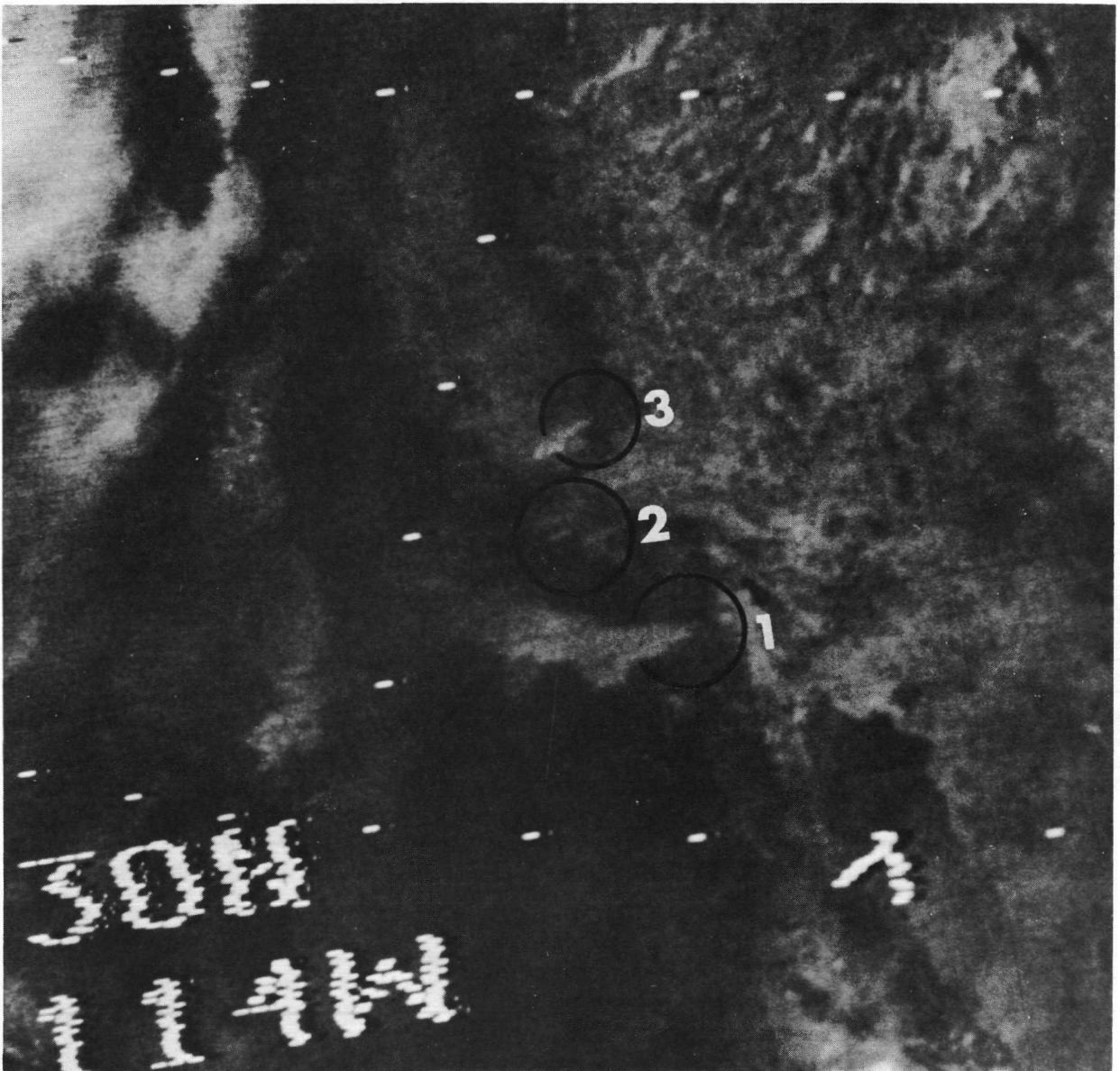
The long, thin, anomalous cloud bands in the Nimbus 3 IDCS pictures shown in Figure 4-16 are most probably ship plumes or "trails." Ship trails were found by Bowley (1967) to be accompanied by the following meteorological conditions:

- 1) Light surface winds, seldom over 10 knots.
- 2) A quasi-stationary anticyclonic system over a large water body.
- 3) Light to heavy fog.



U.S. Department of the Interior / Geological Survey

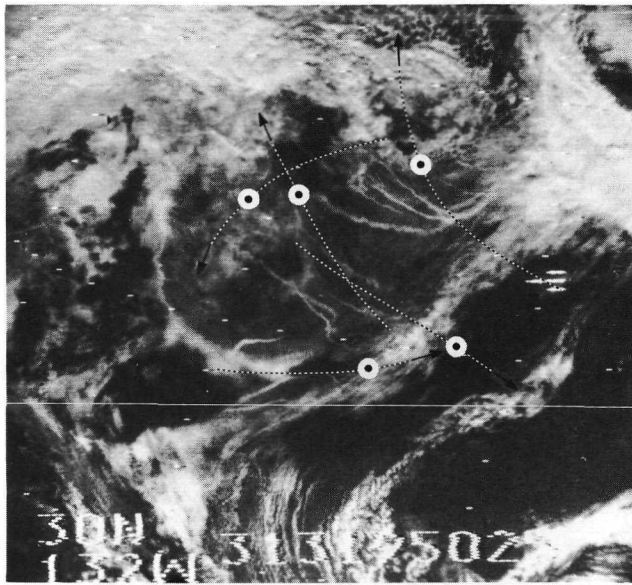
Figure 4-14 Aerial view of 14,410 ft Mt. Rainier, Washington. Radio equipment is located on the rim of the west crater and is used to transmit volcano temperature to the Nimbus 4 satellite (U. S. Geological Survey Photograph). Lower portion of figure shows the telemetry link.



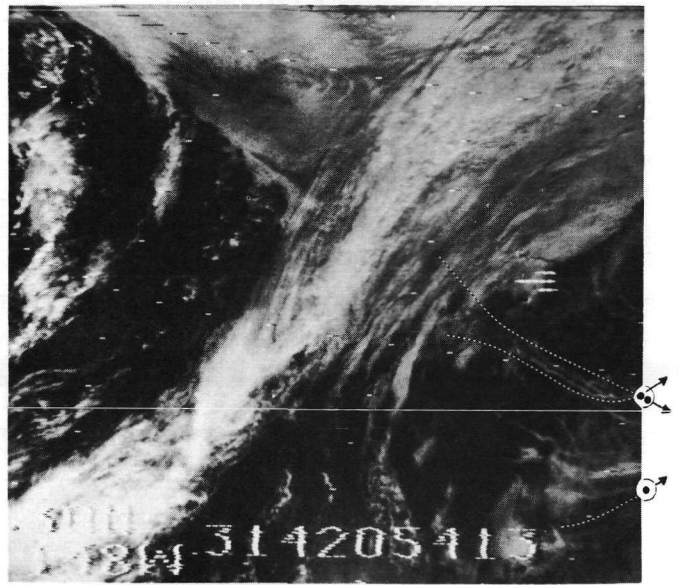
- 1) San Diego - 140,000 acres burning (1 plume)
- 2) Los Angeles - 105,000 acres burned (3 plumes)
- 3) Sequoia National Forest - 5,000 acres burning (1 plume)

(The Great Salt Lake is located in upper-right corner and the Salton Sea is just above (1).)

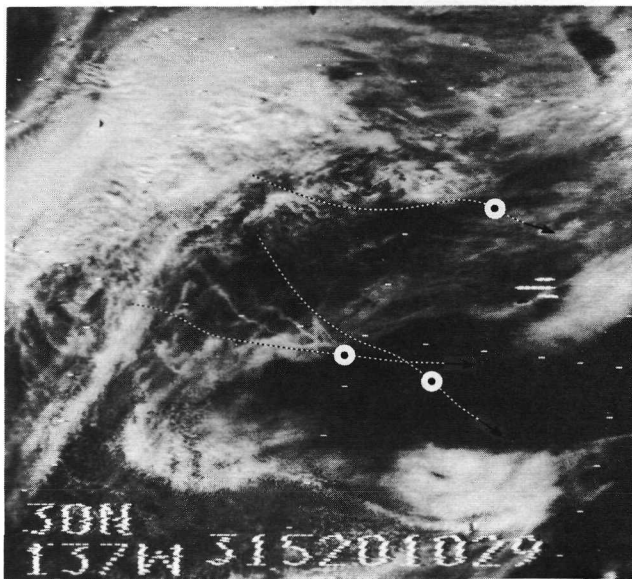
Figure 4-15 Southern California brush fire smoke plumes. This central portion of a Nimbus 4 IDCS picture taken on orbit 2316, 27 September 1970, recorded smoke plumes from five of the major brush fires in Southern California.



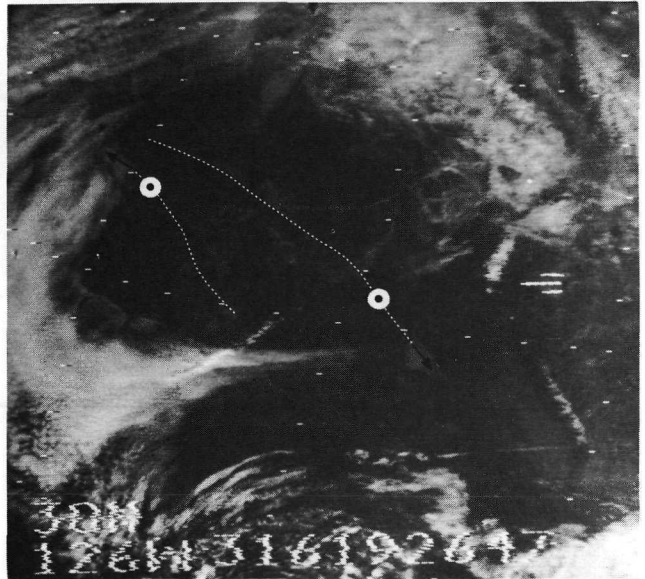
Orbit 2809, 9 November 1969



Orbit 2823, 10 November 1969



Orbit 2836, 11 November 1969



Orbit 2849, 12 November 1969

Reporting ship locations at IDCS picture time are marked with "O".

Figure 4-16 Nimbus 3 IDCS observations of ship plumes in the Northeast Pacific. The long, thin, anomalous cloud bands are probably ship plumes.

- 4) Temperature/dew point spreads of 0° to 3°F .
- 5) Air temperatures equal to, or slightly lower than, the sea water temperatures.
- 6) Air temperatures between 40° to 60°F .
- 7) Saturated conditions in a low unstable surface layer with extremely dry air aloft.

Conover (1966) had previously speculated that, "Aitkin (10^{-7} - 10^{-4} cm) nuclei in ship exhausts are carried upward to form cloud droplets at slight supersaturation." Observation from aircraft reported by Conover (1969) confirmed that ship exhausts were producing "ship trails."

The satellite measurements of ship trails thus provides a significant observation of man-made pollution. A similar cloud plume has been observed over the Caspian Sea, in satellite photographs, which may relate (unconfirmed) to a power station on the eastern shore. Careful examination of existing satellite data may reveal similar man-made plumes from power stations along the U. S. West Coast.

5. CONCLUSIONS AND RECOMMENDATIONS

In this report we have presented a survey of the uses of Nimbus data for studies of the earth and its resources. The value of these data lies in the ability of the Nimbus sensors to provide repeated global and synoptic observations of the earth's surface. Synoptic, small-scale/large-view Nimbus data are of value in illustrating large, conspicuous terrestrial features and in providing low resolution images of high-latitude areas for which no other high resolution satellite coverage is available. Thus, the Nimbus data now available can be used for background studies in preparation for the use of ERTS data designed specifically for earth resources surveys.

Every study discussed in this report or cited in the list of References and Bibliography is offered as a recommendation or suggestion for further research on the use of the Nimbus data. Some of these recommendations may be too optimistic but these suggested studies hold the key to a better understanding of satellite data, their limitations, and their unexpected applications, and are needed to prepare the scientific community for the impact of ERTS.

As part of this study, letters were sent to various individuals and agencies requesting information on current and potential uses of Nimbus data in earth resource surveys. The replies were in the form of published reports, bibliographies, recommendations for future studies, and projects being currently planned. From these replies, we can conclude that, although Nimbus data have not been extensively applied to earth resources problems, the areas in which the data have been used with some degree of success are:

Geology

- Regional rock exposures, faults, joints and lineaments
- Regional structural geology
- Volcanic eruptions

Hydrology

- Basin drainage patterns
- Relative surface moisture in desert areas
- Former river courses
- Snow cover, its changes and runoff
- Lake surface temperatures
- Lake ice

Oceanography

- Sea surface temperatures
- Sea current boundaries

- Upwelling
- Polar ice

Some limited success has been obtained in identification of lithologies, vegetation conditions and vegetation density in the presence of snow.

Applications of Nimbus data not yet fully exploited include:

- Relationships of surface composition and HRIR and THIR temperature variations in time and space.
- Correlation of snow-line changes with snow-melt and subsequent runoff in large watersheds.
- Correlation of Nimbus 3 HRIR reflectances (0.7 to 1.3 μm) with known surface materials, and atmospheric structure, to better understand and prepare for the use of the ERTS Multi-spectral Scanner (MSS) Channel 4 (0.8 to 1.1 μm) measurements.
- Correlation of anomalous sunglint patterns with sea state and surface temperatures using Nimbus 4 THIR and IDCS data.
- Use of bidirectional reflectances as signatures for the identification of clouds, ice, snow, water and other surfaces employing data from the Nimbus 3 daytime HRIR, and the MRIR albedo channels.
- Search for forest and brush fires.
- Search for volcanic activity in Nimbus infrared data.
- Development of new classification systems for lakes and drainage basins based on shape and pattern.
- Comparison of Nimbus HRIR and THIR temperatures of the Great Lakes with ART temperatures.

The application of Nimbus data to both the aforementioned and other potential studies necessitates a more widespread knowledge of the data in the scientific community. This can be achieved by:

- 1) Making the public more aware of the existence and uses of these data. This could be accomplished by wider dissemination of the results and conclusions of researchers already familiar with the data. It is hoped that this technical report will help in achieving this accomplishment.
- 2) Giving consideration to further earth resources remote sensing research with Nimbus as a source of electronically acquired spacecraft data. Additional suggestions and support for this research should be given to interested groups or individuals.

- 3) Continued coordination between the Nimbus program and other existing and future multidisciplinary remote-sensing missions such as ERTS.
- 4) Emphasizing the international aspect of the Nimbus program by the continued support of the exchange of information and ideas between scientists of various nations through official channels which are already established.

It should be pointed out that the potential for earth resources studies using Nimbus data will be greatly enhanced in the future with the additions of the Surface Composition Mapping Radiometer (SCMR) with its 600-meter resolution, and the Electrically Scanning Microwave Radiometer (ESMR) with its ability to "see" through nonprecipitating clouds. These two experiments, to be flown on Nimbus E in 1972, concurrent with ERTS, are explained in detail in Appendix A. The usefulness of the SCMR to earth resources studies lies in its ability to provide high-resolution radiation measurements in the 8 μm and 11 μm bands. The ESMR experiment as precursor to more advanced and higher resolution microwave systems, will pave the way for basic research on the microwave characteristics of surfaces as viewed from satellite heights.

Careful review of the studies summarized in this report should provide substantial information for: (1) The training of potential ERTS data users; (2) further studies of the earth using the unique temporal and spatial observing characteristics of Nimbus; and (3) the development of programs which can make operational use of the Nimbus data in earth resource surveys.

Page Intentionally Left Blank

6. REFERENCES AND BIBLIOGRAPHIES
(BY SECTION)

6.1 Section 1

References

- Barnes, J. C. and D. T. Chang, 1968: Accurate Cloud Cover Determination and its Effects on Albedo Computations, Final Report Contract No. NAS 5-10478, Allied Research Associates, Inc.
- Barnes, J. C., D. T. Chang and J. H. Willand, 1970: Improved Techniques for Mapping Sea Ice from Satellite Infrared Data, Final Report Contract No. E-67-7(N), Allied Research Associates, Inc.
- Glaser, A. H., J. C. Barnes and D. W. Beran, 1968: "Apollo Landmark Sighting: An Application of Computer Simulation to a Problem in Applied Meteorology," J. of Appl. Meteor. 7, 768-779.
- Greaves, J. R., J. H. Willand and D. T. Chang, 1968: Observation of Sea Surface Temperature Patterns and Their Synoptic Changes Through Optimal Processing of Nimbus II Data, Final Report Contract No. NASW-1651, Allied Research Associates, Inc.
- Greaves, J. R., P. E. Sherr and A. H. Glaser, 1969: "Cloud Cover Statistics and Their Use in the Planning of Remote Sensing Missions," J. of Remote Sensing, 1(2), 95-101.
- Greaves, J. R. and D. T. Chang, 1970: Technique Development to Permit Optimum Use of Satellite Radiation Data, Final Report Contract No. N62306-69-C-0027, Allied Research Associates, Inc.
- Hanel, R. A. and B. J. Conrath, 1970: Thermal Emission Spectra of the Earth and Atmosphere Obtained from the Nimbus 4 Michelson Interferometer Experiment, NASA Publication X-620-70-244 (preprint), NASA, Goddard Space Flight Center.
- Kilston, S. D., R. R. Drummond and C. Sagan, 1966: "A Search for Life on Earth at Kilometer Resolution," ICARUS: International Journal of the Solar System, 5(1), 79-98.
- Nordberg, W. and R. E. Samuelson, 1965: "Terrestrial Features Observed by the High Resolution Infrared Radiometer in Observations from the Nimbus I Meteorological Satellite," NASA Publication SP-89, 37-46.
- Sabatini, R. R. and J. E. Sissala, 1968: Project NERO (Nimbus Earth Resources Observations), Technical Report No. 7, Contract No. NAS 5-10343, Allied Research Associates, Inc.

- Salomonson, V. V., 1969: Cloud Statistics in Earth Resources Technology Satellite (ERTS) Mission Planning, NASA Publication X-622-69-386, Goddard Space Flight Center, Greenbelt, Maryland.
- Shenk, W. E. and V. V. Salomonson, 1970: "A Multispectral Technique to Determine Sea Surface Temperature Using Nimbus II Data," Paper presented at the Fall Meeting of the American Geophysical Union, San Francisco, Calif.
- Sherr, P. E., A. H. Glaser, J. C. Barnes and J. H. Willand, 1968: World-Wide Cloud Cover Distributions for Use in Computer Simulations, NASA CR-61226, Contract No. NAS 8-21040, Allied Research Associates, Inc.
- Smith, W. L., P. K. Rao, R. Koffler and W. R. Curtis, 1970: "The Determination of Sea Surface Temperature from Satellite High Resolution Infrared Window Radiation Measurements," Mon. Wea. Rev. 98, 604-611.
- Williamson, E. J. and G. Warnecke, 1969: The Influence of Cloud Distribution on the Global Coverage of Remote Sounding Systems, Inhouse paper - Research conducted by National Academy of Sciences, Resident Research Associates at the Laboratory for Meteorology and Earth Sciences of NASA/GSFC.

Bibliography

- Aeronomy and Meteorology Division, 1965: Nimbus I High Resolution Radiation Data Catalog and User's Manual, NASA, Goddard Space Flight Center, Greenbelt, Maryland.
- Nimbus Project, 1965: Nimbus I User's Catalog: AVCS and APT, prepared by Allied Research Associates, Inc., for NASA, Goddard Space Flight Center, Greenbelt, Maryland.
- Nimbus Project, 1966a: Nimbus II User's Guide, prepared by Allied Research Associates, Inc., for NASA, Goddard Space Flight Center, Greenbelt, Maryland.
- Nimbus Project, 1966b: The Nimbus II Data Catalog, Vols. 1, 2, 3, 4 and 5, prepared by Allied Research Associates, Inc., for NASA, Goddard Space Flight Center, Greenbelt, Maryland.
- Nimbus Project, 1966c: Nimbus II HRIR Montage Catalog, prepared by Allied Research Associates, Inc., for NASA, Goddard Space Flight Center, Greenbelt, Maryland.
- Nimbus Project, 1967a: Nimbus II MRIR Pictorial Data Catalog, Vols. 1 and 2, prepared by Allied Research Associates, Inc., for NASA, Goddard Space Flight Center, Greenbelt, Maryland.

- Nimbus Project, 1967b: The Nimbus II AVCS World Montage Catalog, prepared by Allied Research Associates, Inc., for NASA, Goddard Space Flight Center, Greenbelt, Maryland.
- Nimbus Project, 1969a: The Nimbus III User's Guide, prepared by Allied Research Associates, Inc. (ed: R. R. Sabatini), for NASA, Goddard Space Flight Center, Greenbelt, Maryland.
- Nimbus Project, 1969b: The Nimbus III Data Catalog, Vols. 1, 2, 3, 4, 5 and 6, prepared by Allied Research Associates, Inc., for NASA, Goddard Space Flight Center, Greenbelt, Maryland.
- Nimbus Project, 1970a: The Nimbus IV User's Guide, prepared by Allied Research Associates, Inc. (ed: R. R. Sabatini), for NASA, Goddard Space Flight Center, Greenbelt, Maryland.
- Nimbus Project, 1970b: The Nimbus 4 Data Catalog, Vols. 1, 2, 3, and 4, (additional volumes to be published) prepared by Allied Research Associates, Inc., for NASA, Goddard Space Flight Center, Greenbelt, Maryland.

6.2 Section 2

References

- Ackerman, H. J. and G. A. Rabchevsky, 1971: "Applications of Nimbus Satellite Imagery to the Monitoring of Man-Made Lakes," paper presented at the Symposium on Man-Made Lakes, Knoxville, Tennessee, 3-7 May 1971.
- Ackerman, H. J., 1971: Personal Communication, Allied Research Associates, Inc.
- Aldrich, S. A., F. T. Aldrich and R. D. Rudd, 1969: The Employment of Weather Satellite Imagery in an Effort to Identify and Locate the Forest-Tundra Ecotone in Canada, Interagency Report NASA-169 under Contract W-12589, U. S. Department of the Interior, Geological Survey.
- Anon, 1963: Geologic Map of the Arabian Peninsula: U. S. Geological Survey Miscellaneous Geologic Investigations Map I-270A, Scale 1: 2,000,000.
- Barnes, J. C. and C. J. Bowley, 1968: Operational Guide for Mapping Snow Cover from Satellite Photography, Final Report Contract No. E-162-67(N), Allied Research Associates, Inc.
- Barnes, J. C. and C. J. Bowley, 1969: Satellite Photography for Snow Surveillance in Western Mountains, paper presented at the Western Snow Conference, Salt Lake City, Utah.

- Barnes, J. C. and C. J. Bowley, 1970: The Use of Environmental Satellite Data for Mapping Annual Snow-Extent Decrease in the Western United States, Final Report Contract No. E-252-69(N), Allied Research Associates, Inc.
- Barnes, J. C. and J. J. O. Palgen, 1971: The Use of Satellite-Acquired Hydrology Data for Input to Mekong River Flood Prediction Programs, Internal R&D Scientific Report No. 1001, Allied Research Associates, Inc.
- Belyea, H. and E. W. Best, 1967: "Calgary - Its Geologic Setting," Geotimes, (July-August), 10-13.
- Blodget, H. W., 1971: A Comparative Geologic Study of Spacecraft and Aircraft Imagery, National Aeronautics and Space Administration, Goddard Space Flight Center, X-644-71-204, 56 p.
- Brunt, D., 1932: "Notes on Radiation in the Atmosphere," Quart. J. of the Royal Meteor. Soc., 58(389), 389-420.
- Conti, M. A., 1967: Evaluation of Nimbus I HRIR Imagery, Technical Letter No. NASA-35, Contract R-09-020-011, U. S. Geological Survey.
- Cordeiro, N. V., 1967: "A Large Scale Hydrological Study in Latin America: The Upper Basin of the Rio Paraguay in Brazil," Nature and Resources, Bull. of the International Hydrological Decade, UNESCO, 3(2).
- Ferguson, H. L., H. F. Cork and A. D. J. O'Neill, 1969: "Applications of Satellite Photographs to Hydrology," presented at the 7th Canadian Hydrology Symposium, Victoria, British Columbia.
- Friedman, J. D., R. S. Williams, Jr., C. J. Miller and G. Palmason, 1967: Infrared Survey in Iceland; in 1966: in Surtsey Research Progress Report No. 3, Surtsey Research Society, Reykjavik, Iceland; 99-103.
- Friedman, J. D. and R. S. Williams, Jr., 1968: "Infrared Sensing of Active Geologic Processes," Proc. 5th Symposium on Remote Sensing of the Environment, U. of Michigan; 787-820.
- Friedman, J. D., R. S. Williams, Jr., G. Palmason and C. J. Miller, 1969: "Infrared Surveys in Iceland - Preliminary Report," U. S. Geological Survey, Prof. Paper 650-C; C89-C105.
- Friedman, J. D., R. S. Williams, Jr. and S. Thorarinsson, 1970: "Thermal Emission from Hekla Volcano, Iceland, Before the Eruption of 5 May 1970," Geol. Soc. America, Abstracts with Program, Vol. 2, p. 555.
- Friedman, J. D., 1971: U. S. Geological Survey, Personal Communication.

- Gawarecki, S. J., R. J. Lyon and W. Nordberg, 1965: "Infrared Spectral Returns and Imagery of the Earth from Space and their Application to Geologic Problems," Proc. of the Third Goddard Memorial Symposium, Washington, D. C., 4; 13-33.
- Geological Survey of Canada, 1962: Geological Map of British Columbia, 1: 267,200, Map 932A (Second Edition).
- Geological Survey of Canada, 1951: Geological Map of Alberta, 1: 267,200, Map 1002A.
- Gisler, C. E., 1967: "A Hydrological Synthesis of the Chad Basin," Nature and Resources, Bull. International Hydrological Decade, UNESCO, 3(3).
- Greenwood, J. E.G. W. and D. Bleackley, 1963: "Geology of the Arabian Peninsula, Aden Protectorate:" U. S. Geological Survey Professional Paper 560-C, 96 p.
- Greer, D. C., 1971: Map of Great Salt Lake, Utah, Scale 1: 125,000. Map Supplement No. 14, Annals of the Association of American Geographers, 61(1).
- Griggs, A. B., 1967: Annotated Bibliography of Uses on Remote Sensing Investigations, Technical Letters - NASA (advance copy) Open File Reports, U. S. Geological Survey.
- Hahl, D. C. and A. H. Handy, 1966: Hydrological Interpretation of Nimbus Vidicon Image - Great Salt Lake, Utah, Technical Letter, NASA-61, Contract No. R-09-020-015, U. S. Geological Survey.
- Hasser, E. G., 1966: Evaluation of Nimbus Vidicon Photography Southwest France and Northern Spain, Technical Letter, NASA-53, Contract No. R-09-020-011, U. S. Geological Survey.
- Hauth, F. F. and J. A. Weissman, 1968: "Investigation of Clouds Above Snow Surfaces Utilizing Radiation Measurements Obtained from the Nimbus II Satellite," in Meteorological Satellite Instrumentation and Data Processing, Final Report, NASw-65, Dept. of Meteorology, U. of Wisconsin, Dec. 1968. Also in Remote Sensing of the Environment, 1 (1969), NSF, GA-1020.
- Hovis M., 1966: "Spectral Reflectivity of Common Minerals," Appl. Opt., 5(245).
- Jaeger, J. C. and C. H. Johnson, 1953: "Notes on Diurnal Temperature Variation," Geofisica Pura e Applicata, 24; 104-106.
- Kondrat'yev, K. Ya., V. D. Stephanenko and B. V. Vinogradov, 1968: "Terrain Spectral Imagery from Space in Various Spectral Regions," U. of Leningrad, U. S. S. R., in Manned Laboratories in Space, Second International Orbital Laboratory Symposium (ed: S. F. Singer), New York.

- Kuusela, K. and S. Poso, 1970: "Satellite Pictures in the Estimation of the Growing Stock over Extensive Areas," Photogrammetric Journal of Finland, 4(1).
- Lettau, H., 1951: "Theory of Surface-Temperature and Heat-Transfer Oscillations Near a Level Ground Surface," Trans. Am. Geophys. Union, 32; 189-200.
- Lewis, C. R. and W. E. Davis, 1966: Geological Evaluation of Nimbus Vidicon Photographs, Chesapeake Bay - Blue Ridge, Technical Report No. NASA-6 Contract R-09-020-011, U. S. Geological Survey.
- Lowman, P. D., Jr., 1967: Geologic Applications of Orbital Photography, NASA Technical Note No. TN D-4155.
- Lowman, P. D., Jr., 1971: The Third Planet, Weltflugbild, Zurich.
- Lowman, P. D., Jr., 1971: Personal Communication, NASA, Goddard Space Flight Center.
- MacLeod, N. H., 1970a: Ecological Interpretation of Nimbus III HRIR Data, NASA Publication X-652-70-98, Goddard Space Flight Center, Greenbelt, Maryland.
- MacLeod, N. H., 1970b: Observations of the Inland Delta of the Niger River by Nimbus 3 High Resolution Infrared Radiometer, NASA Publication X-652-70-315, Goddard Space Flight Center, Greenbelt, Maryland.
- MacLeod, N. H., 1971: Personal Communication, NASA, Goddard Space Flight Center.
- McClain, P. and D. R. Baker, 1969: Experimental Large Scale Snow and Ice Mapping with Composite Minimum Brightness Charts, ESSA Technical Memorandum NESCTM-12, Environmental Science Services Administration.
- Merifield, P. M. (ed), J. Cronin, L. L. Foshee, S. J. Gawarecki, J. T. Neal, R. E. Stevenson, R. O. Stone and R. S. Williams, Jr., 1969: "Satellite Imagery of the Earth," Photogrammetric Engineer, 35(7); 654-668.
- Merritt, E. S., 1970: "Comments on Nimbus 4 Observations of Mt. Beerenberg Volcanic Eruption, Jan Mayen Island, 20 September, 1970," J. of Remote Sensing.
- National Aeronautics and Space Administration, 1970: Ecological Surveys from Space, Office of Technology Utilization, Washington, D. C.
- Neal, J. T., 1968: Satellite Monitoring of Lakebed Surfaces in Playa Surface Morphology: Miscellaneous Investigations, AFCRL-68-0133, Air Force Cambridge Research Laboratories, USAF.
- Noble, V. E. and J. C. Wilkerson, 1970: "Airborne Temperature Surveys of Lake Michigan, October 1966 and 1967," Limnology and Oceanography, 15(2), 289-296.

- Nordberg, W. and R. E. Samuelson, 1965: Terrestrial Features Observed by the High Resolution Infrared Radiometer in Observations from the Nimbus I Meteorological Satellite, NASA Publication SP-89; 36-46.
- Norrman, J. O., 1970: The Studies of the Coastal Morphology on Surtsey Island, AFCRL Translation 73, Air Force Cambridge Research Laboratories, USAF.
- Popham, R. W. and R. E. Samuelson, 1965: Polar Explorations with Nimbus in Observations from the Nimbus I Meteorological Satellite, NASA Publication SP-89; 47-49.
- Pouquet, J., 1968a: Remote Detection of Terrain Features from Nimbus I HRIR Nighttime Measurements, NASA TN D-4603, Goddard Space Flight Center, Greenbelt, Maryland.
- Pouquet, J., 1968b: An Approach to the Remote Detection of Earth Resources in Sub-Arid Lands, NASA TN D-4647, Goddard Space Flight Center, Greenbelt, Maryland.
- Pouquet, J., 1969a: "Geopedological Features Derived from Satellite Measurements in the 3.4 to 4.2 μm and 0.7 to 1.3 μm Spectral Regions," Proc. of Sixth International Symposium on Remote Sensing of Environment, II, U. of Michigan; 967-988.
- Pouquet, J., 1969b: "Possibilities for Remote Detection of Water in Arid and Sub-Arid Lands Derived from Satellite Measurements in the Atmospheric Window 3.4 to 4.2 μm ," Proc. of International Conf. on Arid Lands in a Changing World, Tucson, Arizona; also, NASA preprint X-622-69-437, Goddard Space Flight Center, Greenbelt, Maryland.
- Pouquet, J. and G. Rabchevsky, 1970a: The Niger (Africa) Interior Delta (Macina) Remotely Sensed by the Nimbus II and Nimbus III Satellite HRIR Daytime and Nighttime Radiometers, Internal R&D Scientific Report 1002, Allied Research Associates, Inc.
- Pouquet, J. and G. Rabchevsky, 1970b: Seasonal Ground Conditions in the Parana-Paraguay River Basin, South America, Monitored by Nimbus II and III HRIR Daytime and Nighttime Radiometric Observations, Internal R&D Scientific Report 1003, Allied Research Associates, Inc.
- Pouquet, J. and E. Raschke, 1968: A Preliminary Study of the Detection of Geomorphological Features over Northeast Africa by Satellite Radiation Measurements in the Visible and Infrared, NASA TN D-4648, Goddard Space Flight Center, Greenbelt, Maryland.

- Powers, R. W., L. F. Ramirez, C. D. Redmond and E. L. Elberg, Jr., 1966: "Geology of the Arabian Peninsula, Sedimentary Geology of Saudi Arabia," U. S. Geological Survey Professional Paper 560D, 147 p.
- Rabchevsky, G., 1970a: "Nimbus Satellite Views Hydrologic Conditions," Proc. First Western Space Congress, Santa Maria, California.
- Rabchevsky, G., 1970b: "Comments on the Geologic Use of Nimbus I Television Photograph," Proc. First Western Space Congress, Santa Maria, California.
- Rabchevsky, G., 1971: "Hydrologic Conditions Viewed by the Nimbus Meteorological Satellites," International Remote Sensing Workshop (IRSW), U. of Michigan, Ann Arbor.
- Reed, L. O. D. and J. S. Hollister in T. H. Clark and C. W. Stream, 1968: Geological Evolution of North America, The Ronald Press Co., New York.
- Sabatini, R. R. and J. Sissala, 1968: Project NERO, Nimbus Earth Resources Observations, Technical Report No. 7 Contract No. NAS 5-10343, prepared by Allied Research Associates, Inc., for NASA, Goddard Space Flight Center.
- Sabatini, R. R., 1971: "The Feasibility of Using Nimbus HRIR and THIR Measurements for Obtaining Surface Temperature of Lake Michigan," paper presented at the Great Lakes Conf. Meeting, April 1971, Toronto, Canada.
- Short, N., 1971: Personal Communication, NASA, Goddard Space Flight Center.
- Sissala, J., 1970: "The Utilization of the Various Time Scales of Meteorological Satellite Observations to Monitor Terrestrial Changes," paper presented at First Western Space Congress, Santa Maria, California.
- Sissala, J. and G. Rabchevsky, 1970: "Terrestrial Changes Monitored by the Nimbus 3 Satellite Daytime High Resolution Infrared System," paper presented at First Western Space Congress, Santa Maria, California.
- Smithsonian Institution, 1970: "Beerenberg Volcanic Eruption," Center for Short-Lived Phenomena, Event 8970, 1022.
- Strong, A. E., 1967: "The Over-Water Development of a Lake Breeze in an Off-shore Gradient Flow," Proc. Tenth Conference on Great Lakes Research.
- Surtsey Research Society, 1965-1968: Surtsey Research Program Report, 1-4; Reykjavik, Iceland.
- Taggart, C. I., 1965: "Interpretation of Geological Features on a Satellite Photograph," Nature, 207(4996); 513-514.

- Thorarinsson, S., 1966: "Sitt of Hyerju um Surtseyjargosid," Naturufraedingurinn, 35(4); 153-212.
- Thorarinsson, S., 1967: "The Surtsey Eruption and Related Scientific Work," Polar Record, 13(86); 571-578.
- UNESCO, 1970: "Study of Water Resources in the Chad Basin," Nature and Resources, Bull. of International Hydrological Decade, UNESCO, 6(2).
- Vinogradov, B. V., 1967: "The Landscape Regionalization by Means of Air and Space Photography," paper presented at the Meeting of the Commission on Interpretation of Aerial Photography of International Geophysical Union, Ottawa.
- Vinogradov, B. V., 1969: "Interpretation of the Earth's Surface as Imaged by Nimbus I," All State Geographical Society, U.S.S.R. 101(3); 210-217.
- Warnecke, G., L. M. McMillin and L. J. Allison, 1969: Ocean Current and Sea Surface Temperature Observations from Meteorological Satellites, NASA TN D-5142, Goddard Space Flight Center, Greenbelt, Maryland.
- Williams, R. S., Jr., J. D. Friedman, S. Thorarinsson, T. Sigurgeirsson and G. Palmason, 1968: Analysis of 1966 Infrared Imagery of Surtsey, Iceland in Surtsey Progress Report No. 4, 177-192, Surtsey Research Soc., Reykjavik, Iceland.
- Williams, R. S. Jr., 1970: "Satellite Observation of Effusive Volcanism," J. of British Interplanetary Soc., 23; 441-450.
- Woloshin, A., 1965: "Notes on Geologic Interpretation of Nimbus AVCS Image of Southern California," in Multisensor Imagery Collection, U. S. Army Corps of Engineers for NASA Earth Resources Survey Program, 189-191.

Bibliography

- Barnes, J. C. and C. J. Bowley, 1966: Snow Cover Distribution as Mapped from Satellite Photography, Final Report Contract No. Cwb-11269, Allied Research Associates, Inc.
- Barnes, J. C. and C. J. Bowley, 1968b: "Snow Cover Distribution as Mapped from Satellite Photography," Water Resources Research 4(2); 256-272.
- Bowley, C. J., 1969: Use of Nimbus II APT to Determine the Rate of Ice Disintegration and Dispersion in Hudson Bay, Technical Report No. 8, Contract No. NAS 5-10343, Allied Research Associates, Inc.

- Carter, W. D., 1967: Annotated Bibliography of Users Technical Letters - NASA on Remote Sensing Investigations, Open File Reports (advance copy), U. S. Geological Survey.
- Conover, J. H., 1965: "Note on the Flora and Snow Cover Distribution Affecting the Appearance of Northeastern United States as Photographed by TIROS Satellites," Mon. Wea. Rev. 93(10), 644-646.
- Davis, W. E., 1966: Geological Evaluation of Nimbus Vidicon Imagery, Northwest Greenland, Technical Letter No. NASA-56, Contract No. R-09-020-011, U. S. Geological Survey.
- Fritz, S., 1962: "Snow Surveys from Satellite Meteorology," Rocket and Satellite Meteorology, North-Holland Publishing Company, Amsterdam; 419-421.
- Holmes, A., 1965: Principles of Physical Geology, the Ronald Press Co., New York.
- Itten, N., 1969: Geographische Interpretation von Wettersatellitenbildern, Ph. D. Thesis, Geographisches Institut der Universitat Zurich.
- Kaminski, H. and P. Neumann-Mahlkau, 1967: "Kleinmass-Stabliche Luftbilder, Aufgenommen von Wettersatelliten, und Ihre Geologische Aussage," N. JB. Geol. Palaont. MH., 10, 589-596.
- Kaminski, H., 1971: "Infraroutaufnahmen der Erde von Satelliten und Ihre Aussage-Gemoglichkeit," Naturwissenschaftliche Rundschau, Band 24, Heft, 6, 244-252.
- Lobreck, A. K., 1939: Geomorphology, McGraw-Hill Book Co., Inc., New York.
- McGinnies, W. G., B. J. Goldman and P. Paylore (eds), 1970: Deserts of the World, An Appraisal of Research into their Physical and Biological Environments, A U. S. Contribution to the International Hydrologic Decade, U. of Arizona Press.
- Merifield, P. M. and J. Rommelkamp, 1964: Terrain in TIROS Pictures, Report No. LR 17848, Contract No. NAS 5-3390, Lockheed California Company.
- Merritt, E. S., 1963: An Analysis of Stratiform Cloud Patterns in the Canary Islands Region, Scientific Report No. 2, Contract No. AF 19(628)-320, Allied Research Associates, Inc.
- National Research Council, 1970: Remote Sensing with Special Reference to Agriculture and Forestry, Com. on Remote Sensing for Agricultural Purposes, Agricultural Board, National Research Council, National Academy of Sciences, Washington, D. C., 425 p.

- Popham, R. W., A. Flanders and H. Neiss, 1966: "Second Progress Report on Satellite Application to Snow Hydrology," Proc. 23rd Annual Meeting Eastern Snow Conf., Hartford, Connecticut.
- Pouquet, J., 1969 : "Near Infrared Daytime Surface Characteristics from Nimbus III High Resolution Infrared Radiometer Data, Geological Aspects," paper presented at 1969 National Fall Meeting, American Geophysical Union.
- Pouquet, J., 1969 : "First Results of Nimbus III, Geological Aspects," paper presented at the Fall Meeting American Geophysical Union, San Francisco, California.
- Pouquet, J., 1969 : "Les Applications Geographiques des Satellites Artificiels," Assoc., Geographes Francais, No. 371-373.
- Pouquet, J., 1969 : "Geomorphologie et Ere Spatial," Zeitschrift fur Geomorphologie Neue Folge Band 13, Heft 4; 414-471.
- Pouquet, J., 1971: Satellites Artificiels et Cartographie, Bull. Geographie Universite de Montreal, Ottawa, Canada.
- Pouquet, J., 1971: Les Sciences de la Terre a L' Heure des Satellites, Presses Universitaires de France, Collection SUP., Serie Le Physicien
- Smith, R. T., 1966: "Terrain Effects on Precipitation in Washington State," Weatherwise; 204-207.
- Tarble, R. D., 1963: "Areal Distribution of Snow as Determined from Satellite Photographs," Publication 65 of the IASH; 372-375.
- Tarble, R. D., 1963: "Snow Surveys of Western United States with the Use of Satellite Pictures," Proc. of 31st Annual Meeting, Western Snow Conf.
- U. S. Army Corps of Engineers, 1965: "Notes on Geologic Interpretation of Nimbus AVCS Image of Southern California," in Multisensor Imagery Collection, prepared for the Earth Resources Survey Program, Space Applications Programs, NASA.
- Widger, W. J., J. C. Barnes, E. S. Merritt and R. Smith, 1965: Meteorological Interpretation of Nimbus High Resolution Infrared (HRIR) Data, Final Report, Contract NAS 5-9554 (republished as NAS CR-352), Allied Research Associates, Inc.

6.3 Section 3

References

- Allison, L. J. and J. S. Kennedy, 1967: An Evaluation of Sea Surface Temperature as Measured by the Nimbus 1 High Resolution Infrared Radiometer, NASA TN-D-4078, Goddard Space Flight Center, Greenbelt, Maryland.
- Allison, L. J. and E. R. Kreins, 1970: "Color Enhancement of Nimbus High Resolution Infrared Radiometer Data," Appl. Opt. 9; 681-686.
- Barnes, J. C., D. T. Chang and J. Willand, 1970a: "Satellite Infrared Observation of Arctic Sea Ice," Proc. AIAA, Earth Resources Observations and Information Systems Meeting, Annapolis, Maryland.
- Barnes, J. C., D. T. Chang and J. Willand, 1970b: Improved Techniques for Mapping Sea Ice from Satellite Infrared Data, Final Report, Contract E-67-70(N), Allied Research Associates, Inc.
- Blanton, J. O. and F. M. Vukovich, 1969: Physical Oceanography Feasibility Study Utilizing Nimbus 2 HRIR Satellite Data, Final Report, ESSA-E256-68/N, Research Triangle Institute.
- Bowley, C. J., 1969: Use of Nimbus 2 APT to Determine the Rate of Ice Disintegration and Dispersion in Hudson Bay, Tech. Report, Contract NAS 5-10343, Allied Research Associates, Inc.
- Bowley, C. J., J. R. Greaves and S. L. Spiegel, 1969: "Sunlint Patterns: Unusual Dark Patches," Science, 165; 1360-1362.
- Curtis, W. R. and K. P. Rao, 1969: "Gulf Stream Thermal Gradients from Satellite, Ship and Aircraft Observations," J. of Geophys. Res., 724(28); 6984-6990.
- Demaso, J. M., R. P. Rappaport and A. L. Ruiz, 1969: "A Digital Color Printer," Proc. Electro-Optical Systems Design Conference, New York; 663-665.
- Duntley, S. Q. and G. F. Edgerton, 1966: The Use of Meteorological Satellite Photographs for the Measurements of the Sea State, Final Report Contract NOBS-86012, Scripps Institution of Oceanography, U. of California (AD 489-354).
- Greaves, J. R., J. H. Willand and D. T. Chang, 1968: Observations of Sea Surface Temperature Patterns and Their Synoptic Changes through Optimal Processing of Nimbus II Data, Final Report Contract NASW-1651, Allied Research Associates, Inc.

- Greaves, J. R. and C. J. Bowley, 1970: Satellite Augmented Oceanographic Studies, Phase II Report, Contract P.O. 706-30108-0, Allied Research Associates, Inc.
- Kikuchi, K. and T. Kasai, 1968: "Stereoscopic Analysis of Photographs Taken by Nimbus II APT System," J. of Meteor. Soc. Japan, Ser. 2, 46(1); 60-67.
- Knapp, W. W., 1969: "A Satellite Study of the Ice in Antarctic Coastal Waters," Antarctic Journal, IV(5); 222-223.
- LaViolette, P. E. and P. L. Chabot, 1969: "A Method of Eliminating Cloud Interference in Satellite Studies of Sea Surface Temperatures," Deep Sea Research, 16.
- LaViolette, P. E. and S. E. Seim, 1968: Satellite Photography as a Means of Determining Water Temperature Structure, U. S. Naval Oceanographic Office, Informal Report No. 68-76.
- McClain, E. P. and A. E. Strong, 1969: "Anomalous Dark Patches in Satellite-Viewed Sunglint Areas," Mon. Wea. Rev. 97(12); 875-884.
- National Academy of Sciences, 1969: Useful Applications of Earth-Oriented Satellites: Oceanography, National Research Council, Div. of Engineering, NSR-09-012-909.
- Nelson, H. P., S. R. Needham and D. Thomas, 1970: Sea Ice Reconnaissance by Satellite Imagery, Final Report to NASA, Institute of Arctic Environmental Engineering, U. of Alaska, Contract N62306-68-C-0261.
- Popham, R. and R. E. Samuelson, 1965: "Polar Exploration with Nimbus," in Observations from the Nimbus I Meteorological Satellite, NASA, Goddard Space Flight Center, Greenbelt, Maryland. Also in Arctic, Montreal, 18(4); 246-255, December 1965.
- Predoehl, M. C. 1966: "Antarctic Pack Ice - Boundaries Established from Nimbus I Pictures," Science, 153; 861-863.
- Rao, P. K., 1968: "Sea Surface Temperature Measurements from Satellites," Mariners Weather Log, 12(5); 152-154.
- Sabatini, R. R. and J. E. Sissala, 1968: Project NERO (Nimbus Earth Resources Observations), Technical Report No. 7, Contract No. NAS 5-10343, Allied Research Associates, Inc.
- Seim, S. E. and P. E. LaViolette, 1969: "The Cold Wall of the Gulf Stream as Defined by Cloud Cover," paper presented at the 50th Annual Meeting of the American Geophysical Union, Washington, D. C.

- Shenk, W. E. and V. V. Salomonson, 1970: "A Multispectral Technique to Determine Sea Surface Temperature Using Nimbus 2 Data," paper presented at the Fall Meeting of the American Geophysical Union, San Francisco, California.
- Shenk, W. E. and K. H. Szekiolda, 1971: "Satellite Ocean Temperature Analysis of the Indian Ocean" (to be published) in Proc. of Symposium on Indian Ocean and Adjacent Seas; Cochin, India, January 12-18.
- Sissala, J., 1969: "Observations of An Antarctic Ocean Tabular Iceberg from the Nimbus 2 Satellite," Nature, 224(5226); 1285-1287.
- Sissala, J., R. R. Sabatini and H. Ackerman, 1971: "Nimbus Satellite Data for Polar Ice Survey," in preparation.
- Smith, W. L., P. K. Rao, R. Koffler and W. R. Curtis, 1970: "The Determination of Sea Surface Temperature from Satellite High Resolution Infrared Window Radiation Measurements," Mon. Wea. Rev., 48; 604-611.
- Szekiolda, K. H., 1970a: The Effect of Cyclonic and Anticyclonic Water Movements on the Distribution of Organic Matter, NASA Doc. No. X-622-70-40, Goddard Space Flight Center, Greenbelt, Maryland.
- Szekiolda, K. H., 1970b: The Development of Upwelling Along the Somali Coast as Detected with the Nimbus 2 and Nimbus 3 Satellites, NASA Doc. No. X-651-70-419 (preprint), Goddard Space Flight Center, Greenbelt, Maryland.
- Szekiolda, K. H. and W. F. Mitchell, 1971: Oceanographic Application of Color-Enhanced Satellite Imageries, NASA (preprint) X-651-71-53, Goddard Space Flight Center, Greenbelt, Maryland.
- U. S. Navy, 1971: "Report of Operation Deep Freeze 71, 1970-71," U. S. Navy Task Force 43, p. 27.
- Warnecke, G., L. J. Allison, L. M. McMillin and R. H. Szekiolda, 1971: "Remote Sensing of Ocean Currents and Sea Surface Temperature Changes Derived from the Nimbus II Satellite," J. of Phys. Oceanog., 1(1); 45-60.

Bibliography

- Albert, E. G., 1962: "Meteorological Applications of Nimbus Data," Proc. of The Nimbus Program Review, NASA, Goddard Space Flight Center, Greenbelt, Maryland.
- Alishouse, J. C., D. R. Baker, E. P. McClain and H. W. Yates, 1971: Potential of Satellite Microwave Sensing for Hydrology and Oceanography Measurements, NOAA Tech. Memo NESS 26.

- Allison, L. J., L. L. Foshee, G. Warnecke and J. C. Wilkerson, 1967: "An Analysis of the North Wall of the Gulf Stream Utilizing Nimbus 2 High Resolution Infrared Measurements," Proc. 48th Meeting of the American Geophysical Union, Washington, D. C.
- Allison, L. J., L. L. Foshee, G. Warnecke, 1967: Observations of Sea Surface Temperatures and Ocean Currents from Nimbus II, NASA X-622-67-435, Goddard Space Flight Center, Greenbelt, Maryland. Also in Proc. Tenth COSPAR Plenary Meeting, Imperial College of Science and Technology, London, England (July 24-27).
- Allison, L. J., L. M. McMillin and G. Warnecke, 1969: Ocean Current and Sea Surface Temperature Observations from Meteorological Satellites, NASA TN-D-5142, Goddard Space Flight Center, Greenbelt, Maryland.
- Botzam, J. R., 1966: "Nimbus Aids Ocean Studies," Geomarine Technology, 2(6); 24-25.
- Bowley, C. J. and J. R. Greaves, 1970: "The Use of Satellite Cloud Photography to Infer Oceanographic Phenomena," Proc. 7th Space Congress, Canaveral Council of Technical Society.
- Burnett, E. S., 1969: Summary of Tangible Results Achieved by Earth Observation Satellites to Date, NR-H7-00-000-00044, TRW Systems, Redondo Beach, California.
- Capurro, L. R. A., 1967: "Oceanography from Space," Bollettino di Geofisica, 9(33); 3-16.
- Carter, W. D., 1966: Geologic Investigations of Remote Sensing Techniques, Final Report, Technical Letter No. 52, U. S. Geological Survey, Washington, D. C.
- Clark, J. R., M. N. Hall and C. E. Tilden, 1969: Techniques for the Utilization of Satellite Observations in Operational Mapping of Sea Surface Temperatures, Final Report, FAMOS-RR-1-69, Meteorology International, Inc.
- Duing, W. and K. H. Szekiolda, 1971: "Monsoonal Response in the Western Indian Ocean," J. of Geophysical Research, 76(18), pp. 4181-4187.
- Ewing, G. C. (ed), 1965: Oceanography from Space, Woods Hole Oceanographic Institution.
- Frame, D. D. and W. O. Kerman, 1966: Antarctic Temperature Studies Utilizing HRIR Data from Nimbus I, M. S. Thesis, Naval Postgraduate School.

- Glaser, A. H., E. S. Merritt, R. Wexler and W. K. Widger, Jr., 1964: "The Applicability of TIROS and Nimbus Data to Investigate the Feasibility of Sea Surface Temperature Measurements from Satellites," Oceanography, from Space, Proc. Conf. held at Woods Hole, Massachusetts.
- Greaves, J. R., R. Wexler and C. J. Bowley, 1966: The Feasibility of Sea Surface Temperature Determination Using Satellite Infrared Data, NASA CR-474, Allied Research Associates, Inc.
- Haase, E., K. Kaminski and M. Pfannenstiel, 1969: "Versuch einer meeres-morphologischen Deutung von Satelliten-Luftbildern," in German (Essay of An Ocean-Morphological Interpretation of Satellite-Air Pictures), Deutsche Hydrographische Zeitschrift, Heft 5.
- Kee, R. and R. W. Corell, 1968: "Feasibility of Interrogating and Locating Ocean Platforms with Orbiting Satellites," IEEE Trans. of Geoscience Electronics, G. E., 6(4); 176-184.
- LaViolette, P. E., 1969: "Oceanography from Space Now," Oceanology International, 4(5); 28-32.
- LaViolette, P. E. and L. J. Allison, 1969: "Method of Deriving Sea Surface Temperatures from Nimbus II HRIR Data," EOS-American Geophysical Union Transactions, 50(4).
- LaViolette, P. E. and S. E. Seim, 1969: Satellites Capable of Oceanographic Data Acquisition - A Review, Technical Report TR-215, U. S. Naval Oceanographic Office.
- LaViolette, P. E. and P. L. Chabot, 1969: "Nimbus II Satellite Sea Surface Temperatures Versus Historical Data in a Selected Region, A Comparative Study," Deep Sea Research, 15; 617-622.
- McClain, E. P., 1970: Applications of Environmental Satellite Data to Oceanography and Hydrology, ESSA Tech. Memo NESC TM-19., Environmental Sciences Services Administration.
- Moore, R. K. and W. J. Pierson, 1965: "Measuring Sea State and Estimating Surface Winds from a Polar Orbiting Satellite," Proc. International Symposium on Electromagnetic Sensing of the Earth from Satellites, Miami Beach, Florida.
- National Aeronautics and Space Administration, 1967: A Survey of Space Applications "For the Benefit of All Mankind," Space Applications Program Office, Office of Space Science and Applications, NASA SP-142.

- National Council on Marine Resources and Engineering Development, 1967: U. S. Activities in Spacecraft Oceanography, prepared by NASA, Naval Oceanographic Office, Bureau of Commercial Fisheries and ESSA.
- Nelson, R. M., 1967: "Sensing of Ocean Currents from Space," Ocean Industry, 2(5); 40-42.
- Oliver, V. J., 1964: "Nimbus Views of Ice, Snow, Cumulus and Cumulonimbus," Proc. Inter-Regional Seminar on the Interpretation and Use of Meteorological Satellite Data, November 27-December 8, Tokyo, Japan.
- Rao, P. K., W. R. Curtis, A. E. Strong and E. P. McClain, 1969: "Remote Sensing of Sea Surface Temperature," Proc. Sixth Space Congress, Canaveral Council of Technical Societies, Cocoa Beach, Florida.
- Sherman, J. W. and L. Cheney, 1968: "Spacecraft Oceanography - Its Scientific and Economic Implications for the Next Decade," U. N. Conf. on the Exploration and Peaceful Uses of Outer Space, Vienna.
- Stehling, K. R., 1969: "Remote Sensing of the Oceans," Astronautics and Aeronautics, 7(5); 62-67.
- Szekiolda, K. H., V. V. Salomonson and L. J. Allison, 1970: Seasonal Sea Surface Temperature Variations in the Persian Gulf as Recorded by Nimbus 2 HRIR, NASA X-651-70-416 (preprint), Goddard Space Flight Center, Greenbelt, Maryland.
- Szekiolda, K. H., 1971: Upwelling Studies with Satellites, NASA X-651-71-298, Goddard Space Flight Center, Greenbelt, Maryland.
- Szekiolda, K. H., 1971: Anticyclonic and Cyclonic Eddies Near the Somali Coast, Sonderdruck Aus Der Deutschen Hydrographischen Zeitschrift, Band 24, Heft 1.
- Townsend, M., 1967: "Electronic Observations to Monitor Oceans," Ocean Industry, 2(5); 19-25.
- Vukovich, F. M., 1969: Physical Oceanography Feasibility Study Utilizing Nimbus II HRIR Satellite Data, Final Report Contract E-256-68(N), Research Triangle Institute.
- Warnecke, G., L. M. McMillin and L. J. Allison, 1969: Ocean Current and Sea Surface Temperature Observations from Meteorological Satellites, NASA TN-D-5142, Goddard Space Flight Center, Greenbelt, Maryland.
- Widger, W. K., Jr., and J. R. Greaves, 1968: Bibliography on the Use of Satellites for Oceanographic Observations, Contract NASW-1651, Allied Research Associates, Inc.

- Wilkerson, J. C., 1967: "The Gulf Stream from Space," Oceanus, XIII(2 and 3).
- Zaitzeff, J. B. and J. W. Sherman, 1968: "Oceanographic Applications of Remote Sensing," Proc. 5th Symposium Remote Sensing of the Environment, U. of Michigan, Ann Arbor, Michigan.

6.4 Section 4

References

- Aldrich, S. A., F. T. Aldrich and R. D. Rudd, 1969: "The Employment of Weather Satellite Imagery in an Effort to Identify and Locate the Forest-Tundra Ecotone in Canada," U. S. Dept. of the Interior, Geological Survey, Interagency Report NASA-169 for NASA, Contract W-12589, Task No. 160-75-01-32-10.
- Bowley, C. J., 1967: "Comments on Atmospheric Requirements for the Genesis of Anomalous Cloud Lines," J. of Atmos. Sci., 24; 596-597.
- Chief Topographic Engineer, 1965: "Cartographic and Geologic Uses of Nimbus I AVCS Data," Space Applications, NASA SP-137; 60-61.
- Conover, J., 1966: "Anomalous Cloud Lines," J. of Atmos. Sci., 23; 778-785.
- Conover, J., 1969: "New Observations of Anomalous Cloud Lines," J. of Atmos. Sci., 26; 1153-1154.
- Craighead, F. C., J. J. Craighead, E. Cote and H. K. Buechner, 1970: "Feasibility of Tracking Free-Roaming Animals in Natural Environments," Am. Zoologist, 10(4).
- Dept. of the Interior, Canada, 1932: Map of the Dominion of Canada Indicating Vegetation and Forest Cover, 100 miles to 1 inch.
- Forrester, F., 1970: "Satellite Relays Temperature of Mt. Rainier," U. S. Geological Survey News Release (20 October).
- Geological Survey of Canada, Dept. of Energy, Mines and Resources, 1969: Geological Map of Canada, 1250A, 1: 5,000,000.
- Landsberg, H. E., 1970: "Man-Made Climatic Changes," Science, 170(3964); 1265-1274.
- Newberger, 1957: Introduction to Physical Meteorology, Pennsylvania State University Press.

- Nordbeck, S., 1965: "The Law of Allometric Growth," Michigan Inter-University Community of Mathematical Geographers, Discussion Paper No. 7, Dept. of Geography, U. of Michigan; 12-22.
- Norin, E., 1970: Personal Communications, Institute of Minerology and Geology, U. of Uppsala, Sweden.
- Rao, K., 1970: Personal Communication, NESS/NOAA.
- U. S. Geological Survey, 1969: National Atlas, Population Distribution Urban and Rural: 1960, Sheet No. 270.
- Waugh, D. V., 1970: Personal Communication, American Geographical Society, New York.
- Wellar, B. S., 1969: "The Role of Space Photography in Urban and Transportation Data Series," Proc. Sixth International Symposium of Remote Sensing of Environment, II, U. of Michigan.

Page Intentionally Left Blank

APPENDIX A

Section A.1 describes the characteristics of the Nimbus orbit and the orbital parameters of the four Nimbus satellites that have been launched.

Section A.2 presents brief descriptions of the experiments on the Nimbus 1, 2, 3 and 4 satellites and on the Nimbus E and F satellites to be orbited in 1972 and 1973, respectively. For more detailed information on the experiments and data formats, the reader is referred to Nimbus User's Guides and catalogs, obtainable from the National Space Science Data Center of the National Aeronautics and Space Administration at Goddard Space Flight Center, Greenbelt, Maryland.

Section A.3 lists the agencies which archive and disseminate the various Nimbus data.

A.1 The Nimbus Orbit

The nominal Nimbus orbit (Figure A-1) is circular near-polar at a height of 600 n.mi. (1112 km) with a period of approximately 108 minutes and an inclination of 100° (80° retrograde). The height and inclination were chosen to make the orbit sun-synchronous such that the eastward motion of the line of nodes would equal 0.9856° per day, the mean motion of the Right Ascension of the sun. The orbital plane would, therefore, maintain a constant angle to the earth-sun line. Additionally, the launch time was chosen such that ascending nodes occurred near noon local mean time. Such an orbit provides daily worldwide coverage, with good solar illumination of the areas viewed in daytime.

The Nimbus satellites, with the exception of Nimbus 1, were launched into the planned sun-synchronous orbits. Table A-1 gives the orbital characteristics of the four Nimbus satellites. Figure A-2 shows a Nimbus subsatellite track on the earth, with the positions of the subsatellite point at intervals of one minute from the ascending and descending nodes. The track is a fairly accurate representation of the orbits of Nimbus 2, 3 and 4, but it is not as accurate for the relatively elliptic Nimbus 1 orbit. Additional orbit information is presented in the Nimbus catalogs.

A.2 Description of Nimbus Experiments

A.2.1 Nimbus 1 Experiments

The Advanced Vidicon Camera System (AVCS)

The AVCS provided televised pictures of the earth. It consisted of three 800-line vidicon cameras each with a 36.5° field of view. The central camera was oriented straight down, while each of the side cameras was mounted at an angle of

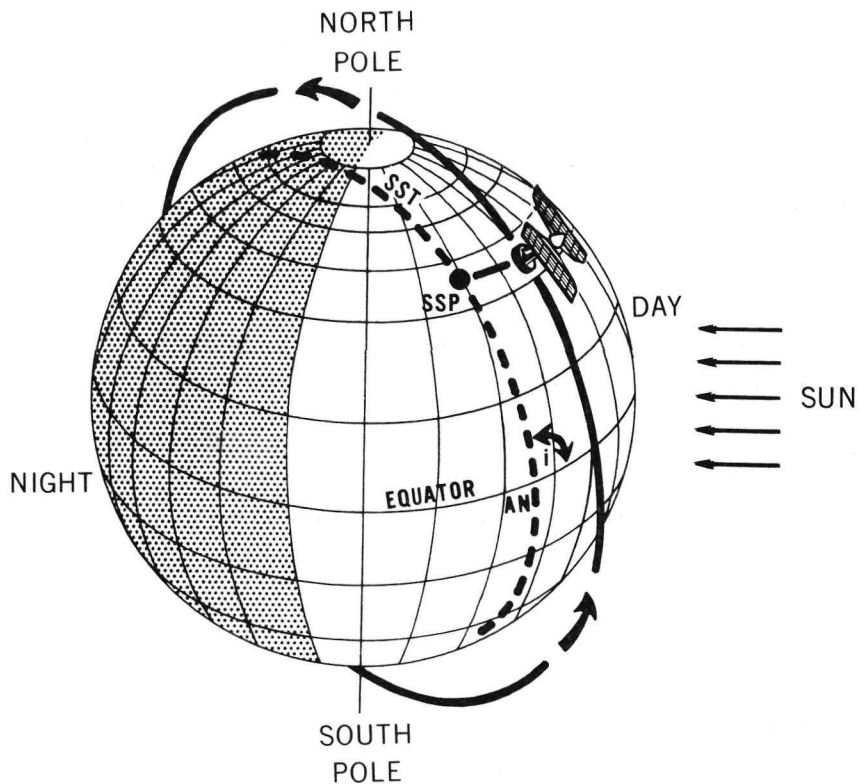


Figure A-1 The Nimbus orbit. The diagram shows the subsatellite track (SST) on the earth's surface crossing the equator at the ascending node (AN) with an inclination (i).

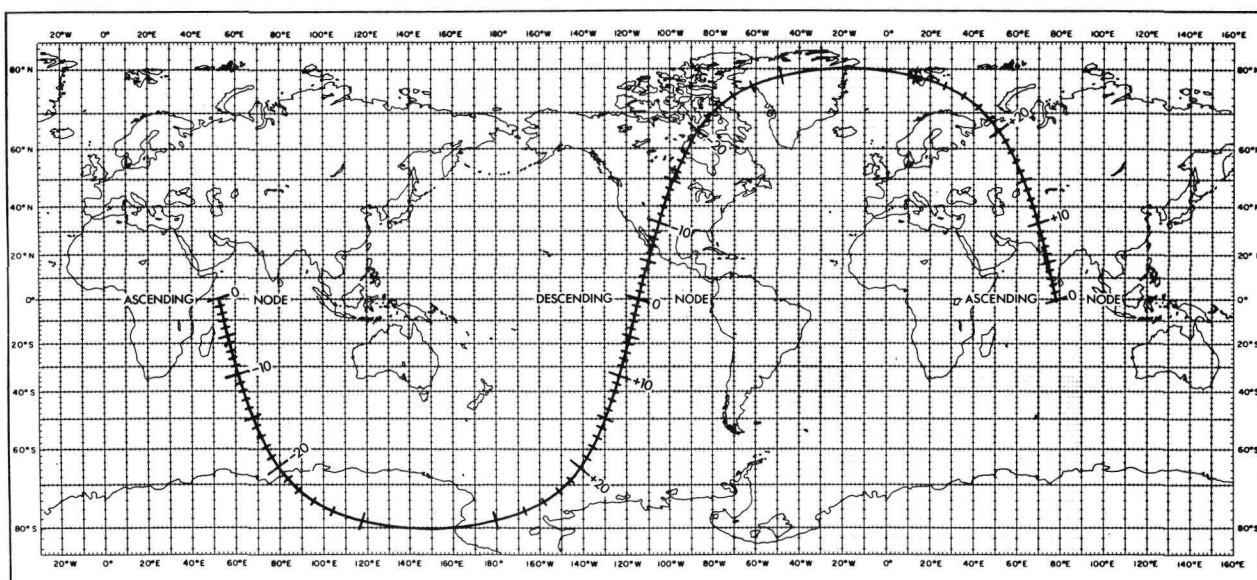


Figure A-2 Nimbus subsatellite track.

TABLE A-1
ORBITAL CHARACTERISTICS

Satellite	Launch Date	Period		Height (km)		Inclination of Orbit (deg)	Local Solar Time at Ascending Node	Change in Ascending Node Local Solar Time in Mins/Month	Date of Last Data Received
		Min	Sec	Apogee	Perigee				
Nimbus 1	28 August 1964	98	19	933	423	98.66	11: 34 am	+8.4	22 Sept. 1964
Nimbus 2	15 May 1966	108	10	1180	1095	100.31	11: 30 am	+1.7	15 Nov. 1966
Nimbus 3	14 April 1969	107	18	1146	1089	99.92	11: 29 am	-0.5	25 Sept. 1970
Nimbus 4	8 April 1970	107	07	1099	1088	99.89	11: 52 am	-2.4	Operational to 8 April 1971

35° to the central camera. Three simultaneous, slightly overlapping pictures were taken at 91-second intervals on the daylight side of the earth.

The low orbit of Nimbus 1 produced the highest resolution pictures of all the Nimbus satellites. AVCS data are available in 35 mm and 70 mm black and white transparencies and 70 mm prints.

The High Resolution Infrared Radiometer (HRIR)

The HRIR provided nighttime infrared mapping of the earth in the 3.4 to 4.2 μm band. The radiometer scanned the earth horizon to horizon normal to the satellite heading direction at 44.7 rpm.

HRIR data are available in the following formats:

- 1) A black and white photofacsimile strip (70 mm transparency or print) of successive scans.
- 2) Nimbus Meteorological Radiation Digital Tapes (NMRT). The original analog data are digitized at a rate of 1000 samples per second, producing approximately 400 temperature values for each horizon to horizon scan.
- 3) Nighttime temperature (surface blackbody equivalent temperature) grid print maps, computer-produced from the NMRT's (Figure C-3). Mercator and Polar Stereographic projection grid print maps at scales down to 1:500,000 with latitude-longitude marks are available from NSSDC. The gridding is usually correct to 30 n.mi. but the accuracy can be greatly improved by reference to landmarks.

The Automatic Picture Transmission System (APT)

The APT system transmitted television pictures of the local area to APT receiving stations within range. The APT camera had a wide-angle lens and 108° diagonal field of view. Pictures were transmitted at 208-second intervals. APT pictures are not centrally archived by the NASA, and may be available only from the local APT stations.

A.2.2 Nimbus 2 Experiments

The High Resolution Infrared Radiometer (HRIR)

Same as the HRIR experiment flown on Nimbus 1.

The Advanced Vidicon Camera System (AVCS)

Same as the AVCS experiment flown on Nimbus 1.

The Automatic Picture Transmission (APT) System

Similar to the APT experiment flown on Nimbus 1. In addition, real-time nighttime HRIR data were transmitted.

The Medium Resolution Infrared Radiometer (MRIR)

The MRIR radiometer scanned the earth-atmosphere system through five spectral bands: the 6.4 to 6.9 μm water vapor band, 10 to 11 μm window, 14 to 16 μm CO_2 band, 5 to 30 μm infrared band, and the 0.2 to 4.0 μm reflected solar energy band.

Data are available in pictorial format and computer-produced radiation maps.

The five wavelength regions, each with a brief description of its purpose, were as follows:

6.5 to 7.0 μm - This channel covered the 6.7 μm water vapor absorption band. Its purpose was to provide information on water vapor distribution in the upper troposphere and, in conjunction with the other channels, to provide data concerning relative humidities at these altitudes.

10.0 to 11.0 μm - Operating in an atmospheric "window", this channel measured surface or near-surface temperatures over clear portions of the atmosphere. It also provided cloud cover and cloud height information (day and night).

14.5 to 15.5 μm - This channel, centered about the strong absorption band of CO_2 at 15 μm ; measured radiation which emanated primarily from the stratosphere. The information gained here is of primary importance in following seasonal stratospheric temperature changes.

5.0 to 30.0 μm - This channel measured the emitted long wavelength infrared energy and, in conjunction with the reflected solar radiation channel, furnishes data on the heat budget of the planet.

0.2 to 4.0 μm - This channel covered more than 99% of the solar spectrum and yielded information on the intensity of reflected solar energy from the earth and its atmosphere.

A.2.3 Nimbus 3 Experiments

The High Resolution Infrared Radiometer (HRIR)

The Nimbus 3 HRIR experiment provided, on a full-time basis, both daytime and nighttime radiation measurements. The radiometer scanned the earth normal to the satellite heading direction at 48 rpm. Nighttime data (in the 3.4 to 4.2 μm

range) provided cloud top or surface temperatures as in the Nimbus 1 and 2 HRIR experiments. Through the use of a dual bandpass filter, daytime data (in the 0.7 to 1.3 μm range) provided cloud mapping information and effective reflectances. HRIR data were also transmitted by the Real Time Transmission System (RTTS-DRIR) to appropriately modified APT ground stations throughout the world.

The data formats are the same as those described for Nimbus 1 HRIR. Daytime grid print maps show reflectance values rather than temperatures.

The Medium Resolution Infrared Radiometer (MRIR)

The MRIR experiment was essentially the same as that flown on Nimbus 2. One exception was the replacement of the 5 to 20 μm filter with a 20 to 23 μm water-vapor band filter.

The Image Dissector Camera System (IDCS)

The IDCS used an image dissector tube aligned along the spacecraft local vertical axis. The camera unit supplied horizontal deflection and a portion of the vertical displacement while the satellite motion completed the vertical displacement. Scanning was at the rate of four lines per second. The system provided daylight pictures 1600 n.mi. square with a resolution of 800 television lines. There were approximately 17 pictures taken over the sunlit portion of the earth on each orbit at 208 second intervals. IDCS data are available in 70 mm black and white transparencies and prints.

The IDCS replaced the AVCS and APT cameras flown on Nimbus 1 and 2. Direct Readout Image Dissector (DRID) photographs were also transmitted by the Real Time Transmissions System to APT stations throughout the world.

Infrared Interferometer Spectrometer (IRIS)

Spectral response measurements of the earth-atmosphere system were made in the 5 to 20 μm region with a Michelson-type interferometer. The interferometer produced about 400 interferograms per orbit. On the ground the required spectrum of sensed flux was obtained by computing the Fourier cosine transform of the interferogram function. Specific intensity was recorded with a resolution of five wave numbers. The measurements permitted the deduction of vertical temperature profiles in the atmosphere, the distribution of ozone, water vapor and some of the minor gas constituents (i. e., CH_4), and the accurate determination of surface temperature. The ground resolution is about 150 km.

The Satellite Infrared Spectrometer (SIRS)

The SIRS measured radiation from seven spectral intervals in the 15 μm CO_2 band. From the radiation measurements vertical temperature profiles for the atmosphere were inferred. These temperature profiles were used operationally by the U. S. Weather Bureau as inputs to the Numerical Weather Prediction system. The ground resolution is about 200 km.

The Monitor of Ultraviolet Solar Energy (MUSE)

This instrument consisted of five sensors that measured the solar flux in the 1100 \AA to 3000 \AA spectral region. The primary purpose of the experiment was to determine whether the solar flux changes, and, if so, by how much. Secondary purposes were: (1) To make absolute measurements of the flux, (2) to measure the rate of decrease of flux as the satellite enters the earth's shadow near the Poles, and possibly (3) to measure atmospheric ozone.

The Interrogation, Recording and Location System (IRLS)

The IRLS interrogated and collected data from both stationary and moving platforms. The instrumented platforms measured temperature, pressure, ocean currents, salinity, wind speeds, and a variety of other geophysical parameters; these data were then transmitted to the Nimbus satellite upon command. There were about 14 fixed and moving platforms throughout the world during the Nimbus 3 experiment.

A.2.4 Nimbus 4 Experiments

The Image Dissector Camera System (IDCS)

The IDCS experiment is essentially the same as the one flown on Nimbus 3.

The Temperature Humidity Infrared Radiometer (THIR)

The THIR is a scanning (48 rpm) radiometer with two channels: (1) A window channel at 10 to 12 μm with a resolution of 8 km at the subpoint; and (2) a water vapor channel at 6.7 μm with a resolution of about 22 km at the subpoint. The window channel operates day and night providing cloud top or surface temperatures. The water vapor channel operates mostly at night and gives information on the water vapor content of the upper troposphere and stratosphere. THIR window channel data are also normally transmitted at night by the Real Time Transmission System (RTTS-DRIR) to appropriately modified APT ground stations throughout the world. Data formats are the same as those previously described for Nimbus 1 HRIR.

The Satellite Infrared Spectrometer (SIRS)

The SIRS on Nimbus 4 is a Fastie-Ebert grating spectrometer which measures radiation at various intervals of the $15 \mu\text{m}$ CO_2 band, and the 20 to $40 \mu\text{m}$ water vapor band. Radiation measurements are used to determine the vertical temperature structure and water vapor content of the atmosphere; the usefulness of these measurements in numerical weather prediction is currently being assessed.

The Monitor of Ultraviolet Solar Radiation (MUSE)

This experiment monitors ultraviolet solar flux in five spectral intervals to detect variations of relative intensity with time. The instrument measures solar flux with a sensor consisting of five photo diodes having peak sensitivities at 1500 \AA , 1800 \AA , 2100 \AA , 2600 \AA and 1216 \AA . The ultraviolet energy input into the terrestrial atmosphere and its variation with time at different wavelengths can be related to the formation of the ozonosphere, the establishment of photo-chemical equilibrium, and the heating of the upper regions of the stratosphere.

The Filter Wedge Spectrometer (FWS)

The FWS experiment monitors the vertical water vapor content in the atmosphere along a continuous strip 150 km wide under the orbital path. The spectrum is scanned from 3 to $7 \mu\text{m}$ with a rotating filter wedge. Vertical water vapor distribution is derived from the spectra by mathematical inversion techniques.

The Backscatter Ultraviolet Spectrometer (BUV)

The BUV experiment monitors the global distribution of atmospheric ozone by measuring the intensity of ultraviolet radiation backscattered from the earth's atmosphere at 12 wavelengths in the 2500 \AA to 3400 \AA spectral region. The knowledge of atmospheric ozone distribution on a global scale is needed for studies of the energy balance and photo-chemistry of the stratosphere, the mass exchange between the lower stratosphere and troposphere, and the general atmospheric circulation.

The Infrared Interferometer Spectrometer (IRIS)

The IRIS is a Michelson-type interferometer which measures radiation from the earth-atmosphere system in the 8 to $40 \mu\text{m}$ region. The spectral resolution is 2.5 cm^{-1} ; the ground resolution, approximately 100 km . Spectral distributions are obtained by computing the Fourier transforms of the recorded interferograms. The spectral measurements permit computation of atmospheric temperature profiles, water vapor and ozone contents, and surface temperatures.

The Interrogation, Recording and Location System (IRLS)

The IRLS interrogates and collects data from both stationary and moving experimental platforms throughout the world. IRLS also position-fixes moving platforms. The instrumented platforms measure and record a variety of geophysical parameters, including temperatures, pressure, ocean currents, salinity, wind speeds, and transmit these data to the Nimbus satellite upon command. The Nimbus satellite, in turn, retransmits all the collected data from the platforms to the CDA facilities at Alaska and Rosman. The Nimbus 4 satellite supports a greatly expanded IRLS program which includes constant level balloons.

The Selective Chopper Radiometer (SCR)

The SCR experiment determines the temperature of six successive layers of the atmosphere by radiometric measurements of the emission of carbon dioxide in the 15 μm band. The SCR consists of six channels, each of which contains its own optical and electronic components. The six channels and their filter bandwidths are $668 \pm 1.5 \text{ cm}^{-1}$, $775 \pm 6 \text{ cm}^{-1}$, 935 cm^{-1} , $675 \pm 5 \text{ cm}^{-1}$, $697 \pm 5 \text{ cm}^{-1}$, and $712 \pm 5 \text{ cm}^{-1}$. The field of view for the upper channels (1 and 2) is circular and 160 km in diameter. Channels 3 through 6 have a field of view of 110 km square.

A.2.5 Nimbus E Experiments

The Nimbus E satellite will be labeled Nimbus 5 after its launch in 1972. Two new experiments on Nimbus E, the SCMR and the ESMR, will be applicable to earth resource surveys, and therefore will be described in detail.

The Surface Composition Mapping Radiometer (SCMR)

The SCMR's main objective is to determine surface composition by measuring the reststrahlen effect in the 8 to 12 μm band. The surface radiation in the 8.4 to 9.48 μm and the 10.2 to 11.4 μm intervals will be measured with a 600-meter ground resolution. A third channel in the 0.8 to 1.1 μm interval will measure the near infrared reflected solar radiation in the daytime only. Radiation measurements translated to equivalent temperatures for the two infrared channels and effective reflectance for the near infrared channel will be presented in pictorial photographic format and in computer-produced maps.

The two infrared channels in the 8 to 12 μm interval will give different equivalent temperatures, depending on the emissivity of the surface. Silicates, the dominant rock mineral group of the earth's surface, have strong absorption peaks (reststrahlen effect) corresponding to lower emission in the infrared from about 8.5 to 12 μm , the position of the peak shifting toward longer wavelengths as the

silicon oxygen (Si-O) content of the mineral is lowered. Quartz (SiO_2), for example, absorbs sharply at $9 \mu\text{m}$ producing a lower emission and, therefore, a lower temperature from the 8.4 to $9.48 \mu\text{m}$ channel measurement than from the 10.2 to $11.4 \mu\text{m}$ channel. On the other hand, olivine, Fe_2SiO_4 , absorbs around $11.5 \mu\text{m}$ giving a lower temperature in the 10.2 to $11.4 \mu\text{m}$ channel. Similarly, granite rocks which contain quartz and feldspar absorb broadly from 8.5 to $9.5 \mu\text{m}$ (producing lower temperatures in the 8.4 to $9.48 \mu\text{m}$ channel) and basalts, i. e., feldspar and pyroxene, absorb at $10.1 \mu\text{m}$ (producing lower temperatures in the 10.2 to $11.4 \mu\text{m}$ channel). The reason for the two channel measurements is to bypass the effect of the strong $9.6 \mu\text{m}$ absorption band of atmospheric ozone. Measurements will be made at either side of this band; the difference of the equivalent temperature obtained from the two channel measurements (related to the Si-O content) will give a general idea of the type of mineral surface.

Over water with emissivity of nearly one, both SCMR channels in the 8 to $12 \mu\text{m}$ band will indicate surface equivalent blackbody temperatures with a small error due to atmospheric absorption. The temperatures recorded would be 1 to 2°K lower than the actual temperatures for average atmospheric conditions.

The 0.8 to $1.1 \mu\text{m}$ channel, operative during daytime only, will map the reflected near-infrared energy from the surface. This channel will be used intermittently in lieu of one of the two channels in the 8 to $12 \mu\text{m}$ band.

The Electrically Scanning Microwave Radiometer (ESMR)

The main objective of this experiment is to map, globally and contiguously, the thermal radiation emitted by the earth's surface and atmosphere at a wavelength of approximately 1.55 cm . The resolution is approximately 25 km at the subsatellite point. The mapped patterns of absolute intensity of this radiation will reflect a number of important physical properties of the surface, as well as the meteorological conditions above it. Over water, brightness temperatures measured by the satellite in the nadir direction will vary between 120 and 240°K depending primarily on the thickness and liquid water content of the overlying clouds. Heavy rain clouds which, for example, may be indistinguishable in the visible or infrared from cirrus or stratus clouds containing little liquid water will be easily identified and tracked at this wavelength.

In polar regions, one expects to observe an equally large contrast between the liquid and frozen surfaces of the sea and of lakes. Stratus and cirrus clouds which generally predominate in polar regions will have little effect on these observations. Thus, it will be possible to map the distribution of ice over the polar seas, regardless of cloud cover and solar illumination.

Over land, contrasts in the measured radiation will be less uniquely related to physical parameters than over water. Nevertheless, it is expected that by making use of Nimbus E infrared radiation observations and other information available on

the properties of the observed land areas, heavy rain clouds will still be contrasted very strongly against land. This should be especially true in tropical regions where rain clouds have a very high water content, and over areas of dense vegetation where high cloud reflectances contrast sharply with low surface reflectances. Thus, areas of precipitation and severe storm activity can be identified, tracked and distinguished from other, less important, cloud formations over land, as well as over water.

In the absence of thick rain clouds and precipitation, contrasts between different degrees of vegetation will be most prominent. Over barren lands the strongest radiation contrasts will be due to moisture content of the surface soil; brightness temperature variations up to 30°C are expected in these cases. A secondary objective is, therefore, to demonstrate the value and limitations of satelliteborne microwave imaging devices for hydrologic, geomorphologic and agricultural purposes.

The Temperature Humidity Infrared Radiometer (THIR)

Same as the THIR experiment flown on Nimbus 4.

The Infrared Temperature Profile Radiometer (ITPR)

The ITPR will measure the earth-atmosphere radiation in the following spectral bands: (1) Two intervals in atmospheric window regions (near 3.8 and 11 μm), (2) six intervals in the 15 μm CO₂ absorption band, and (3) one interval in the water vapor rotational band near 20 μm. These radiation measurements will yield the vertical temperature profile of the atmosphere and the total water vapor content of an atmospheric column.

The Nimbus E Microwave Spectrometer (NEMS)

The NEMS will measure microwave radiation from the earth-atmosphere in five spectral bands including an atmospheric window at 27.23 GHz, a water vapor band at 31.4 GHz, and three oxygen absorption bands at 53.65, 54.90 and 58.80 GHz. The radiation measurements will yield tropospheric temperature profiles, atmospheric water vapor abundance, cloud water content and land temperature, even in the presence of clouds which block infrared sensors.

The Tracking and Data Relay Experiment (T&DRE)

The T&DRE will provide a communication link between Nimbus E and the ground via the Applications Technology Satellite, ATS-F. The experiment's objectives are:

- 1) To establish the tracking capability between a low polar orbiting satellite and a synchronous satellite.

- 2) To compare the orbital precession of the two satellites as measured by ground-to-satellite and satellite-to-satellite techniques.
- 3) To evaluate atmospheric and multipath problems for future low-to-synchronous satellite data systems which may be used to eliminate onboard storage devices on the low satellites.
- 4) To determine gravitational model uncertainties.

The Selective Chopper Radiometer (SCR)

The SCR will measure the earth-atmosphere radiation in 16 spectral channels separated into four groups:

Group A - Four CO₂ channels over the range of 13.8 to 14.8 μm.

Group B - Four CO₂ channels at approximately 15 μm.

Group C - A window channel at 11 μm, an H₂O channel at 18.6 μm, and channels at 46.5 and 100 μm.

Group D - Channels at 2.08, 2.59, 2.65 and 3.5 μm.

The objectives of the experiment are:

- 1) Observe global temperature structure of the atmosphere at altitudes up to 50 km over an extended period in time.
- 2) Make supporting observations of water vapor distribution.
- 3) Determine the density of ice particles in cirrus cloud.

A.2.6 Nimbus F Experiments

Of the dozen or so experiments currently being considered for the Nimbus F satellite, to be launched in 1973, two of them, the THIR and the ESMR, show promise for non-meteorological earth resources observations. These experiments are similar to the previously described THIR on Nimbus 4 and the ESMR planned for Nimbus E.

A.3 Archival and Dissemination of Nimbus Data

The nature and format of the data available from the Nimbus experiments are explained in detail in the Nimbus User's Guides. Nimbus data are archived and available as follows:

- 1) AVCS photographic data in 35 mm transparency format are archived and available from the National Climatic Center (NCC), National

Oceanic and Atmospheric Administration, Federal Building, Asheville, North Carolina 28801.

Limited amounts of photographic data in 70 mm transparency or print formats are available from the Nimbus Data Utilization Center, NASA/GSFC, Greenbelt, Maryland 20771.

- 2) IDCS photographic data in 70 mm transparency format are archived and available from the National Climatic Center.
- 3) HRIR and THIR photographic data are archived and available in 70 mm transparency or print formats from the National Space Science Data Center (NSSDC), Goddard Space Flight Center, Code 601, Greenbelt, Maryland 20771.
- 4) MRIR photographic data are archived and available in 4" x 5" transparency or 4" x 5" and 8" x 10" print formats from the NSSDC.
- 5) HRIR, THIR, and MRIR grid print maps, computer produced from the NMRT, are available from the NSSDC.
- 6) HRIR, THIR, SCR, FWS, BUV, IRIS, and MUSE digital data in computer tape format (Nimbus Meteorological Radiation Digital Tapes, NMRT) are archived and available from the NSSDC.
- 7) SIRS digital data are archived and available from two sources. Digital data tapes containing radiance values are archived in the NSSDC. Digital data tapes containing temperature profiles are archived in the NCC.

AVCS and IDCS photographic data and SIRS digital data are available from the NCC at cost. The NSSDC can furnish to qualified investigators limited quantities of all other data without charge. A charge for production and dissemination costs may be established by NSSDC if a large volume of data is requested. Whenever it is determined that a charge is required, a cost estimate will be provided to the user prior to filling his data request.

All requests from non-United States researchers for HRIR, THIR, MRIR, SCR, FWS, BUV, IRIS, SIRS or MUSE data, archived and available through NSSDC, must be specifically addressed to: Director, World Data Center A for Rockets and Satellites, Code 601, Goddard Space Flight Center, Greenbelt, Maryland 20771, U. S. A.

Browsing files of all Nimbus pictorial data (AVCS, IDCS, HRIR, THIR, MRIR) are maintained at Goddard Space Flight Center, Greenbelt, Maryland 20771 and are available for study and reference.

Page Intentionally Left Blank

APPENDIX B

SURFACE EMISSIVITY AND ATMOSPHERIC EFFECTS ON NIMBUS HRIR AND THIR DATA

B.1 Introduction

The temperatures derived from the Nimbus HRIR (3.8 μm window) and THIR (11.5 μm window) radiation measurements differ from actual surface temperatures because of atmospheric attenuation effects, or because surface emissivities are less than one. The reflectances derived from measurements by the Nimbus 3 daytime HRIR channel (1.0 μm window) include residual infrared radiation sensed in the 3.8 μm window and atmospheric absorption effects and, therefore, do not correspond to actual surface reflectance. In this appendix, the effects of surface emissivities and atmospheric absorption on the derived surface temperatures and reflectances are discussed in detail.

B.2 Surface Emissivity and Atmospheric Effects on Nimbus HRIR and THIR Temperatures

B.2.1 Effects of Surface Emissivity

The temperatures mapped from the HRIR and THIR measurements are obtained by means of Planck's Law for a blackbody:

$$dI_b = \frac{C_1 \lambda^{-5}}{\exp\left(\frac{C_2}{\lambda T_b}\right) - 1} d\lambda. \quad (\text{B-1})$$

Planck's equation expresses the maximum radiation intensity, I_b , emitted by an object at temperature T_b as a function of wavelength, λ . I_b and T_b are referred to as intensity of blackbody radiation and temperature, respectively. C_1 and C_2 are numerical constants.

The intensity, I_m , measured by the Nimbus radiometer assuming blackbody radiation and an ideal atmospheric "window" (no absorption of radiation) is

$$I_m = \int_{\lambda_1}^{\lambda_2} \phi(\lambda) \frac{C_1 \lambda^{-5}}{\exp\left(\frac{C_2}{\lambda T_b}\right) - 1} d\lambda = \int_{\lambda_1}^{\lambda_2} \phi(\lambda) B(\lambda, T_b) d\lambda \quad (\text{B-2})$$

where

$B(\lambda, T_b)$ is the blackbody function

and

$\phi(\lambda)$ is the instrument's filter function over the wavelength interval λ_1 to λ_2 (3.4 to 4.2 μm for Nimbus 1, 2 and 3 HRIR nighttime channel, and 10 to 12 μm for Nimbus 4 THIR channel).

Eq. (B-2) is the basis for deriving surface temperatures from radiometric measurements. However, the unique relationship between I_m and T_b as defined above is strictly true only in the case of a perfect blackbody. For surfaces which do not radiate as blackbodies, the inferred temperatures, T_b , using Eq. (B-2), are "equivalent blackbody temperatures." With the exception of water surfaces and moist vegetated land which radiate nearly as blackbodies in the infrared, most of the surfaces of the earth radiate as "gray bodies" emitting infrared intensities at a fraction of the emissivity, \bar{E} , of a blackbody at the same temperature. Table B-1 lists emissivities, \bar{E} , of some common terrain features in the 3 to 5 μm and 8 to 13 μm bands. Laboratory measurements by Hovis and Callahan (1966) indicate that infrared emissivities of many minerals in their natural state may be much less than unity. For these surfaces, a more accurate expression of the intensity, I_m , measured by the Nimbus radiometer is

$$I_m = \bar{E} \int_{\lambda_1}^{\lambda_2} \phi(\lambda) B(\lambda, T_b) d\lambda \quad (\text{B-3})$$

where

\bar{E} is the average emissivity of the surface in the wavelength interval $\lambda_1 \leq \lambda \leq \lambda_2$.

Since $\bar{E} \leq 1$, the intensity measured by a radiometer over a "gray body" surface would be less than that over a blackbody at the same temperature. Therefore, the "equivalent blackbody temperature" inferred from Eq. (B-2) would be less than the actual surface temperature.

The emissivity of a surface thus affects the accuracy of the derived HRIR or THIR temperature map. Except for water surfaces and moist vegetated land with emissivities nearly equal to one, the temperatures mapped using Eq. (B-2) are lower than the actual surface temperatures. Figure B-1 gives the relationship between the measured intensities, I_m , and the equivalent blackbody temperatures for $\bar{E} = 1$ and $\bar{E} = 0.9$ for the 3.4 to 4.2 μm channels of the Nimbus 1, 2 and 3 radiometers. Figure B-2 presents a similar relationship for the 11.5 μm THIR channel of Nimbus 4. These figures show that a surface emissivity of 0.9 would result in deduced equivalent blackbody temperatures of approximately 288°K and 287°K for measurements in the 3.8 μm band and the 11.5 μm band, respectively, when the

TABLE B-1 -

REFLECTANCE (\bar{r}) AND EMISSIVITY (\bar{E}) OF COMMON
TERRAIN FEATURES (after Wolfe, 1965)

	Spectral Regions			
	0.7-1.0 μ	1.8-2.7 μ	3.0-5.0 μ	8.0-13.0 μ
Green Mountain Laurel	$\bar{r} = 0.44$	$\bar{E} = 0.84$	$\bar{E} = 0.90$	$\bar{E} = 0.92$
Young Willow Leaf (dry, top)	0.46	0.82	0.94	0.96
Holly Leaf (dry, top)	0.44	0.72	0.90	0.90
Holly Leaf (dry, bottom)	0.42	0.64	0.86	0.94
Pressed Dormant Maple Leaf (dry, top)	0.53	0.58	0.87	0.92
Green Leaf Winter Color - Oak Leaf (dry, top)	0.43	0.67	0.90	0.92
Green Coniferous Twigs (Jack Pine)	0.30	0.86	0.96	0.97
Grass - Meadow Fescue (dry)	0.41	0.62	0.82	0.88
Sand - Hainamanu Silt Loam - Hawaii	0.15	0.82	0.84	0.94
Sand - Barnes Fine Silt Loam - South Dakota	0.21	0.58	0.78	0.93
Sand - Gooah Fine Silt Loam - Oregon	0.39	0.54	0.80	0.98
Sand - Vereininging - Africa	0.43	0.56	0.82	0.94
Sand - Maury Silt Loam - Tennessee	0.43	0.56	0.74	0.95
Sand - Dublin Clay Loam - California	0.42	0.54	0.88	0.97
Sand - Pullman Loam - New Mexico	0.37	0.62	0.78	0.93
Sand - Grady Silt Loam - Georgia	0.11	0.58	0.85	0.94
Sand - Colts Neck Loam - New Jersey	0.28	0.67	0.90	0.94
Sand - Mesita Negra - lower test site	0.38	0.70	0.75	0.92
Bark - Northern Red Oak	0.23	0.78	0.90	0.96
Bark - Northern American Jack Pine	0.18	0.69	0.88	0.97
Bark - Colorado Spruce	0.22	0.75	0.87	0.94

Note: $\bar{E} + \bar{r} = 1$

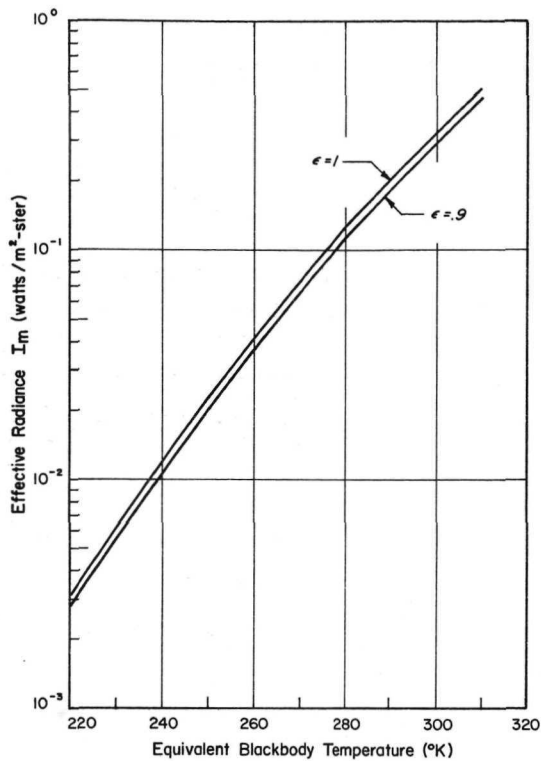


Figure B-1 Relationship between effective radiance, I_m , measured by the 3.4 to 4.2 μm channels of the Nimbus 1, 2, and 3 HRIR and equivalent blackbody temperature for an emissivity of 1 and 0.9.

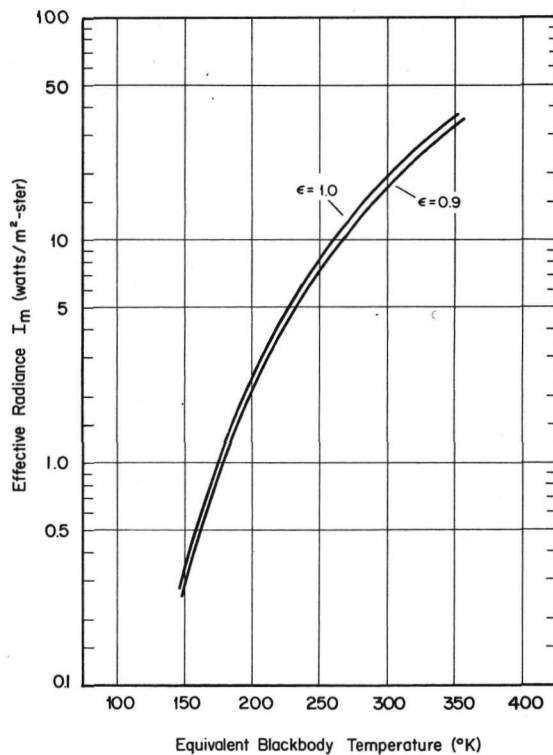


Figure B-2 Relationship between effective radiance measured by the 11.5 μm channel of the Nimbus 4 THIR and equivalent blackbody temperature for an emissivity of 1 and 0.9.

actual surface temperature is 290°K . These figures also show that the greatest errors (2 to 4°K) due to surface emissivity effects occur in the $3.8\ \mu\text{m}$ band over sand because of the relatively low emissivities of sand in this band.

B.2.2 Effects of Atmospheric Absorption

In reality, no absolutely transparent "window" exists in the atmosphere. Absorption in the HRIR and THIR bands is mainly due to water vapor, carbon dioxide, and ozone, and varies mainly with the distribution and temperature of these gases along the optical path. In this report, no absorption effects of atmospheric dust in the infrared will be considered, although these, at times, may be large, especially over and near deserts from which large dust storms originate. A THIR photofacsimile of a dust storm over the Sahara (Figure B-3) shows the drastic attenuation of temperatures (gray areas) caused by the dust which is also visible in a concurrent IDCS picture of the area (see also Figure 2-14).

Theoretical radiative transfer calculations for three model atmospheres were performed by Kunde (1965) to determine the effect of atmospheric absorption on the radiation measured by the $3.8\ \mu\text{m}$ HRIR channel of Nimbus 1. Table B-2 shows the main characteristics of the three atmospheres used in the calculations. The results, expressed as the departure of the HRIR equivalent blackbody temperature from the theoretical surface temperature, are presented in Figure B-4. Kunde also considered the surface emissivity effect on the theoretical temperature difference. This effect for a surface emissivity of 0.9 is shown in Figure B-5 for the High Latitude Winter and Tropical Model atmospheres. Figure B-4 shows that on the average a correction of 1 to 2°K will be sufficient for zenith angles of about 30° . For surface emissivities less than unity, an additional correction is needed. In general, decreasing the surface emissivity to 0.9 increases the temperature difference by about 2°K for low zenith angles ($<30^{\circ}$) as shown in Figures B-5, B-2 and B-1.

Using the same three model atmospheres as Kunde, Smith et al (1970) performed similar radiative calculations for the nearly similar Nimbus 2 HRIR $3.8\ \mu\text{m}$ channel. The results are shown in Figure B-6. In general, the temperature corrections for Nimbus 2 HRIR are about 0.5°K greater than Nimbus 1 HRIR, the difference probably due to the slightly different filter functions and water vapor and carbon dioxide transmittances used in the two sets of calculations.

Because atmospheric temperature and moisture structure and, therefore, attenuation of radiation by the atmosphere, have been found to be highly correlated to the surface temperature, it is possible to express the temperature correction as a function only of the observed equivalent blackbody temperature and the viewing angle of measurement. Smith et al (1970) thus expressed the temperature correc-

tion, ΔT , for Nimbus 2 HRIR caused by atmospheric attenuation as

$$\Delta T = \left[a_0 + a_1 \left(\frac{\theta}{60^\circ} \right)^{a_2} \right] \ln \left(\frac{100}{310^\circ - T_b} \right) \quad (B-4)$$

for

$$\theta \leq 60^\circ; \quad 210^\circ\text{K} \leq T_b \leq 300^\circ\text{K}$$

where

ΔT is the quantity added to the measured T_b to correct for atmospheric absorption

$$a_0 = 1.13$$

$$a_1 = 0.82$$

$$a_2 = 2.48$$

and

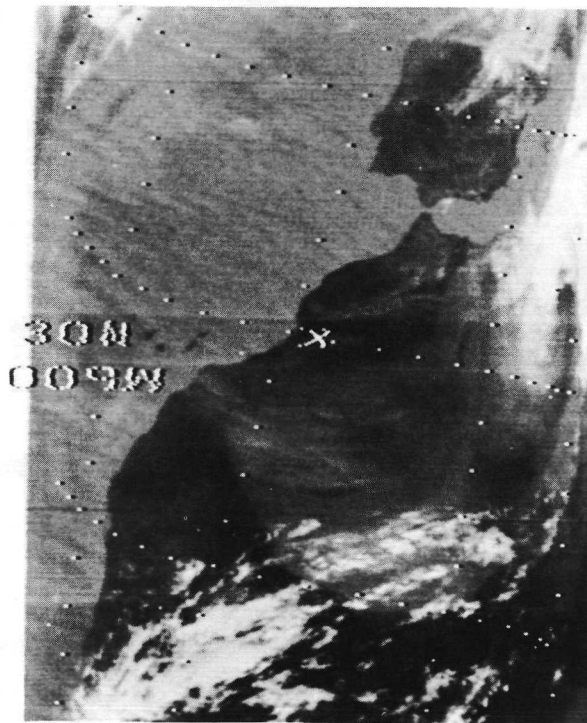
θ is the local zenith angle of measurement.

The corrections for T_b greater than 300°K or less than 210°K can be assumed to be equal to those for 300°K and 210°K , respectively.

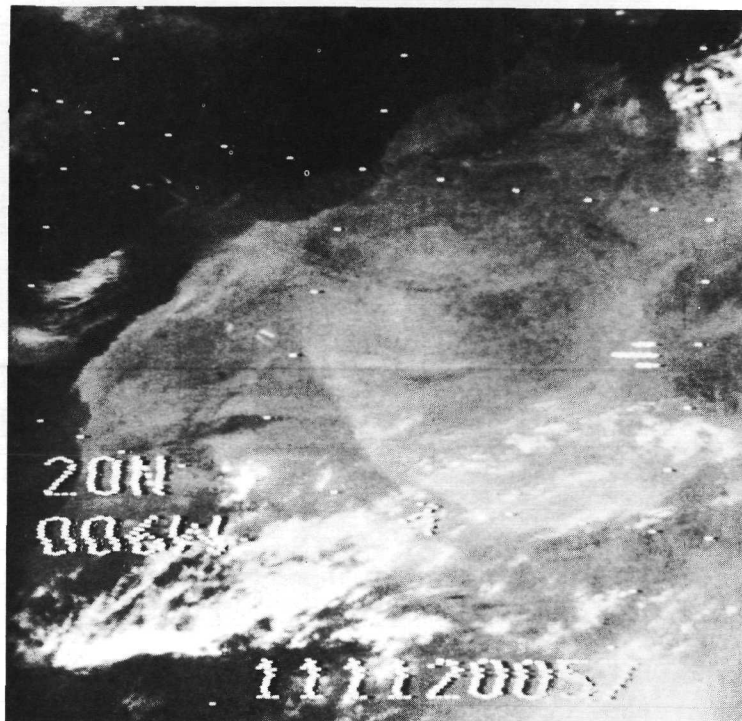
Atmospheric absorption corrections to the observed surface temperatures calculated for the Nimbus 1 and 2 instruments are also valid for the nearly identical Nimbus 3 HRIR $3.8 \mu\text{m}$ channel. Corrections for the Nimbus 4 THIR $11.5 \mu\text{m}$ measurements have been calculated by V. Salomonson of NASA/GSFC (personal communication, September 1970) for ten different model atmospheres. The results and the main characteristics of the atmospheres used are presented in Figure B-7 and Table B-3. Figure B-8 shows the correction due to atmospheric absorption as a function of the observed equivalent blackbody temperatures. The curve was obtained by a "best fit" of the results by Salomonson. The corrections are valid for low zenith angles ($\leq 30^\circ$), and are in addition to the corrections due to surface emissivity effects.

B.3 Daytime $3.8 \mu\text{m}$ HRIR Measurements

A few Nimbus 1 and 2 HRIR measurements were made in the daytime. These daytime measurements do not approximate the true surface temperatures because there is an appreciable contribution by reflected solar radiation in the 3.4 to $4.2 \mu\text{m}$ band of the radiometer. In the case of Nimbus 1, daytime measurements are not even susceptible to meaningful quantitative analyses since they are highly contaminated by spurious shortwave radiation entering the radiometer, most probably caused by an uncoated rim or crack of the interference filter (Kuers, 1968). The following analysis applies, therefore, only to the Nimbus 2 daytime measurements.



a. Nimbus 4 THIR



b. Nimbus 4 IDCS

Figure B-3 Comparison of a Nimbus 4 THIR photofacsimile and a concurrent IDCS picture taken on orbit 177, 21 April 1970, showing the effect of a dust storm over the Sahara Desert.

TABLE B-2

SURFACE TEMPERATURES AND TOTAL GAS CONTENT FOR
MODEL ATMOSPHERES OF FIGURE B-4 AT ZENITH ANGLE OF 0°
(Kunde, 1965)

Atmosphere	Surface Temperature (K°)	Carbon Dioxide u(cm-atm)	Water Vapor u(pr-cm)
Tropical	305.0	247.4	4.70
ARDC Std (1959)	288.0	247.3	1.16
High Latitude Winter-Cold	246.5	247.8	0.14

TABLE B-3

COMPUTATIONS OF ATMOSPHERIC EFFECTS ON
THR-DERIVED TEMPERATURES (Salomonson, 1970)

Atmosphere*	Temperature Surface	Precipitable Water	"Observed" Equivalent Blackbody Temperatures at Nadir Angles of:			
	(deg Kelvin)	(cm)	0°	15°	30°	50°
1) Standard	288.15	1.96	283.38	283.24	282.77	280.70
2) Tropical	299.65	3.63	294.37	294.23	293.74	291.56
3) Subtropical Summer	301.15	3.94	294.77	294.60	294.02	291.45
4) Subtropical Winter	287.15	1.93	284.02	283.93	283.61	282.18
5) Mid-Latitude Summer	294.15	2.64	290.29	290.19	289.79	287.95
6) Mid-Latitude Winter	272.59	0.74	270.64	270.58	270.41	269.53
7) Sub-Arctic Summer	287.15	1.84	283.59	283.49	283.13	281.55
8) Sub-Arctic Winter (Cold)	257.28	0.36	256.58	256.56	256.48	256.13
9) Arctic Summer	278.15	1.65	274.51	274.39	274.00	272.24
10) Arctic Winter (Mean)	249.22	0.18	248.95	248.95	248.91	248.74

*Reference: Shea, L. Valley (ed), 1965: Handbook of Geophysics and Space Environments, USAF Cambridge Research Laboratories, Office of Aerospace Research.

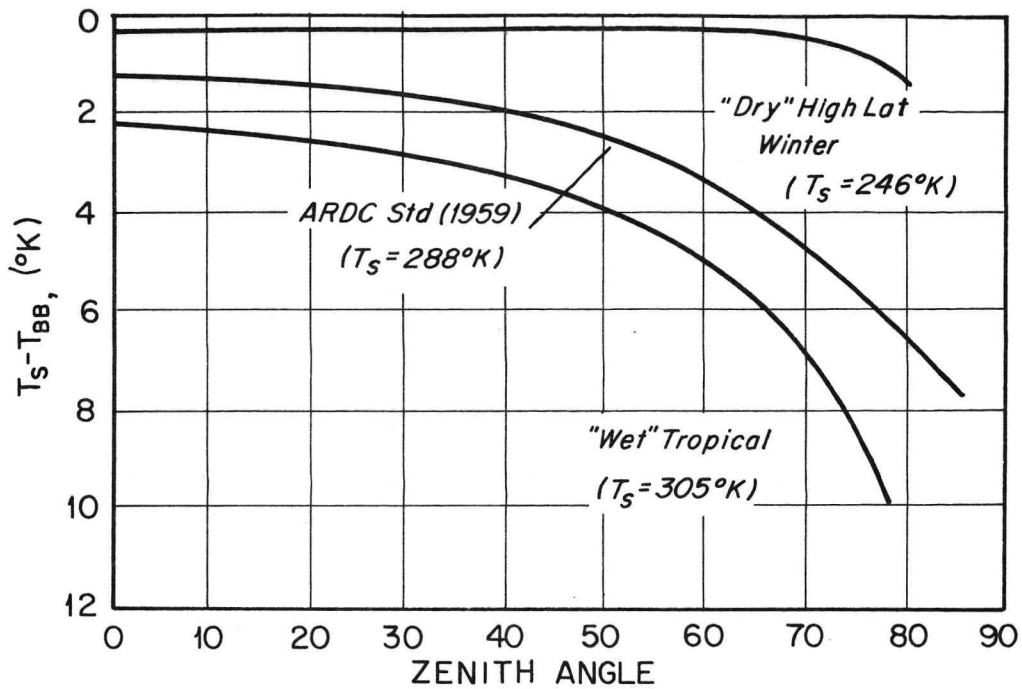


Figure B-4 Theoretical surface temperature minus HRIR equivalent black-body temperature as a function of zenith angle for the model atmospheres of Table B-2. A gray-body surface emissivity of unity and clear-sky conditions have been assumed. (Kunde, 1965)

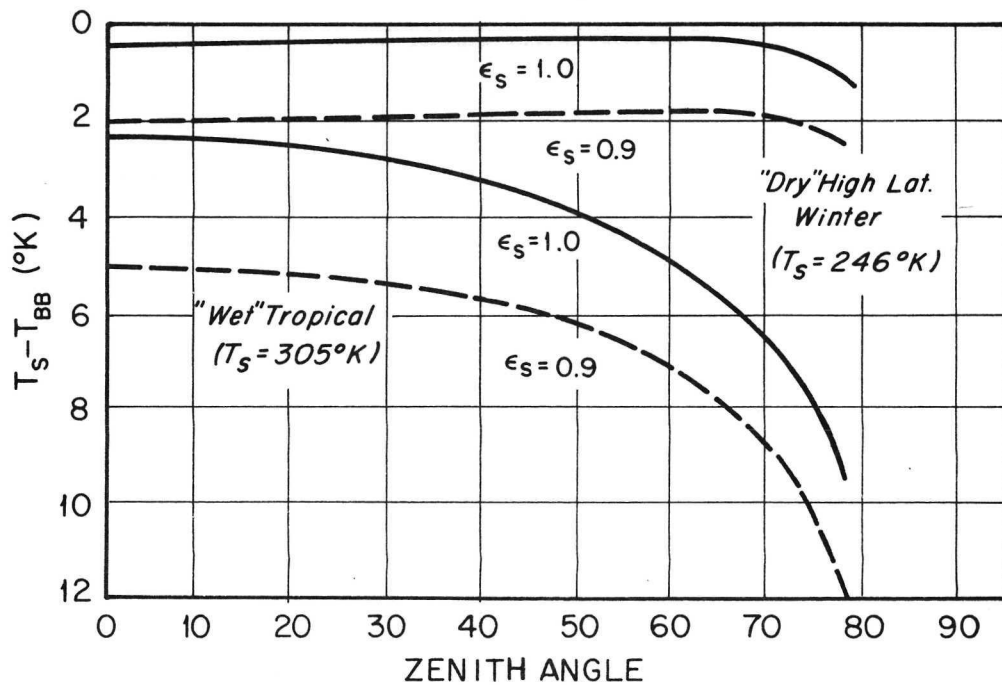


Figure B-5 Surface emissivity effect on the theoretical temperature differences as a function of zenith angle. Clear-sky conditions and a gray-body surface emissivity are assumed. (Kunde, 1965)

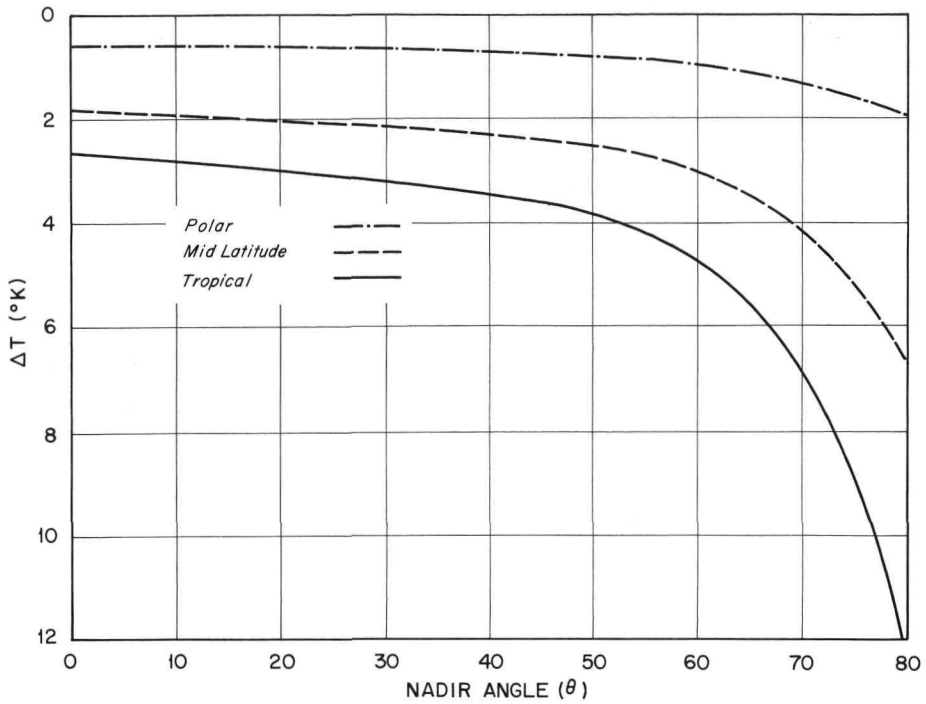


Figure B-6 Calculated departure of Nimbus 2 HRIR equivalent blackbody temperatures from ground surface temperature as a function of local zenith angle for three different air masses. (Smith et al, 1970)

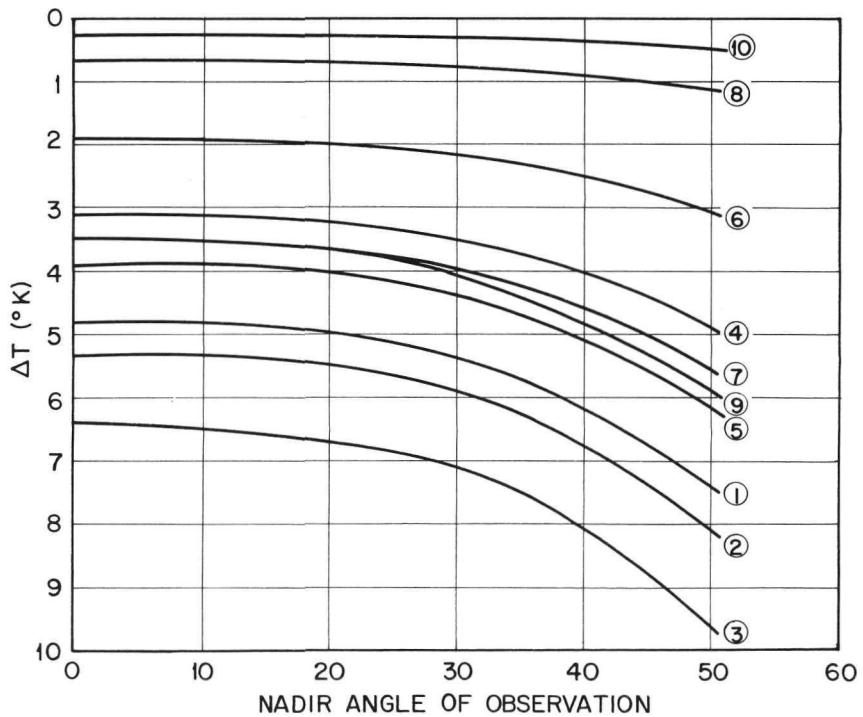


Figure B-7 Calculated departure of Nimbus 4 THIR 11.5 μm channel temperatures from ground surface temperature as a function of local zenith angle for 10 different atmospheres specified in Table B-3. (Salomonson, 1970)

As in the case with the nighttime data, maps of daytime Nimbus 2 HRIR data show values of equivalent blackbody temperatures, T_b , corresponding to the measured radiation, I_m , and are obtained by means of Eq. (B-2). However, in the interpretation of the daytime data, the effect of surface reflectivity must be considered. Neglecting the second-order effects of atmospheric scattering and absorption, the measured daytime radiation, I_m , is

$$I_m = \bar{r} \int_{3.4}^{4.2} S(\lambda) \phi(\lambda) d\lambda + \bar{E} \int_{3.4}^{4.2} B(\lambda, T_b) \phi(\lambda) d\lambda \quad (B-5)$$

where

$S(\lambda)$ is the spectral solar irradiance, i. e., $\int_0^{\infty} S(\lambda) d\lambda$ is the solar constant and \bar{r} is the reflectivity or "albedo" of the surface averaged over the 3.4 to 4.2 μm band.

The second term in the equation, representing the emissive contribution by the surface is identical to that describing the nighttime situation. Eq. (B-5) is the more general form of Eq. (B-3) and, by reference to Kirchhoff's law which states that $\bar{E} = 1 - \bar{r}$, is reduced to Eq. (B-3) when $\bar{r} = 0$ (or $\bar{E} = 1$). From Eq. (B-5), it is evident that the significance of the reflective contribution is dependent on the magnitude of \bar{r} (i. e., $1 - \bar{E}$) and on $S(\lambda)$. It was shown in Table B-1 that for most natural surfaces $\bar{r} \neq 0$, (i. e., $\bar{E} \neq 1$), and since during daylight hours solar irradiance, $S(\lambda)$, in the 3.4 to 4.2 μm band is quite substantial, the reflective term is no longer negligible as is in the nighttime case. Even a small departure of the emissivity from unity, as is the case for most natural surfaces, will cause the mapped equivalent blackbody temperatures to depart considerably from the actual surface temperatures.

Eq. (B-5) can be more simply expressed as

$$I_m = (1 - \bar{E}) I_s + \bar{E} I_b \quad (B-6)$$

where

I_s and I_b are, respectively, the solar and terrestrial radiation sensed by the radiometer.

With Eq. (B-5) or (B-6) it is possible to estimate the effect of solar radiation and surface emissivities on the measured daytime radiation, I_m , and the equivalent blackbody temperature, T_b . For solar radiation at nearly vertical incidence, I_s is approximately 1 watt meter⁻² steradian⁻¹. I_b , the terrestrial radiation sensed by the radiometer as a function of the equivalent blackbody temperature, can be obtained from the instrument's calibration (see Nimbus II User's Guide).

Eq. (B-6) was evaluated for different values of emissivity. The results are presented in Figure B-9, which shows the overwhelming effect of solar radiation, totally masking the surface temperature except for $\bar{\epsilon} = 1$. At temperatures above 280°K the solar radiation contribution is of the same magnitude as the telluric radiation* for emissivities of 0.9 or less. Thus, at these high temperatures the daytime data can yield an estimate of the surface temperature only when the surface emissivity is accurately known. Conversely, when the surface temperature is known, accurate measurement of surface emissivities can be made. At low temperatures, emissivities can be estimated without a knowledge of the temperature. For example, at temperatures below 270°K , even with high emissivities, the telluric radiation (last term of Eq. (B-6)) is one order of magnitude or less than the solar reflected radiation, and may be neglected.

B.4 Daytime Nimbus 3 HRIR Measurements

As in the case of the HRIR of Nimbus 1 and 2, the daytime Nimbus 3 HRIR measurements are a combination of reflected solar radiance and thermal emission from the earth. As such, Eq. (B-5) applies. However, the daytime channel of the Nimbus 3 HRIR was specially designed with a spectral response function, $\phi(\lambda)$, centered at $\sim 1.0 \mu\text{m}$ such that during the daylight hours the reflected solar radiation component is larger than the thermal emission component by more than an order of magnitude under the expected conditions of the earth-atmosphere system. Therefore, except for situations involving very warm emitting surfaces having low reflectances, the daytime measurement can be interpreted approximately in terms of reflected short-wavelength radiation alone, within an accuracy of 10% or less (Nimbus III User's Guide, p. 46). For this reason, the quantity presented in the Nimbus 3 daytime HRIR maps produced by the National Space Science Data Center is an "effective reflectance" and not an "equivalent blackbody temperature."

Following the nomenclature used in the Nimbus III User's Guide (p. 46), the HRIR measurements can also be expressed in terms of radiance, N ($\text{watt meter}^{-2} \text{steradian}^{-1}$) instead of intensity, I (Eq. (B-5)), as follows:

$$\bar{N}_d = \int_0^{\infty} N_s(\lambda) \phi(\lambda) d\lambda + \int_0^{\infty} N_E(\lambda) \phi(\lambda) d\lambda \quad (\text{watt meter}^{-2} \text{steradian}^{-1}) \quad (\text{B-7})$$

where

- \bar{N}_d is the effective radiance measured by the HRIR
- $N_s(\lambda)$ is the spectral radiance of reflected and scattered solar radiation at the top of the atmosphere in the direction of the satellite

*Radiation due solely to the earth's surface temperatures.

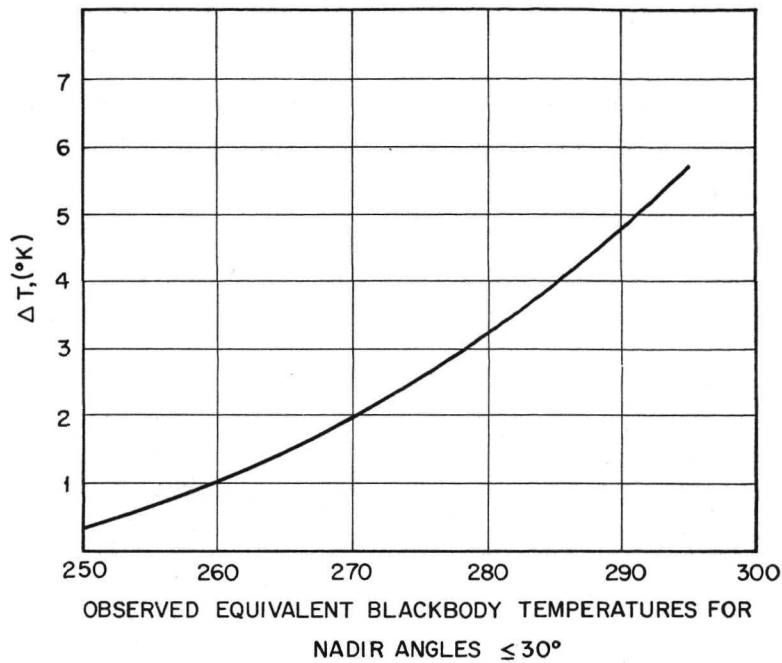


Figure B-8 Average correction due to atmospheric absorption as a function of the observed Nimbus 4 THIR equivalent blackbody temperatures for nadir angles of observation $\leq 30^\circ$.

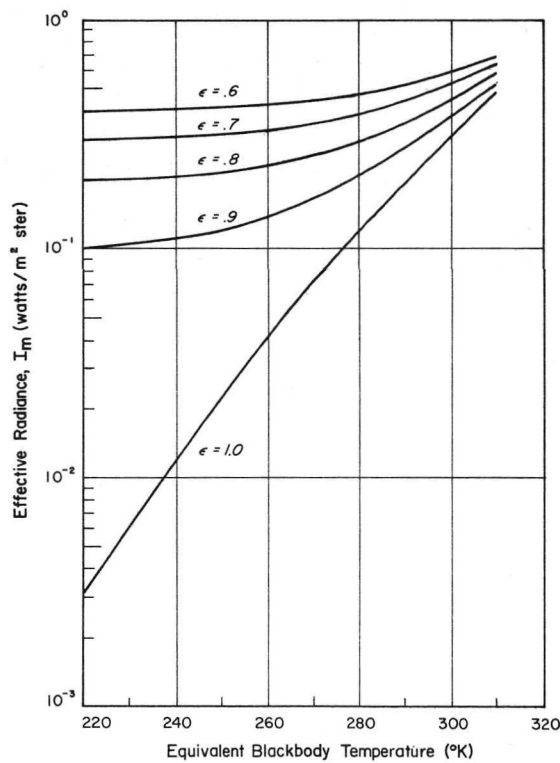


Figure B-9 Daytime effective radiance I_m , measured by the Nimbus 2 HRIR and equivalent surface temperature for various surface emissivities. The solar radiation detected by the radiometer at normal incidence and 100% reflectivity (zero emissivity) is assumed to be 1 watt/m² steradian, in the calculations.

$N_E(\lambda)$ is the spectral radiance due to thermal emission from the earth-atmosphere system emerging at the top of the atmosphere in the direction of the satellite

and

$\phi(\lambda)$ is the effective spectral response of the instrument shown in Figure B-10.

It is clear that the individual terms in Eq. (B-7) include atmospheric effects since both $N_s(\lambda)$ and $N_E(\lambda)$ are the radiance values at the "top" of the atmosphere. The "effective reflectance" $\bar{\rho}$ presented in the Nimbus 3 daytime HRIR maps is defined as

$$\bar{\rho} = \frac{\pi \bar{N}_d}{\bar{S} \cos \alpha} \quad (\text{B-8})$$

where

$\bar{S} = \int_0^{\infty} S(\lambda) \phi(\lambda) d\lambda$ watt meter⁻² is the effective solar irradiance obtained by integrating the product of the spectral solar irradiance, $S(\lambda)$, and the spectral response function of the instrument, $\phi(\lambda)$, (Figure B-10).

α is the zenith angle of the sun.

In the maps* produced by the National Space Science Data Center, the $\bar{\rho}$ values are derived from Eq. (B-8) using an \bar{S} of 32.3 watt meter⁻² evaluated from the spectral irradiance $S(\lambda)$ values reported by Johnson (1961) and shown in Figure B-11.

We will now examine how the satellite measurements of effective reflectance, $\bar{\rho}$, are affected by the atmosphere, surface temperature and surface reflectance. Figure B-12 shows the path of the solar radiance from the sun, through the atmosphere, to the surface, and back up through the atmosphere to the sensor. Solar irradiance, $S(\lambda)$, is depleted in its trip to the surface, and to the satellite, proportional to the spectral transmissivity, $T(\lambda)$, of the atmosphere and the spectral reflectance, $r(\lambda)$, of the surface. The radiance due to reflected

*No correction is applied to the grid print maps for the various angles of view (from horizon to horizon) of the measurements. This correction is negligible for measurements made at nadir angles $\leq 30^\circ$ used in grid print maps, and will not be considered in our analysis.

Also, no correction is applied for the warming up of the detector cell temperature during the Nimbus 3 lifetime (Cherrix, 1971, personal communication). All "effective reflectance" values on the grid print maps were calculated with the assumption that the cell temperature remained at -77°C . The cell temperature gradually warmed up to -65°C during the lifetime of Nimbus 3. Preliminary analyses by Cherrix show that "effective reflectances" decreased by about 10-15% two months after launch and remained nearly stable thereafter.

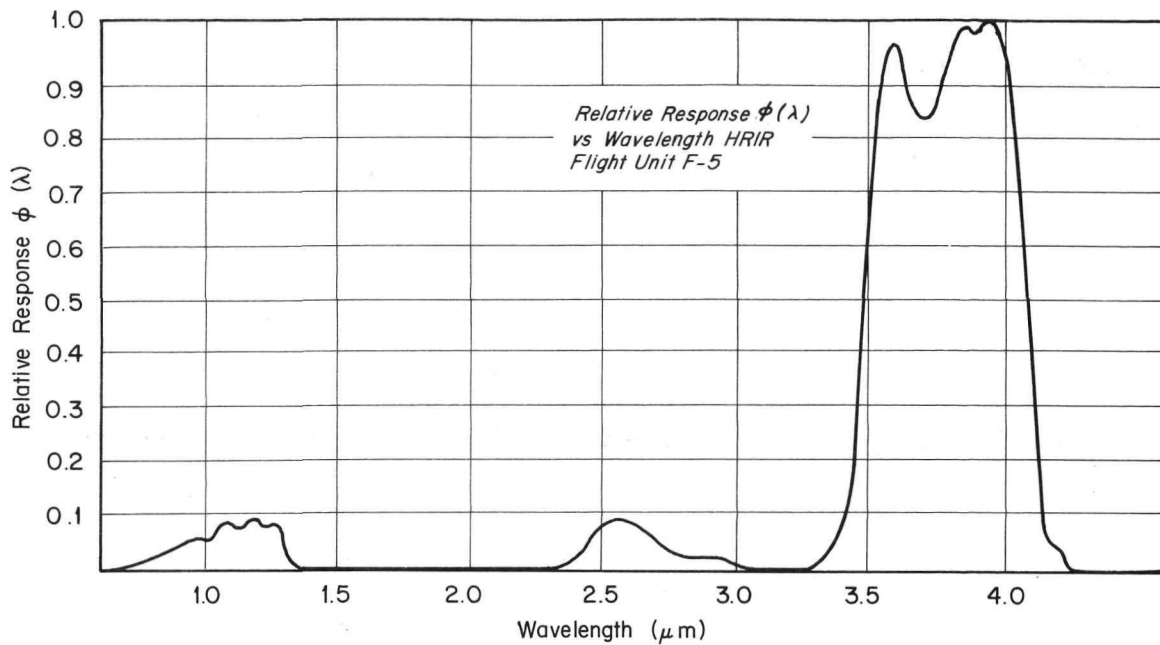


Figure B-10 Effective spectral response of the Nimbus 3 HRIR instrument. (The Nimbus III User's Guide)

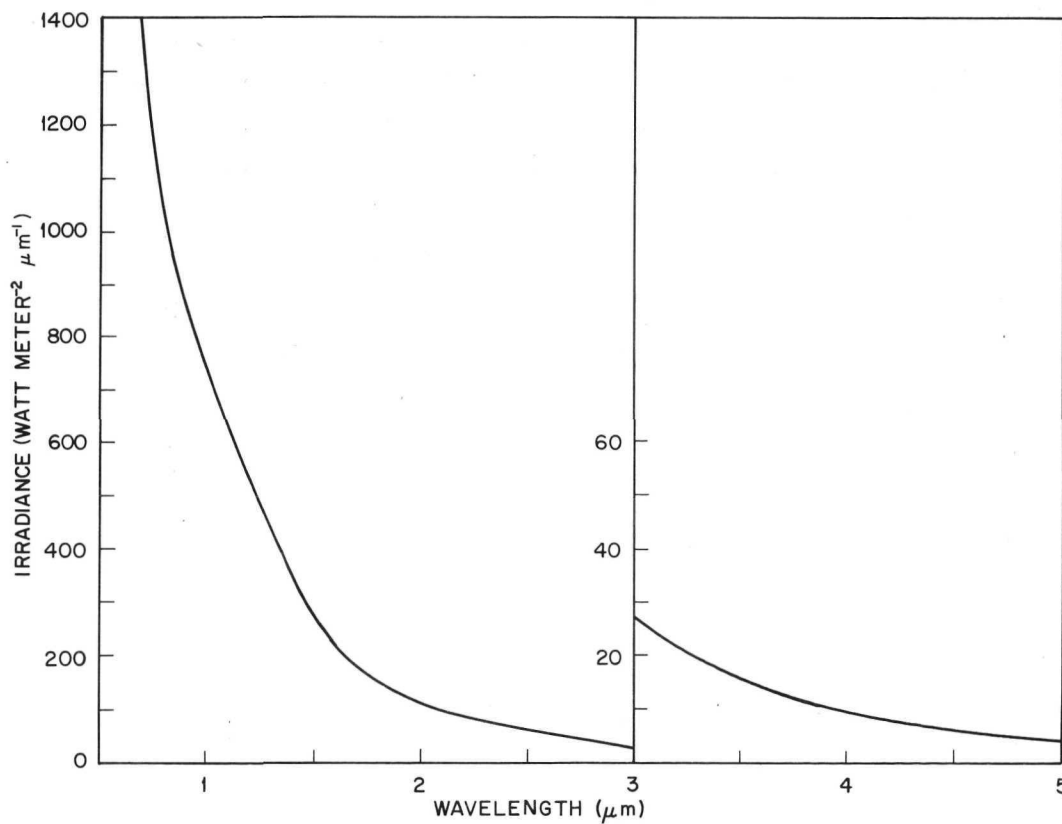


Figure B-11 Spectral solar irradiance received on a normal surface at the top of the atmosphere. (Constructed from Johnson's Data, 1961)

and backscattered solar radiation, the first term on the right of Eq. (B-7) is therefore

$$\begin{aligned} \bar{N}_s &= \int_0^{\infty} N_s(\lambda) \phi(\lambda) d\lambda \\ &= \frac{\cos \alpha}{\pi} \int_0^{\infty} S(\lambda) \phi(\lambda) T_{\alpha}(\lambda) T_{\theta}(\lambda) r(\lambda) d\lambda + R_{ATM} \end{aligned} \quad (B-9)$$

(watt meter⁻² steradian⁻¹)

where

$T_{\alpha}(\lambda)$ and $T_{\theta}(\lambda)$ are the spectral transmissivities of the atmosphere at zenith angles α and θ of the incoming and outgoing solar radiation, respectively.

$r(\lambda)$ is the spectral reflectance of the surface and is a function of the angles of incident radiation and observation (zenith and azimuth).

For perfectly diffuse reflectance (Lambert surface) $r(\lambda)$ is constant for all angles of incidence and observation. Natural surfaces, especially at low angles of incidence and observation, depart somewhat from the Lambert concept. The $\cos \alpha$ term expresses the departure of the incoming solar radiation from normal incidence and the division by π expresses the radiation per unit solid angle (steradian⁻¹). R_{ATM} is the contribution of the solar radiation scattered to space by the atmosphere and can be estimated from the tabulated values given by Coulson et al (1960). This atmospheric term is very small, of the order of 0.05 watt meter⁻² steradian⁻¹ between 0.7 to 1.3 μm , and may be neglected.

Using average transmissivities, \bar{T}_{α} , \bar{T}_{θ} , and reflectances, \bar{r} , in the three spectral intervals of the radiometer response shown in Figure B-10, and neglecting R_{ATM} , Eq. (B-9) becomes

$$\begin{aligned} \bar{N}_s &= \frac{\cos \alpha}{\pi} \bar{T}_{\alpha_1} \bar{T}_{\theta_1} \bar{r}_1 \int_{0.7}^{1.3} S(\lambda) \phi(\lambda) d\lambda \\ &+ \frac{\cos \alpha}{\pi} \bar{T}_{\alpha_2} \bar{T}_{\theta_2} \bar{r}_2 \int_{2.3}^{3.0} S(\lambda) \phi(\lambda) d\lambda \\ &+ \frac{\cos \alpha}{\pi} \bar{T}_{\alpha_3} \bar{T}_{\theta_3} \bar{r}_3 \int_{3.4}^{4.2} S(\lambda) \phi(\lambda) d\lambda \end{aligned} \quad (B-10)$$

where the subscripts, 1, 2 and 3 refer to the three spectral intervals defined in Figure B-10. The radiance contributed by thermal emission, N_E , obtained by integration of the second term in Eq. (B-7), is essentially the effective radiance to which the radiometer responds at night and is given in Figure B-13 from the Nimbus II User's Guide. Substituting Eq. (B-10) for the first term in Eq. (B-7) and representing the second term of Eq. (B-7) by N_E , Eq. (B-8) becomes:

$$\bar{\rho} = \frac{\cos \alpha \bar{T}_{\alpha_1} \bar{T}_{\theta_1} \bar{r}_1 \int_{0.7}^{1.3} S(\lambda) \phi(\lambda) d\lambda + \cos \alpha \bar{T}_{\alpha_2} \bar{T}_{\theta_2} \bar{r}_2 \int_{2.3}^{3.0} S(\lambda) \phi(\lambda) d\lambda}{\cos \alpha \int_0^{\infty} S(\lambda) \phi(\lambda) d\lambda} + \frac{\cos \alpha \bar{T}_{\alpha_3} \bar{T}_{\theta_3} \bar{r}_3 \int_{3.4}^{4.2} S(\lambda) \phi(\lambda) d\lambda + \pi N_E}{\cos \alpha \int_0^{\infty} S(\lambda) \phi(\lambda) d\lambda} \quad (B-11)$$

Using the solar irradiance curve in Figure B-11 and the spectral response function in Figure B-10, the following are obtained:

$$\int_{0.7}^{1.3} S(\lambda) \phi(\lambda) d\lambda / \int_0^{\infty} S(\lambda) \phi(\lambda) d\lambda = 0.744$$

$$\int_{2.3}^{3.0} S(\lambda) \phi(\lambda) d\lambda / \int_0^{\infty} S(\lambda) \phi(\lambda) d\lambda = 0.040$$

$$\int_{3.4}^{4.2} S(\lambda) \phi(\lambda) d\lambda / \int_0^{\infty} S(\lambda) \phi(\lambda) d\lambda = 0.216$$

and

$$\pi / \int_0^{\infty} S(\lambda) \phi(\lambda) d\lambda = 0.097.$$

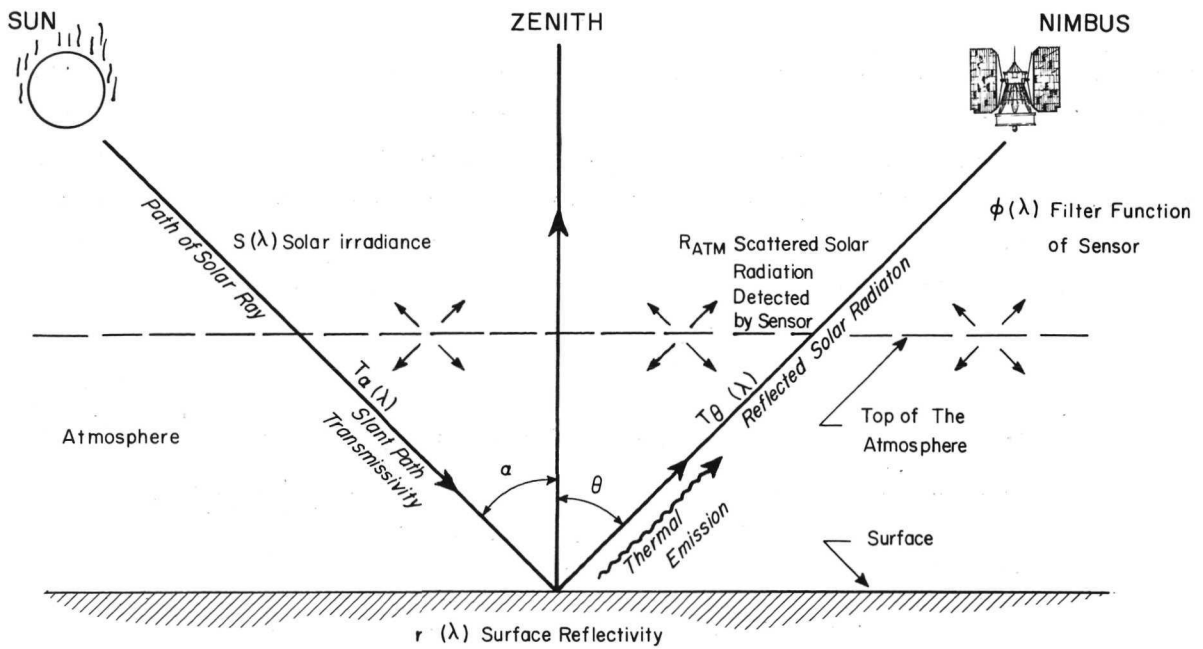


Figure B-12 Path of solar radiation through the atmosphere to the Nimbuss HRIR sensor.

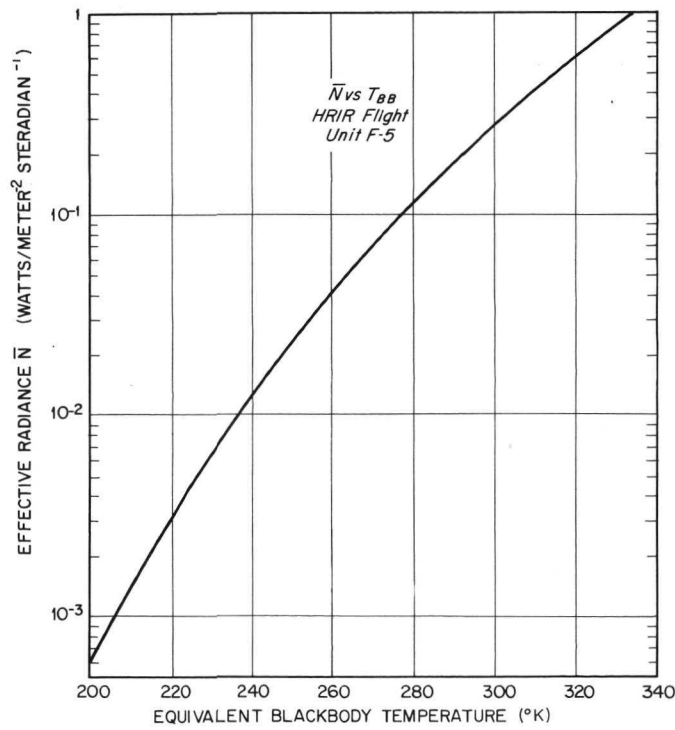


Figure B-13 Effective radiance vs equivalent blackbody temperature for the Nimbuss 3 HRIR. (The Nimbuss III User's Guide)

Substituting these values in Eq. (B-11), the effective reflectance is then expressed as

$$\bar{\rho} = 0.744 \bar{T}_{\alpha_1} \bar{T}_{\theta_1} \bar{r}_1 + 0.040 \bar{T}_{\alpha_2} \bar{T}_{\theta_2} \bar{r}_2 + 0.216 \bar{T}_{\alpha_3} \bar{T}_{\theta_3} \bar{r}_3 + \frac{0.097 N_E}{\cos \alpha} \quad (\text{B-12})$$

Eq. (B-12) permits us to relate $\bar{\rho}$, the effective reflectance plotted on the day-time HRIR maps, with the actual surface reflectance, \bar{r} , and explore its variations with atmospheric transmissivity and surface temperature. The transmissivity of the atmosphere is small in the 2.3 to 3.0 μm band because of strong water vapor and carbon dioxide absorption bands at 2.7 μm . The result is that the second term on the right side of Eq. (B-12) becomes very small compared to the other terms and can be neglected. The atmospheric transmissivity in the other two wavelength intervals (0.7 to 1.3 and 3.4 to 4.2 μm) is mainly a function of the slant path length of propagation and the water vapor and the aerosol contents of the atmosphere along the path. Estimates of the atmospheric transmissivity in these two spectral intervals were made using Elterman's (1968) spectral attenuation model. Since Elterman's model does not include water vapor effects, additional computations to incorporate these effects in the 0.7 to 1.3 μm band were performed using Fowle's water vapor attenuation data as reported in the Smithsonian Meteorological Tables. The results showing computed transmissivity for a dry atmosphere, and atmospheres with 1, 2 and 3 cm of total precipitable water*, are presented in Figure B-14. For the 3.4 to 4.2 μm band the transmissivities of the atmosphere, \bar{T}_{α_3} and \bar{T}_{θ_3} , are about 0.94 for zenith angles up to 40°. The total transmissivity, $\bar{T}_{\alpha_3} \bar{T}_{\theta_3}$, of the two-way path of the radiation in this spectral interval is ≈ 0.88 . With this estimate, the effective reflectance is then given by

$$\bar{\rho} \approx 0.744 \bar{T}_{\alpha_1} \bar{T}_{\theta_1} \bar{r}_1 + 0.190 \bar{r}_3 + 0.097 \frac{N_E}{\cos \alpha} \quad (\text{B-13})$$

The largest contributor to the effective reflectance, $\bar{\rho}$, as defined by Eq. (B-13) is the first term, that due to the 0.7 to 1.3 μm band. The total transmissivity of the two-way path of the radiation ($\bar{T}_{\alpha_1} \bar{T}_{\theta_1}$) through an average atmosphere of 2 cm of precipitable water, and for observations at the zenith and $\pm 20^\circ$ from nadir is shown in Figure B-15 to be in the 0.5 to 0.6 range. Figure B-16 shows the contribution of the 0.7 to 1.3 μm band to $\bar{\rho}$ as a function of surface reflectance and total trans-

*The total atmospheric water vapor contained in a vertical column of unit cross-sectional area extending between the surface and the top of the atmosphere. It is expressed in terms of the height to which that water substance would stand if completely condensed and collected in a vessel of the same unit cross-section. The U. S. Standard Atmosphere of 1962, for example, contains 1.96 cm of precipitable water, and an average relative humidity of 63% in the first 10 km.

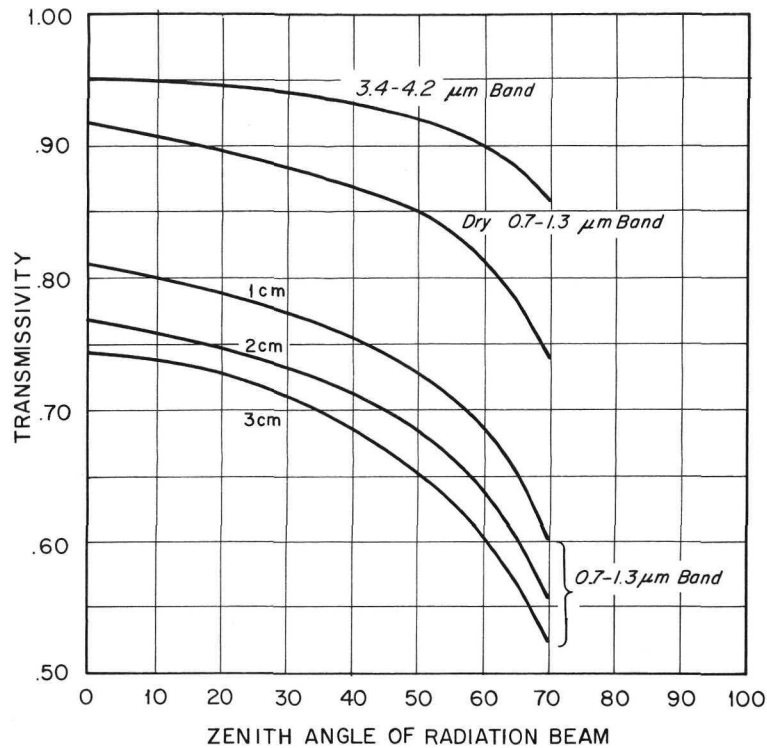


Figure B-14 Transmissivity of turbid atmosphere in the 0.7 to 1.3 and 3.4 to 4.2 μm bands of the HRIR, for dry atmosphere and for atmosphere formed from Elterman's (1968) data on turbid atmosphere and Fowle's water vapor transmission. (Smithsonian Meteorological Tables, p. 426)

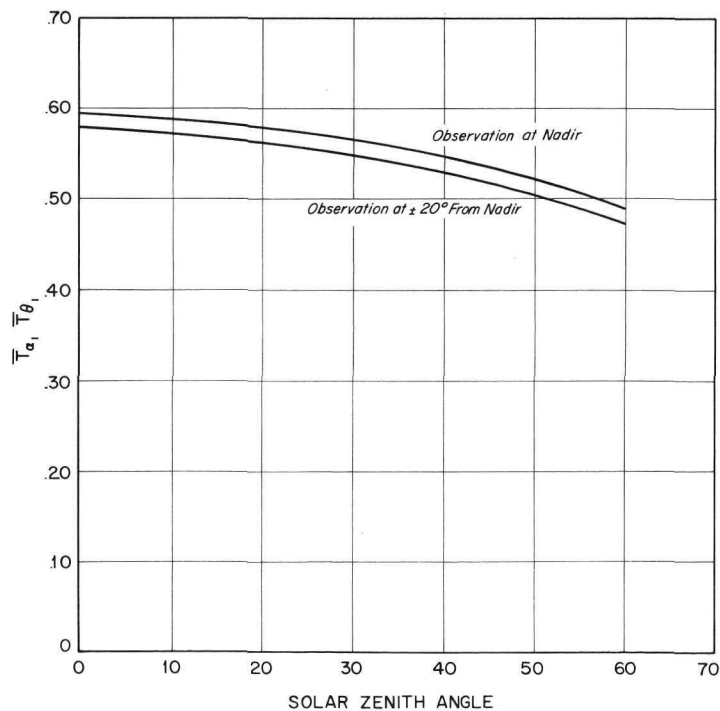


Figure B-15 Total path transmissivity, $\bar{T}_{\alpha_1} \bar{T}_{\theta_1}$, of the atmosphere in the 0.7 to 1.3 μm band with 2 cm of precipitable water, for observations at the nadir and at $\pm 20^\circ$ from nadir.

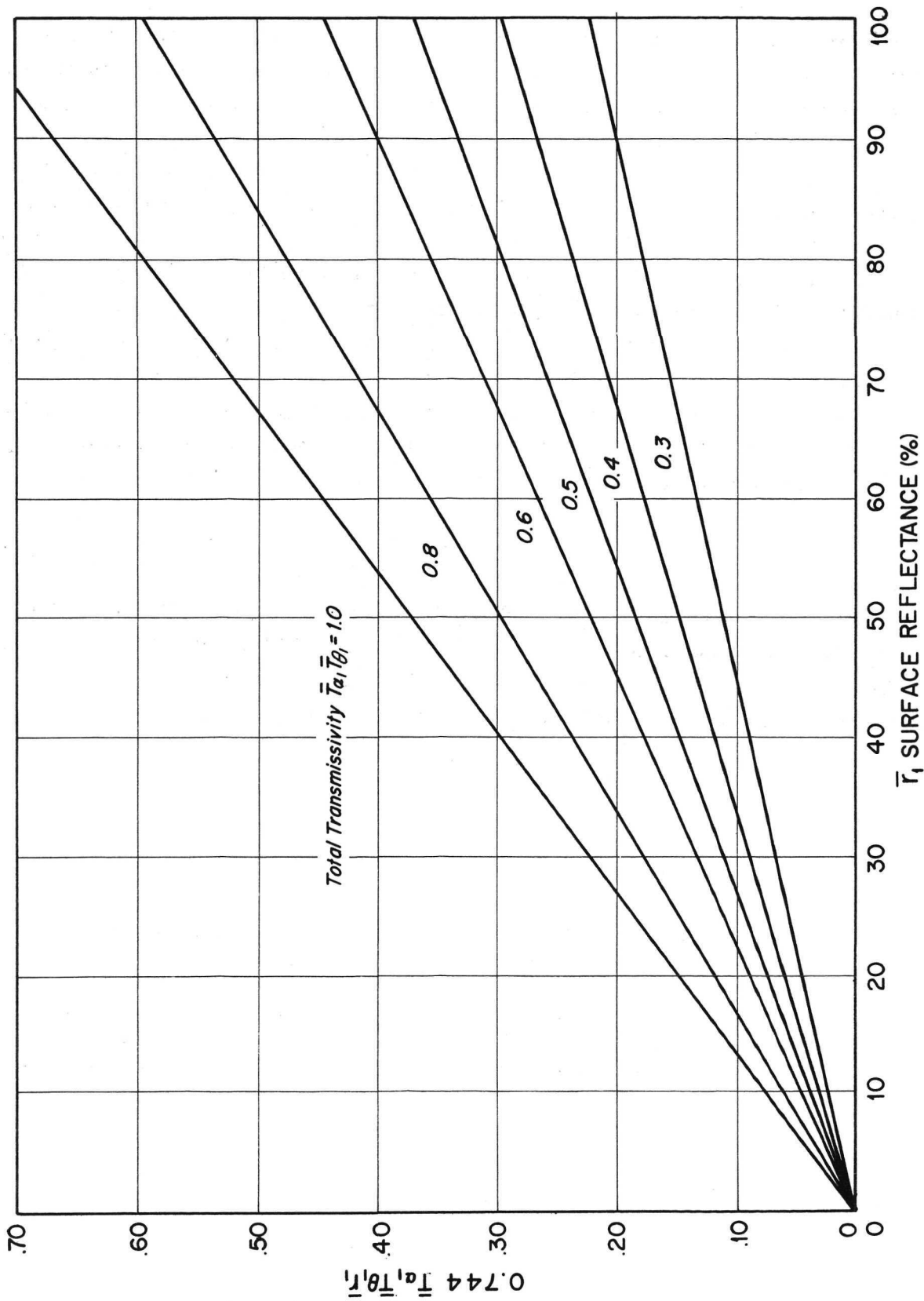


Figure B-16 Contribution of the 0.7 to 1.3 μm band to the effective reflectance, $\bar{\rho}$, measured by the Nimbus 3 daytime HRIR, as a function of surface reflectance, r_1 , and total atmospheric path transmissivity.

missivity. As an example, the contribution of the 0.7 to 1.3 μm band to $\bar{\rho}$ is ~ 0.012 for a water surface with $\bar{r}_1 = 0.03$ and a two-way atmospheric transmissivity of 0.55. For the same atmosphere, the contribution to $\bar{\rho}$ in this same spectral interval for sand ($\bar{r}_1 = 0.40$) is ~ 0.16 .

The 3.4 to 4.2 μm band also contributes appreciably to $\bar{\rho}$ and cannot be neglected. Surface reflectances in the 3.4 to 4.2 μm band are generally one-half to one-third those in the 0.7 to 1.3 μm band as shown by Table B-1. The contribution to $\bar{\rho}$ by radiation in this longer wavelength band is about .006 for water ($\bar{r} \sim .03$), and 0.02 to 0.05 for sand (\bar{r}_3 ranging from 0.1 to 0.25).

The significance of the emission term involving N_E depends on the magnitude of the surface temperature. At temperatures less than 280 $^\circ\text{K}$, the contribution by this term to $\bar{\rho}$ is less than 0.01 as shown in the data presented in Table B-4. At higher temperatures, the contribution increases proportionately and becomes significant, especially in those situations in which the surface reflectance is low.

B.5 Conclusion

The discussion, graphs, and equations that have been presented in this Appendix are intended to aid the users of the Nimbus HRIR and THIR data in estimating surface and atmospheric effects. These effects must be understood to fully utilize the data in the detection of surface characteristics.

TABLE B-4
CONTRIBUTION OF THERMAL RADIATION TERM
TO $\bar{\rho}$ AT SOLAR ZENITH $\leq 30^\circ$

Surface Temperature ($^\circ\text{K}$)	$0.097 N_E / \cos \alpha$
280	.01
290	.02
300	.03
310	.04
320	.06

APPENDIX B

REFERENCES

- Cherrix, T., 1971: Personal Communication, NASA/GSFC
- Coulson, K. L., I. V. Dave and Z. Sekera, 1960: Tables Related to Radiation Emerging from a Planetary Atmosphere with Rayleigh Scattering, Univ. of California Press.
- Elterman, L., 1968: UV, Visible, and IR Attenuation for Altitudes to 50 km, Air Force Cambridge Research Laboratories, AFCRL-68-0153.
- Fraser, R. S., 1964: "Computed Intensity and Polarization of Light-Scattered Outwards from the Earth and an Overlaying Aerosol," J. of Opt. Soc. Am., 54(2), 157-168.
- Hovis, W. A., Jr., 1966: "Infrared Spectral Reflectance of Some Common Minerals," Appl. Opt., 5(2), 245-248.
- Hovis, W. A., Jr., and W. R. Callahan, 1966: "Infrared Reflectance Spectra of Rocks, Tuffs and Red Sandstone from 0.5 to 22 μ m," J. of Opt. Soc. Am., 56(5), 639-643.
- Johnson, F. S., 1961: Satellite Environment Handbook, Stanford University Press, Stanford, Connecticut.
- Kuers, G., 1968: Interpretation of Daytime Measurements by the Nimbus I and II HRIR, NASA TND-4552.
- Kunde, V. G., 1965: "Theoretical Relationship Between Equivalent Blackbody Temperatures and Surface Temperatures Measured by the Nimbus HRIR," Observations from the Nimbus I Meteorological Satellite, NASA, SP-89, 23-36.
- List, R. J., 1966: Smithsonian Meteorological Tables, Sixth Revised Edition, Smithsonian Institution, Washington, D. C.
- National Aeronautics and Space Administration, 1966: The Nimbus II User's Guide, Goddard Space Flight Center, Greenbelt, Maryland.
- National Aeronautics and Space Administration, 1968: The Nimbus III User's Guide, Goddard Space Flight Center, Greenbelt, Maryland.
- National Aeronautics and Space Administration, 1970: The Nimbus IV User's Guide, Goddard Space Flight Center, Greenbelt, Maryland.
- Office of Naval Research, 1965: Handbook of Military Infrared Technology, Dept. of the Navy, Washington, D. C. 75 p.

APPENDIX B
REFERENCES, contd.

- Sabatini, R. R. and J. E. Sissala, 1968: Project NERO, Nimbus Earth Resources Observations, Contract No. NAS 5-10343, Tec. Rpt. No. 7, Allied Research Associates, Inc.
- Salomonson, V., 1970: Personal Communication, September 1970, NASA/GSFC.
- Sissala, J. E. and G. A. Rabchevsky, 1970: "Terrestrial Changes Monitored by the Nimbus Meteorological Satellites," paper presented at the First Western Space Congress, Santa Maria, California, 26-29 October 1970.
- Smith, W. L., P. K. Rao, R. Koffler and W. R. Curtis, 1970: "The Determination of Sea-Surface Temperature from Satellite High Resolution Infrared Window Measurements," Mon. Wea. Rev., 48; 604-611.

APPENDIX C

SYSTEM NOISE IN THE NIMBUS AVCS, IDCS, HRIR, AND THIR DATA

C.1 Introduction

System noise deleterious to the resolution of the Nimbus pictorial data is present in varying amounts in all AVCS, IDCS, HRIR, and THIR data. Noise also deteriorates the accuracy of the mapped HRIR and THIR temperatures and reflectances. This Appendix briefly discusses the effects of noise on the data and some attempts to develop smoothing and filtering routines.

C.2 Nimbus 1

C.2.1 HRIR

The Nimbus 1 HRIR system noise contains a periodic component at 16 Hz, and large oscillatory components at 100, 200, 300 and 400 Hz (Fujita and Bandeen, 1965). The 16 Hz noise shows up on the photofacsimile as diagonal lines. These large noise components, and the limited amount of Nimbus 1 data preclude the use of these readings in any extensive quantitative application.

C.2.2 AVCS

Nimbus 1 AVCS images were relatively free of noise although some of the images were affected by a "ghosting" effect. When a very bright scene was recorded on the vidicon tube, a "ghost" of the bright pattern was retained in the successive image. Figure C-1 shows this "ghosting" effect on a sequence of AVCS images of the snow-capped Andes of South America.

C.3 Nimbus 2

C.3.1 HRIR

The Nimbus 2 HRIR readings are much cleaner than the Nimbus 1 HRIR measurements. Figure C-2 from Williamson (1970) shows the root mean square (rms) variation due to noise in a single Nimbus 2 HRIR data point as a function of target temperature. While the data are relatively reliable in the temperature interval of major interest (rms near 1.6 at 285°K), below 230°K the rms values become very large and make the data unreliable. Of course, individual measurements could

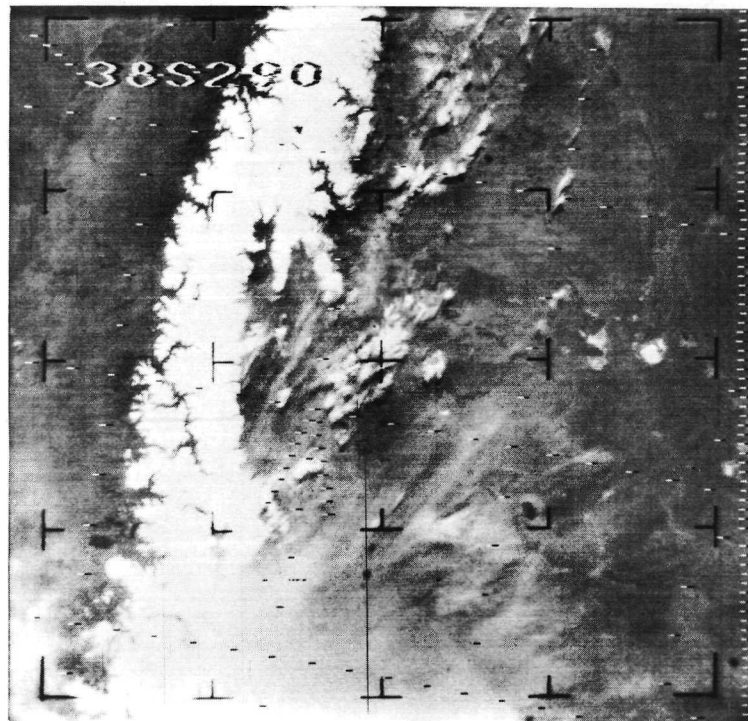
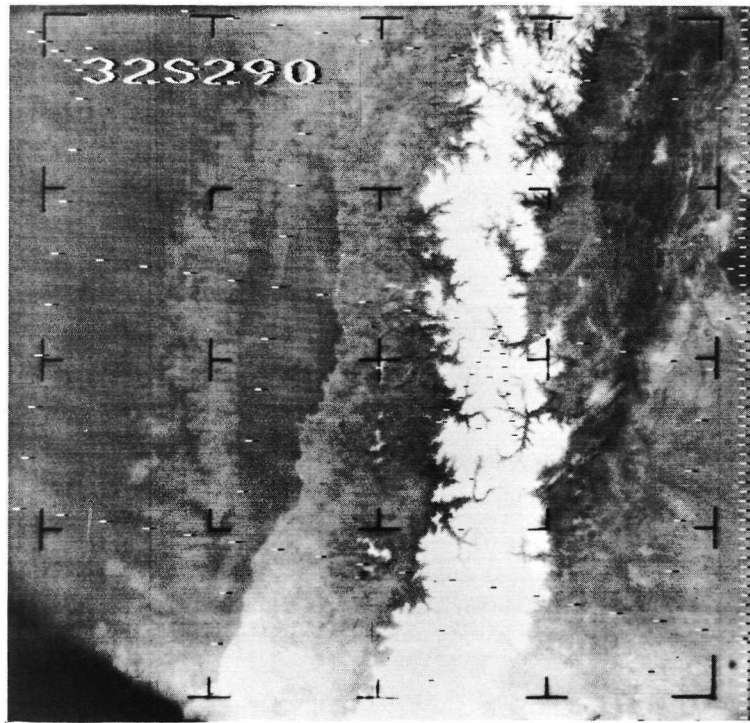


Figure C-1 Two sequential Nimbus 1 AVCS pictures taken on orbit 196 of the Andes in South America, showing the "ghosting" effect. The top picture was taken 91 seconds after the bottom picture. The bright pattern on the bottom picture representing the snow-covered Andes reappears on the top picture against the dark background of the Pacific Ocean.

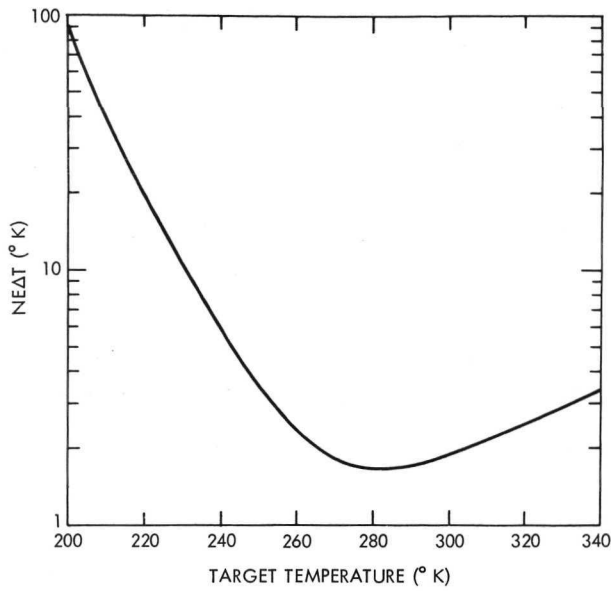


Figure C-2 Noise equivalent temperature difference for Nimbus 2 HRIR as a function of target temperature. (Williamson, 1970)

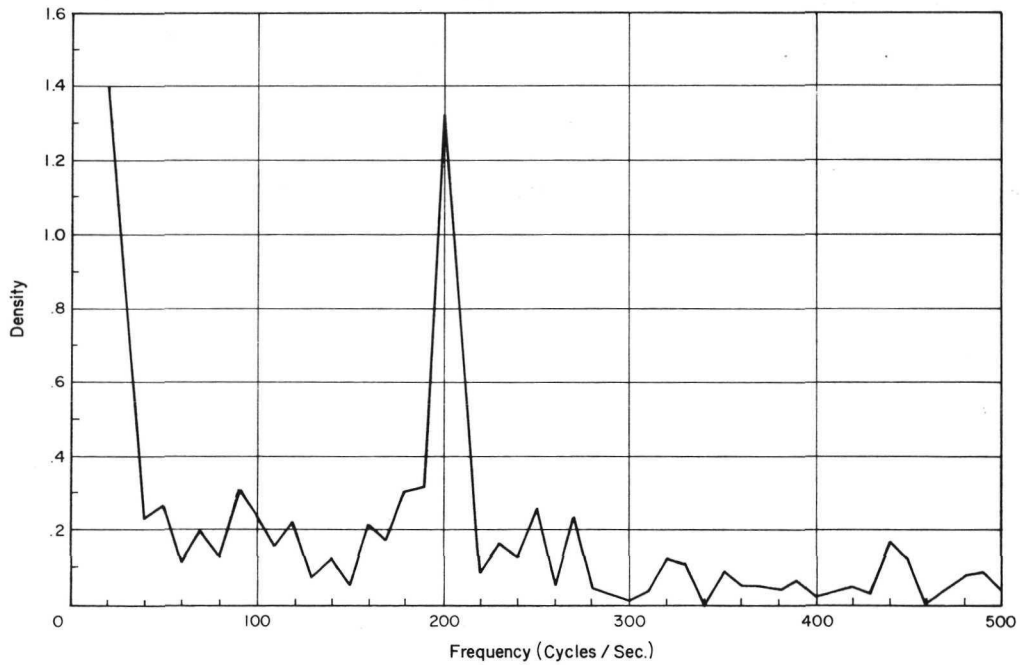


Figure C-3 Spectrum analysis performed on a Nimbus 2 HRIR analog visi-corder scan. The relatively uniform backscan portion was used for the analysis.

contain errors considerably greater than the rms value. Warnecke et al (1969) found average system noise of $\pm 4^{\circ}\text{K}$ peak-to-peak from random measurements on Nimbus 2 HRIR analog visicorder records.

A spectrum analysis on the analog data (Figure C-3) revealed an oscillatory noise component that peaked at 200 Hz (McMillin, 1969) with an amplitude of about 2°K . A mathematical smoothing routine which attenuates the 200 Hz noise component was developed by McMillin (1969) and is available as an optional subroutine to the computer program used by the National Space Science Data Center (NSSDC) to produce temperature maps from Nimbus 2 Meteorological Radiation Tapes (NMRT). The effect of McMillin's routine is shown in Figure C-4b which is a smoothed version of the Lake Michigan area shown in Figure C-4a. The smoothing routine reduces the rms variation due to noise by about 25% (Williamson, 1970).

The spatial two-dimensional arithmetical averaging that takes place in the production of temperature maps is sometimes sufficient to adequately attenuate the 200 Hz periodic noise, if the number of points in each average approaches 15 or 20 as, for example, in a 1:3 million map. In a 1:1 million map, only one to five individual scan spots are averaged per grid square; thus the numerical smoothing routine should be applied (Warnecke, McMillin, Allison, 1969).

The Nimbus 2 HRIR data also contain a second, sporadic noise component due to scattered sunlight entering the radiometer near satellite sunrise and sunset. The scattered sunlight causes approximately two minutes of data in the satellite day-night transition zone (45° to 55° north and south) to be approximately 6°K warmer. The effect is clearly evident on the photofacsimile display as darker stripes across the picture (Figure C-5).

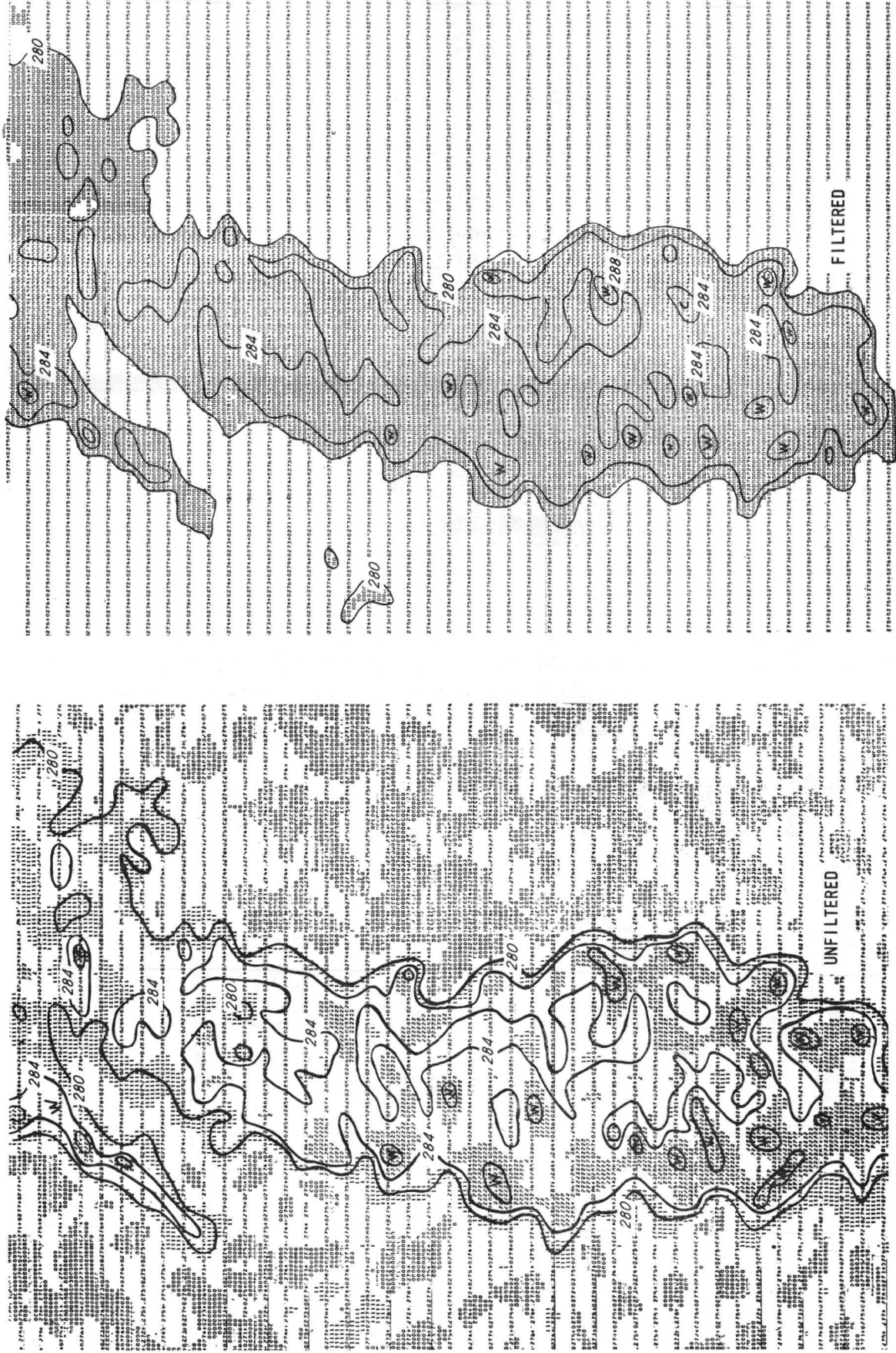
C.3.2 AVCS

A 10 kHz interference pattern is evidenced on all Nimbus 2 AVCS pictures. The interference was generated by the beacon transmitter on the spacecraft and appears as narrow vertical lines superimposed on the image. Examples of this 10 kHz interference can be seen in Figures 3-20 and 3-21. The AVCS images have not been filtered for this 10 kHz interference.

C.4 Nimbus 3

C.4.1 HRIR

Nimbus 3 HRIR data were usually stored and played back to a ground station alternatively from two tape recorders on board the satellite. The HRIR data recorded on HDRSS-A tape recorder after orbit 1605 contain noise caused



a. Unfiltered

b. Filtered

Figure C-4 A comparison of filtered and unfiltered computer-produced Nimbus 2 HRIR temperature maps of Lake Michigan taken on orbit 1916, 6 October 1966.

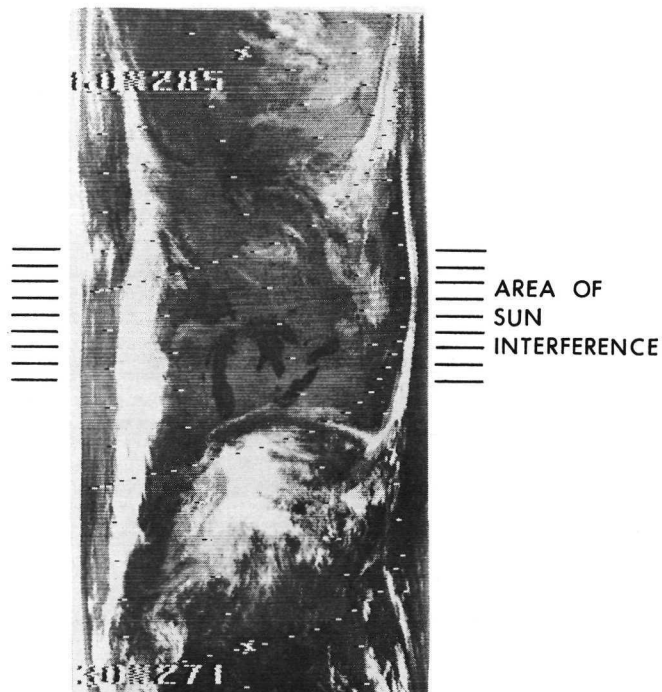


Figure C-5 Photofacsimile print of Nimbus 2 HRIR data taken on 13 August 1966 on orbit 1197 showing, as indicated, the area of reflected sunlight interference during satellite day-night transition, recognizable by a broad band of darker stripes across the film strip. (Warnecke et al, 1969)

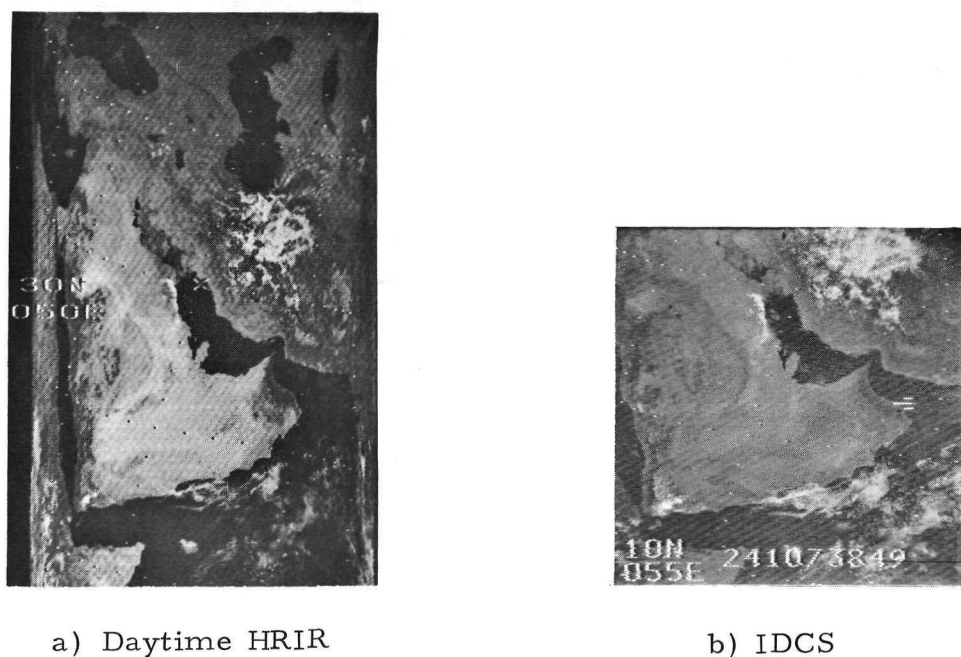


Figure C-6 Sample Nimbus 3 HRIR and IDCS pictorial data from orbit 1837, 29 August 1969, containing noise attributed to flutter in the HDRSS-A tape recorder. The noise shows up as lines slanting from the lower left to the upper right of the pictures.

by a flutter in the tape recorder. Figure C-6a is a sample of HRIR data from HDRSS-A showing the effect of noise. Data from HDRSS-B tape recorder contained less noise than data from HDRSS-A tape recorder as shown by spectrum analyses performed by T. Cherrix (personal communication) of the Laboratory for Meteorology and Earth Sciences of GSFC (Figures C-7a and C-7b). The noise would also affect any temperature and radiation map produced from the NMRT. Figure C-8 shows the rms variation of a temperature measurement due to noise. The rms averaged 3 to 4^oK for the HDRSS-B data, while it reached 9.4^oK by orbit 3045 for the noisier HDRSS-A data (Cherrix, 1970).

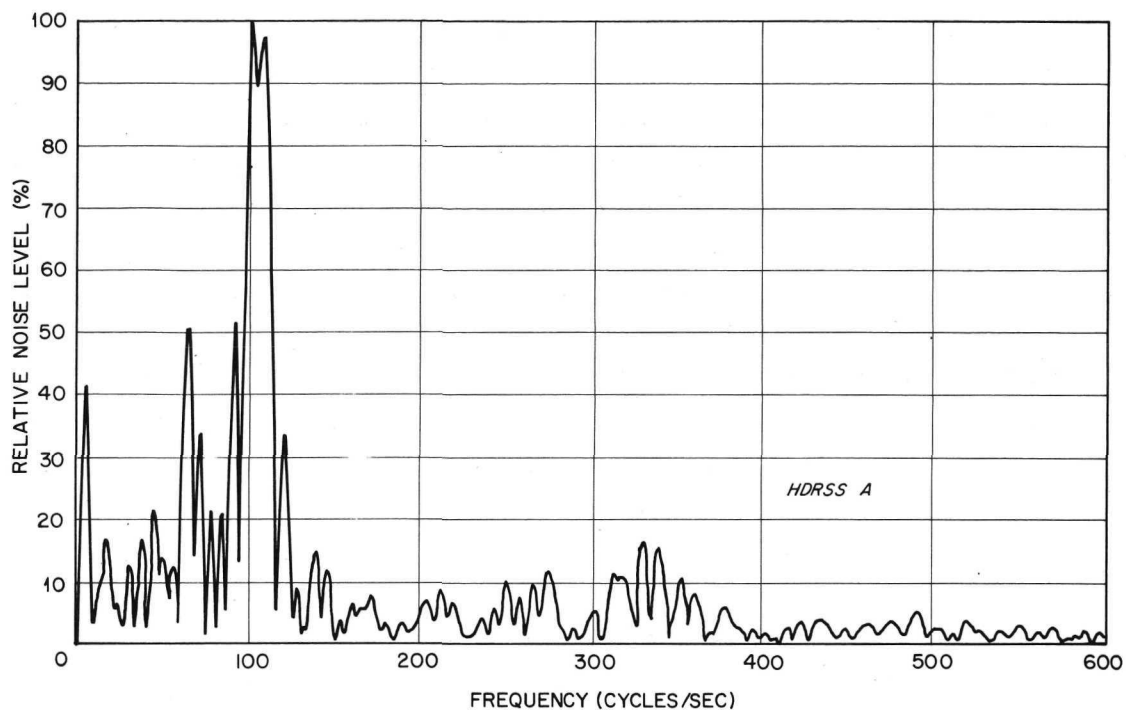
The McMillin smoothing routine is not applicable to Nimbus 3 HRIR data because the filter was "custom made" for Nimbus 2 HRIR data with different noise characteristics and digitizing rates.*

A versatile filter subroutine for mapping Nimbus 3 HRIR data has been developed by M. Forman of LMES at Goddard Space Flight Center (personal communication) and is being used at LMES to produce limited amounts of improved temperature and reflectance maps. Figures C-9a and C-9b show spectra of improved HDRSS-A and HDRSS-B data whose unfiltered spectra are shown in Figures C-7a and C-7b. The filter subroutine calculates an average noise spectrum for selected lines of data, decides what frequencies to attenuate and by what percentage, and generates an appropriate filter function in the frequency domain. This filter is then applied to the Fourier transformed data. The filtered data are then subjected to an inverse one-dimensional Fourier transformation into their original form. The main disadvantage of this filter subroutine is that it requires an appreciable amount of computer time and, therefore, can only be applied to limited quantities of data.

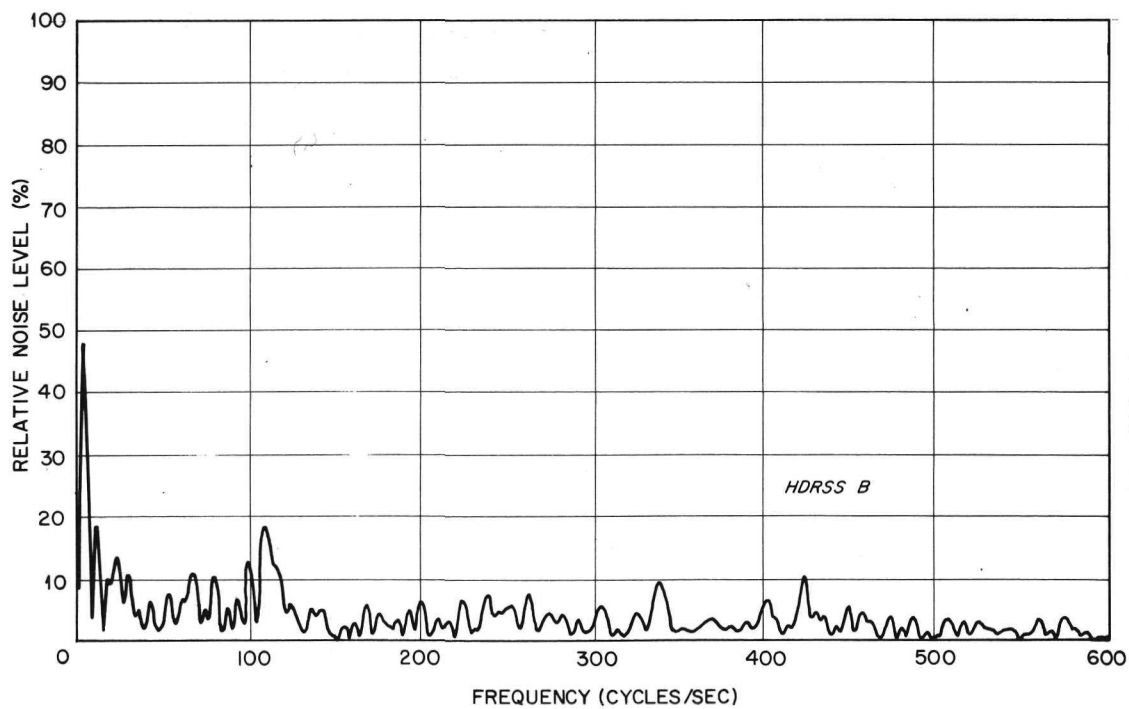
C.4.2 IDCS

The IDCS data recorded on HDRSS-A after data orbit 1605 contain noise caused by flutter in the HDRSS-A tape recorder. Data from the HDRSS-B tape recorder were normal. Figure C-6b is a sample IDCS frame from HDRSS-A with the noise lines. The noise is generally less evident on the IDCS pictures than on the HRIR. No attempt has been made to filter the noise on the IDCS pictures.

* The digitizing rate for Nimbus 3 HRIR data was 1250 values per second compared to 1000 values per second for Nimbus 2 HRIR data.



a. HDRSS A



b. HDRSS B

Figure C-7 Spectral analyses of unfiltered Nimbus 3 HRIR data from HDRSS-A and HDRSS-B tape recorders, orbit 3046, 27 November 1969. (The noise level is relative to the peak noise (set at 100%) found in these data.)

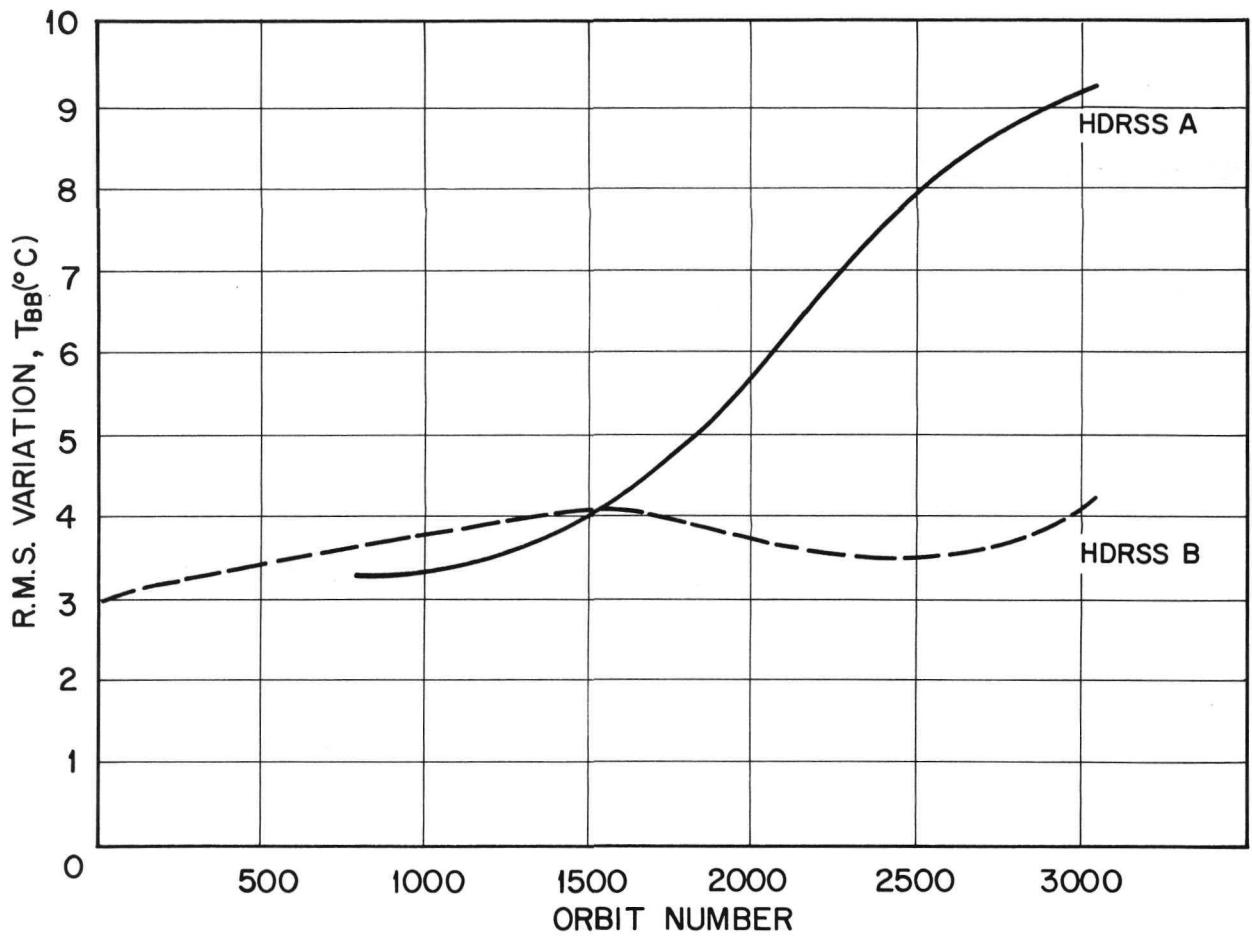
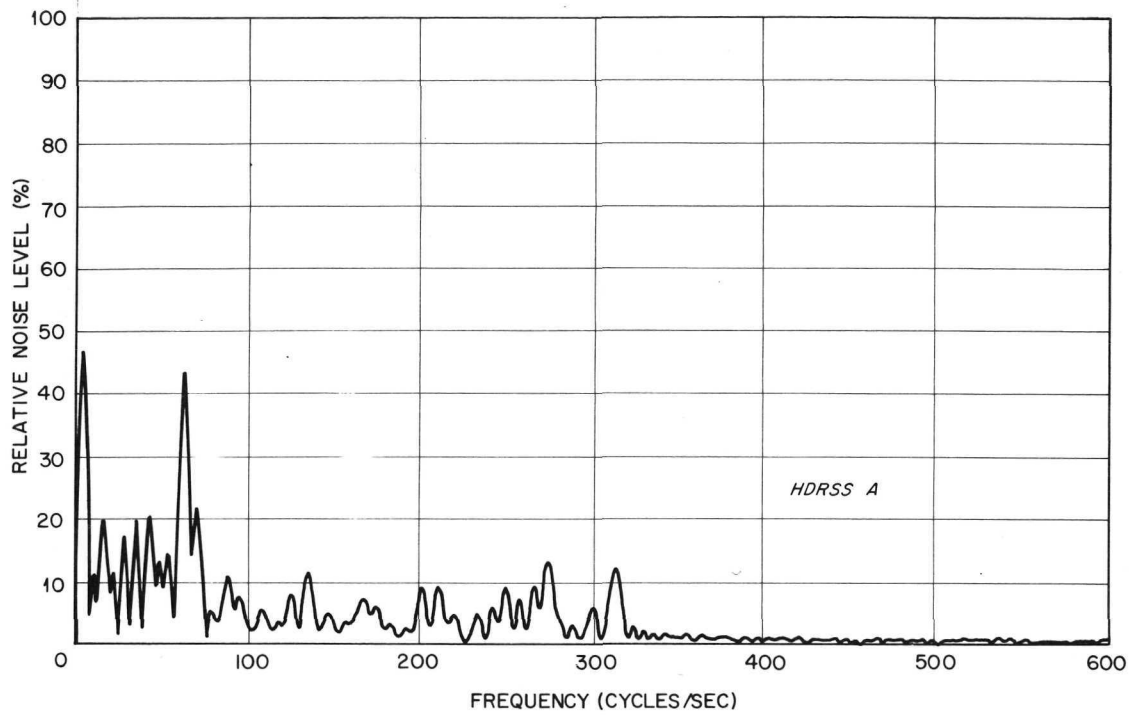
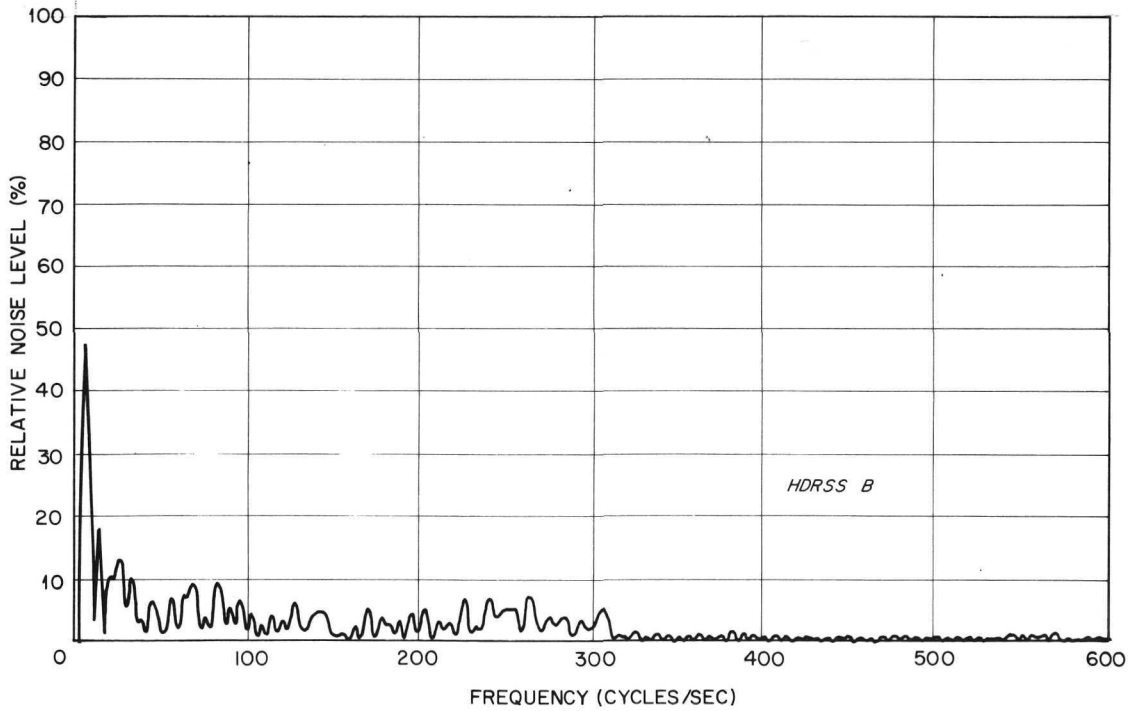


Figure C-8 Root mean square (rms) variation of the equivalent blackbody temperatures in the range 270 to 290°K from the Nimbus 3 HRIR night-time data.



a. HDRSS A



b. HDRSS B

Figure C-9 Spectral analyses of filtered Nimbus 3 HRIR data from HDRSS-A and HDRSS-B tape recorders, orbit 3046, 27 November 1969. (The noise level is relative to the peak noise (set at 100%) found in these data.)

C.5 Nimbus 4

C.5.1 THIR

Nimbus 4 THIR data, like Nimbus 3 HRIR data, were stored and played back alternatively from two tape recorders on board the satellite; again the system noise in the data was generated mainly by the tape recorder. As in Nimbus 3 HRIR, data from HDRSS-A tape recorder were considerably noisier than data from HDRSS-B tape recorder. Figure C-10b is a sample THIR image from HDRSS-A showing the effect of the noise. The four noise spectra in Figure C-11 from HDRSS-A and B data compare the level of the noise in an early orbit with the level months later. The noise in the HDRSS-A data became progressively worse with time, while the noise in the HDRSS-B data remained at a nearly constant low tolerable level. This is further demonstrated in Figure C-12 which shows the progression with the time of the rms variation of the temperature due to noise in the HDRSS-A and B data. The rms variation remained relatively low, below 2°K , for HDRSS-B data, while it steadily increased for HDRSS-A data, reaching 6°K by orbit 2065 on 9 September 1970, five months after launch. HDRSS-A data in the later orbits are unusable for quantitative analyses on large-scale digital maps 1:500,000 to 1:2,000,000, unless the noise is attenuated by means of filtered techniques. Forman's filter subroutine described in Section 4 is applicable to THIR data and is currently the only operational means to obtain limited amounts of usable filtered HDRSS-A data.

C.5.2 IDCS

The IDCS data recorded on HDRSS-A after data orbit 450 contain noise caused by flutter in the HDRSS-A tape recorder. Data from the HDRSS-B tape recorder were normal. Figure C-10a is a sample IDCS frame from HDRSS-A with the noise lines.

C.6 Electronic Filtering

The numerical filter subroutines of McMillin (for Nimbus 2 HRIR) and Forman (for Nimbus 3 HRIR and Nimbus 4 THIR) are applied "off-line" to limited amounts of data because of computer time limitations, just before the temperature/radiation maps are produced (see Figure C-13); thus the routines do not improve the pictorial quality of the data. A more expedient way to clean all data in near-real time is to filter the data electronically before they are digitized or displayed on the photofacsimile. Tests using electronic filtering techniques have been con-

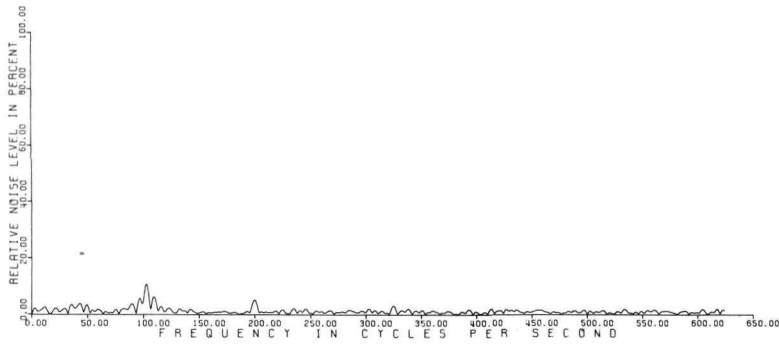


a) IDCS

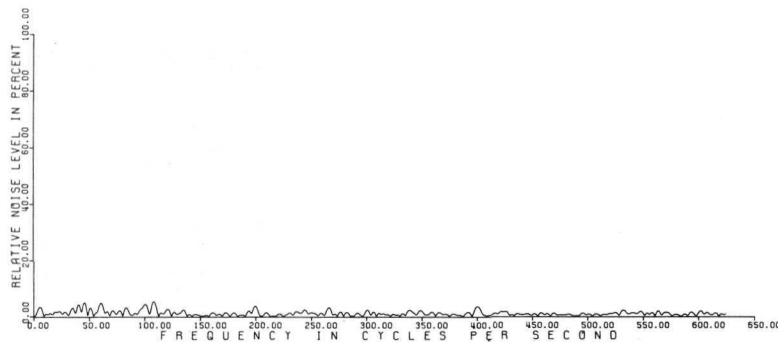


b) THIR 11.5 μm

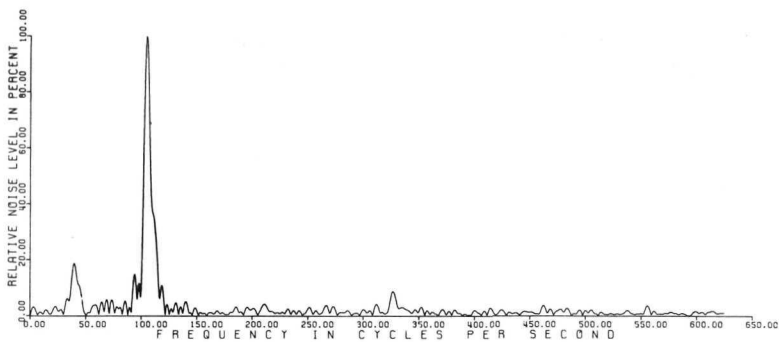
Figure C-10 Sample Nimbus 4 IDCS and THIR pictorial data containing noise attributed to flutter in the HDRSS-A tape recorder.



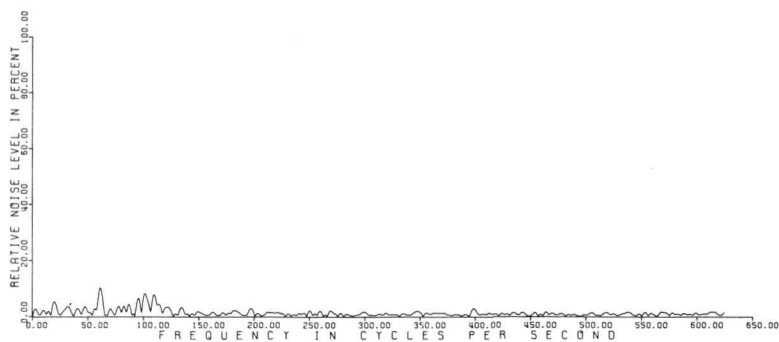
a) Nimbus 4 THIR 11.5 μm data, orbit 204, HDRSS-A



b) Nimbus 4 THIR 11.5 μm data, orbit 205, HDRSS-B



c) Nimbus 4 THIR 11.5 μm data, orbit 2068, HDRSS-A



d) Nimbus 4 THIR 11.5 μm data, orbit 2165, HDRSS-B

Figure C-11 Spectral analyses of unfiltered Nimbus 4 THIR data from HDRSS-A and HDRSS-B tape recorders. (The noise level is relative to the peak noise (set at 100%) found in these data.)

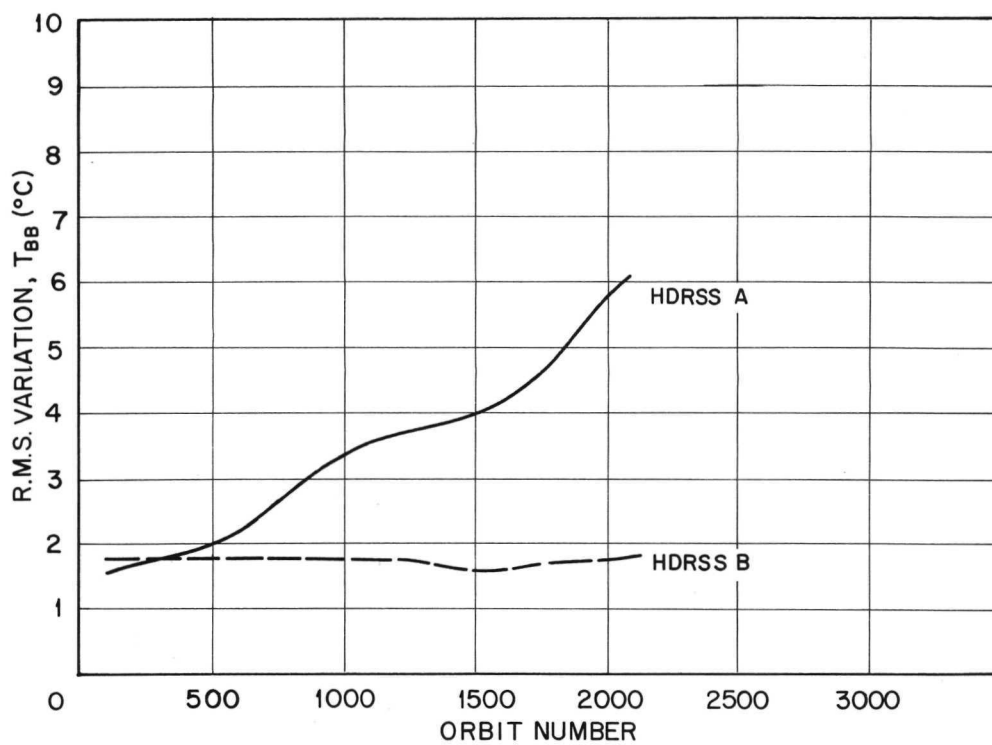


Figure C-12 Root mean square (rms) variation of the equivalent blackbody temperatures in the range 270 to 290°K from the Nimbus 4 THIR 11.5 μ m channel.

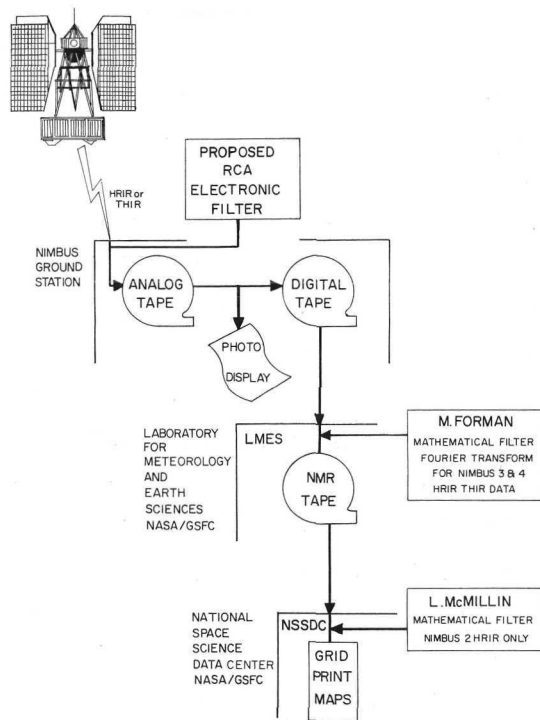
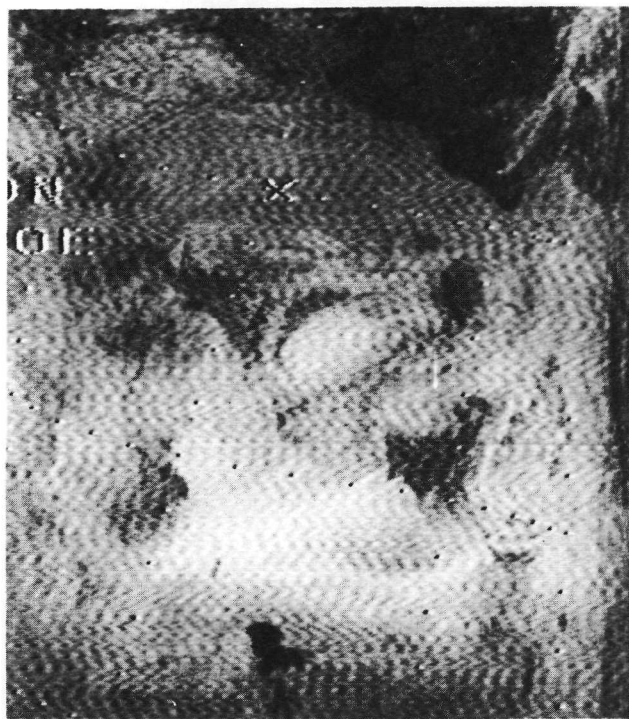


Figure C-13 Nimbus HRIR and THIR data flow showing the points at which the various filters available can be applied.



Raw



Filtered

Figure C-14 A comparison of filtered and unfiltered Nimbus 3 daytime HRIR image taken on orbit 3045, 27 November 1969.

ducted by RCA for NASA/GSFC using Nimbus HRIR and THIR data. Preliminary results show some improvement on the pictorial data, as indicated by Figure (C-14), which compares a filtered and an unfiltered Nimbus 3 HRIR image (Palgen, 1970). Further tests are underway at LMES/GSFC to assess the effect of the filter on the digitized maps. McCulloch (1971), the LMES/GSFC THIR experimenter, reports that the electronic filter also improves the quality of the digitized THIR data by reducing the rms error of the noisy HDRSS-A data to approximately 3°K . Palgen (1970) presents a discussion of pictorial noise evaluation and filtering methods, including the RCA electronic filter technique, and expresses concern that although the filter improves the "aesthetic" quality of the images, its "aliasing effects" would introduce false information on the images which may be erroneously interpreted as real. Based on the Nimbus experience, Palgen concludes that an ERTS filtering system should be more sophisticated than the present electronic filter being tested for Nimbus, and that possibly the ERTS system should be based on a two-dimensional Fourier transform.

APPENDIX C

REFERENCES

- Cherrix, T., 1970: Personal Communication, NASA/GSFC.
- Forman, M., 1970: Personal Communication, NASA/GSFC.
- Fujita, T. and W. Bandeen, 1965: "Resolution of the Nimbus HRIR," J. of Appl. Meteor. 4(4).
- McCulloch, A. W., 1971: Personal Communication, NASA/GSFC.
- McMillin, L., 1969: A Procedure to Eliminate Periodic Noise Found in Nimbus II HRIR Measurements, Technical Report No. 9, Contract NAS 5-10343, Allied Research Associates, Inc.
- Palgen, J. J. O., 1970: "Pictorial Noise Evaluation in Space Imagery," paper presented at the SPIE 15th Annual Technical Symposium, Anaheim, California.
- Warnecke, G., L. McMillin and L. J. Allison, 1969: Ocean Current and Sea Surface Temperature Observations from Meteorological Satellites, NASA TN D-5142, Goddard Space Flight Center, Greenbelt, Maryland.
- Williamson, E. J., 1970: The Accuracy of the High Resolution Infrared Radiometer on Nimbus II, NASA TN D-5551, Goddard Space Flight Center, Greenbelt, Maryland.

Page Intentionally Left Blank

APPENDIX D
GLOSSARY OF TERMS

D.1 Definitions and Acronyms

A

- "A" soil horizon - The upper part of soil. It consists of mineral layers of maximum organic accumulation.
- Aeolian - See eolian
- Albedo - The ratio of the amount of electromagnetic radiation reflected by a body to the amount incident upon it, usually expressed as a percentage. Most frequently applied to reflected solar radiation in the spectral range 0.2 to 4 μm .
- Alluvium - A general term for all detrital deposits resulting from the operations of modern rivers, thus including the sediments laid down in river beds, flood plains, lakes, fans at the foot of mountain slopes, and estuaries. Alluvium may become lithified, as has happened frequently in the past, and then may be termed "ancient alluvium."
- Anticline - A fold that is convex upward or had such an attitude at some stage of development.
- Apogee - The point in its orbit at which the satellite is farthest from the center of the earth. (i. e., point of maximum satellite altitude.)

B

- "B" soil horizon - The soil below the "A" horizon. It consists of weathered material with an accumulation of clay, iron, or aluminum; or is characterized by blocky or prismatic structure.
- Basalt - A fine-grained igneous rock dominated by dark-colored minerals, consisting of over 50% plagioclase feldspars with the remaining percentage ferromagnesian silicates.
- Bituminous - Containing much organic, or at least carbonaceous matter, mostly in the form of the tarry hydrocarbons usually described as bitumen.

C

- "C" soil horizon - The soil under the "B" horizon, a layer of unconsolidated, weathered parent material.
- Cambrian - The oldest of the systems into which the paleozoic rocks are divided; also, the corresponding geologic period.
- Cenozoic - Latest of the four eras into which geologic time, as recorded by the stratified rocks of the earth's crust, is divided; it extends from the Mesozoic era to, and including, the present.
- Coastal Plain - Any plain which has its margin on the shore of a large body of water, particularly the sea, and generally represents a strip of recently emerged sea bottom.
- Cretaceous - The third and latest of the periods included in the Mesozoic era; also the system of strata deposited in the Cretaceous period.

D

- Dendritic drainage - The drainage patterns characterized by irregular branching in all directions with the tributaries joining the main stream at all angles.
- Detritus - Material or deposit produced by the disintegration and weakening of rocks that have been moved from their site of origin.
- Devonian - The fourth in order of age of the periods in the Paleozoic era, following Silurian and succeeded by the Mississippian. Also the system of strata deposited at that time.
- Diastrophism - The process or processes by which the crust of the earth is deformed, producing continents and ocean basins, plateaus and mountain flexures and folds of strata and faults.
- Dike - A tabular body of igneous rock that cuts across the structure of adjacent rocks or cuts massive rocks.
- Dip - The angle at which a stratum or any planar is inclined from the horizontal.

E

- Eolian (Aeolian) - Applied to the erosive action of the wind, and to deposits which are due to the transporting action of the wind.
- Evaporites - Sediments which are deposited from aqueous solution as a result of extensive or total evaporation of the solvent.

- Evapotranspiration - A term embracing that portion of the precipitation returned to the air through direct evaporation or by transpiration of vegetation, no attempt being made to distinguish between the two.
- Exogenous - Applied to processes originating at or near the surface of the earth, such as weathering and denudation; and to rocks, ore deposits, and land forms which owe their origin to such processes.
- F
- Fault - A fracture or fracture zone along which there has been displacement of the sides relative to one another parallel to the fracture.
- Fault Scarp - The drift formed by a fault. Most fault scarps have been modified by erosion since the faulting.
- Ferruginous (Ferrugineous) - Of, or pertaining to, or containing iron.
- Flood Plain - That portion of a river valley, adjacent to the river channel, which is built of sediments during the present regimen of the stream and which is covered with water when the river overflows its banks at flood stages.
- Formation - The primary unit in lithostratigraphy consisting of a succession of strata useful for mapping or description.
- G
- Group - A lithostratigraphic unit consisting of two or more formations.
- I
- Igneous - Rocks formed by solidification from a molten or partially molten state.
- J
- Joint - Fracture in rock, generally more or less vertical or transverse to bedding, along which no appreciable movement has occurred.
- Jurassic - The middle of the three periods in the Mesozoic era. Also the system of strata deposited during that period.
- K
- K - Identifies Kelvin thermometric scale; 0°K is absolute zero and equals -273.16°C or -459.4°F .

L

- Lacustrine - Of, or pertaining to, or inhabiting lakes.
- Large scale map - Map which shows a small area of the surface of the earth in great detail.
- Lateritic - Pertaining to a red residual soil developed in humid tropical and subtropical regions of good drainage.
- Lineament - A topographic line that is structurally controlled. Also, lines of landscape which reveal the structural features of the earth's surface and the rock basement.

M

- Meanders - One of a series of somewhat regular and looplike bends in the course of a stream developed when the stream is flowing at grade, through lateral shifting of its course toward the convex sides of the original curves.
- Mesozoic - One of the grand divisions or eras of geologic time, following the Paleozoic and succeeded by the Cenozoic era; comprising the Triassic, Jurassic and Cretaceous periods.
- Metamorphic - Pertaining to all those rocks which have formed in the solid state in response to pronounced changes of temperature, pressure, and chemical environment, which take place, in general, below the shells of weathering and cementation.
- Metamorphism - Process by which consolidated rocks are altered in composition, texture or internal structure by conditions and forces not resulting primarily from burial and the weight of subsequently accumulated over-burden.

O

- Offlap Marine Series - An area where a shoreline has retreated seaward and progressively younger strata have been deposited in layers offset seaward.
- Orogeny (Orogenic) - The process of forming mountains, particularly by folding and thrusting.
- Orthoquartzite - A clastic sedimentary rock composed of silica-cemented quartz sand.
- Outcrop - The exposure of bedrock or strata projecting through the overlying cover of detritus and soil.

P

- Paleogeomorphology - The geomorphology of an area at some specified time in the past.
- Paleozoic - The oldest of the three eras of geologic times, succeeded by the Mesozoic era.
- Perigee - The point in its orbit at which the satellite is closest to the center of the earth. (i.e., point of minimum satellite altitude.)
- Piedmont - Lying or formed at the base of mountains.
- Playa - Shallow basin of a desert plain, in which water gathers after a rain and is evaporated.
- Pleistocene - The earlier of the two epochs in the Quaternary period, in the classification generally used.

Q

- Quaternary - The younger of the two geologic periods or systems in the Cenozoic era.

R

- Rectangular drainage - The pattern characterized by right-angled bends in both the main stream and its tributaries.
- Regolith - The layer or mantle of loose, incoherent rock material of whatever origin, that nearly everywhere forms the surface of the land and rests on the hard or "bed" rocks.
- Reststrahlen Effect - Characteristic absorption peaks (corresponding to lower emission) in the infrared spectrum of silicates; the most important located from 8 to 12 μm . The position of this peak shifts toward lower wavelengths as the silicon-oxygen (Si-O) of the mineral is lowered.
- Riverine - Pertaining to a river.

S

- Sandstone - A cemented or otherwise compacted detrital sediment composed predominantly of quartz grains, the grades of the latter being those of sand. Other mineralogical varieties of sandstone are also recognized.
- Scablands - Used in the Pacific Northwest to describe areas where denudation has removed or prevented the accumulation of a mantle of soil and the underlying rock is exposed or covered largely with its own coarse angular debris.

- Sedimentary - Descriptive term for rock formed of sediment; or rock formed by precipitation from solution.
- Sill - An intrusive body of igneous rock of approximately uniform thickness and relatively thin compared with its lateral extent, which has been emplaced parallel to the bedding or schistosity of the intruded rocks.
- Small Scale Map - Map showing only general features. It covers a large area of the earth but with little detail.
- Stratum - A sedimentary bed or layer of approximately the same kind of rock material, regardless of thickness.
- Stream Piracy - The diversion of the upper part of a stream by the headward growth of another stream.
- Strike - The course or bearing of the outcrop of an inclined bed or structure on a level surface. It is perpendicular to the direction of the dip.
- Strike-Slip Fault - A fault in which the net slip is practically in the direction of the fault strike.
- Subsatellite Point (Subpoint)
(satellite subpoint) - Intersection of the local vertical passing through the satellite with the earth's surface (i. e., the nadir point beneath the satellite), or this point as identified on a picture.
- Syncline - A fold in rocks in which the strata dip inward from both sides toward the axis.
- T
- Tectonics - A study of the broader structural features of the earth and their causes.
- Tertiary - The earlier (older) of the two geologic periods in the Cenozoic era, in the classification generally used. Also, the system of strata deposited during that period.
- Thrust Fault - A reverse fault that is characterized by a low angle of inclination with reference to a horizontal plane.
- Trellis Drainage - A stream pattern in which master and tributary streams are arranged nearly at right-angles with respect to one another.
- W
- Wadi - A ravine or water course, dry except in the rainy season. Some wadies are permanently dry.

APPENDIX E
ABBREVIATIONS

APT	-	Automatic Picture Transmission
ARA	-	Allied Research Associates, Inc.
ART	-	Airborne Radiation Thermometer
ATS	-	Applications Technology Satellite
AVCS	-	Advanced Vidicon Camera System
BUV	-	Backscatter Ultraviolet Radiometer
CDA	-	Command and Data Acquisition
CMB	-	Composite Minimum Brightness Chart
DRID	-	Direct Readout Image Dissector Camera System
DRIR	-	Direct Readout Infrared Radiometer
EOS	-	Earth Observatory Satellite
EROS	-	Earth Resources Observation System
ERTS	-	Earth Resources Technology Satellite
ESMR	-	Electrically Scanning Microwave Radiometer
FWS	-	Filter Wedge Spectrometer
GSFC	-	Goddard Space Flight Center
HDRSS	-	High Data Rate Storage System
HRIR	-	High Resolution Infrared Radiometer
IDCS	-	Image Dissector Camera System
IR	-	Infrared
IRIS	-	Infrared Interferometer Spectrometer
IRLS	-	Interrogation Recording and Location System
ITOS	-	Infrared Television Observation Satellite
ITPR	-	Integrated Temperature Profile Radiometer
LMES	-	Laboratory for Meteorology and Earth Sciences (formerly Laboratory for Atmospheric and Biological Sciences)
MRIR	-	Medium Resolution Infrared Radiometer
MUSE	-	Monitor of Ultraviolet Solar Energy
μm	-	Micrometer

NAS	-	National Academy of Science
NASA	-	National Aeronautics and Space Administration
NCC	-	National Climatic Center
NEMS	-	Nimbus E Microwave Spectrometer
NERO	-	Nimbus Earth Resources Observations
NMRT	-	Nimbus Meteorological Radiation Tape
NOAA	-	National Oceanic and Atmospheric Administration
NSSDC	-	National Space Science Data Center
RCA	-	Radio Corporation of America
RTTS	-	Real Time Transmission System
SCMR	-	Surface Composition Mapping Radiometer
SCR	-	Selective Chopper Radiometer
SDDS	-	Spatial Data Datacolor System
SIRS	-	Satellite Infrared Spectrometer
T&DRE	-	Tracking and Data Relay Experiment
THIR	-	Temperature Humidity Infrared Radiometer